Maximum Power Point Tracking and Power Reserve Control for Photovoltaic System

Thesis submitted in accordance with the requirements of the University of Liverpool for the degree of Doctor in Philosophy by

Xingshuo Li

Department of Electrical Engineering and Electronics
School of Electrical Engineering and Electronics and Computer Science
University of Liverpool

February, 2019

Acknowledgment

I would like to express my special thanks of gratitude to my main supervisor Dr. H. Wen for his kindly helped and guided my research. With his supervision, I published many a substantial high-quality papers. I also would like to thanks my second supervisor Dr. L. Jiang for his kindly encouragement.

I offer my regards and blessings to all of the members of my lab, EE405, especially Mr. H. Shi, Mr. G. Chu and Mr. Q. Pu. My thanks also go to the Department of Electrical Engineering and Electronics at Xi'an Jiaotong-Liverpool University and University of Liverpool for providing the research facilities that made it possible for me to carry out this research.

Finally, I would thanks to my family for their support, encouragement and patience during my pursuit of PhD degree.

Publications

Journals

1. **Li, X.**, Wen, H., Hu, Y., Jiang, L., Xiao, W., "A Novel Sensorless Photovoltaic Power Reserve Control With Simple Real-Time MPP Estimation", *IEEE Transactions on Power Electronics*, Accepted.

2. **Li, X.**, Wen, H., Hu, Y., Jiang, L., "Drift-Free Current Sensorless MPPT Algorithm in Photovoltaic Systems", *Solar Energy*, Accepted.

3. **Li, X.**, Wen, H., Hu, Y., Jiang, L., "A novel beta parameter based fuzzy-logic controller for photovoltaic MPPT application", *Renewable Energy*, 130, pp. 416-427, 2019.

4. **Li, X.**, Wen, H., Chu, G., Hu, Y., Jiang, L., "A novel power-increment based GMPPT algorithm for PV arrays under partial shading conditions", *Solar Energy*, 169, pp. 353-361, 2018.

5. **Li, X.**, Wen, H., Hu, Y., Jiang, L., Xiao, W., "Modified Beta Algorithm for GMPPT and Partial Shading Detection in Photovoltaic Systems", *IEEE Transactions on Power Electronics*, 33 (3), pp. 2172-2186, March 2018.

6. **Li, X.**, Wen, H., Jiang, L., Xiao, W., Du, Y., Zhao, C., "An Improved MPPT Method for PV System with Fast-Converging Speed and Zero Oscillation", *IEEE Transactions on Industry Applications*, 52 (6), pp. 5051-5064, November/December, 2016.

7. **Li, X.**, Wen, H., Jiang, L., Hu, Y., Zhao, C., "An improved beta method with autoscaling factor for photovoltaic system", *IEEE Transactions on Industry Applications*, 52 (5), pp. 4281-4291, September/October, 2016.

8. **Li, X**., Wen, H., Jiang, L., Lim, E.G., Du, Y., Zhao, C., "Photovoltaic modified -parameter-based MPPT method with fast tracking", *Journal of Power Electronics*, 16 (1), pp. 9-17, January 2016.

9. **Li, X.**, Wen, H., "Research on an improved β-based variable step MPPT algorithm", *Dianli Xitong Baohu yu Kongzhi/Power System Protection and Control*, 44 (17), pp. 58-63, 2016.

10. **Li, X.**, Wen, H., Luo, H., "A Comparative Study of the Main Incremental Conductancebased MPPT Techniques for Photovoltaie Applications", *Dianli Dianzi Jishu/Power Electronics*, 50 (12), pp. 91-94+98, 2016.

11. Ma, J., Pan, X., Man, K.L., **Li, X.**, Wen, H., Ting, T.O., "Detection and Assessment of Partial Shading Scenarios on Photovoltaic Strings", *IEEE Transactions on Industry Applications*, 2018, in press.

12. Chu, G., Wen, H., Jiang, L., Hu, Y., **Li, X.**, "Bidirectional flyback based isolated-port submodule differential power processing optimizer for photovoltaic applications", *Solar Energy*, 158, pp. 929-940, 2017.

13. Luo, H., Wen, H., **Li, X.**, Jiang, L., Hu, Y. "Synchronous buck converter based low-cost and high-efficiency sub-module DMPPT PV system under partial shading conditions", *Energy Conversion and Management*, 126, pp. 473-487, 2016.

Conference

1. **Li, X.**, Wen, H., Xiao, W., "A modified MPPT technique based on the MPP-locus method for photovoltaic system", *Proceedings IECON 2017-43rd Annual Conference of the IEEE Industrial Electronics Society*, pp. 2338-2343, 2017.

2. **Li, X.**, Wen, H., Chu, G., Ye, Z. "A novel PV faults diagnosis method based on the structure of differential power processing", *6th International Conference on Renewable Energy Research and Applications, ICRERA 2017*, pp. 685-689, 2017.

3. **Li, X.**, Wen, H., "Evaluation of different maximum power point tracking techniques by using EN 50530 dynamic test standard", *IEEE International Conference on Power Electronics, Drives and Energy Systems, PEDES 2016*, pp. 1-6, 2016.

4. **Li, X.**, Wen, H. "A fuzzy logic controller with beta parameter for maximum power point tracking of Photovoltaic systems", *2016 IEEE 8th International Power Electronics and Motion Control Conference, IPEMC-ECCE Asia 2016*, pp. 1550-1555, 2016.

5. **Li, X.**, Wen, H., Hu, Y., "Evaluation of different maximum power point tracking (MPPT) techniques based on practical meteorological data", *2016 IEEE International Conference on Renewable Energy Research and Applications, ICRERA 2016*, pp. 696-701, 2016.

6. **Li, X.**, Wen, H., Zhao, C., "Improved beta parameter based MPPT method in photovoltaic system", *2015 IEEE 7th International Power Electronics and Motion Control Conference, IPEMC-ECCE Asia 2015*, pp. 1405-1412, 2015.

7. Chu, G., Wen, H., Ye, Z., **Li, X.**, "Design and optimization of the PV-virtual-bus differential power processing photovoltaic systems", *6th International Conference on Renewable Energy Research and Applications, ICRERA 2017*, pp. 674-679, 2017.

8. Ye, Z., Wen, H., Chu, G., **Li, X.**, "Minimum-power-tracking for PV-PV differential power processing systems", *6th International Conference on Renewable Energy Research and Applications, ICRERA 2017*, pp. 696-700, 2017.

9. Ma, J., Zhang, T., Shi, Y., **Li, X.**, Wen, H., "Shading Pattern Detection Using Electrical Characteristics of Photovoltaic Strings", *IEEE International Conference on Power Electronics, Drives and Energy Systems, PEDES 2016*, pp. 1-4, 2016.

10. Ma, J., Bi, Z., Zhu, L., Jiang, Y., **Li, X.**, Wen, H., "On-line soft-sensing model based maximum power point tracking for photovoltaic generation systems", *IEEE International Conference on Power Electronics, Drives and Energy Systems, PEDES 2016*, pp. 1-4, 2016.

11. Luo, H., Wen, H., **Li, X.**, "Distributed MPPT control under partial shading condition", *2016 IEEE 8th International Power Electronics and Motion Control Conference, IPEMC-ECCE Asia 2016*, pp. 928-932, 2016.

12. Du, Y., **Li, X.**, Wen, H., Xiao, W. "Perturbation optimization of maximum power point tracking of photovoltaic power systems based on practical solar irradiance data", *2015 IEEE 16th Workshop on Control and Modeling for Power Electronics, COMPEL*, 2015,

13. Xu, H., Wen, H., **Li, X.**, "Design and evaluation of a solar based single inductor multiple outputs LED lighting", *International Conference on Renewable Power Generation (RPG 2015)*, 2015.

Abstract

As global energy consumption is gradually increasing, a problem facing us is the environmental issues caused by the increasing energy demand. In order to overcome this problem, photovoltaic (PV) energy has been widely used in many countries around the world. Since the power generated by the PV systems mainly depends on the weather conditions, how to effectively obtain the maximum possible power from the PV system under various conditions is still a main problem. Furthermore, PV systems are also required to provide ancillary service as grid regulations and network codes have been also continuously revised. Therefore, the PV technology issues associated with the operating efficiency and system reliability improvement are still the ultimate goal to meet the rising energy demand.

In this thesis, the PV-side control, such as maximum power point tracking (MPPT), global maximum power point tracking (GMPPT) and power reserve control (PRC), are studied. The MPPT and GMPPT based on modified Beta methods are proposed to overcome the technology issues involved with fast-changing weather conditions and PV mismatching condition, respectively. The MPPT dynamic and steady-state efficiency are firstly improved by Beta methods. Then, a PV string equivalent model is proposed to allow Beta methods to work under PV mismatching condition. Both of the simulation and experimental results are validated the effectiveness of the proposed Beta methods.

Furthermore, a novel PRC method is also proposed to provide the ancillary service. With the simple real-time MPP estimation, the proposed PRC method exhibits fast speed and high robustness to estimate the MPP, and good compatibility with existing PV systems. The effectiveness of the proposed PRC method is also validated by simulation and experimental results.

Key Words: Maximum Power Point Tracking (MPPT), Global Maximum Power Point Tracking (GMPPT), Power Reserve Control (PRC) and Photovoltaic (PV) System

Declaration

The author hereby declares that this thesis is a record of work carried out in the Department of Electrical Engineering and Electronics at the University of Liverpool during the period from June 2015 to May 2018. The thesis is original in content except where otherwise indicated.

Contents

List of Figures

List of Tables

List of Abbreviations and Notations

Abbreviations

ABC	Artificial Bee Colony
ACO	Ant-colony Optimization
AEO	Annual Energy Outlook
ASF-Beta	Adaptive Scaling Factor Beta
CCR	Constant Current Region
CPGC	Constant Power Generation Control
CPR	Constant Power Region
CVR	Constant Voltage Region
DIRECT	Dividing Rectangles
DMPPT	Distributed Maximum Power Point
DPP	Differential Power Processing
EIA	Energy Information Administration
EPIA	European Photovoltaic Industry Association
FA	Firefly Algorithm
FLC	Fuzzy Logic Control
FPP	Full Power Processing
FOCV	Fractional Open-circuit Voltage
FSCC	Fractional Short-circuit Current

GMPP	Global Maximum Power Point
GMPPT	Global Maximum Power Point Tracking
GWO	Grey Wolf Optimization
HSU	Humboldt State University
INC	Incremental Conductance
LMPP	Local Maximum Power Point
LSQ	Least Squares
MFs	Membership Functions
MPP	Maximum Power Point
MPPT	Maximum Power Point Tracking
Mtoe	Million Tons of Oil Equivalent
NB	Negative Big
NQI	Newton Quadratic Interpolation
NREL	National Renewable Energy Laboratory
NS	Negative Small
P&O	Perturb and Observe
PB	Positive Big
RoCof	Rate of Change of Frequency
POI	Potentially Optimal Interval
PRC	Power Reserve Control
PRRC	Power Ramp-rate Control
PS	Positive Small
PSC	Partial Shading Condition
PSO	Particle Swarm Optimization

SA	Simulated Annealing
SC	Soft Computing
SDM	Single-diode Model
SM	Sliding Mode
STC	Standard Test Condition
THD	Total Harmonic Distortion
UNLV	University of Nevada, Las Vegas
VSSINC	Variable Step Size Incremental Conductance
ZO-PO	Zero oscillations perturb and observe

Notations

β	Value of β
β_{eq}	Equivalent β Value of the Key Module
β_g	Guiding Parameter for β
β_{max}	Upper Bounding Value for β
β_{min}	Lower Bounding Value for β
η	Reverse Ideality Factor
ω_n	Natural Frequency
ξ	Damping Factor
ΔD	Changes in Duty Cycle
ΔG	Changes in Solar Irradiance
ΔI	Changes in Current
ΔP	Changes in Power
$\Delta P_{interval}$	Power Search Step
ΔV	Changes in Voltage
ΔX	Changes in Step Size
c	Diode Constant for Beta Method
C_{in}	Input Capacitor of DC-DC Converter
C_{out}	Output Capacitor of DC-DC Converter
d	Duty Cycle of DC-DC Converter
E_g	Bandgap Energy of the Semiconductor
G	Solar Irradiance
G_{STC}	Solar Irradiance at the STC
k	Boltzmann Constant

K_{FOCV}	Coefficients of Fractional Open-circuit Voltage
K_{FSCC}	Coefficients of Fractional Short-circuit Current
K_v	Temperature Coefficients of Open-circuit Voltage
K_i	Temperature Coefficients of Short-circuit Current
I_d	Shockley Diode Equation
I_{in}	Input Current for DC-DC Converter
I_{mpp}	Current at the MPP
I_{out}	Output Current for DC-DC Converter
I_{ph}	Photon Current
$I_{ph,STC}$	Photon Current at the STC
I_{pv}	Output Current of PV Source
I_s	Reverse Saturation Current of the Diode
$I_{s,STC}$	Reverse Saturation Current of the Diode at the STC
I_{sc}	Short-circuit Current
I_{string}	Output Current of PV String
L	Inductor for DC-DC Converter
N	Scaling Factor
$M(d)$	Voltage Conversion Ratio
P_{avai}	Maximum Available Power
P_{limit}	Power at Curtailed Level
P_{loss}	Power Loss
P_{max}	Theoretical Maximum Power
P_{mpp}	Power at the MPP
P_{ref}	Reference Power

P_{pv}	Output Power of PV Source
q	Electron Charge
R_{in}	Input Resistance
R_{load}	Load Resistance
R_{out}	Output Resistance
R_{mpp}	Equivalent Resistance at the MPP
R_p	Parallel Resistance
R_{pv}	Equivalent Resistance of PV Source
$R_{pv,ref}$	Reference Equivalent Resistance of PV Source
R_s	Series Resistance
T	Temperature
T_ε	Setting Time for DC-DC Converter
T_p	Sampling Period of MPPT
T_{STC}	Temperature at the STC
V_{eq}	Equivalent Voltage of the Key Module
V_d	Forward Voltage Drop of Bypass Diode
V_{in}	Input Voltage for DC-DC Converter
V_{mpp}	Voltage at the MPP
V_{oc}	Open-circuit Voltage
V_{out}	Output Voltage for DC-DC Converter
V_{pv}	Output Voltage of PV Source
V_{ref}	Reference Voltage
V_s	Linear Voltage Source
V_{string}	Output Voltage of PV String
V_t	Thermal Voltage of the Diode

Chapter 1

Introduction

1.1 Background

The role of energy is important to human being and it is also important to poverty alleviation and economic development [1]. Fig. 1.1 shows the projected global energy consumption from 1990 to 2040 by different energy sources [2]. As shown in Fig. 1.1, it can be seen that the demand of the global energy consumption is gradually increasing and expected to rise around 18,000 million tons of oil equivalent (Mtoe) by 2040, which is approximately 1.5 times compared to that by 2016. Therefore, access to sufficient energy becomes a problem pressing many countries, particularly in development countries, such as China [3].

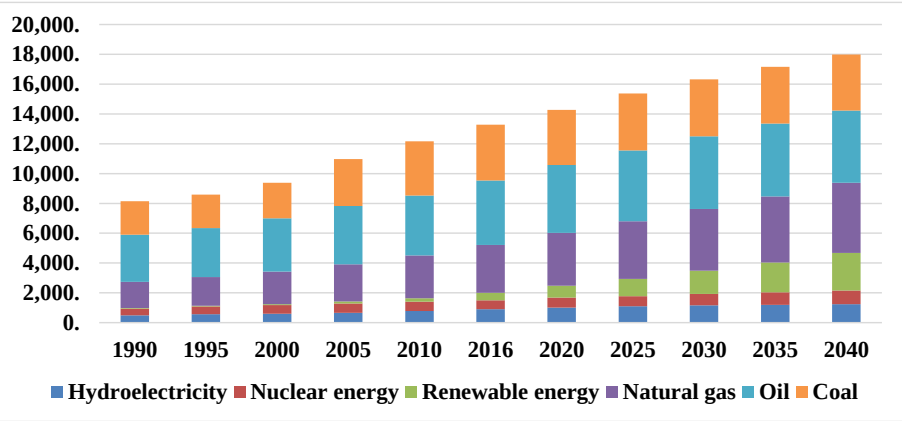

Fig. 1.1: Projected global energy consumption from 1990 to 2040 by energy source (in million metric tons of oil equivalent).

However, the increasing energy demand will also cause environmental issues [3]. As shown in Fig. 1.1, the historical and current energy consumption are dominated by fossil fuels, such as coal, oil and natural gas. The consumption of the fossil fuels will produce carbon dioxide and other greenhouse gases, and will consequently cause global climate

change [4]. Therefore, there is a tradeoff between the economic development associated with the increasing energy demand and the environmental impacts associated with the fossil fuel consumption.

In order to balance this tradeoff, a transition from the current energy system dominated by fossil fuels to a low-carbon one, such as renewable energies, is really essential. However, a problem facing this transition is the relatively high cost of the renewable energies compared to the fossil fuel energies [5]. Generally, the levelized cost of electricity (LCOE) is used as an index to compare different sources of electricity on a consistent groundwork [6]. It can be given as:

$$\text{LCOE} = \frac{\text{sun of costs over lifetime}}{\text{sum of electrical energy produced over lifetime}} \tag{1.1}$$

Since 2010, the US Energy Information Administration (EIA) has published the Annual Energy Outlook (AEO), with yearly LCOE-projections for future utility-scale facilities to be commissioned in about five years' time [7]. Table 1.1 shows the historical summary of EIA's LCOE projections [7]. From Table 1.1, it can be seen that the LCOE of the renewable energies have a significant decrease, especially Photovoltaic (PV) energy. It is expected that the LCOE of PV will be 59.1 USD per megawatt-hour in 2023, which is really cost-effective compared to the other energies.

Table 1.1: Historical summary of EIA's LCOE projections (2010 - 2018)

Estimation		Coal	Natural Gas	Nuclear	Wind		PV
in year	for year				onshore	offshore	
2010	2015	100.4	79.3	119.0	149.3	191.1	396.1
2011	2016	95.1	62.2	114.0	96.1	243.7	211.0
2012	2017	97.7	63.1	111.4	96.0	N/A	152.4
2013	2018	100.1	65.6	108.4	86.6	221.5	144.3
2014	2019	95.6	64.4	96.1	80.3	204.1	130.0
2015	2020	95.1	72.6	95.2	73.6	196.9	125.3
2016	2021	NB	57.2	102.8	64.5	158.1	84.7
2017	2022	NB	53.8	96.2	55.8	NB	73.7
2018	2023	NB	48.1	90.1	48.0	124.6	59.1

[1] Unit in $/MWh.
[2] NB refers to "Not built".

Furthermore, according to Global market outlook 2018-2022 from European Photovoltaic Industry Association (EPIA), PV alone experienced more net power generating capacity added than coal, natural gas and nuclear combined in 2017, as shown in Fig. 1.2 (a) [8]. Furthermore, it also reports that China alone installed nearly 1/3 of the world's PV capacities, as shown in Fig. 1.2 (b).

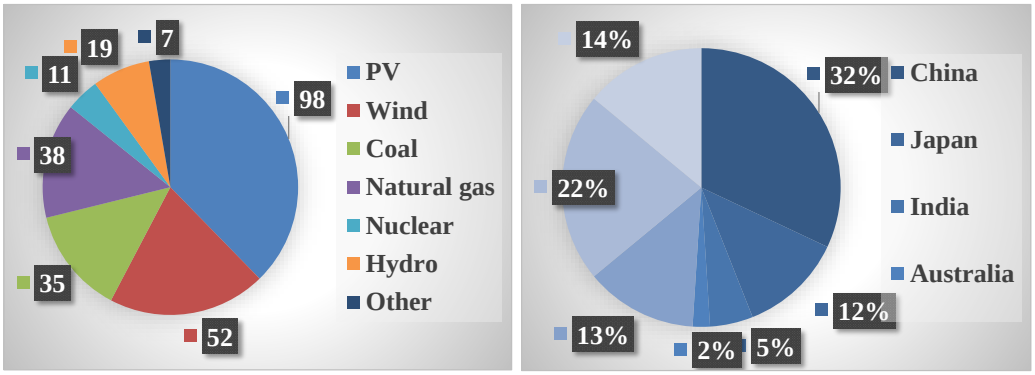

(a) (b)

Fig. 1.2: Global market outlook 2018-2022 from EPIA. (a) Net power generating capacity (unit in GW) added in 2017; (b) Global PV markets total installed shares by end of 2017.

From the aforementioned discussion, it can be seen that the solar energy plays an increasingly important role of balance the challenge between economic development and environmental issues. However, the government policy and subsidies are still the major motivation for the PV development [9]. Furthermore, unlike the fossil fuel energy, the output power of the PV system are various and dependent on different weather conditions. Therefore, the main problem facing us is how to obtain the maximum possible power from the PV system [10]. Besides, as increasing penetration of PV system, a number of conventional power plants will be replaced by PV power plants. As a consequence, it may lead to critical frequency stability challenges [11]. Therefore, the PV technology issues associated with cost reduction, operating efficiency and system reliability improvement is still an ultimate goal to meet the rising energy demand.

1.2 Motivations and Objectives

1.2.1 Brief Introduction of PV System

According to [8], the grid-connected PV system are the most popular one in the current PV market. Fig. 1.3 shows general block diagrams of a grid-connected PV configuration with single-stage and two-stage [12].

As shown in Fig. 1.3 (a), the single-stage configuration consists of four parts, namely PV generator, DC-AC inverter, LCL filter and power grid. Here, the PV generator converts sunlight into DC electricity and the DC electricity is then converted into AC electricity through the DC-AC inverter. Then, the AC electricity is delivered to the LCL filter and a satisfactory total harmonic distortion (THD) of the injected current to the power grid is finally achieved. It should be noted that the DC-link capacitor C_{dc} is to achieve the power

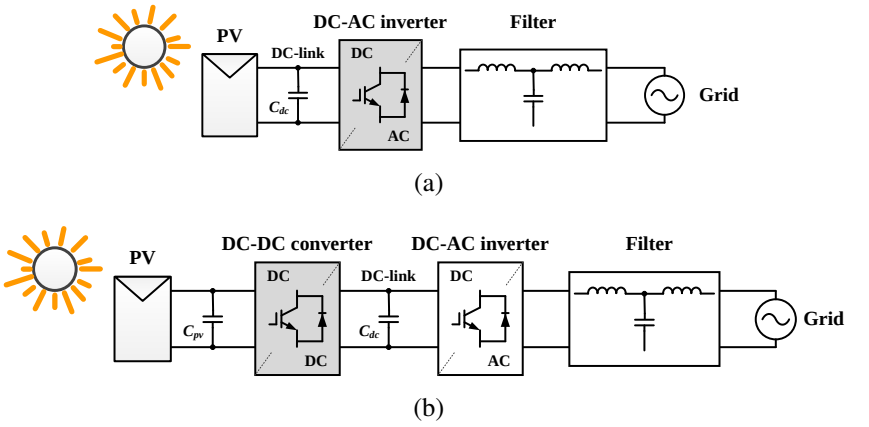

Fig. 1.3: General block diagrams of the grid-connected PV configuration. (a) Single-stage; (b) Two-stage.

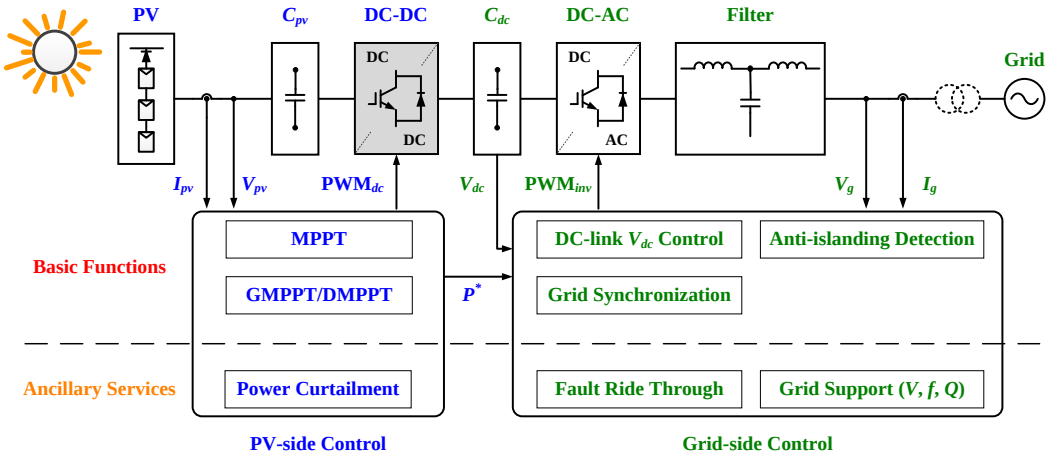

Fig. 1.4: General control blocks of the the grid-connected PV system.

decoupling in this configuration.

For the two-stage configuration, a DC-DC converter is added between the PV source and the DC-AC inverter. Since a boost converter or a buck-boost converter can be integrated into the DC-AC inverter, an accepted DC-link voltage can be achieved. It should be also noted that C_{dc} is changed to the location between the DC-DC converter and the DC-AC inverter.

Fig. 1.4 shows the general control blocks of the the grid-connected PV system [12]. According to [13], the control objectives of the grid-connected PV system can be divided into two parts, namely PV-side control and Grid-side control. As increasing penetration of PV system, some advanced functions, such as grid frequency regulation [11], become a basic requirement. Therefore, the control objectives can be further divided into basic functions and ancillary services [12].

1.2.2 Fast-changing Weather Conditions

The electrical characteristics of a PV module under different weather conditions are plotted in Fig. 1.5. The I-V and P-V curves show the maximum power point (MPP), which represents the maximum power output extracted from the PV generator under certain environmental conditions [14]. Therefore, maximum power point tracking (MPPT) is extremely important, which can extract the maximum power from the PV generator.

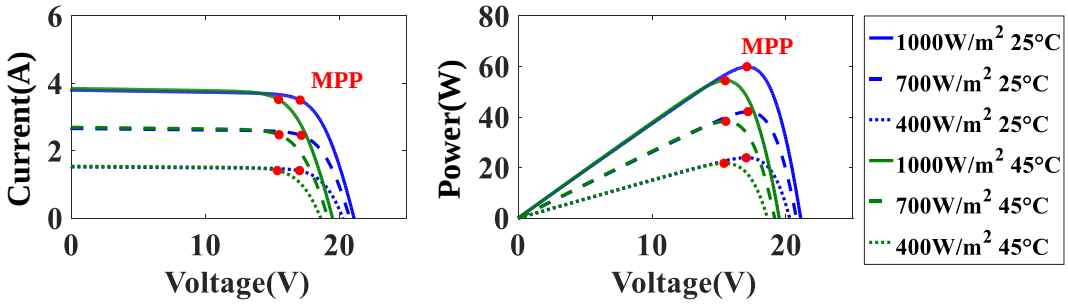

Fig. 1.5: I-V and P-V curves for PV characteristic under different weather conditions.

According to [15, 16], many MPPT methods have been proposed in the previous research. Although these conventional MPPT methods provide a simple way to achieve maximum power, the slow response to fast-changing weather conditions restrict the performance of these MPPT methods.

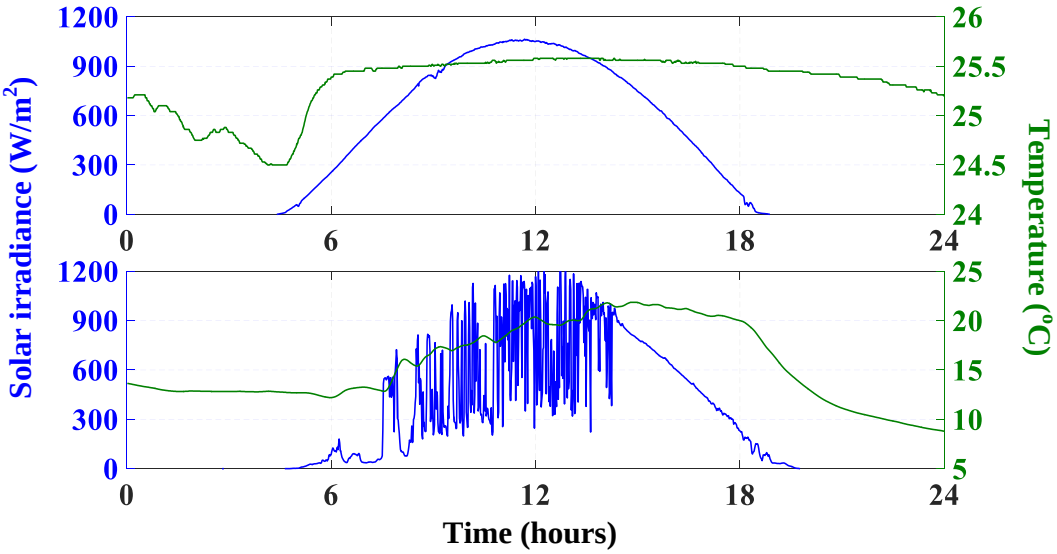

Fig. 1.6: Meteorological data of the desert location and the coastal location in June 9th, 2018. Top: UNLV, Nevada; and bottom: HUS, California.

The meteorological data of Humboldt State University (HSU) and University of Nevada, Las Vegas (UNLV), in June 9th, 2018 are given in Fig. 1.6 [17]. The solar irradiance

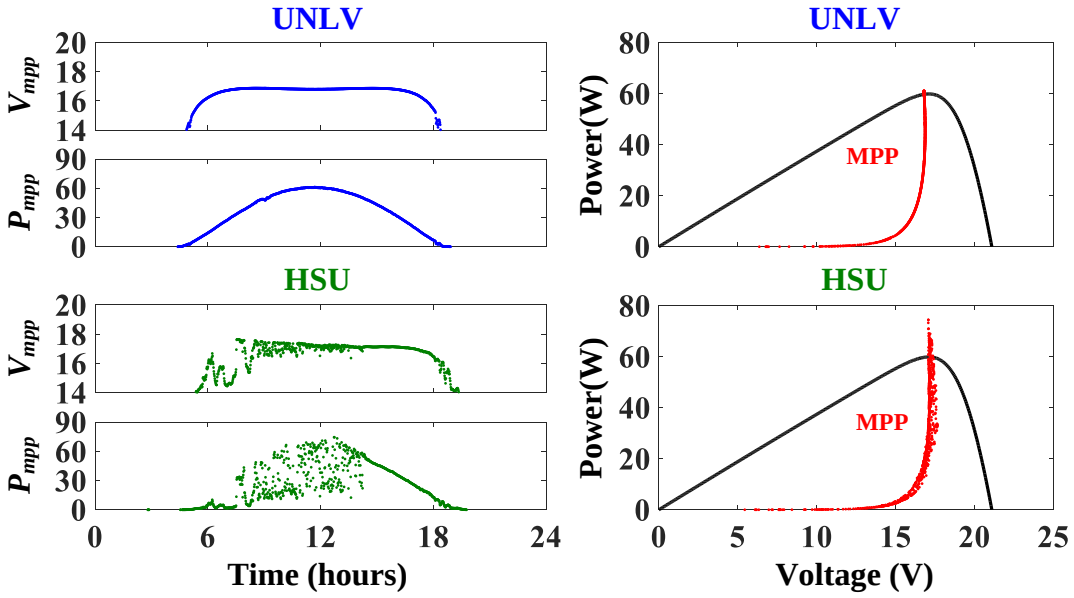

Fig. 1.7: Changes of the MPPs in the HSU and UNLV based on the meteorological data in June 9th, 2018.

in the HSU changes more frequently and dramatically than that of the UNLV due to the different meteorological conditions. The temperature in the HSU is between 10°C and 20°C, while that in the UNLV is around 25°C. Based on this meteorological data, the changes of the MPPs in the HSU and the UNLV can be plotted in Fig. 1.7.

Since the changes of the MPPS is so significant during the time around from 8:00 to 14:00, the tracking the MPPs in the HSU is really challenging. Therefore, it is really necessary to propose a fast-converging speed MPPT method.

1.2.3 PV Mismatching Condition

PV mismatching condition refers to some PV cells or modules which have different operating conditions from one another [18]. As shown in Fig. 1.8, the PV mismatching condition is caused by some PV cells or modules in a PV string or PV array are shaded or aged in the different degrees.

Under this condition, the characteristics of the PV string or PV arrays show multiple local maximum power points (LMPP) and a global maximum power points (GMPP). Although many MPPT methods have been proposed in the previous research, the main drawback of these MPPT methods is that they can only track the single MPP under the uniform condition [19]. In order to solve this drawback, many global maximum power point tracking (GMPPT) methods are also proposed [19]. However, the main drawback of these conventional GMPPT methods is that they may overlook the GMPP and be trapped

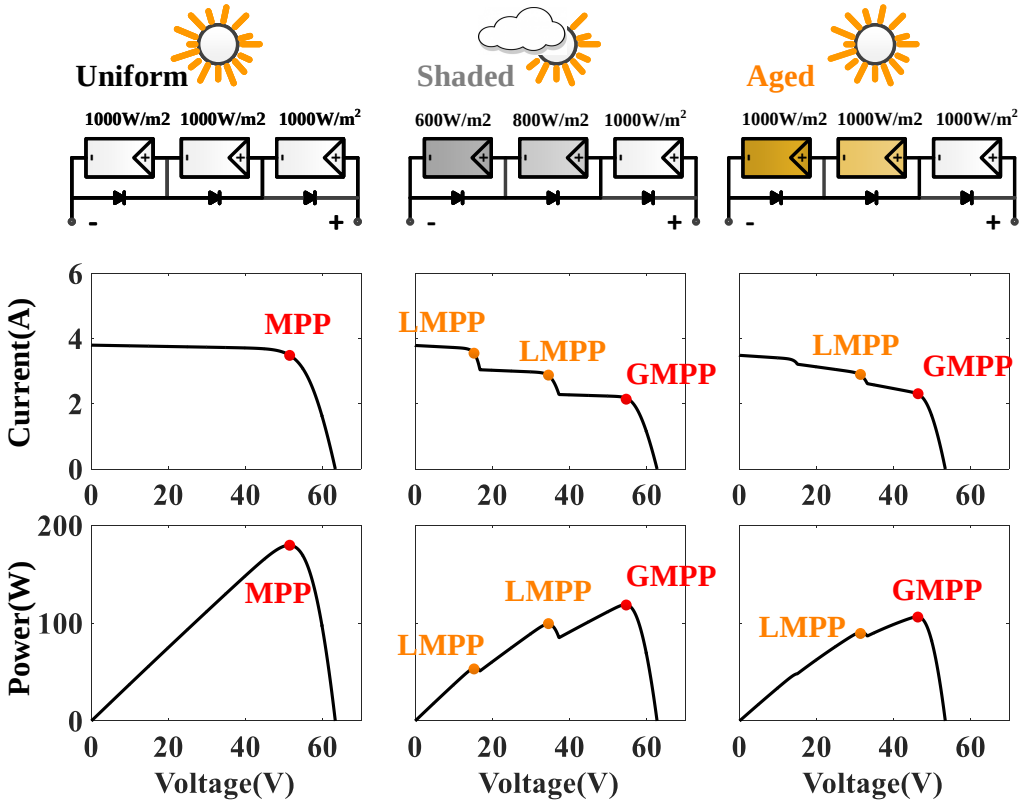

Fig. 1.8: PV mismatching condition caused by some PV cells or modules in a PV string or PV array are shaded or aged in the different degrees.

at the LMPP. Therefore, a more accurate GMPPT method under various PSC patterns is really essential to be proposed.

1.2.4 Ancillary Service Requirement

As increasing penetration of PV system, a large number of conventional power plants will be replaced by the PV power plants. However, since the PV generations do not have rotating parts, no inertial response in the PV systems can be provided during major power disturbances [20]. As shown in Fig. 1.9, the frequency regulation capability is affected if the PV system without ancillary service in the frequency support during load increase. By contrast, the PV system based on the power electronics devices is able to provide a fast frequency regulation if the PV system is involved with the ancillary service. Therefore, the ancillary service requirement on the PV plants to participate in the frequency regulation, becomes more and more important [21].

Power curtailment is believed as a cost-effected method for the grid frequency regulation [22]. With the aid of the power curtailment method, the PV systems can be regulated to work at a suboptimal power level rather the maximum power of the PV source, and then the active power can be reserved in order to realize potential grid support. This method

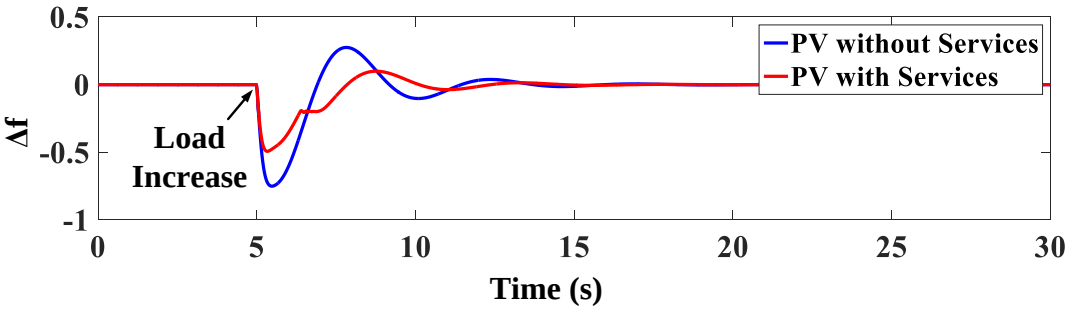

Fig. 1.9: Grid frequency deviation during load increase.

is also famous as power reserve control (PRC). Although some PRC methods have been proposed, they may be not effective under various weather conditions, especially under fast solar irradiance changing. Besides, how to estimate the MPP in the real time is also a difficulty. Therefore, it is really essential to propose a more effective PRC method.

1.3 Main contributions

As previously discussed, the control objectives can be divided into the basic functions, such as the MPPT and the GMPPT, and the ancillary services, such as power curtailment method. Therefore, this thesis is focused on three aspects as follow:

- A fast-converging speed MPPT method under the fast-changing weather conditions is proposed to improve the MPPT performance under fast-changing weather conditions. The guideline of determination of the β parameters considering meteorological data in different locations is provided. The adaptive scaling factor Beta (ASF-Beta) method and zero oscillations perturb and observe (ZO-PO) method are proposed to improve the MPPT dynamic and steady-state efficiency, respectively. The simulation and experimental results validate that the proposed MPPT method outperforms the various conventional MPPT methods. The related research is published on top journals as shown below:

    1. **Li, X.**, Wen, H., Jiang, L., Xiao, W., Du, Y., Zhao, C., "An Improved MPPT Method for PV System with Fast-Converging Speed and Zero Oscillation", *IEEE Transactions on Industry Applications*, 52 (6), pp. 5051-5064, November/December, 2016.

    2. **Li, X.**, Wen, H., Jiang, L., Hu, Y., Zhao, C., "An improved beta method with auto-scaling factor for photovoltaic system", *IEEE Transactions on Industry Applications*, 52 (5), pp. 4281-4291, September/October, 2016.

3. **Li, X**., Wen, H., Jiang, L., Lim, E.G., Du, Y., Zhao, C., "Photovoltaic modified -parameter-based MPPT method with fast tracking", *Journal of Power Electronics*, 16 (1), pp. 9-17, January 2016.
4. **Li, X.**, Wen, H., Hu, Y., Jiang, L., "A novel beta parameter based fuzzy-logic controller for photovoltaic MPPT application", *Renewable Energy*, 130, pp. 416-427, 2019.

- A GMPPT method is proposed to overcome the drawbacks of the conventional GMPPT methods, such as slow tracking speed and tracking failures. Then, a PV string equivalent model is proposed to allow the modified Beta method to work under PV mismatching condition. Finally, the improvement with the proposed method has been validated by comparing with the other GMPPT methods under different PSC patterns. The related research is published on top journals as shown below:

  1. **Li, X.**, Wen, H., Hu, Y., Jiang, L., Xiao, W., "Modified Beta Algorithm for GMPPT and Partial Shading Detection in Photovoltaic Systems", *IEEE Transactions on Power Electronics*, 33 (3), pp. 2172-2186, March 2018.
  2. **Li, X.**, Wen, H., Chu, G., Hu, Y., Jiang, L., "A novel power-increment based GMPPT algorithm for PV arrays under partial shading conditions", *Solar Energy*, 169, pp. 353-361, 2018.

- A novel PRC method with simple real-time MPP estimation is proposed to overcome the drawbacks of the previous PRC method. The developed strategy exhibits fast speed and high robustness to estimate the MPP, and good compatibility with existing PV systems. The effectiveness of the PRC proposed method is also validated by simulation and experimental results. The related research is published on top journals as shown below:

  1. **Li, X.**, Wen, H., Hu, Y., Jiang, L., Xiao, W., "A Novel Sensorless Photovoltaic Power Reserve Control With Simple Real-Time MPP Estimation", *IEEE Transactions on Power Electronics*, Accepted

1.4 Outlines

There are six chapters in this thesis, details of every chapter are introduced as follow:

- Chapters 1 presents the background and introduction of this whole thesis. The motivations and objectives of the PV-sides control, namely MPPT, GMPPT and PRC, are introduced.

- Chapters 2 is a survey of MPPT. The PV output characteristics and models are introduced. The MPPT operating principle is analysed. Various MPPT methods based on three different groups are compared and discussed.

- Chapters 3 proposes an MPPT method which is improved by adaptive scaling factor Beta (ASF-Beta) method and zero oscillations perturb and observe (ZO-PO) method. The guideline of determination of the β parameters is firstly provided. Then, the control mechanism of the ASF-Beta method and the ZO-PO method, which are used to increase tracking speed and minimize oscillations around the MPP, are demonstrated Finally, various of simulation and experimental results are provided to validate the superior performance of the proposed MPPT method over traditional MPPT methods.

- Chapters 4 firstly reviews and compares the various of GMPPT methods. Then, a PV string equivalent model and an modified GMPPT method are proposed, which is more accurate to track the GMPP than the previous methods. Finally, the improvement with the proposed method has been validated by comparing with the other GMPPT methods under different PSC patterns.

- Chapters 5 firstly reviews and compares the various of PRC methods. Then, a novel PRC method with simple real-time MPP estimation is proposed to overcome the drawbacks of the previous PRC method. The developed strategy exhibits fast speed to estimate the MPP, high robustness, and good compatibility with existing PV systems. Simulation and experimental results under various scenarios are provided to validate the effectiveness of the proposed strategy.

- Chapters 6 presents conclusion and future work.

Chapter 2

Literature Review on Maximum Power Point Tracking (MPPT)

2.1 PV Output Characteristics and Models

2.1.1 PV Output Characteristics

I-V and P-V curves are usually used to illustrate the outputs of PV output characteristics [23, 24]. Generally, there are five main parameters to demonstrate the PV output characteristics, such as such as open-circuit voltage V_{oc}, short-circuit currentI_{sc}, voltage at the MPP V_{mpp}, current at the MPP I_{mpp} and power at the MPP P_{mpp}, as shown in Fig. 2.1.

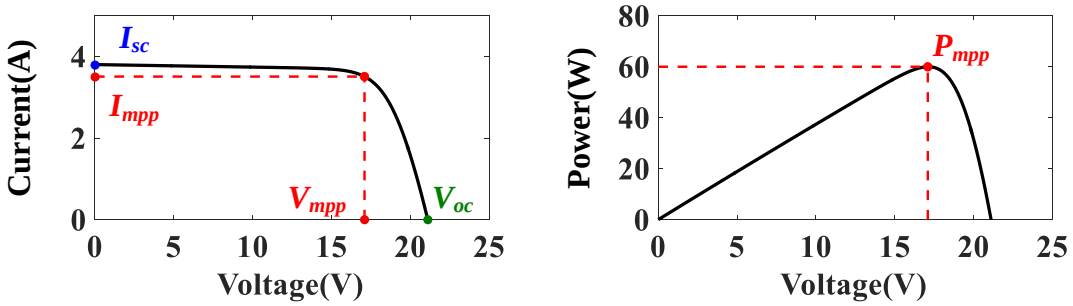

Fig. 2.1: Five main parameters for the PV output characteristics.

The PV manufacturing data sheet normally provides these parameters at standard test condition (STC), where the solar irradiance is at $1000W/m^2$ and the cell temperature is at $25°$. In this thesis, the Solarex MSX-60W is chosen and its electrical characteristics are shown in Table 2.1.

Except the five main parameters as discussed above, temperature coefficients of open-circuit voltage K_v and short-circuit current K_i are also very important to derive the PV characteristics under different weather conditions. Fig. 2.2 demonstrates the strong dependence of the PV output performances on different temperature and solar irradiance

Table 2.1: The electrical characteristics of the MSX-60W

Parameter	Variable	Value
Maximum power	P_{mpp}	$60W$
Voltage at maximum power	V_{mpp}	$17.1V$
Current at maximum power	I_{mpp}	$3.5V$
Open-circuit voltage	V_{oc}	$21.1V$
Short-circuit current	I_{sc}	$3.8V$
Temperature coefficient of V_{oc}	K_v	$-80mV/°C$
Temperature coefficient of I_{sc}	K_i	$0.065\%/°C$

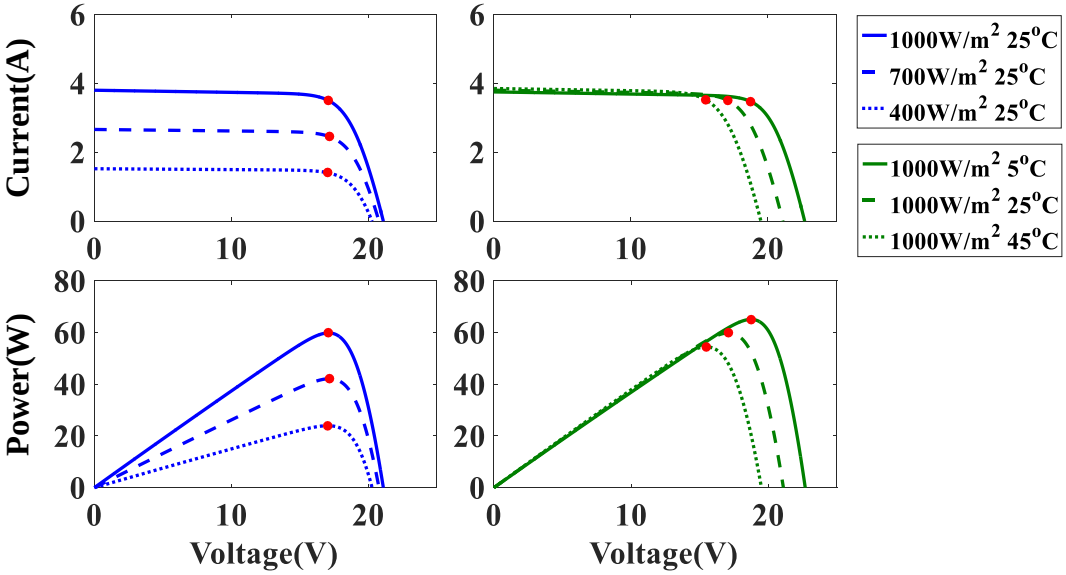

Fig. 2.2: PV characteristics under different weather conditions..

levels [23]. The temperature has a significant effect on V_{oc} but a negligible effect on I_{sc}. At the meanwhile, V_{oc} is logarithmic dependence on the solar irradiance and I_{sc} is linearly dependent on the irradiance.

In order to analyze the behavior of the PV output characteristics, it is necessary to adopt an equivalent circuit model and relevant equations describing it.

2.1.2 PV Equivalent Circuit Models

An equivalent circuits model is usually used to represent PV cells or PV modules. Single-diode model (SDM) is widely used in the previous research [25].

As shown in Fig. 2.3, the currentvoltage (I-V) characteristics according to the SDM model are expressed as

$$I_{pv} = I_{ph} - I_d - \frac{V_d}{R_p} \tag{2.1}$$

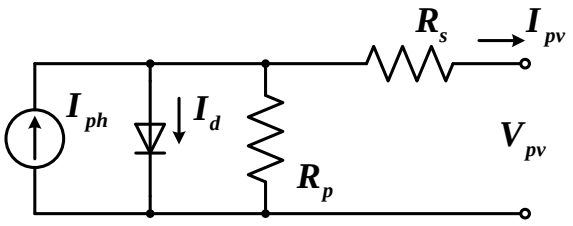

Fig. 2.3: Equivalent circuit of single-diode model (SDM).

where I_{ph} represents the photon current. I_d is Shockley diode equation, which can be expressed as:

$$I_d = I_s \left[e^{\frac{V_d}{\eta V_t}} - 1 \right] \tag{2.2}$$

where I_s is the reverse saturation current of the diode and η is the diode ideality factor. V_d and V_t refer to

$$V_d = V_{pv} + I_{pv} R_s \tag{2.3}$$

$$V_t = \frac{kT}{q} \tag{2.4}$$

where V_t is the thermal voltage, k is Boltzmann constant ($1.38 \times 10^{-23} J/K$), T(in Kelvin) is the temperature of the p–n junction, and q is the electron charge ($1.602 \times 10^{-19} C$). Substitute (2.2-2.4) into (2.1), it can be rearranged as:

$$I_{pv} = I_{ph} - I_s \left[e^{\frac{V_{pv} + I_{pv} R_s}{\eta V_t}} - 1 \right] - \frac{V_{pv} + I_{pv} R_s}{R_p} \tag{2.5}$$

Since there are five unknown parameters in (2.5), this SDM is also known as five-parameter PV model [25].

In order to obtain these unknown parameters, many parameter estimation techniques have been proposed and evaluated in [26]. In this thesis, National Renewable Energy Laboratory (NREL) System Advisor Model is used to obtain the parameters. Therefore, the five unknown parameters can be obtained from Table 2.1 based on the NREL System Advisor Model. The obtained values of the five parameters at the STC are given in Table 2.2.

In this thesis, the parameters η, R_p and R_s are assumed constant when the weather conditions are changed [27]. I_{ph} and I_s under different solar irradiance and temperature can be expressed as:

$$I_{ph} = \left[I_{ph,STC} + K_i (T - T_{STC}) \right] \frac{G}{G_{STC}} \tag{2.6}$$

$$I_s = I_{s,STC} \left(\frac{T_{STC}}{T} \right)^3 e^{\frac{qE_g}{\eta K} \left(\frac{1}{T_{STC}} - \frac{1}{T} \right)} \tag{2.7}$$

where G and T refer to values of solar irradiance and temperature; G_{STC} and T_{STC} refer to values of solar irradiance and temperature at the STC; $I_{ph,STC}$ and $I_{s,STC}$ refer to I_{ph}

Table 2.2: Obtained five parameters based on National Renewable Energy Laboratory (NREL) System Advisor Model

Parameter	Variable	Value at the STC
Photon current	I_{ph}	3.8091A
Diode saturation current	I_s	2.452e^{-10}A
Reverse ideality factor	η	0.97359
Parallel resistance	R_p	161.0752Ω
Series resistance	R_s	0.38659Ω

and I_s at the STC; E_g is the bandgap energy of the semiconductor ($E_g = 1.12eV$ for the polycrystalline Si at $25°$).

2.2 MPPT Introduction

2.2.1 MPPT Operating Principle

The principle behind MPPT is the impedance match between the PV generator output and the load condition [24]. Assuming that a PV panel is directly connected with a resistor load, which is shown in Fig. 2.4 (a). The operating point is plotted as the intersection between the I–V curve and load line when the resistance is 7.61Ω. If the PV module is connected with a variable resistor, the operating point can move alone the PV I–V curve by adjusting the value of the resistor, as shown in Fig. 2.4 (b).

Generally, the load requires either constant current or voltage, so the load impedance cannot always be adjusted for the MPPT. Therefore, a controlled power interface, as shown in Fig. 2.5, is connected between the PV generator and load to realise an equivalent resistance to match the MPP. Assuming that a DC-DC converter is used as the controlled power interface, where I_{in} and V_{in} are input current and voltage, respectively; I_{out} and V_{out} are output current and voltage, respectively; d refers to the duty cycle of the DC-DC converter.

Assuming that the DC-DC converter is ideal, the mathematical expression for the DC-DC converter can be given by:

$$V_{in} = \frac{V_{out}}{M(d)} \tag{2.8}$$

$$I_{in} = M(d) \cdot I_{out} \tag{2.9}$$

where $M(d)$ is the voltage conversion ratio. Divide (2.8) by (2.9), it can be derived as:

$$R_{in} = \frac{V_{in}}{I_{in}} = \frac{V_{out}/M(d)}{M(d) \cdot I_{out}} = \frac{1}{M(d)^2} \cdot \frac{V_{out}}{I_{out}} = \frac{R_{out}}{M(d)^2} \tag{2.10}$$

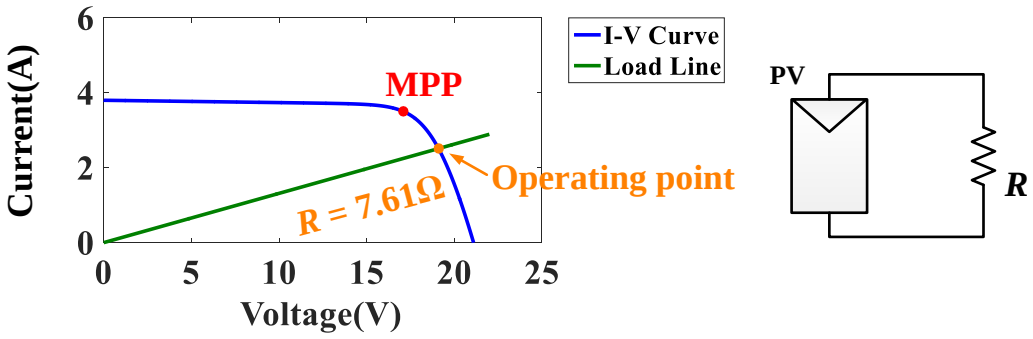

(a)

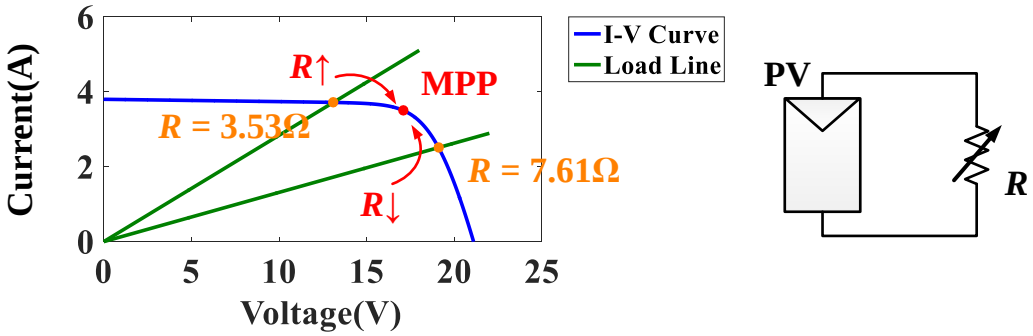

(b)

Fig. 2.4: Impedance match for the MPPT: (a) direct load match; (b) variable load match.

where R_{in} refers to the input resistance and R_{out} refers to the output resistance. Since the input of the DC-DC converter is the PV source, (2.10) can be rewritten as:

$$R_{pv} = \frac{R_{load}}{M(d)^2} \tag{2.11}$$

where R_{pv} refers to the equivalent resistance of the PV source, and R_{load} represents the load resistance.

It should be noted that there are different $M(d)$ for different DC-DC converters, as summarized in Table 2.3. Taking the boost converter as an example, its $M(d)$ is given as below:

$$M(d) = \frac{1}{1-d} \tag{2.12}$$

Substitute (2.12) into (2.11), it can be derived as:

$$R_{pv} = R_{load}(1-d)^2 \tag{2.13}$$

From discussion above, the left terms in (2.13) can be regarded as the equivalent resistance. Here, assuming a boost converter is used and R_{load} is set to 25Ω, the corresponding I-D-V curve is plotted in Fig. 2.6. By adjusting the value of d, the operating point alone the PV I-V curve can be changed. With a certain value of d, the MPP can be located.

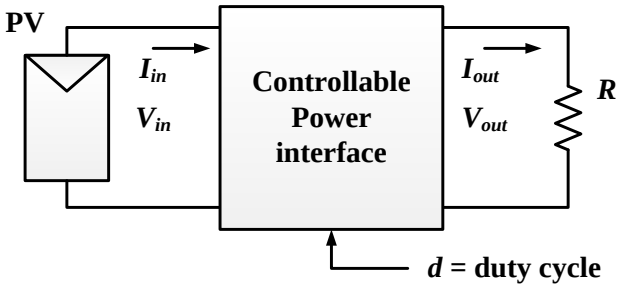

Fig. 2.5: Controlled power interface between the PV generator and load.

Table 2.3: Summarization of $M(d)$ and R_{pv} for different DC-DC converters

Converter	$M(d)$	R_{pv}
Buck	d	$\frac{1}{d^2}R_{load}$
Boost	$\frac{1}{1-d}$	$(1-d)^2 R_{load}$
Buck-Boost	$-\frac{d}{1-d}$	$\frac{(1-d)^2}{d^2}R_{load}$
Cuk	$-\frac{d}{1-d}$	$\frac{(1-d)^2}{d^2}R_{load}$
SEPIC	$\frac{d}{1-d}$	$\frac{(1-d)^2}{d^2}R_{load}$

2.2.2 MPPT Categorization Base on Algorithmic Characteristics

Generally, there are two aspects that need consideration to evaluate the performance of MPPT methods [28], namely steady-state MPPT efficiency and dynamic MPPT efficiency The steady-state MPPT efficiency refers to the efficiency of MPPT methods during the steady-state stage when the weather conditions are not changed. Since the operating point is around the MPP during the steady-state stage, the steady-state MPPT efficiency is also used to describe the accuracy of the located MPP. Normally, the steady-state MPPT efficiency should be very high (typically larger than 99%).

When the weather conditions are changed, the MPP needs to be relocated and this process is called dynamic stage. During the dynamic stage, the efficiency of MPPT methods demonstrates the speed that the MPP is relocated. According to the previous research, the dynamic MPPT efficiency could be higher than 98% [10].

So far, a large number of MPPT have been proposed in the literature [15, 16, 29]. Based on the characteristics of the available MPPT methods, they can be roughly divided into three groups [30, 31]:

- Heuristic method

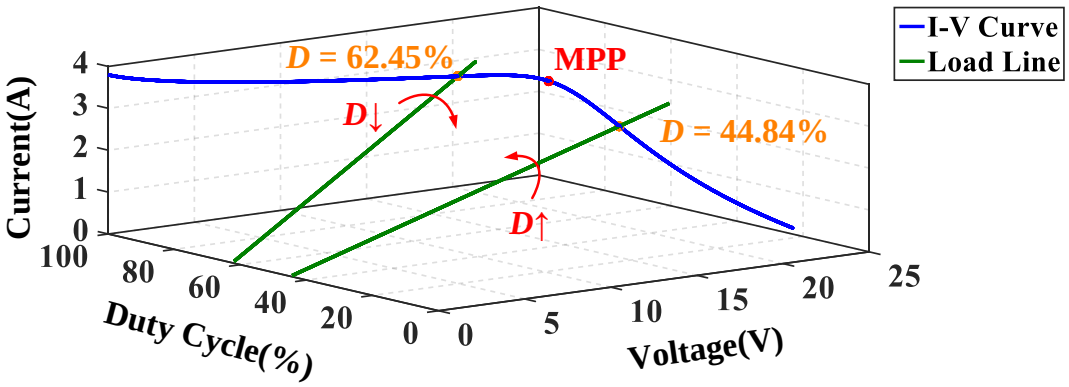

Fig. 2.6: I–D–V curve for impedance match with controlled power interface.

- Model-Based method
- Hybrid method

The heuristic method is based on trial-and-error approach [30, 31]. Firstly, the PV system is disturbed by the algorithm. Then, the algorithm observes the effect caused by this disturbance and take a proper action. This process is repeated until the optimal point is found. Generally, the heuristic method is relatively simple and very effective under different weather conditions. However, the drawback of such algorithms is its poor performance in fast-changing weather conditions [31].

The model-based method relies on the mathematical model of the PV generator [32]. The MPP can be analytically determined by these algorithms, so the dynamic performance of this algorithm is generally better than the heuristic method. However, the effectiveness of the model-based method is affected by the PV model accuracy.

The hybrid method combines the heuristic method and the model-based method, which adopts the their advantages and overcomes their drawbacks. [30, 31]. Generally, the hybrid method has two stages. In the dynamic stage, the model-based method is used to estimate the vicinity of the MPP. Then, the heuristic method is used to locate the exact MPP after the dynamic stage is changed to the steady-state stage.

2.2.3 MPPT Categorization Base on MPPT Implementation

Except the algorithmic characteristics, the MPPT methods can be also divided into five groups based on the MPPT implementation, as shown in Fig. 2.7. Fig. 2.7 (a) shows the most common implementation where the PV-side current sensor and/or voltage sensor are required. It should be noted that the majority of the available MPPT methods are based on this implementation [15]. By contrast, the output voltage sensor and/or current sensor can be also used to realise the MPPT, as shown in Fig. 2.7 (b). However, this kind of

implementation cannot guarantee the true MPPT [15].

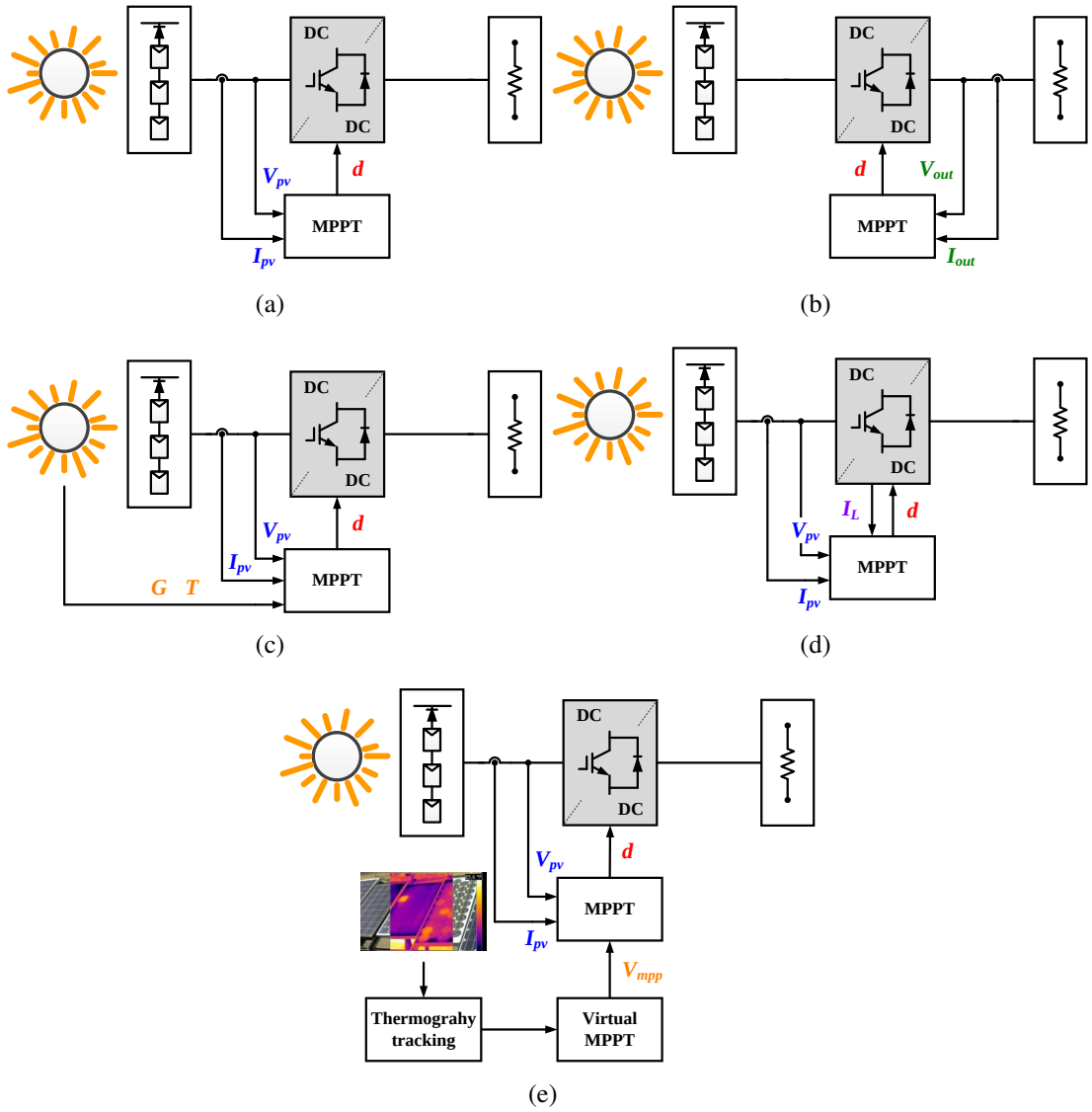

Fig. 2.7: Different MPPT implementations: (a) PV-side sensors; (b) Output sensors; (c) Additional sensors with solar irradiance and/or temperature; (d) Additional sensors with inductor current; (e) Additional sensors with thermography camera.

Additional sensors are also used in some MPPT implementations. As shown in Fig. 2.7 (c), the solar irradiance and/or temperature are measured and sent to the MPPT controller. Generally, only the model-based methods and some MPPT methods also require this implementation [31]. Besides, some MPPT method also requires to measure the inductor current, such as sliding mode (SM) control [33], as shown in Fig. 2.7 (d). In recent years, the thermography-based virtual MPPT is proposed in [34] where a thermography camera is used to assist the MPPT, as shown in Fig. 2.7 (e). Although the effectiveness of these implementations with additional sensors are validated, the cost and complexity of them

are generally high due to more sensors used.

As aforementioned discussion, the MPPT implementation with the PV-side sensors is the most generic MPTT algorithm. Therefore, in this thesis, only the MPPT methods based on this implementation are studied.

2.3 Heuristic Method

2.3.1 Perturb and Observe and incremental conductance method

Perturb and observe (P&O) and incremental conductance (INC) method are the most basic heuristic method [30, 31]. The operating principle of the P&O method and the INC method are summarized in Fig. 2.8 [35–39]. From Fig. 2.8, perturbation direction and perturbation step size are needed to be decided by both of the P&O method and the INC method [40, 41].

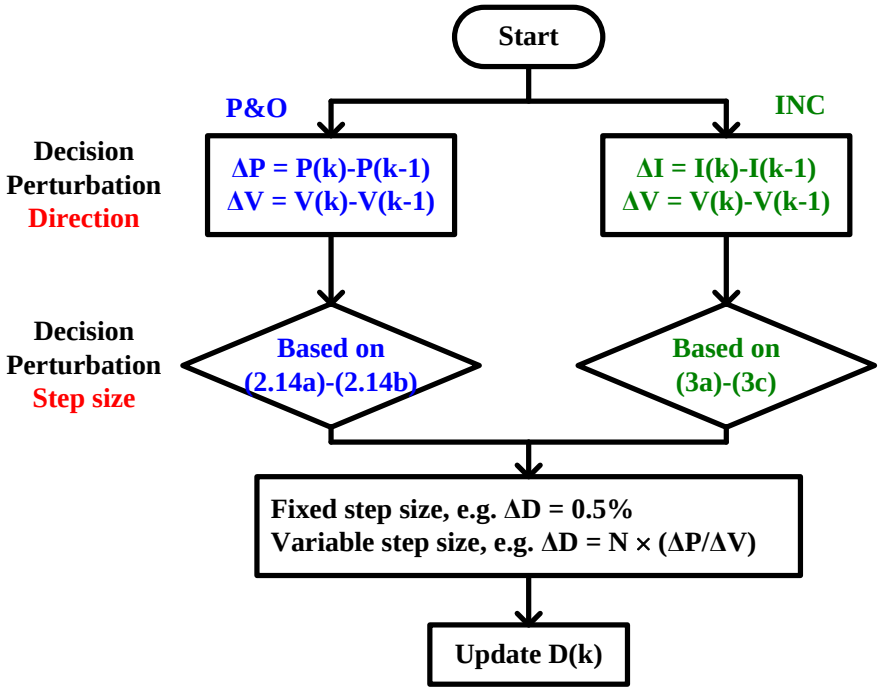

Fig. 2.8: The summarized flowchart of the P&O method and the INC method.

Fig. 2.9 illustrates the how to determine the perturbation direction for the P&O method and the INC method. As illustrated in Fig. 2.9, the perturbation direction for the P&O method and the INC method are derived from the P-V characteristics, which can be summarized as

$$P\&O \begin{cases} \dfrac{\Delta P}{\Delta V} > 0, \text{ Left of MPP} & \text{(2.14a)} \\ \dfrac{\Delta P}{\Delta V} < 0, \text{ Right of MPP} & \text{(2.14b)} \end{cases}$$

$$INC \begin{cases} \dfrac{\Delta I}{\Delta V} > -\dfrac{I}{V}, & \text{Left of MPP} \quad (2.15a) \\ \dfrac{\Delta I}{\Delta V} = -\dfrac{I}{V}, & \text{At MPP} \quad (2.15b) \\ \dfrac{\Delta I}{\Delta V} < -\dfrac{I}{V}, & \text{Right of MPP} \quad (2.15c) \end{cases}$$

where ΔP, ΔV and ΔI refer to the changes in power, voltage and current, respectively.

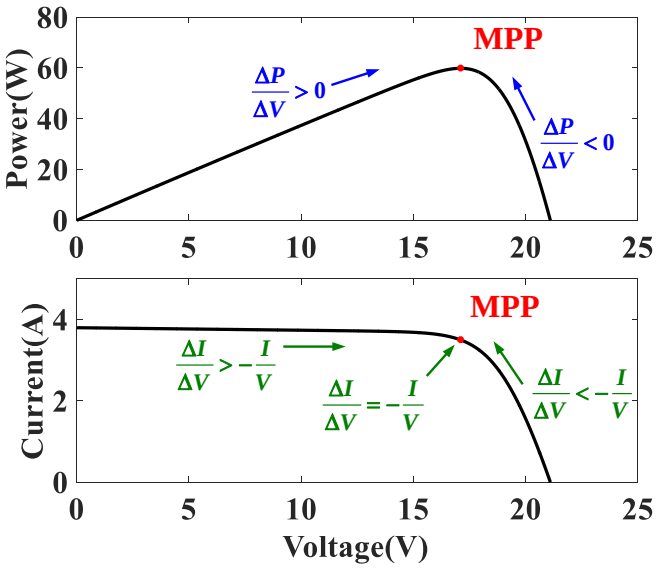

Fig. 2.9: Determination of the perturbation direction for the P&O method and the INC method.

Fig. 2.10 demonstrates the behaviors of the P&O method and the INC method during the steady-state stage. The point A and C refer to the location on the left of the MPP and the right of the MPP, respectively. The point B refers to the nearly coincident location with the MPP. Assuming the operating point moves from the point A to the point B, (2.14a) and (2.15a) are satisfied. Thus, the operating point will keep moving towards the right side and reach the point C. At the point C, (2.14b) and (2.15c) are satisfied, so the operating point moves back to the point B. Then, the operating point will keep moving towards the left side since (2.14b) and (2.15c) are still satisfied. Finally, the operating point will repeat this process following the trajectory (A) $\rightarrow$ (B) $\rightarrow$ (C) $\rightarrow$ (B) $\rightarrow$ (A). Since there are three power/voltage levels in the steady-state stage, this behavior is also famous as three-level oscillations [35].

In most of cases, both of these methods are able to make a correct movement towards the MPP. However, these methods may make a wrong movement and drift from the MPP under a sudden solar irradiance increase [10]. Fig. 2.11 shows the movement of the operating point under the sudden irradiance changes. When the solar irradiance is suddenly

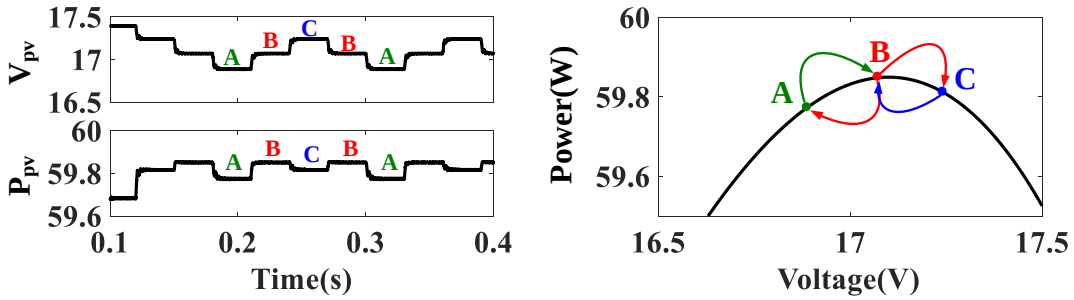

Fig. 2.10: Steady-state three-level oscillations around the MPP.

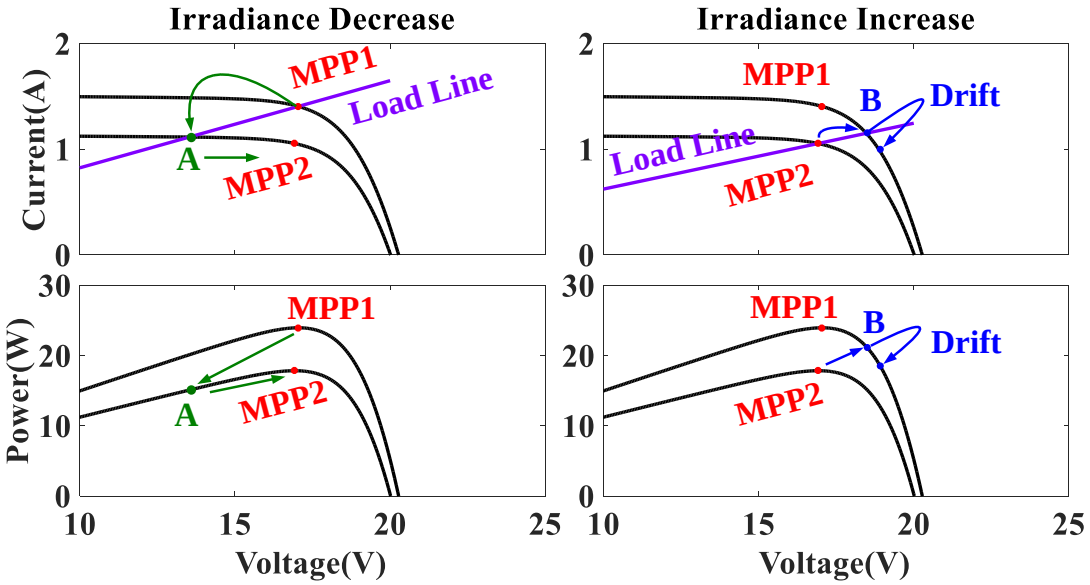

Fig. 2.11: Movement of the operating point under the sudden irradiance changes.

decreased, d is not changed at that moment. Hence, the operating point immediately moves from MPP1 to A through the load line. At this time, since ΔP, ΔV and ΔI are decreased, both of (2.14a) and (2.15a) are satisfied. Therefore, the P&O method and the INC method correctly make a right movement towards MPP2 and there is no drift happened. When the solar irradiance is suddenly increased, the operating point immediately moves from MPP2 to B. However, ΔP, ΔV and ΔI are increased and (2.14a) and (2.15a) are also satisfied. Therefore, a wrong step change is made by the P&O method and the INC method, and the operating point drifts away from the MPP1.

In terms of the perturbation step size, the fixed-step size is generally used for the P&O and INC methods [35]. However, simultaneous optimization of the steady-state performance and the dynamic performance is very difficult [10]. Fig. 2.12 shows that the different fixed-step sizes for the P&O and INC method. Assuming that two different fixed-step sizes, namely 1V and 0.5V, are used to track the MPP at the same starting point. From Fig. 2.12, it can be seen that the method with the larger step size has a better

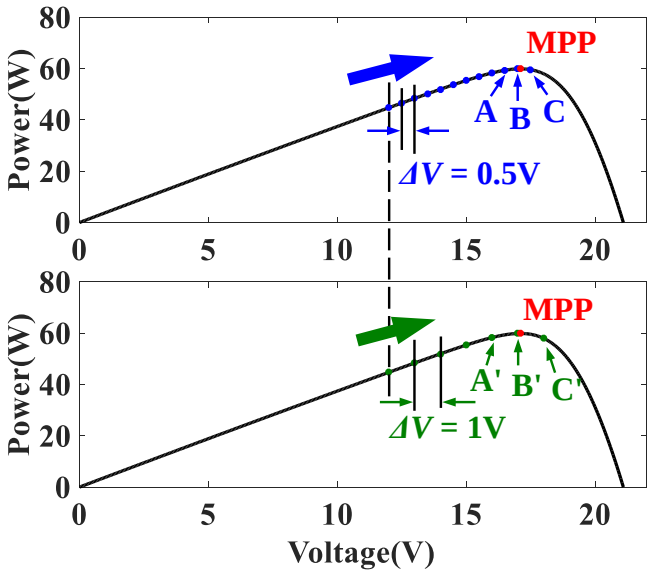

Fig. 2.12: Performance of the different fixed-step size for the P&O and INC method.

dynamic performance. The method with the larger step size only requires 6 steps to reach the MPP while that with the smaller step size needs 11 steps. After the MPP is reached, the system oscillates around the MPP. As a consequence, the method with the smaller step size has a better steady-state performance.

As aforementioned discussion, there are three drawbacks for the basic P&O and INC methods:

- Steady-state oscillations during the steady-state stage
- Drift conditions under the sudden irradiance changes
- Simultaneous optimization of the steady-state performance and the dynamic performance

In order to solve these problems, many modified or improved P&O and INC methods are proposed and will be reviewed in the following sections.

2.3.2 Drift-Free Methods

In order to avoid the drift condition, there are many drift-free methods to solve this, such as setting a constraint on step size [35] or power threshold ΔP [42]. However, it is difficult to tune these parameters, and they may not be suitable for all of the weather conditions.

As a matter of fact, another solation has been proposed in [43, 44] by incorporating the information of ΔI in the decision part. Since the drift condition is normally happened during the irradiance increases, it is only required to incorporate ΔI in (2.14a) and

(2.15a). Therefore, (2.14a) can be rewritten as below:

$$\begin{cases} \dfrac{\Delta P}{\Delta V} > 0 & \Delta I > 0, \text{ Right of MPP} \quad (2.16a) \\ \dfrac{\Delta P}{\Delta V} > 0 & \Delta I < 0, \text{ Left of MPP} \quad (2.16b) \end{cases}$$

and (2.15a) can be rewritten as below:

$$\begin{cases} \dfrac{\Delta I}{\Delta V} > -\dfrac{I}{V} & \Delta I > 0, \text{ Right of MPP} \quad (2.17a) \\ \dfrac{\Delta I}{\Delta V} > -\dfrac{I}{V} & \Delta I < 0, \text{ Left of MPP} \quad (2.17b) \end{cases}$$

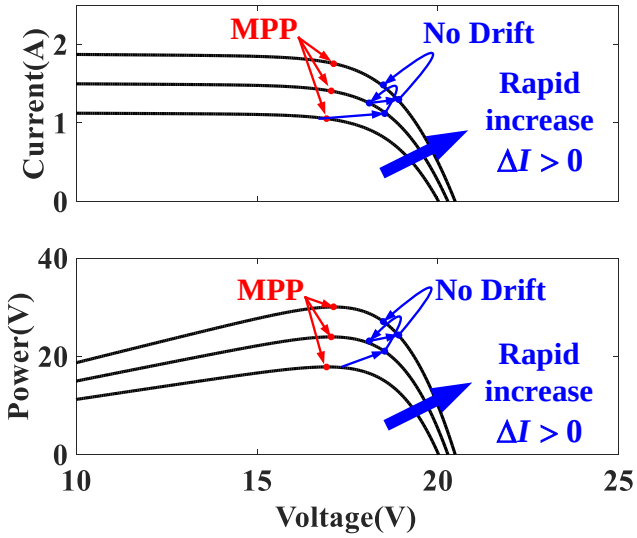

Fig. 2.13: Movement of the operating point for the drift-free modified P&O method and INC method.

Fig. 2.13 shows how the operating point changes under the rapid irradiance increase for these drift-free methods. With the aid of ΔI incorporation, the drift-free method can successfully eliminate the drift condition. Compared to the other drift-free methods in [35, 42], the solution in [43, 44] is much simpler and more adaptive in different weather conditions.

2.3.3 Variable-Step Methods

Generally, the variable-step size is used to solve the tradeoff between the steady-state and dynamic performance. The step size can be automatically adjusted by the P-V curve gradient [45–48], P-I curve gradient [49] and P-D curve gradient [50].

Among these methods, the P-V curve gradient is the most commonly used. Thus, the step size ΔX can be expressed as below:

$$\Delta X = N \times \left| \frac{\Delta P}{\Delta V} \right| \quad (2.18)$$

where ΔX are commonly used as ΔD or ΔV, N is a fixed scaling factor adjusted at the sampling period to regulate the step size [45].

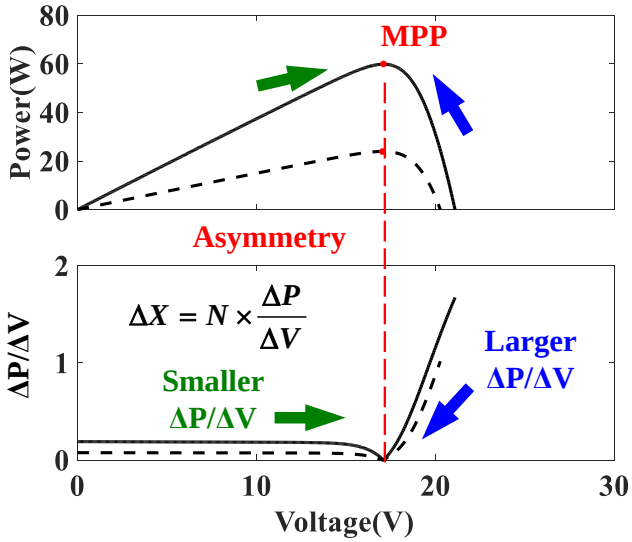

Fig. 2.14: Asymmetrical variable-step size method.

Fig. 2.14 shows the curve of the term, namely $\Delta P/\Delta V$, is highly asymmetrical relative to the MPP. Consequently, it will result in a larger step size in the right-hand side of the MPP and a smaller step size in the left-hand. Therefore, the value of N must be used and tuned to balance this right-and-left asymmetry of the gradient of the P-V curve. However, this value of N may not be suitable for all of the weather conditions. For example, this asymmetry becomes more significant, when the solar irradiance decreases, as marked in black dash lines in Fig. 2.14.

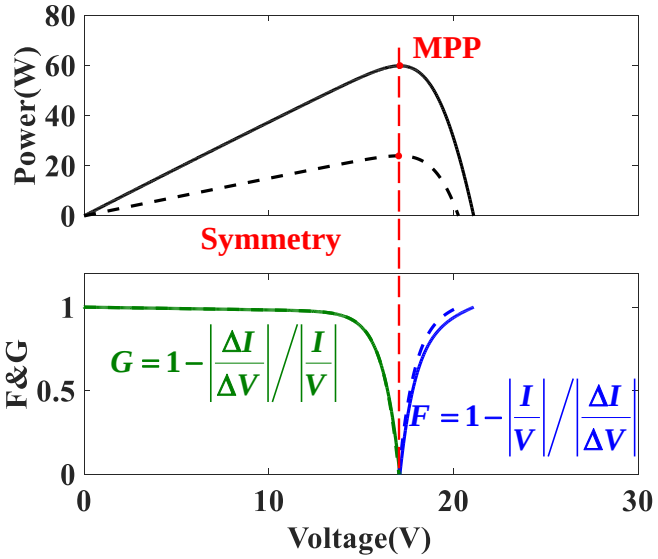

Fig. 2.15: Symmetrical variable-step size method.

Unlike the aforementioned asymmetrical variable-step size MPPT methods, a symmetrical variable-step size MPPT method is proposed in [51]. This method uses two parameters, namely F and G, to regulate the step size, as shown below:

$$\begin{cases} G = 1 - \left|\dfrac{\Delta I}{\Delta V}\right| \Big/ \left|\dfrac{I}{V}\right|, \text{ Left of MPP} & \text{(2.19a)} \\ F = 1 - \left|\dfrac{I}{V}\right| \Big/ \left|\dfrac{\Delta I}{\Delta V}\right|, \text{ Right of MPP} & \text{(2.19b)} \end{cases}$$

Then, the step size ΔX can be derived as below:

$$\Delta X = \begin{cases} \Delta N \times G, \text{ Left of MPP} & \text{(2.20a)} \\ \Delta N \times F, \text{ Right of MPP} & \text{(2.20b)} \end{cases}$$

As shown in Fig. 2.15, the curve of F and the curve of G are highly symmetrical relative to the MPP. Furthermore, even if the weather condition changes, such as irradiance decreases, the symmetry between F and G is still maintained. Therefore, this symmetrical variable-step size MPPT method is more adaptive than the asymmetrical variable-step size MPPT methods.

2.3.4 Parabolic Prediction

Parabolic prediction method is another heuristic method [52–54]. It can be demonstrated that a parabolic curve gives a good approximation of the P-V characteristics, as shown in Fig. 2.16. A quadratic polynomial can be written as:

$$P_{pv} = aV_{pv}^2 + bV_{pv} + c \tag{2.21}$$

Assuming that three points in the P-V curve are known, namely (V_1 P_1), (V_2 P_2) and (V_3 P_3). The parameters a, b and c can be obtained:

$$a = \frac{P1}{\Delta V12 \cdot \Delta V13} + \frac{P2}{\Delta V21 \cdot \Delta V23} + \frac{P3}{\Delta V31 \cdot \Delta V32} \tag{2.22}$$

$$b = -\frac{P1(V2+V3)}{\Delta V12 \cdot \Delta V13} + \frac{P2(V1+V3)}{\Delta V21 \cdot \Delta V23} + \frac{P3(V1+V2)}{\Delta V31 \cdot \Delta V32} \tag{2.23}$$

$$c = \frac{P1 \cdot V2 \cdot V3}{\Delta V12 \cdot \Delta V13} + \frac{P2 \cdot V1 \cdot V3}{\Delta V21 \cdot \Delta V23} + \frac{P3 \cdot V1 \cdot V2}{\Delta V31 \cdot \Delta V32} \tag{2.24}$$

where

$$\Delta V_{ij} = V_i - V_j \quad i, j = 1, 2, 3. \tag{2.25}$$

The iteration process for the parabolic prediction method is demonstrated in Fig. 2.17. Initially, three points on the P-V curve are measured and a, b and c can be obtained. Then, the operating point will move to the reference voltage V_{ref}:

$$V_{ref} = -\frac{b}{2a} \tag{2.26}$$

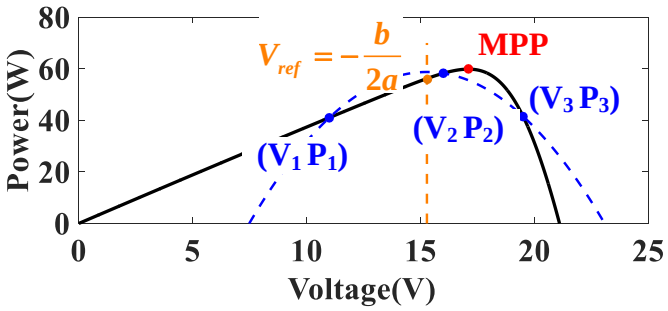

Fig. 2.16: Approximation of the P-V characteristics by a parabolic curve.

After the operating point moves to the new position, the power value at this new position P_4 will be compared with P_1, P_2 and P_3. The lowest power point of the four will be dropped and the rest of the three points will be used for the next iteration. This iteration will be continuously repeated until the MPP is reached.

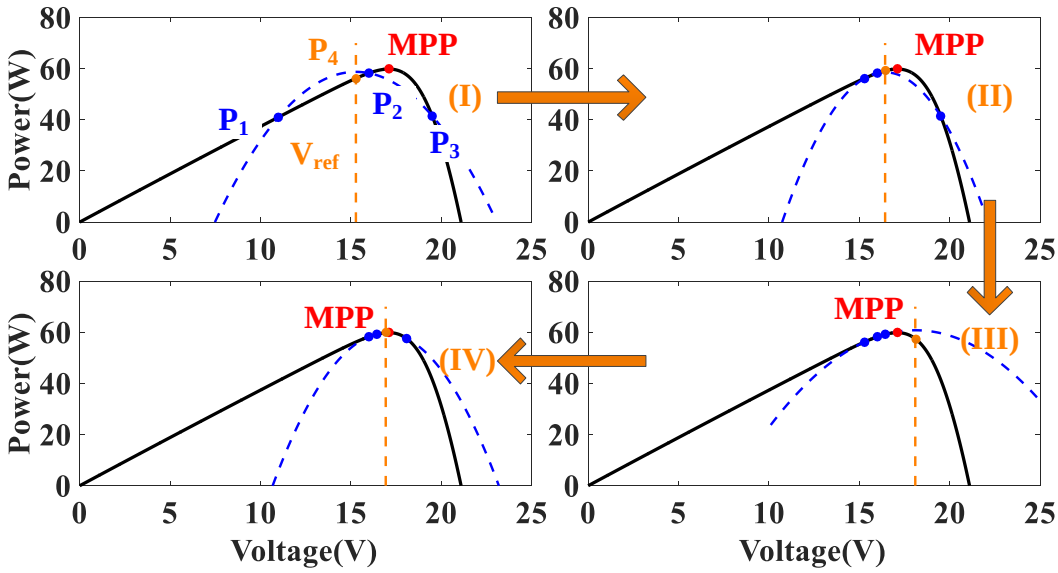

Fig. 2.17: Iteration process for the parabolic prediction method.

The advantage of this method is its fast convergence speed. However, this convergence speed is highly depended on the selected initial points. Besides, the implementation of this method is also difficult since an extra consideration should be enforced if the solar irradiance is changed [54].

2.3.5 Fuzzy Logic Control (FLC)

Fuzzy logic control can be also regarded as a heuristic method. Generally there are three stages for the the FLC method [15], which is shown in Fig. 2.18. In the first stage, the numerical input variables are converted into equivalent linguistic variables as input fuzzy

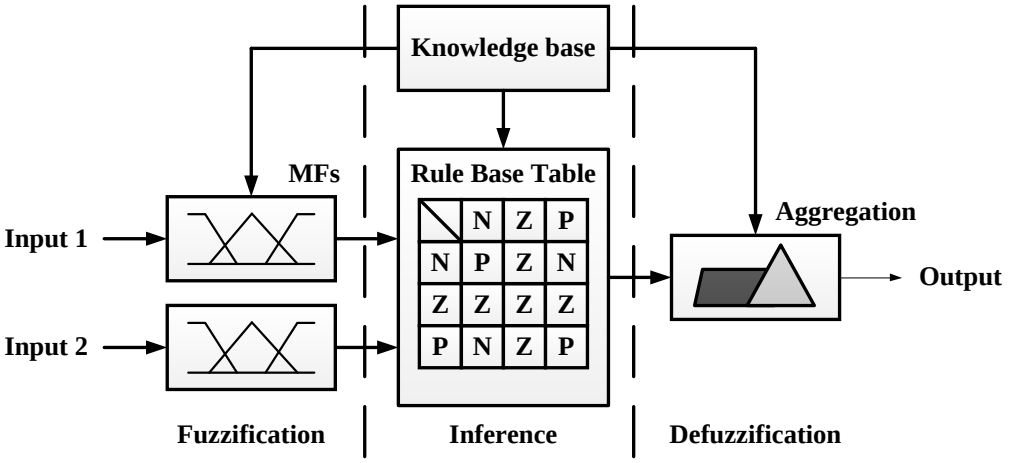

Fig. 2.18: Structure of the fuzzy logic controller.

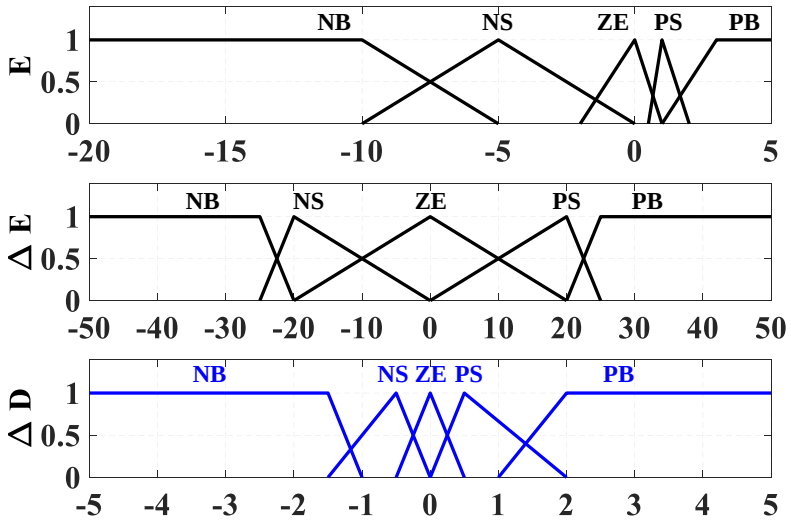

Fig. 2.19: Membership functions of five fuzzy levels.

sets. In the second stage, the input fuzzy sets are converted into output fuzzy sets through the inference with the fuzzy rule base table. Finally, the output fuzzy sets are converted into the numerical variables as the output.

To be more specific, the input variables could be the error E and the change in error ΔE, which can be calculated by the gradient of P-V curve [55] as follow:

$$E(k) = \frac{P(k) - P(k-1)}{V(k) - V(k-1)} \tag{2.27}$$

$$\Delta E(k) = E(k) - E(k-1) \tag{2.28}$$

where $P(k)$ and $V(k)$ are PV output power and voltage respectively at time k.

Five fuzzy levels are used for membership functions (MFs), such as NB (negative big), NS (negative small), ZE (zero), PS (positive small), and PB (positive big). Since the

Table 2.4: Rule base table with five fuzzy levels.

E \ ΔE	NB	NS	ZE	PS	PB
NB	PB	PB	PS	PB	PB
NS	PB	PS	PS	PS	PB
ZE	NS	NS	ZE	PS	PS
PS	NB	NS	NS	NS	NB
PB	NB	NB	NS	NB	NB

$\Delta P/\Delta V$ curve is highly asymmetric at the MPP, as illustrated in Fig. 2.14, the MFs of $E(k)$ with five fuzzy levels have to be carefully designed in order to ensure the symmetric feature of the output variable ΔD [56]. The designed MFs with five fuzzy levels are demonstrated in Fig. 2.19, which shows that the output variable ΔD is symmetric around zero. These specific 25 fuzzy rules are also clearly shown in Table 2.4.

The FLC method generally exhibits a better performance than other heuristic methods especially under varying atmospheric conditions [56–58]. However, the performance of the FLC is heavily relied on the designer's knowledge of the system. For example, the number of fuzzy rules is high, which increases the difficult of FLC design and implementation.

2.4 Model-Based Method

2.4.1 Linear Approximation

Linear approximation methods are based on the linear relationship, as shown in Fig. 2.20. The fractional open-circuit voltage (FOCV) method [59] and fractional short-circuit current (FSCC) method [60] use the linear relationship between the V_{mpp} and V_{oc}, and I_{mpp} and I_{sc}, respectively. For the FOCV method, the linear relationship is expressed as below

$$V_{mpp} \approx K_{FOCV} V_{oc} \tag{2.29}$$

where K_{FOCV} is a constant of proportionality, which is between 0.71 and 0.78. Similarly, the linear relationship for the FSCC method is described as

$$I_{mpp} \approx K_{FSCC} I_{sc} \tag{2.30}$$

where K_{FSCC} is a constant of proportionality, which is generally found to be between 0.78 and 0.92.

The FOCV method and FSCC method provide a simple and effective way to estimate the MPP. The advantages of these methods are their fast tracking speed, no steady-state

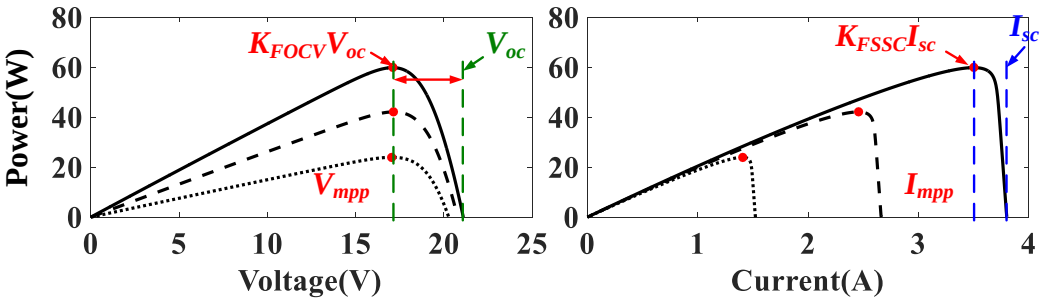

Fig. 2.20: Linear relationship between the V_{mpp} and V_{oc}, and I_{mpp} and I_{sc}.

oscillations and no drift conditions. However, it is not so accurate to obtain a high steady-state MPPT efficiency. Besides, both of these methods need an additional circuit for online measurements of I_{pv} and V_{pv} [60]. As a consequence, a short circuit or periodical disconnection are required, which results in more power loss and higher cost of the system.

2.4.2 I-V Curve-fitted Method

I-V curve-fitted method is usually used to extract the physical parameters, such as R_s, R_p and even the solar irradiance [61]. Recently, some new I-V curve-fitted Methods are proposed, which is based on polynomial models [62, 63]. This kind of the methods requires pairs of voltage and current values to estimate the parameters of the polynomial models.

Taking [63] as an example, equation (2.1) is firstly simplified as (2.31). The details of this simplification can be found in [63].

$$I = \alpha + \beta V^{\gamma} \tag{2.31}$$

where α, β and γ are constants and can be calculate by only three pairs of voltage and current values namely (v_1 i_1), (v_2 i_2) and (v_3 i_3). Taking the first derivative of (2.31), it can be written as:

$$I' = \beta.\gamma.V^{(\gamma-1)} \tag{2.32}$$

The means of the three pairs of voltage and current values can be written as

$$I'_{12} = \frac{i_2 - i_1}{v_2 - v_1} \quad I'_{23} = \frac{i_3 - i_2}{v_3 - v_2} \tag{2.33}$$

$$V_{12} = \frac{v_1 + v_2}{2} \quad V_{23} = \frac{v_2 + v_3}{2} \tag{2.34}$$

Combining (2.32) with (2.33) and (2.34) yields

$$I'_{12} = \beta.V_{12}^{(\gamma-1)} \quad I'_{23} = \beta.V_{23}^{(\gamma-1)} \tag{2.35}$$

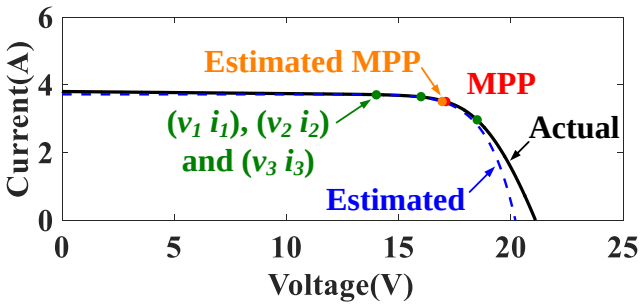

Fig. 2.21: Demonstration of the I-V curve-fitted method.

Then, γ can be calculated as

$$\gamma = \frac{\ln(\frac{I'_{12}}{I'_{23}})}{\ln(\frac{V_{12}}{V_{23}})} + 1 \tag{2.36}$$

Combining (2.35) with (2.36) yields

$$\beta = \frac{I'_{12}}{\gamma . V_{12}^{(\gamma-1)}} \tag{2.37}$$

Finally, α can be obtained

$$\alpha = I_1 - \beta . V_1^{\gamma} \tag{2.38}$$

After α, β and γ are obtained, the estimated I-V curve as well as the estimated MPP can be obtained too. As illustrated in Fig. 2.21, it can be seen that the estimated MPP is very close to the actual MPP.

Compared to the heuristic methods, the I-V curve-fitted method only requires four steps to reach the vicinity of MPP. It is also validated that the dynamic performance of the I-V curve-fitted method is generally better than the heuristic methods [63]. However, this I-V curve-fitted method requires proper selection of the location for three pairs of voltage and current. It is pointed out that the first point (v_1 i_1) must be in the left of the MPP, the third one (v_3 i_3) must be in the left and the second one (v_2 i_2) must be between the first and the third. If all of the points are located in the left side of right side of the MPP, the accuracy of the estimation will be significantly affected, as illustrated in Fig. 2.22.

2.5 Hybrid Method

2.5.1 MPP-locus Method

M. Sokolov and D. Shmilovitz proposed the standard MPP-Locus method in [64]. The basic principle of this method is demonstrated in Fig. 2.23.

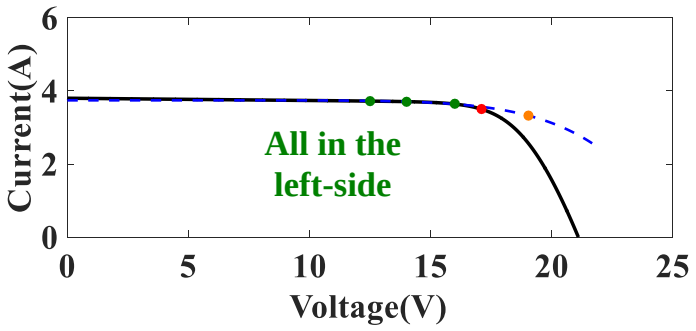

(a)

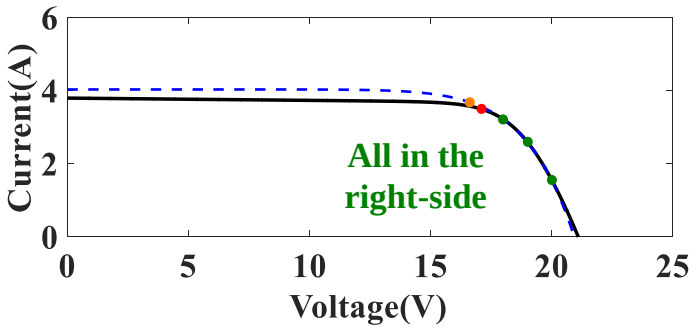

(b)

Fig. 2.22: Bad selection of the location for three pairs of voltage and current: (a) all of the points are located in the left side; (b) all of the points are located in the right side.

As shown in Fig. 2.23, the locations of the MPPs under the different solar irradiance are nearly to form an emulated straight line [65]. Based on this fact, this method is always to force the operating point to nearly maintain on this straight line to reduce the tracking time. Assuming that the weather condition, such as solar irradiance, is changed, the operating point moves from the point 1 to the point $2'$. Then, the operating point directly moves to the point 2 by the MPP-Locus method. Finally, the P&O method or the INC method will be used to exactly locate the MPP position [66].

The advantages of this method is its good dynamic performance, especially when the solar irradiance is suddenly changed. However, this method has a poor tracking performance under low solar irradiance levels or various temperature conditions [67].

2.5.2 Beta Method

Beta method is a very unique MPPT method. Unlike the aforementioned MPPT methods, an intermediate variable, β, rather than power or voltage is used to track the MPP The theory of the Beta method is illustrated in [68] and the intermediate variable β is given as:

$$\beta = \ln\left(\frac{I_{pv}}{V_{pv}}\right) - c \times V_{pv} \tag{2.39}$$

where $c = q/(N_s \eta k T)$ is the diode constant.

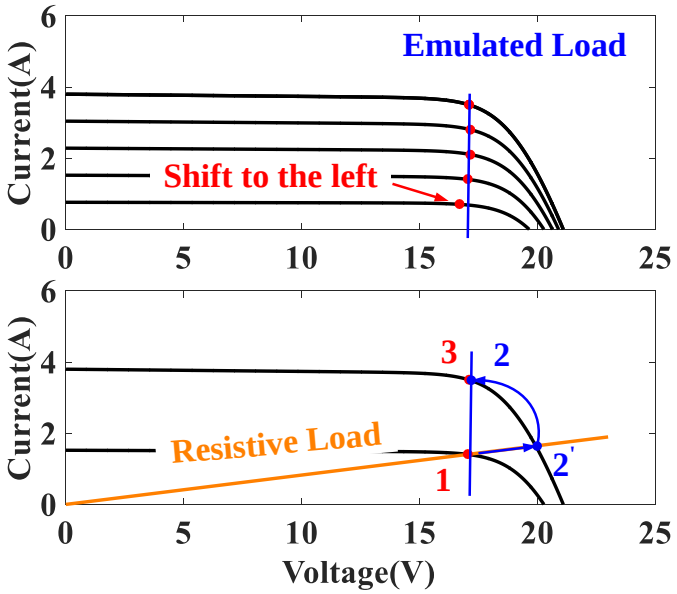

Fig. 2.23: Basic principle of the MPP-Locus method.

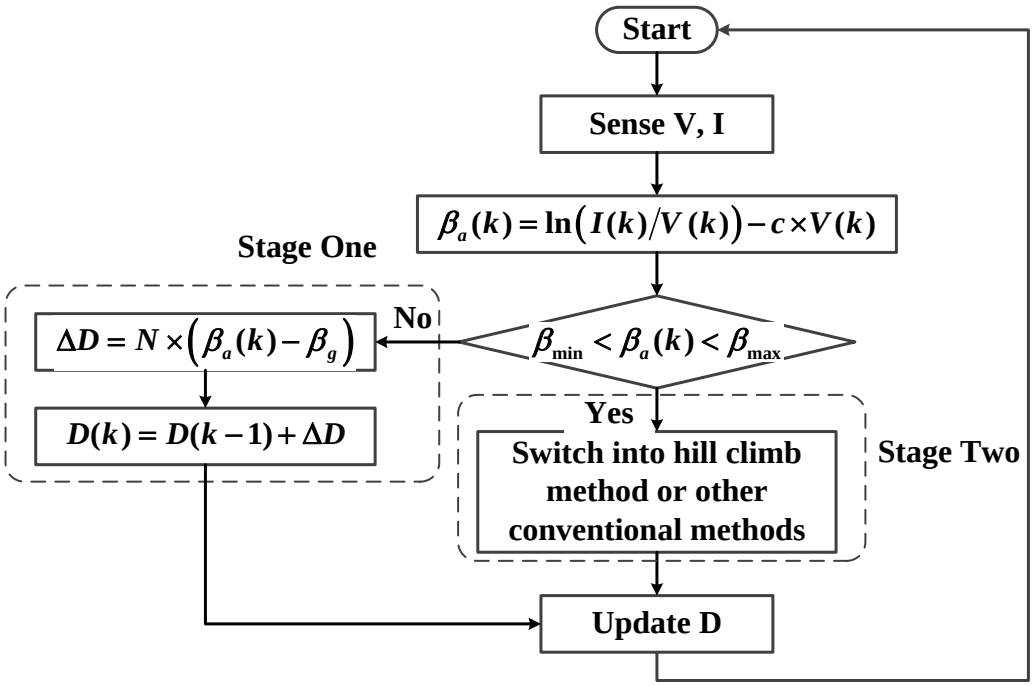

Fig. 2.24: Flowchart of the Beta method.

Firstly, the Beta method is required to determine the bounding range of β, namely β_{min}, β_{max}, which is based on the weather conditions. Then, if the value of β is within the range of β, it means that the operating point is close the MPP. Thus, the fixed step P&O method can be used to exactly locate the MPP. Otherwise, if the value of β is out of this range, it means that the operating point is far from the MPP. Hence, a variable step ΔD is used, which can be expressed as:

$$\Delta D = N \times \big(\beta(k) - \beta_g\big) \tag{2.40}$$

where $\beta(k)$ is the present value of β, N is the scaling factor, and β_g is a guiding parameter. This process can be summarized in Fig. 2.24.

The previous simulation and experimental results from [69, 70] comprehensively evaluated main MPPT methods and it is believed that the Beta method exhibits a fast tracking speed in the dynamic stage, small oscillations in the steady-state stage and relatively easy implementation. However, some parameters, such as N and β_g, have to be tuned carefully to avoid the bad performance [71]. In other words, the dynamic performance of this method will be affected if N and β_g are not properly tuned. Furthermore, the steady-state oscillations still exists, which is affected the steady-state efficiency. Besides, how to design the bounding range of β is also not clearly defined and evaluated. Therefore, the potential of this method is not fully exploited.

2.6 Summarization of the reviewed aforementioned MPPT methods

Fig. 2.25 summarized the reviewed aforementioned MPPT methods. The aforementioned MPPT methods are categorized into three groups as previously discussed in Section 2.2.2.

There are 8 different common features for the MPPT methods, which are summarized and shown at the bottom of Fig. 2.25. The three different colors, red, yellow and green, are referred to negative, neutral and positive, which are related to these 8 MPPT features.

From Fig. 2.25, it is clearly to evaluate each of these MPPT methods. Most of the MPPT methods are able to track the true MPP except the linear approximation method. Only parabolic prediction method and the I-V curve-fitted method are required to set a proper initial points.

It should be noted that the tracking speed is generally good for half of the MPPT methods, especially for the model-based method and hybrid method. However, it requires proper tuning of the parameters related to the characteristic of the algorithm. Besides, the steady-state oscillations for the most of the MPPT method are not really eliminated, which are also quite important.

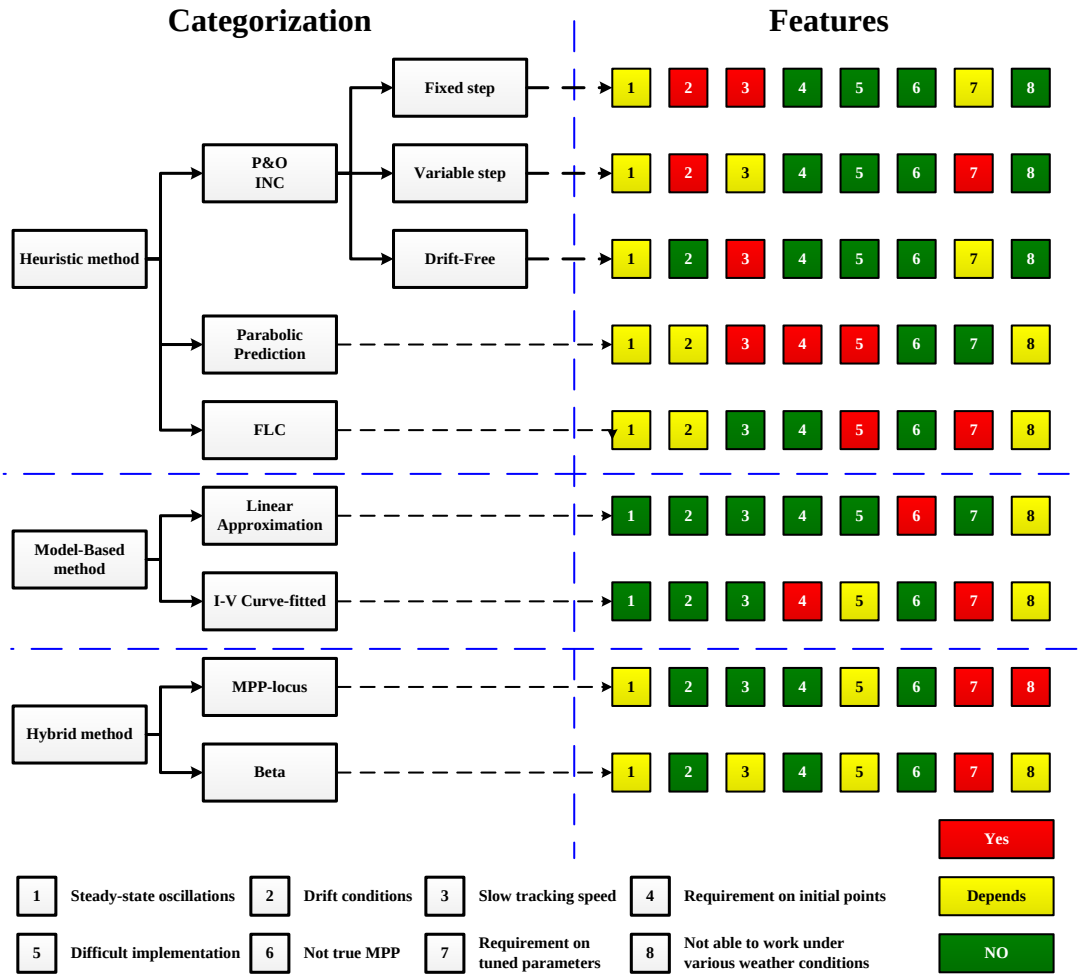

Fig. 2.25: Summarization of the reviewed aforementioned MPPT methods.

Chapter 3

An Improved Beta Method With Adaptive Scaling Factor and Zero Oscillation

In this chapter, an improved Beta method is proposed, which consists of two sub-algorithms:

1. Adaptive scaling factor Beta (ASF-Beta) method for the dynamic stage.
2. Zero oscillations perturb and observe (ZO-PO) method for the steady-state stage.

The content of this chapter has been published in the following paper:

1. **Li, X.**, Wen, H., Hu, Y., Jiang, L., "A novel beta parameter based fuzzy-logic controller for photovoltaic MPPT application", *Renewable Energy*, 130, pp. 416-427, 2019.

2. **Li, X.**, Wen, H., Jiang, L., Xiao, W., Du, Y., Zhao, C., "An Improved MPPT Method for PV System with Fast-Converging Speed and Zero Oscillation", *IEEE Transactions on Industry Applications*, 52 (6), pp. 5051-5064, November/December, 2016.

3. **Li, X.**, Wen, H., Jiang, L., Hu, Y., Zhao, C., "An improved beta method with auto-scaling factor for photovoltaic system", *IEEE Transactions on Industry Applications*, 52 (5), pp. 4281-4291, September/October, 2016.

4. **Li, X**., Wen, H., Jiang, L., Lim, E.G., Du, Y., Zhao, C., "Photovoltaic modified -parameter-based MPPT method with fast tracking", *Journal of Power Electronics*, 16 (1), pp. 9-17, January 2016.

3.1 Proposed Improved Beta Method

The main loop of the proposed method is illustrated in Fig. 3.1. Compared to the conventional Beta method, an adaptive scaling factor is used by the proposed ASF-Beta method.

Table 3.1: Values of β under various irradiance and temperature

No.	Irradiance	temperature	β
1	$1000W/m^2$	$45°C$	-15.4505
2	$1000W/m^2$	$5°C$	-18.3431
3	$300W/m^2$	$45°C$	-15.9587
4	$300W/m^2$	$5°C$	-19.0214

Therefore, the ASF-Beta method becomes less dependent on tuned parameters. Furthermore, the the steady-state oscillations can be totally eliminated by the ZO-PO method. As a consequence, the steady-state efficiency can be significantly improved.

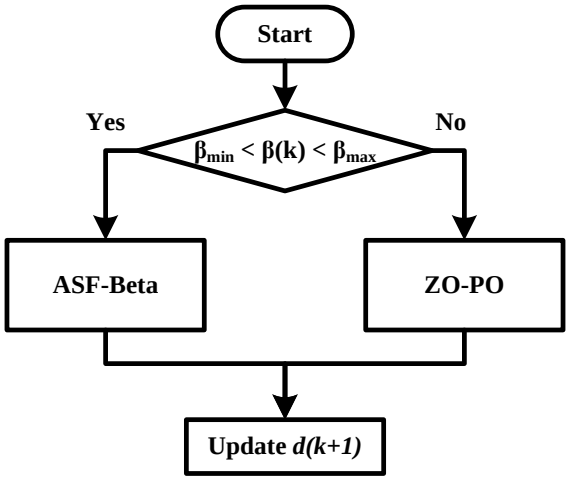

Fig. 3.1: Main loop of the proposed method.

3.1.1 Determination of Beta Parameters

According to [68, 70–72], the range of β depends on the working environment of the PV system. Table 3.1 demonstrates working environmental conditions and the calculated magnitudes of β. The relationship among β, voltage and power under various irradiation and temperature conditions is indicated in Fig. 3.2. From Table 3.1 and Fig. 3.2, the range of β is determined as $\beta_{min} = -19.02$ and $\beta_{max} = -15.45$.

In [73], the authors pointed out that the evaluation and performance on MPPT should consider non-ideal factors depended on weather conditions. Moreover, the performance of P&O method by using the meteorological data of two distinct locations is explored to evaluate the optimal step size. Therefore, it is also essential to use the meteorological data to evaluate the range of β. In this thesis, the meteorological data of the HSU and the UNLV are used, which are plotted in Fig. 3.3.

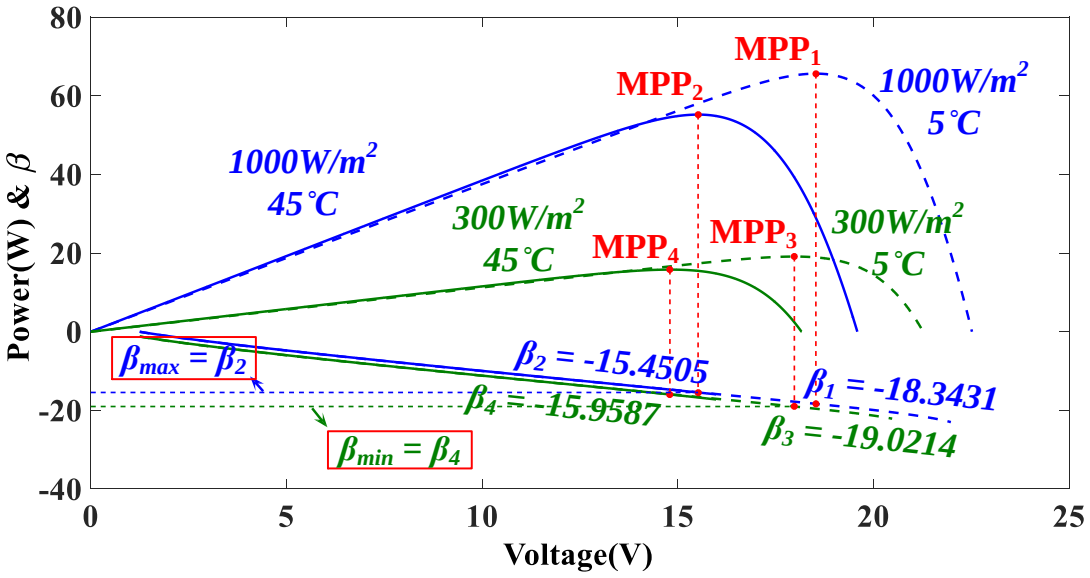

Fig. 3.2: Determination of β range based on the working environmental conditions.

Fig. 3.4 illustrates the corresponding simulated values of power and β at the MPP in the daytime. Since the solar irradiance has more remarkable effect on the generated power than temperature, it can be seen that the simulated power has a similar trend as the solar irradiance. However, the temperature has more remarkable effect on the values of β compared to the solar irradiance. Therefore, the trends of the temperature and the values of β are the similar.

Furthermore, during the daytime, the corresponding simulated values of β generally stays within the range between β_{min} and β_{max}. It proves that the set of β parameters in Table 3.1 and Fig. 3.2 are able to work in the whole year under the real weather condition.

3.1.2 Adaptive Scaling Factor Beta (ASF-Beta) Method

Generally, the scaling factor for the conventional Beta method is based on trial-and error method [72]. Fig. 3.5 demonstrates that different values of the scaling factor N are implemented for the conventional Beta method.

From Fig. 3.5, it can be seen that the larger value of N shows the better performance when the irradiation changes significantly. However, too large value of N can cause the too large duty cycle, which can result in the undesired performance. In contrast, the smaller N can avoid this undesired situation. However, the tracking speed is relatively slow when the irradiation increasing. Therefore, the medium value of N is chosen for optimization in the previous research [72].

In order to avoid the tuning the values of scaling factor by trial-and error method, adaptive scaling factor is really necessary. Therefore, the adaptive scaling factor Beta

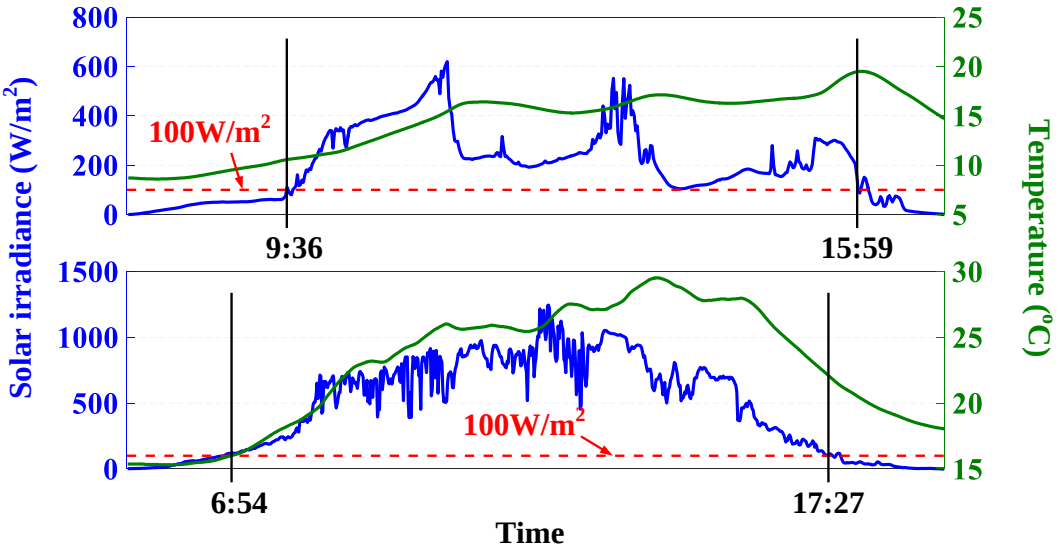

(a)

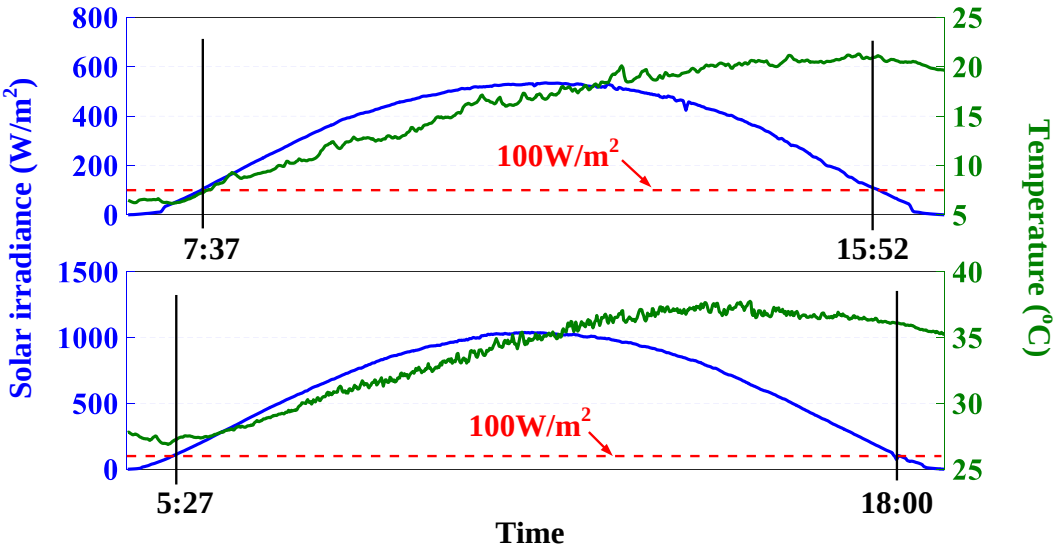

(b)

Fig. 3.3: Meteorological data of the HSU and the UNLV in the daytime: (a) HSU in 2015/01/19 (top) and 2015/07/31 (bottom); (b) UNLV in 2015/01/16 (top) and 2015/07/24 (bottom).

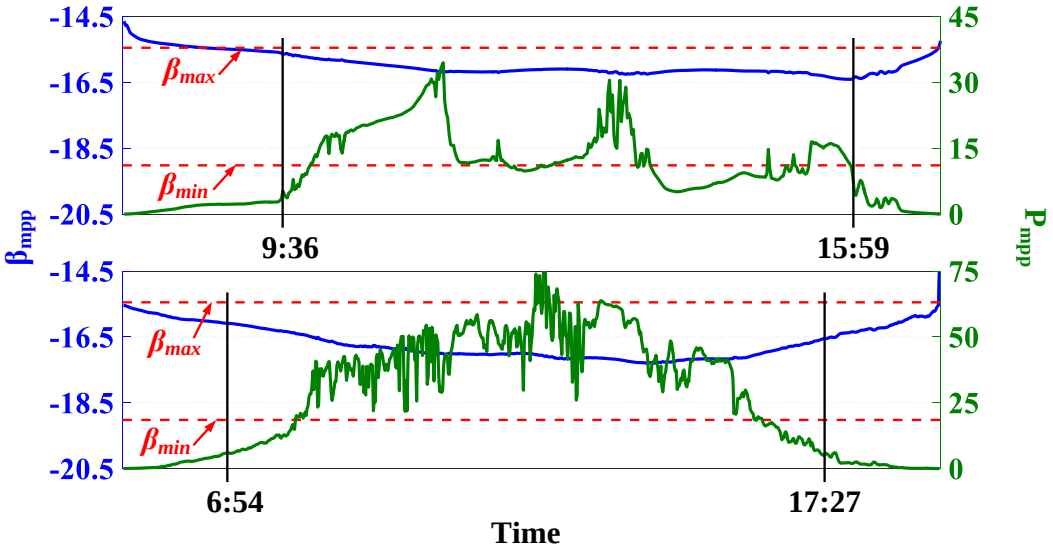

(a)

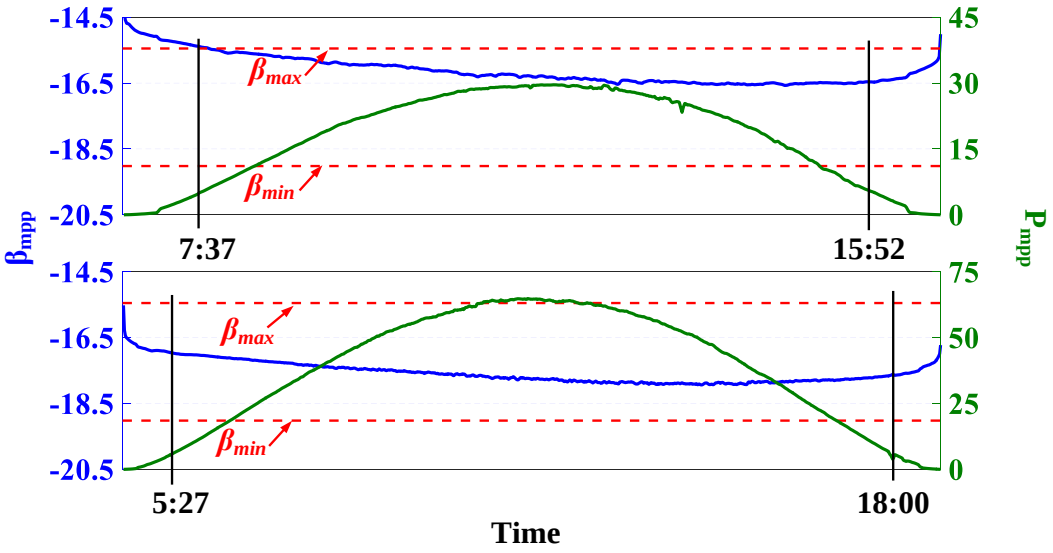

(b)

Fig. 3.4: The corresponding simulated value of power and β at the MPP in the daytime: (a) HSU in 2015/01/19 (top) and 2015/07/31 (bottom); (b) UNLV in 2015/01/16 (top) and 2015/07/24 (bottom).

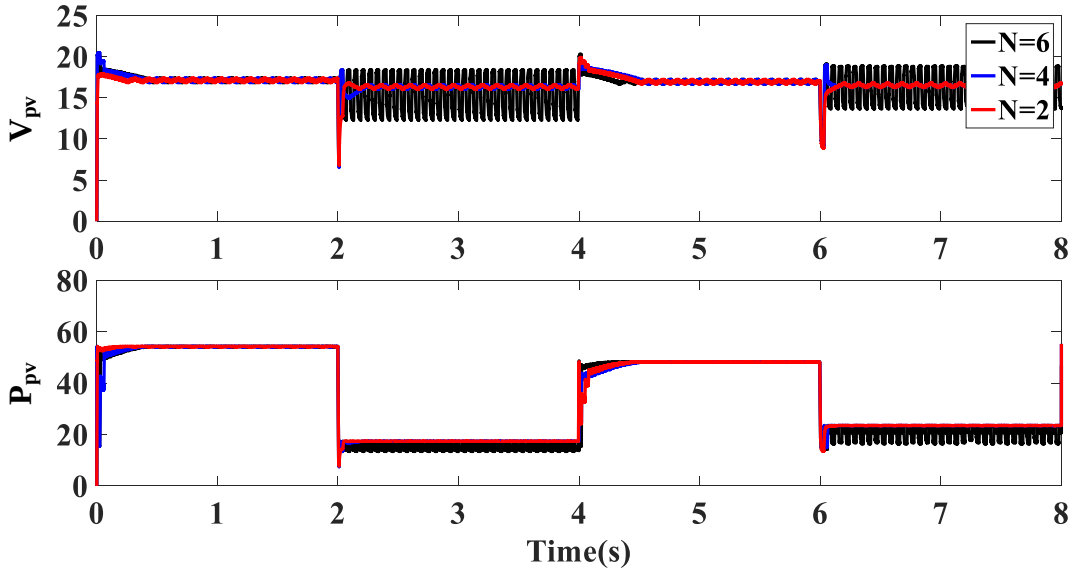

(a)

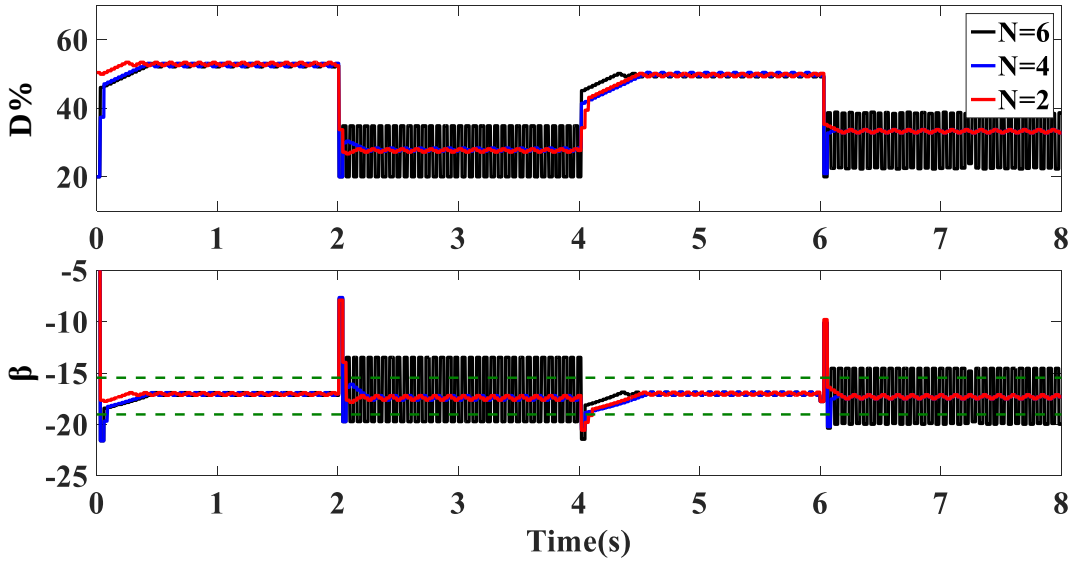

(b)

Fig. 3.5: Scaling factor sweeping for the conventional Beta method.

(ASF-Beta) method is proposed to overcome this problem in this thesis [71].

Compared to (2.40), the guiding parameter β_g is removed and the step size is updated as:

$$\Delta D = \begin{cases} N \times (\beta_a(k) - \beta_{min}), \text{ for } \beta_a(k) > \beta_{max} & \text{(3.1a)} \\ N \times (\beta_a(k) - \beta_{max}), \text{ for } \beta_a(k) < \beta_{min} & \text{(3.1b)} \end{cases}$$

where (3.1a) and (3.1b) refer to the step size when the solar irradiance is decreased and increased, respectively. Then, the adaptive scaling factor N shown in (3.1) is derived by:

$$N = \begin{cases} 1, & \text{for } \beta(k-1) < \beta_{max} & \text{(3.2a)} \\ \frac{\beta(k)-\beta_{min}}{\beta(k-1)-\beta(k)}, & \text{for } \beta(k-1) > \beta_{max} & \text{(3.2b)} \end{cases}$$

$$N = \begin{cases} 1, & \text{for } \beta(k-1) > \beta_{min} & \text{(3.3a)} \\ \frac{\beta(k)-\beta_{max}}{\beta(k-1)-\beta(k)}, & \text{for } \beta(k-1) < \beta_{min} & \text{(3.3b)} \end{cases}$$

where (3.2) and (3.3) refer to the changes of N when the solar irradiance is decreased and increased, respectively; $\beta(k-1)$ refers to the previous value of β.

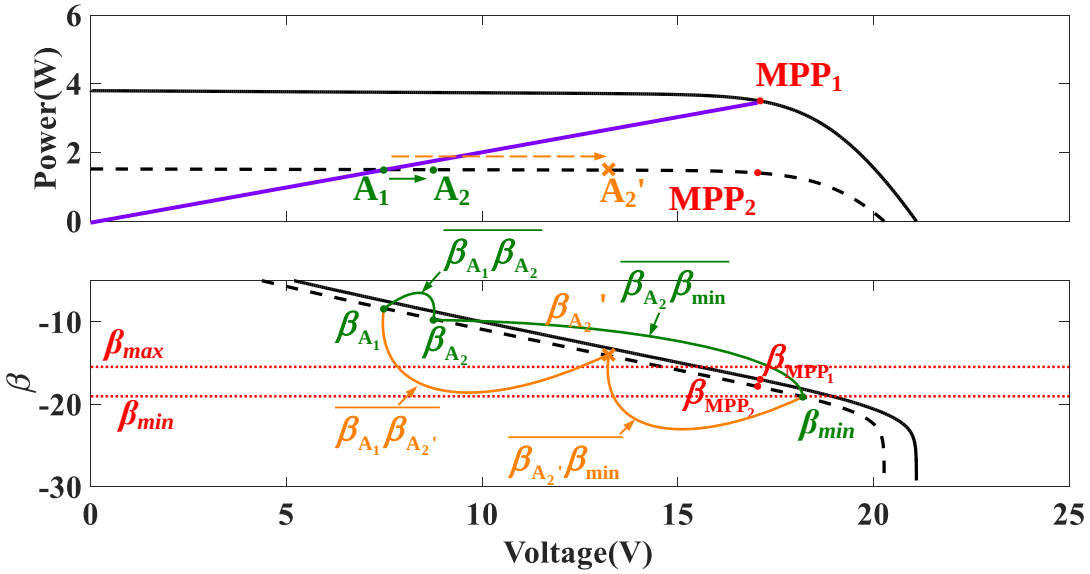

Fig. 3.6: Demonstration of the ASF-Beta method under the sudden irradiance changes.

Fig. 3.6 demonstrates the tracking process of the ASF-Beta method. When solar irradiance is decreased, the operating point will move from the point MPP_1 to A_1. At this time, the present and previous of β have relationships as below:

$$\begin{cases} \beta(k) = \beta_{MPP_1} < \beta_{max} & \text{(3.4a)} \\ \beta(k-1) = \beta_{A_1} > \beta_{max} & \text{(3.4b)} \end{cases}$$

(3.1a) and (3.2a) are used to derivative the step size and its scaling factor, respectively. Then, when the operating point moves to the point A_2, both of $\beta(k)$ and $\beta(k-1)$ are larger than β_{max}:

$$\begin{cases} \beta(k) = \beta_{A_1} > \beta_{max} & \text{(3.5a)} \\ \beta(k-1) = \beta_{A_2} > \beta_{max} & \text{(3.5b)} \end{cases}$$

Thus, the scaling factor is tuned by (3.2b):

$$N = \frac{\overline{\beta_{A_1}\beta_{A_2}}}{\overline{\beta_{A_2}\beta_{min}}} = \frac{\beta(k) - \beta_{min}}{\beta(k-1) - \beta(k)} \tag{3.6}$$

where $\overline{\beta_{A_1}\beta_{A_2}}$ and $\overline{\beta_{A_2}\beta_{min}}$ refer to the length between the point A_1 and A_2, and the point A_2 and β_{min}, respectively. If A_2 is far from the MPP_2, $\overline{\beta_{A_1}\beta_{A_2}}$ is smaller than $\overline{\beta_{A_2}\beta_{min}}$. Consequently, the value of N and the step size becomes larger, and the operating point moves faster. By contrast, if A_2' is close to the MPP_2, $\overline{\beta_{A_1}\beta_{A_2'}}$ is larger than $\overline{\beta_{A_2'}\beta_{min}}$. Therefore, the value of N becomes smaller and the step size can be well tuned. After serval repeats of this process, the operating point moves into the range of β, and the P&O method is used to locate the exact MPP. Finally, the working principle of the ASF-Beta method is summarized in Fig. 3.7.

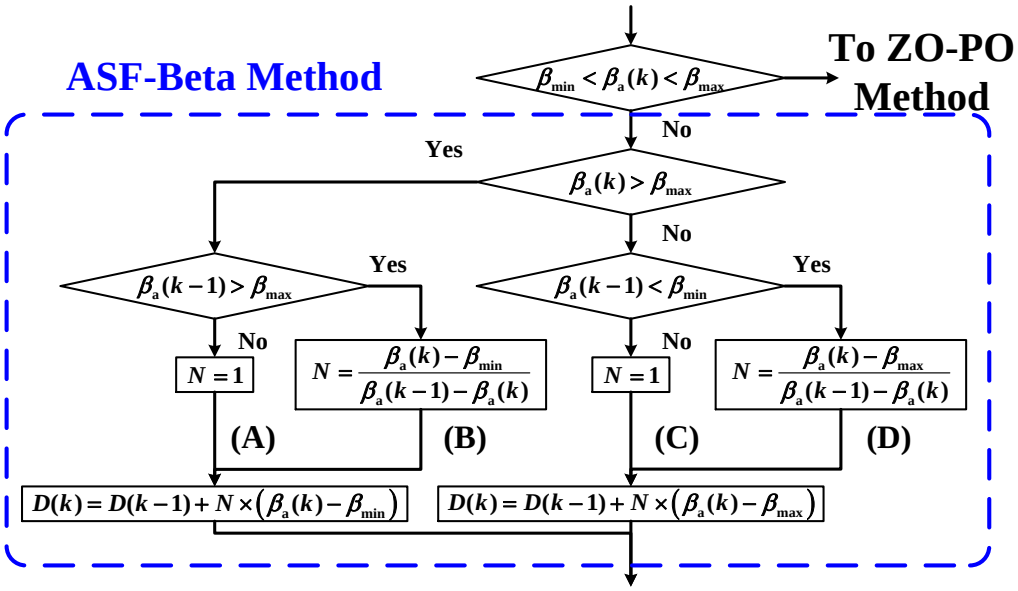

Fig. 3.7: The flowchart of the ASF-Beta method.

When the solar irradiance is increased or the load is changed, similar processes to obtain N and step size can be analyzed as aforementioned discussion, which will not be presented here.

3.1.3 Zero Oscillations Perturb and Observe (ZO-PO) Method

According to [35], three-level perturbations around the MPP point are typically happened when the conventional P&O method reaches its steady-state stage. As shown in Fig. 3.8 (a), the levels of power and duty cycle are following the trajectory A $\rightarrow$ B $\rightarrow$ C $\rightarrow$ B $\rightarrow$ A. The level of duty cycle, B, is the middle level, D_{mid}, which occurs twice in every four sampling periods of T_p. Moreover, the corresponding power level, P_{mid}, is the highest compared to the other levels. As description in Section 2.3.1, the operating point will repeat the following trajectory A $\rightarrow$ B $\rightarrow$ C $\rightarrow$ B $\rightarrow$ A, as shown in the top of Fig. 3.9. In order to eliminate the steady-state oscillations, the ZO-PO method is used to identify and maintain D_{mid} during the steady-state stage.

Fig. 3.8 (b) demonstrates the basic idea of the ZO-PO method. $D1$, $D2$, $D3$ and $D4$ refer to the values of the duty cycle in every four sampling periods of T_p. The criterion, "$D1$ = $D3$" or "$D2$ = $D4$", is used to identify D_{mid}. Once the defined criterion is satisfied, the algorithm makes sure that the operating point has reached the MPP. Then, a variable "$counter$" is activated and this variable will be self-increased until it is equal to four. The reason for setting "$counter$" is to avoid the measurement errors caused by noise.

Once $counter$ is equal to four, the ZO-PO method will consequently maintain at P_{mid} until an environmental change is happened. The power difference ΔP during each period is continually calculated and a threshold e is defined. If ΔP is larger than e, it indicates that the environmental change has been happened. The reason for setting e is used to avoid the small power variation caused by the measurement error, such as noise.

Fig. 3.10 demonstrates the principle of the ZO-PO method. Initially, the MPP is not reached yet and $counter$ equals to 0. At time 0.81s, the algorithm finds that $D2$ equals to $D4$, so $counter$ is self-increased and $counter$ becomes 1. After the whole period of $4T_p$, $counter$ becomes to 4 and the middle point is identified. As a consequence, the middle level will be maintained until weather conditions are changed. Finally, the working principle of the ZO-PO method is summarized in Fig.3.11.

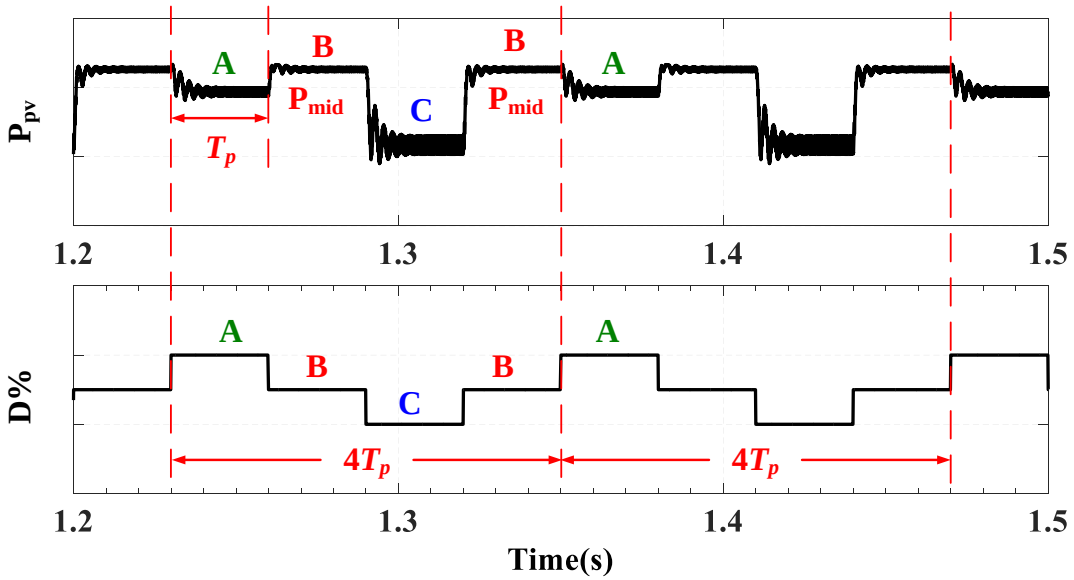

(a)

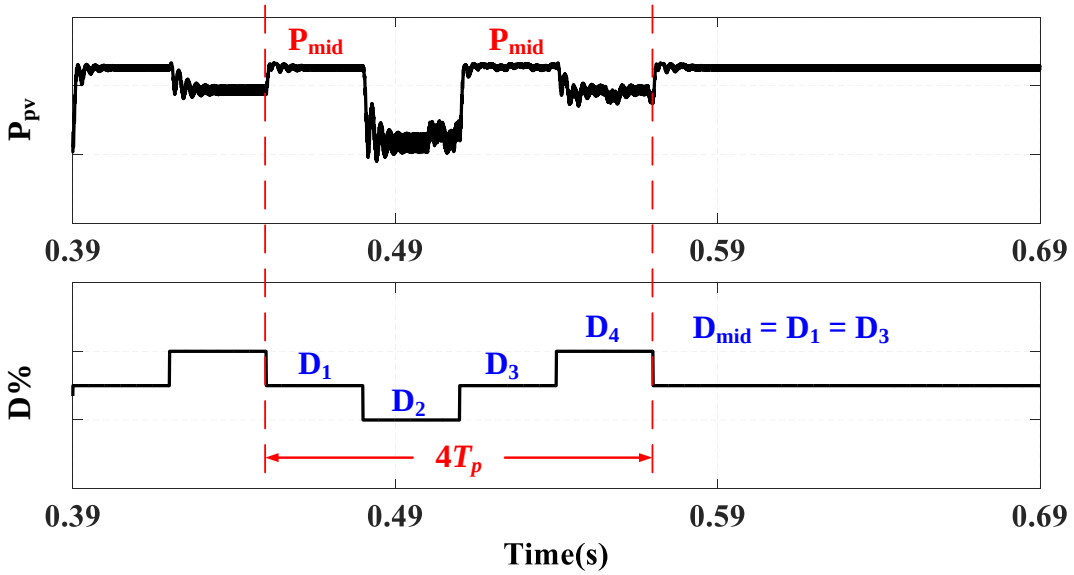

(b)

Fig. 3.8: Waveforms of the power and duty cycle under the steady-state stage: (a) conventional P&O method; (b) ZO-PO.

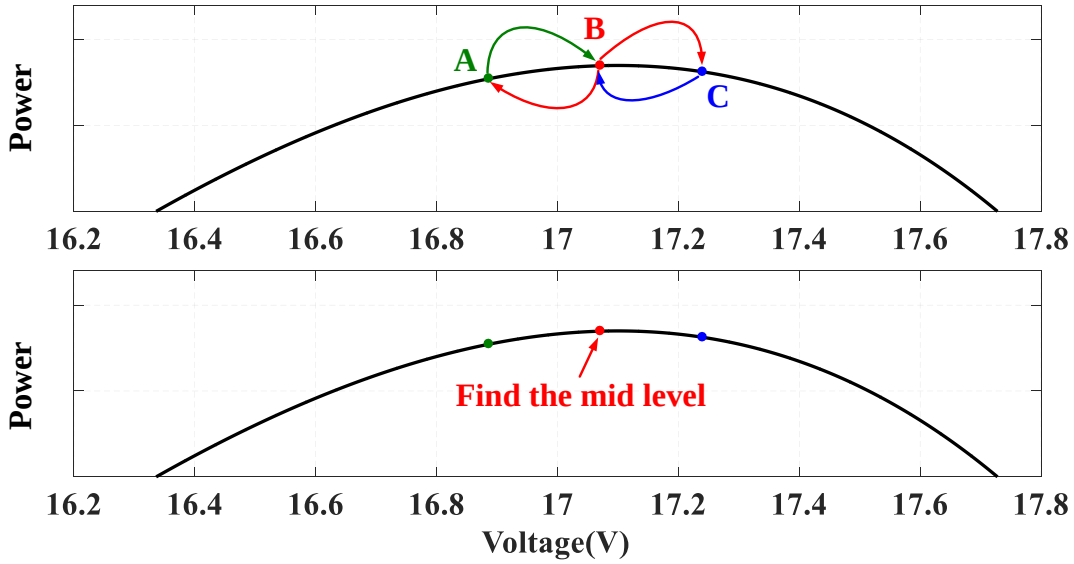

Fig. 3.9: Demonstration of the difference between the conventional P&O method (top) and the ZO-PO method (bottom).

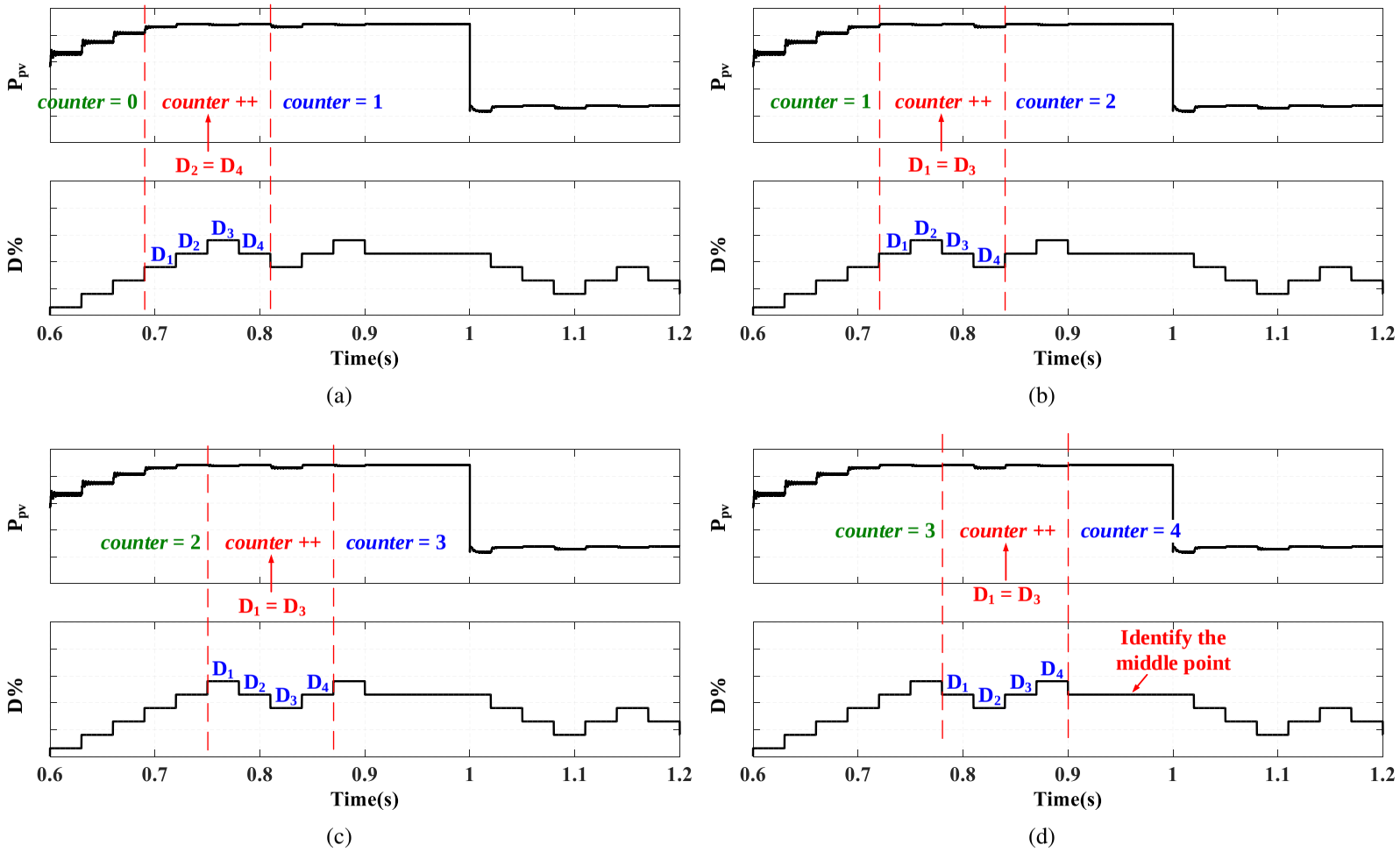

Fig. 3.10: Demonstration of the ZO-Po method: (a) $counter = 1$; (b) $counter = 2$; (c) $counter = 3$; (d) $counter = 4$.

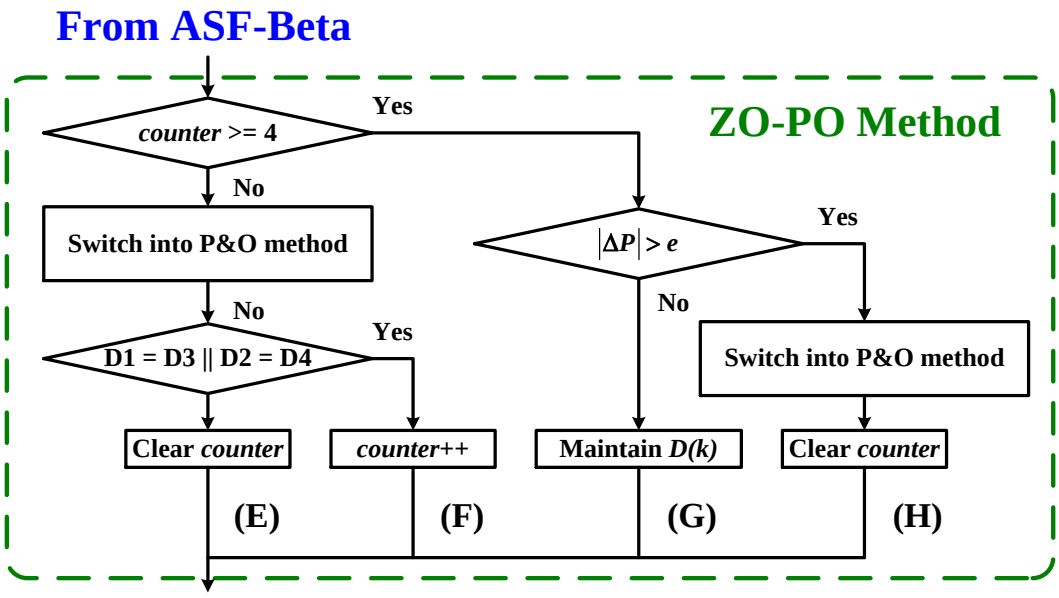

Fig. 3.11: The flowchart of the ZO-PO method.

3.2 Simulation Results

3.2.1 Simulation Setup

Fig. 3.12 shows the schematic of the proposed PV system. Generally, it consists of a PV generation (like a PV module), a DC-DC converter, an load and an MPPT controller. The data sheet of the PV module used in the simulation is shown in 2.1. The input capacitor C_{in}, output capacitor C_{out}, inductor L and switching frequency for the boost converter are 470uF, 47uF, 1mH and 10kHz, respectively. A variable resistor is used as the load.

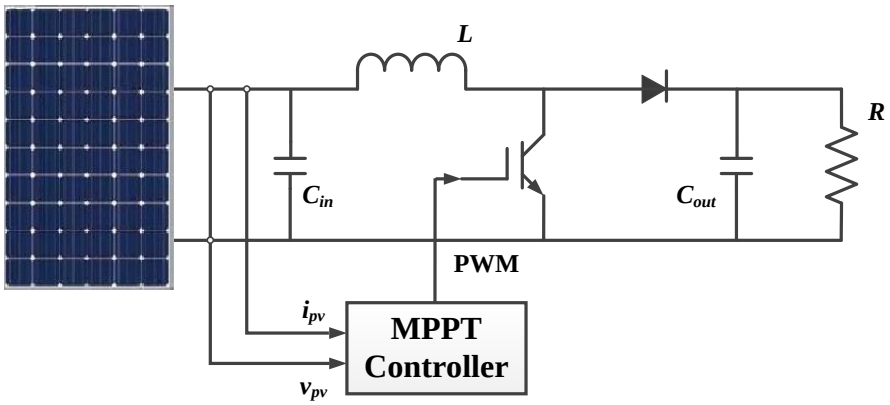

Fig. 3.12: Schematic of the proposed PV system.

The sampling time for the MPPT controller, T_p, is derived from [35], which is calcu-

lated by

$$T_p \geq T_\varepsilon \cong -\frac{1}{\xi \cdot \omega_n} \cdot \ln(\varepsilon) \tag{3.7}$$

where $\omega_n = 1/\sqrt{L \cdot C_{in}}$, $\xi = 1/(2 \cdot R_{mpp}) \cdot \sqrt{L/C_{in}}$, and $\varepsilon = 0.1$. In this thesis, $\omega_n = 1459 rad/s$, $R_{mpp} = 4.89\Omega$ and $\xi = 0.1493$ (at 1000W/m^2), $R_{mpp} = 11.70\Omega$ and $\xi = 0.0623$ (at 400W/m^2). Consequently, $T_\varepsilon = 0.0106s$ (at 1000W/m^2) and $T_\varepsilon = 0.0253s$ (at 400W/m^2). Therefore, T_p is set as 0.03s, which is slightly larger than T_ε = 0.0253s at 400W/m^2.

3.2.2 Simulation Results for the Proposed Method

Fig. 3.13 illustrates the simulation results of the proposed method under the strong solar irradiance variation. I_{pv}, V_{pv} and P_{pv} refer to the current, voltage and power extracted by the different methods; D is the duty cycle of the DC-DC converter. The solar irradiance level decreases from 1000W/m^2 to 400W/m^2 at 0.5s and increases to 1000W/m^2 at 2.5s. The load resistance is fixed at 30Ω during this period.

From Fig. 3.13, it can be seen that the proposed has a fast tracking speed during the solar irradiance changes. Besides, there is no oscillations during the steady-state stage. Detailed tracking process is illustrated in Fig.3.14 and Fig. 3.15.

Fig. 3.14 shows the zoom view and tracking process of the simulation results when the solar irradiance decreases. Initially, the solar irradiance is 1000W/m^2 from 0s to 0.5s. At this period, the operating point is working at the point A and the branch (G) is used according to Fig. 3.11. At 0.5s, the solar irradiance decreases to 400W/m^2. At this time, the operating point immediately moves from the point A to the point B via the load line. When the point B is reached at the next sample point 0.51s, the ASF-Beta method is used via the branch (A) according to Fig. 3.7. As a consequence, the operating point moves from the point B to the point B$_1$. Then, the algorithm goes through the branch (B) and the operating point moves to the point B$_2$ at 0.54s. After this, the ZO-PO method is activated via the branch (E). After the ZO-PO method is activated, the ZO-PO method identifies D_{mid} at 0.75s since the criterion "D1 = D3" is firstly satisfied. Then, the algorithm goes through the branch (F) and D_{mid} is detected after a time of $4T_p$. Finally, the algorithm goes through the branch (G) and d is maintained at 38.3%. As a consequence, there is no oscillations after 0.84s.

When the solar irradiance is increased, a similar process is illustrated in Fig. 3.15. However, it should be noted that the ASF-Beta method is used through the branch (C) and (D) rather than the branch (A) and (B). It is clearly seen that the difference between the performance of the ASF-Beta method during the solar irradiance increase and decrease. As shown in Fig. 3.14 (b), the operating point "jumps" roughly same distance as the

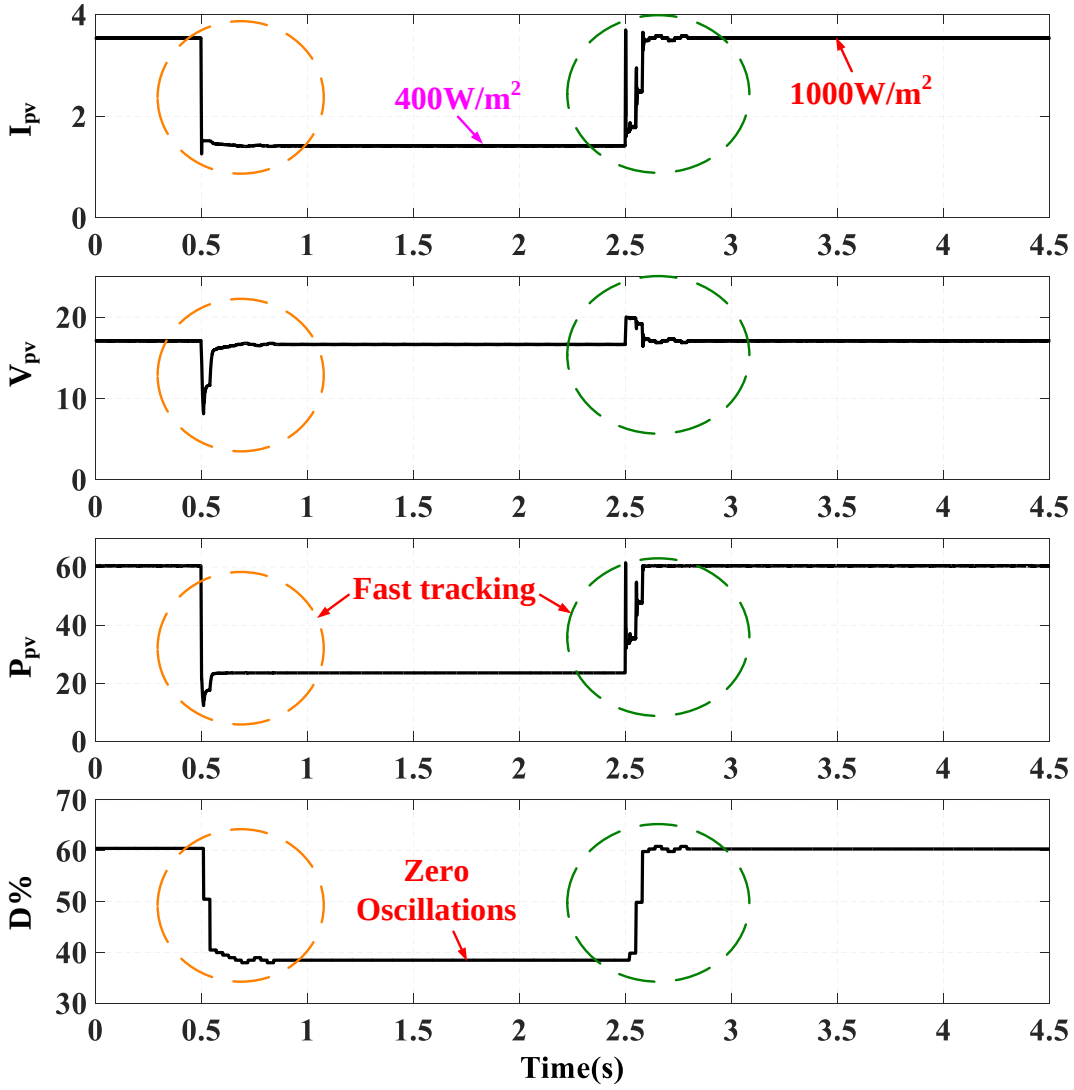

Fig. 3.13: Simulation results of the proposed method under strong solar irradiance variation.

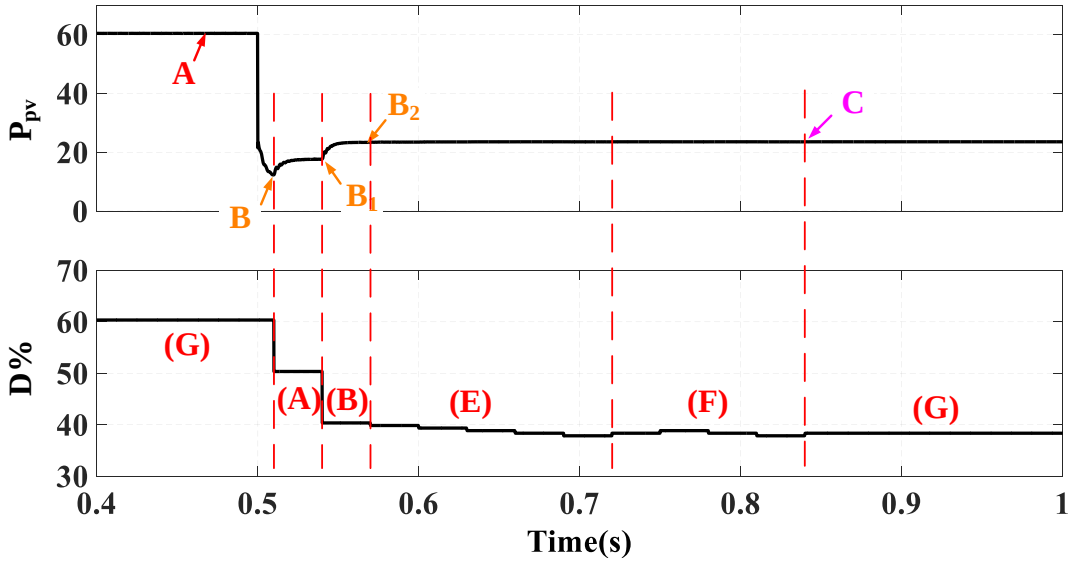

(a)

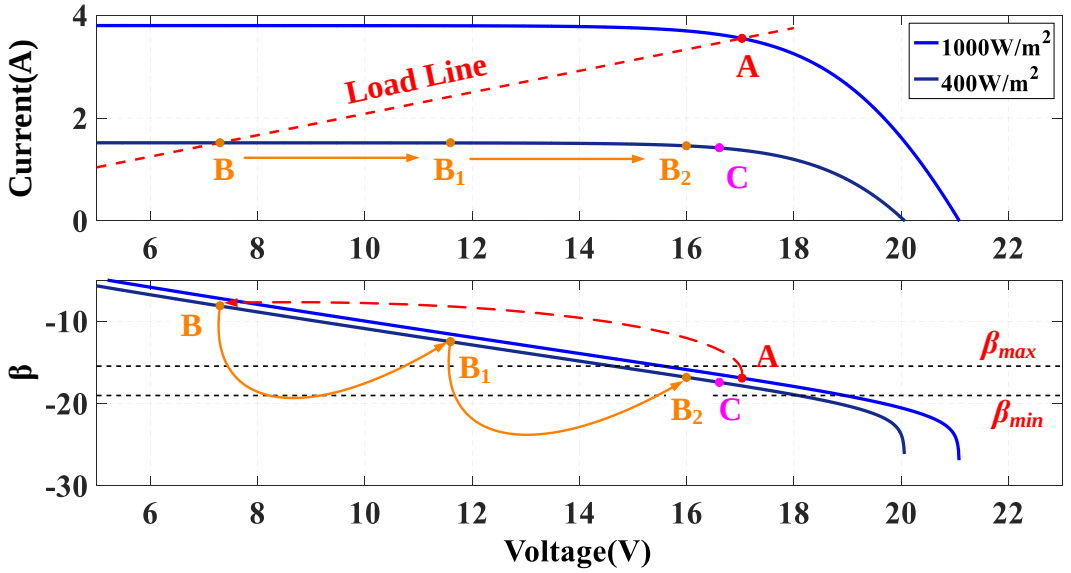

(b)

Fig. 3.14: Zoom view and tracking process of the simulation results when the solar irradiance decreases: (a) power and duty cycle waveforms; (b) current and β waveforms.

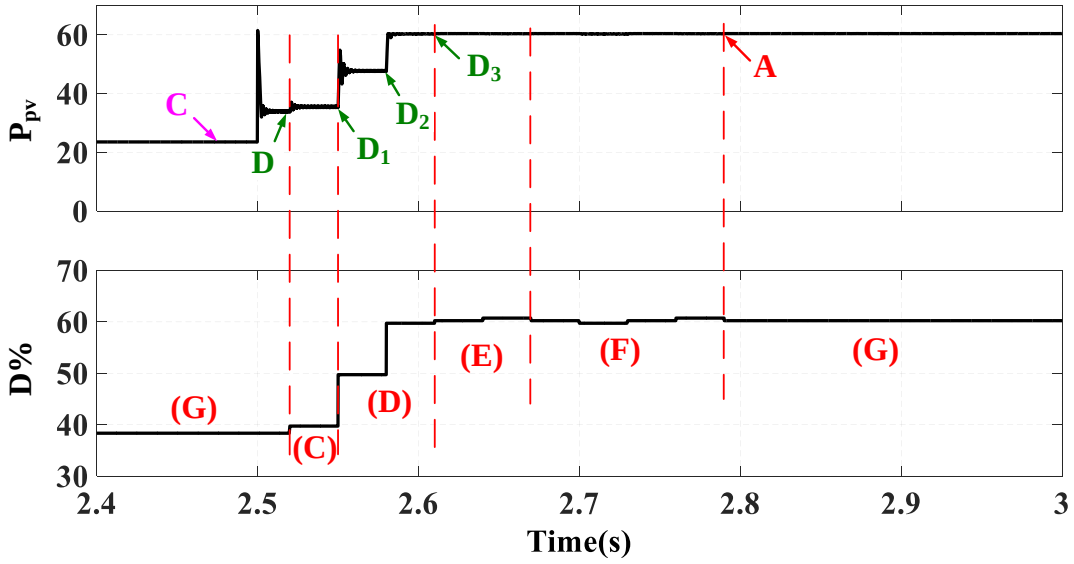

(a)

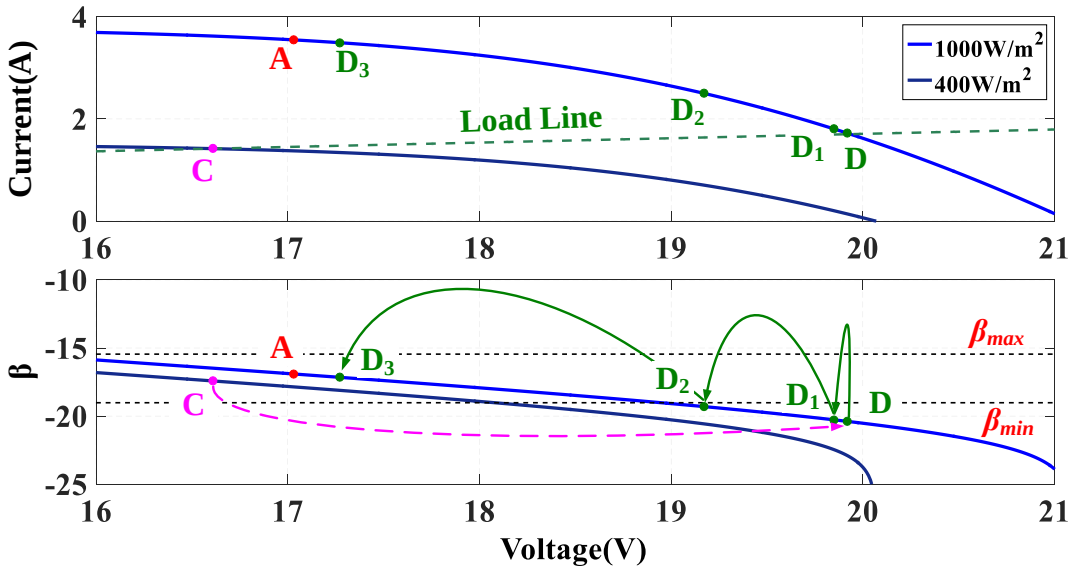

(b)

Fig. 3.15: Zoom view and the tracking process of the simulation results when the solar irradiance increases: (a) power and duty cycle waveforms; (b) current and β waveforms.

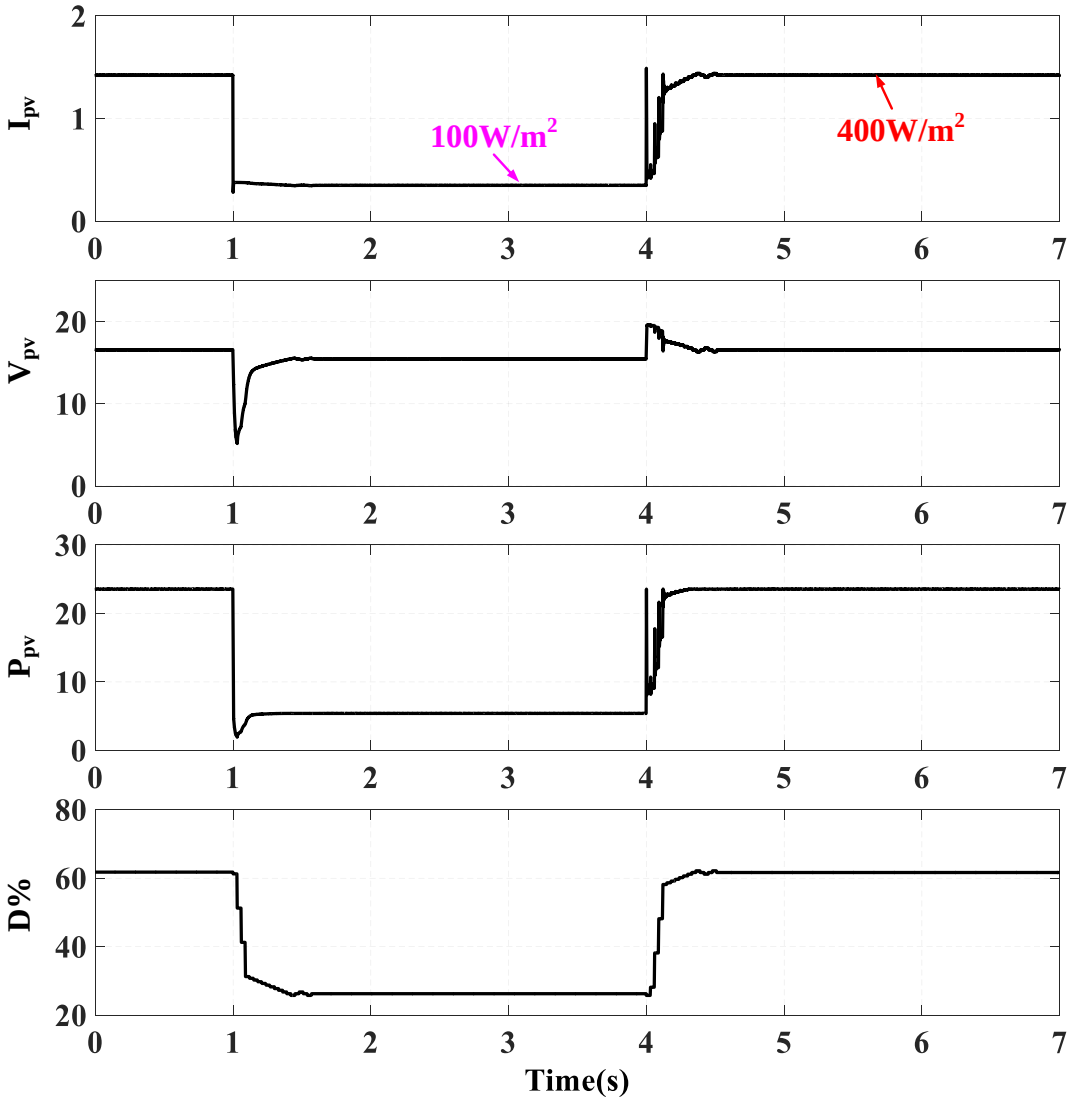

Fig. 3.16: Simulation results of the proposed method under week irradiance variation.

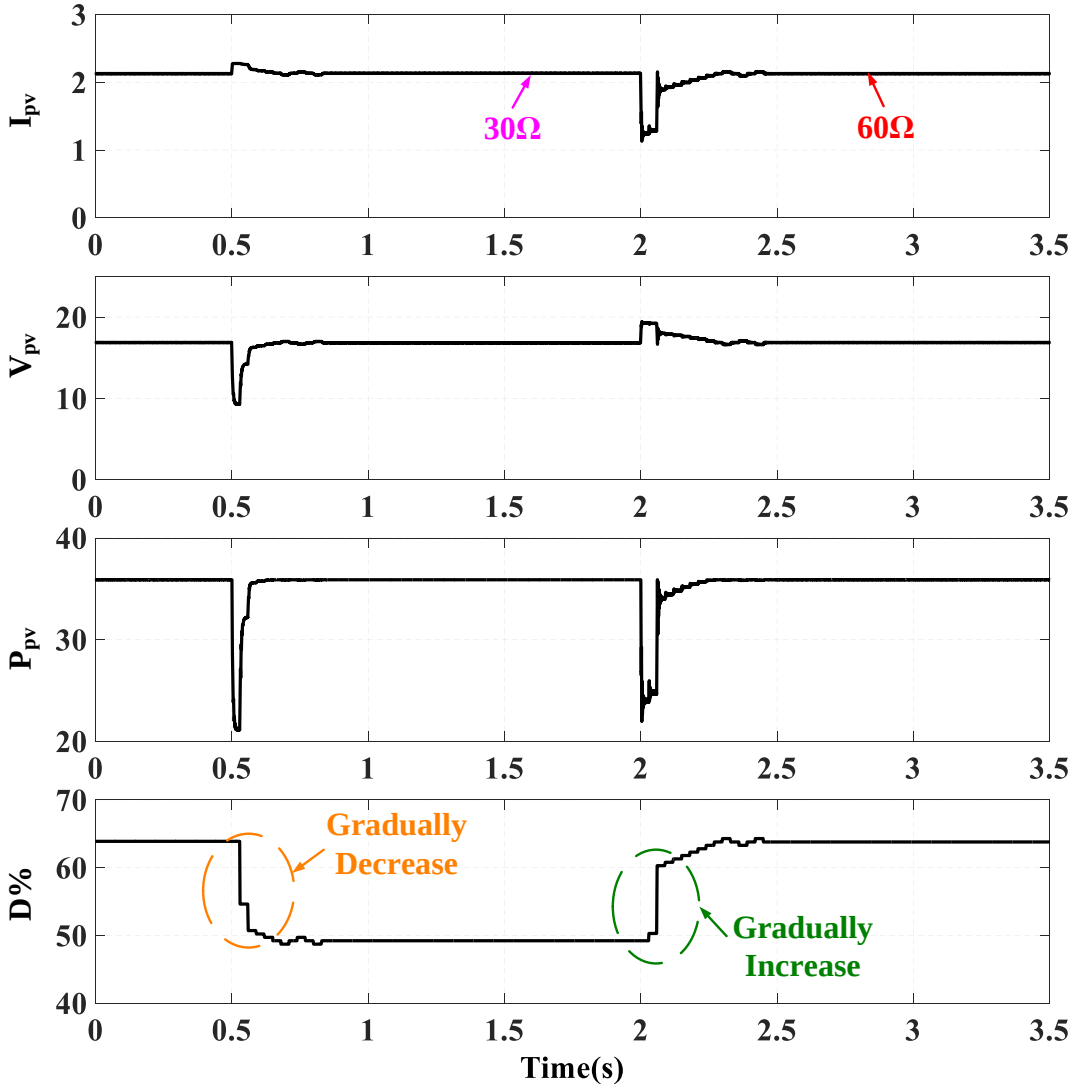

Fig. 3.17: Simulation results of the proposed method under under the load variation.

trajectory B→B_1→B_2. By contrast, the operating point gradually "jumps" further as the trajectory D→D_1→D_2→D_3. The simulation results validate that the proposed ASF-Beta method is successful to adaptively tune its step size.

Fig. 3.16 illustrates the simulation results of the proposed method under the week solar irradiance variation. The solar irradiance level decreases from 400W/m^2 to 100W/m^2 at 0.5s and increases to 400W/m^2 at 2.5s. During this period, the load resistance is fixed at 80Ω. As shown in Fig. 3.16, the similar results, such as adaptively tuning step size and no oscillations, can be found.

Fig. 3.17 illustrates the simulation results of the proposed method under the load variation. The load resistance decreases from 60Ω to 30Ω at 0.5s, and then increases back to 60Ω at 2s. The solar irradiance level is kept constant at 600W/m^2 during this period. From Fig. 3.17, the similar results, such as adaptively tuning step size and no oscillations, can be found.

3.2.3 Comparison Between the Proposed Method and Other MPPT Methods

Fig. 3.18, Fig. 3.19 and Fig. 3.20 shows the simulation results of the fixed step size P&O method, variable step size INC (VSSINC) method, Beta and the proposed method under strong solar irradiance variation, week solar irradiance variation and load variation, respectively.

From these simulation results, it can be seen that the P&O method takes the longest time to track the MPP when the solar irradiance or load is changed. A total time around 1.3s is required to track the MPP under the strong solar irradiance variation and the load variation; while a much longer time around 2.2s is needed during the week solar irradiance variation. The slow tracking speed of the P&O method definitely results in significant dynamic power loss. Besides, three-level oscillations can cause the extra power losses during the steady-state stage.

Compared to the P&O method, the VSSINC method has a better performance in the dynamic stage. The VSSINC method generally has a fast tracking speed when the solar irradiance is changed to the high level (e.g. 400W/m^2 to 1000W/m^2). By contrast, the VSSINC method has a poor performance if the solar irradiance is changed to the low level. Taking Fig. 3.19 as an example, when the solar irradiance is decreased from 400W/m^2 to 100W/m^2, the VSSINC method is unable to track the MPP within 3s. As shown in (2.18), the step size of the VSSINC method is determined by two factors: one is $\Delta P/\Delta V$ and the other is N. When the solar irradiance is low, the value of $\Delta P/\Delta V$ is much lower than that under high solar irradiance level. As a consequence, the step size of the VSSINC under the low solar irradiance level is smaller than that under the high level. Although

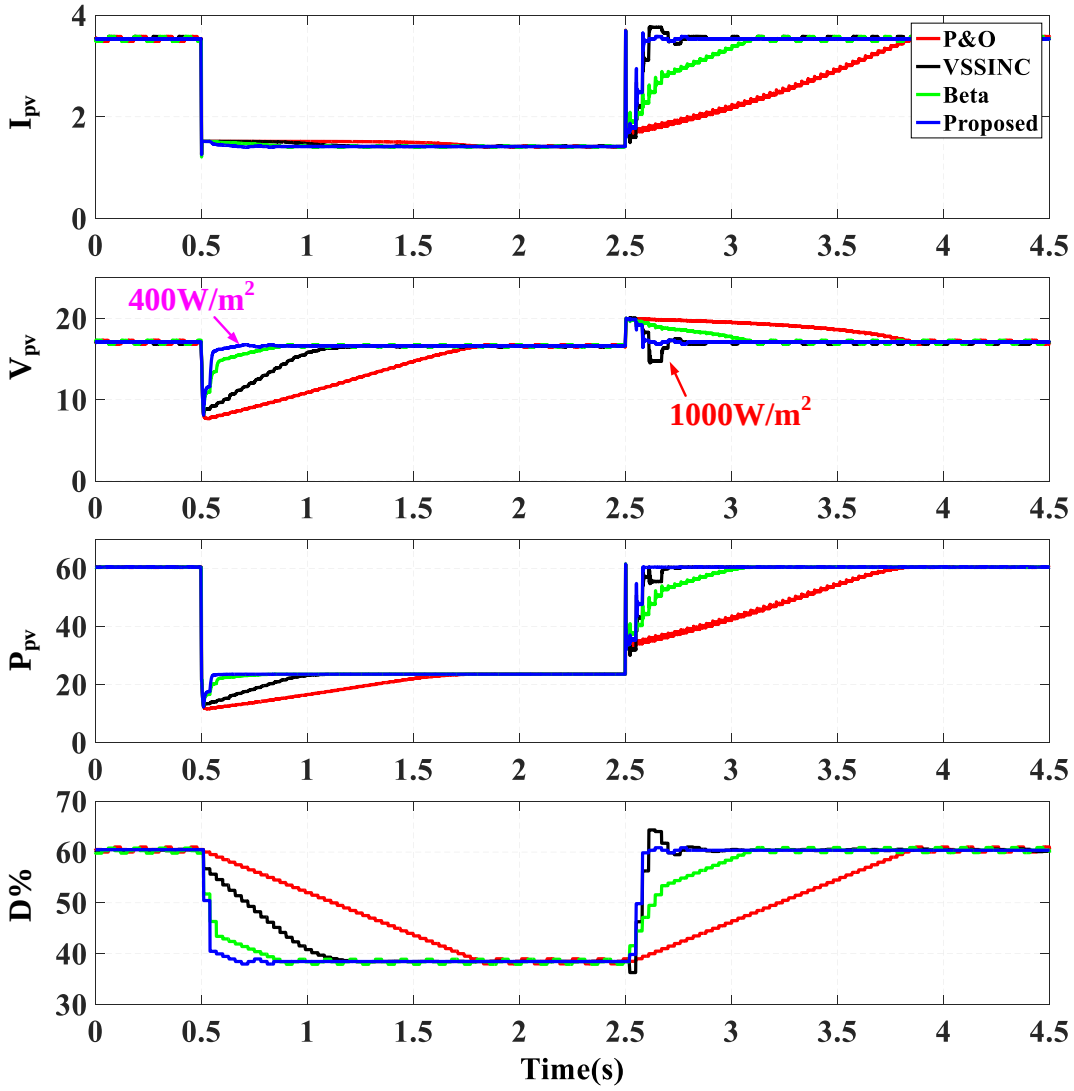

Fig. 3.18: Comparisons of the simulation results under the strong solar irradiance variation.

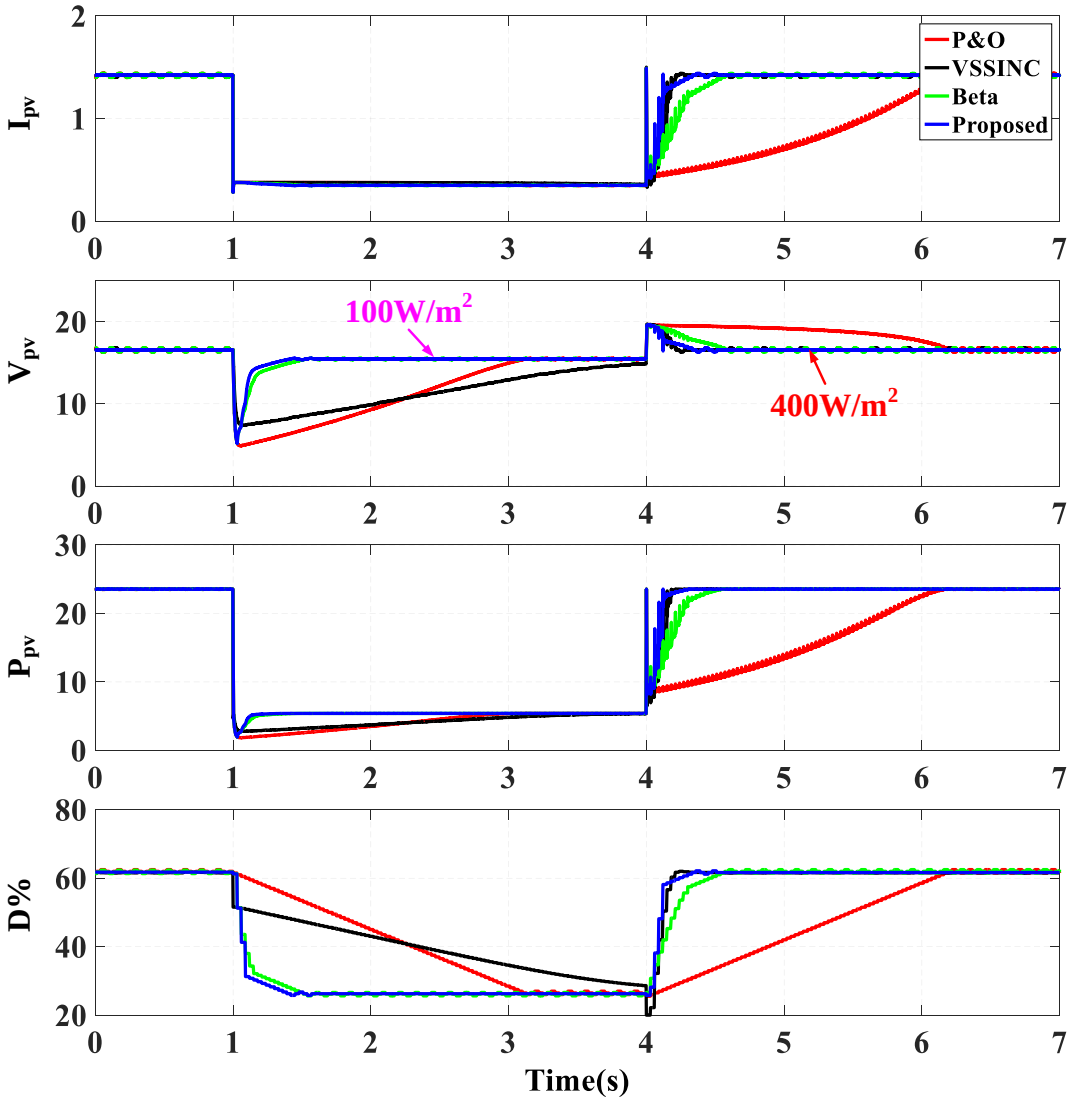

Fig. 3.19: Comparisons of the simulation results under the week solar irradiance variation.

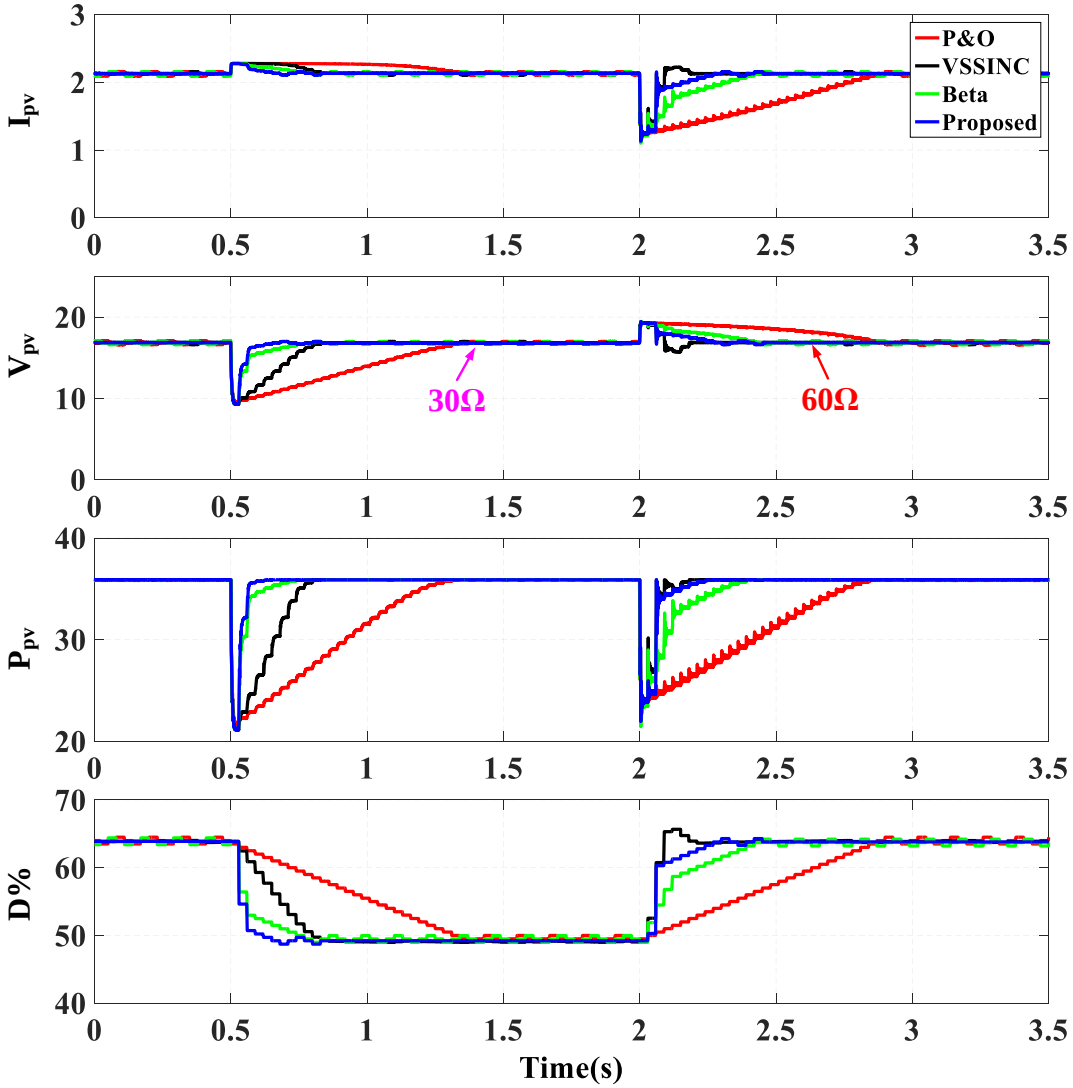

Fig. 3.20: Comparisons of the simulation results under the load variation.

tuning a larger value of N can remedy the embarrassed circumstances under the lower solar irradiance level to some degrees, it may affect the performance under the higher level.

Regardless to the changes of the solar irradiance levels, the conventional Beta method generally has a good performance in the dynamic stage, especially when the solar irradiance is changed to the low level (e.g. 1000W/m^2 to 400W/m^2 and 400W/m^2 to 100W/m^2). However, when the solar irradiance is changed to the high level, such as 400W/m^2 to 1000W/m^2, the conventional Beta method is relatively slow. The reason for it is that the value of N is too small. However, if the value of N is too big, it may cause the undesired performance shown in Fig. 3.5.

Apart from the dynamic performance, it is clearly seen that the P&O method, the VSSINC method and the conventional Beta method have the steady-state oscillations.

3.2.4 Comparison of the Power Loss Caused by Different MPPT Methods

In order to highlight the advantages of the proposed method, the power loss for dynamic stage and steady-state stage P_{loss} is defined as [72, 74, 75]:

$$P_{loss} = \frac{\sum P_{max}(t) - \sum P_{pv}(t)}{\sum P_{max}(t)} \tag{3.8}$$

where P_{max} is the theoretical maximum power under a certain solar irradiance value; t refers to the total tracking time used by the different MPPT methods to find the MPP for the dynamic stage or the time after reaching the MPP if the steady-state stage is considered.

Fig. 3.21 compares the power loss caused by different MPPT methods during the dynamic stage and the steady-state stage. The calculated power loss during the dynamic stage with the P&O method is the highest among all of the simulated MPPT methods. Apart from the scenario that the load is increased from 30Ω to 60Ω, the calculated power loss during the dynamic stage with the proposed method is the lowest. Since a fixed step size is used by the P&O method and the conventional Beta method, the power loss during the steady-state stage for them are almost same, which are higher than other methods. Due to a variable step size, the power loss for the VSSINC method during the steady-state stage is smaller than that with P&O method and the conventional Beta method. Furthermore, the power loss for the proposed method during the steady-state stage is the smallest one under all irradiance levels due to no oscillations.

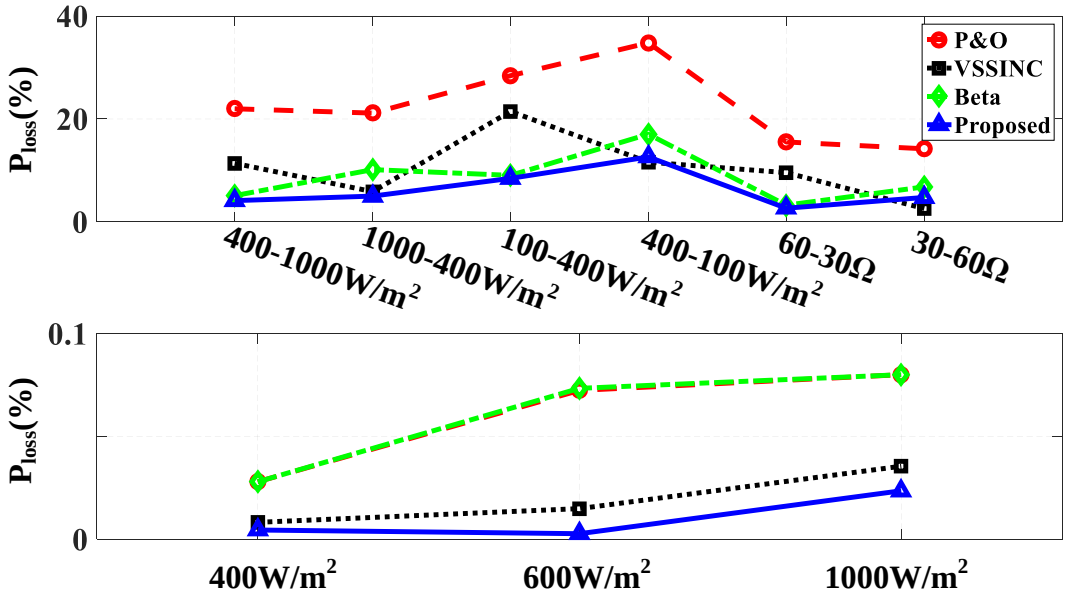

Fig. 3.21: Comparison of the power loss caused by different MPPT methods

3.3 Experimental Results

In order to verify the effectiveness of the proposed method, several experiments were performed on the experimental prototypes, as shown in Fig. 3.22. A boost converter is used as the power interface and its specifications are illustrated in Table 3.2. The PV emulator, Chroma ATE-62050H-600S, is used to emulate the PV module characteristics. The dSPACE DS1104 is used as a control platform where the various MPPT methods are implemented. The electronic load, IT8514C+, is used for load variation.

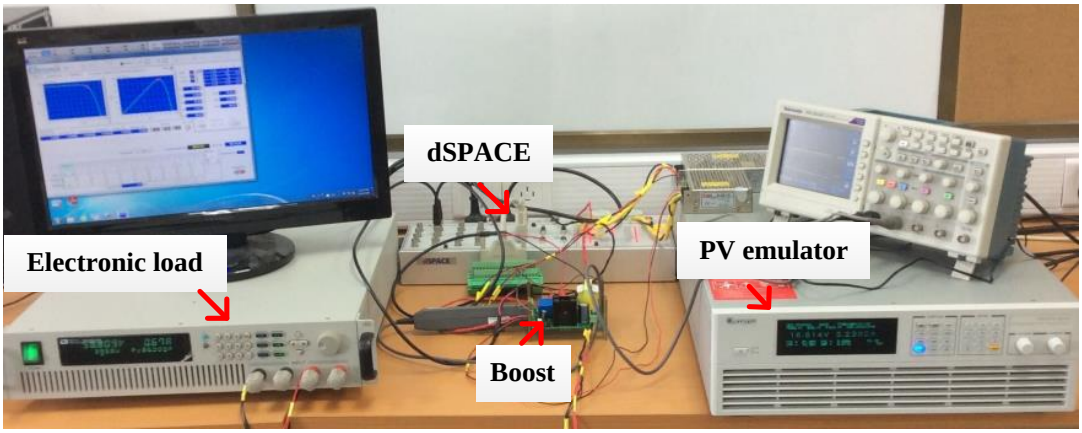

Fig. 3.22: Experimental prototype of the PV system with MPPT control.

The parameters in terms of solar irradiance and load variation in the experiments are the same as those in the simulation. The experimental results of the P&O method are illustrated in Fig. 3.23. From Fig. 3.23, it can be seen that the average time to track the

Table 3.2: Main components for the boost converter

Parameter	Value
Electrolytic capacitor C1 (PV side)	470uF
Electrolytic capacitor C2 (Load side)	47uF
Inductor L	1mH
IGBT	IRG4PH50U
Diode	RHRG30120
Current transducer	LA25-NP
Voltage transducer	LV25-P
Switching frequency	10kHz

new MPP for the P&O method is around 10s. Besides, the steady-state oscillations are very obvious in all cases, which results in power loss.

Fig. 3.24 shows that the experimental results of the VSSINC method. Generally, the tracking time for the failing transient is much longer than that for the rising transient. Moreover, it can be seen that the VSSINC method can not track the MPP during the failing transient (400W/m^2 to 100W/m^2). It is also clear to see the oscillations in the steady-state stage.

Fig. 3.25 shows that the experimental results of the conventional Beta method. The average tracking time for it is around 2s-5s. Besides, the performance of the failing transient is slightly better than that for the rising transient. The steady-state oscillations are also obvious in all cases.

Fig. 3.26 demonstrates that the proposed method exhibits the shortest time to track the MPP compared with the other MPPT methods. During the steady-state stage, no oscillations can be observed by unitizing the proposed method. Therefore, the overall performance under both of the dynamic stage and the steady-state stage is better than the other MPPT methods.

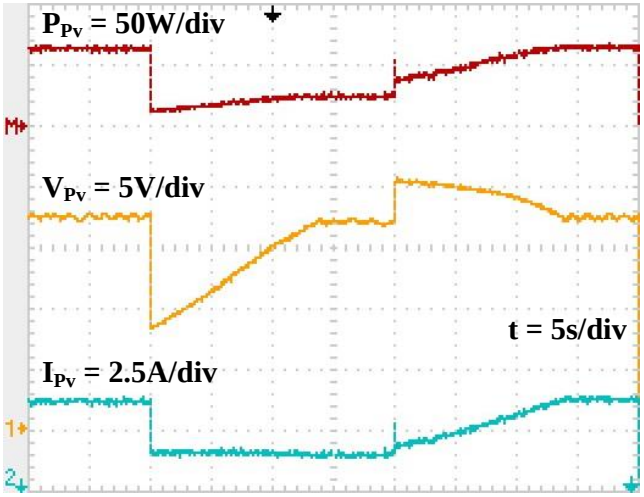

(a)

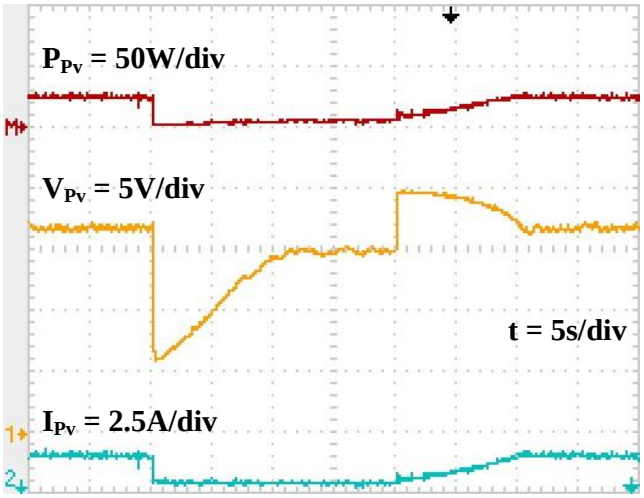

(b)

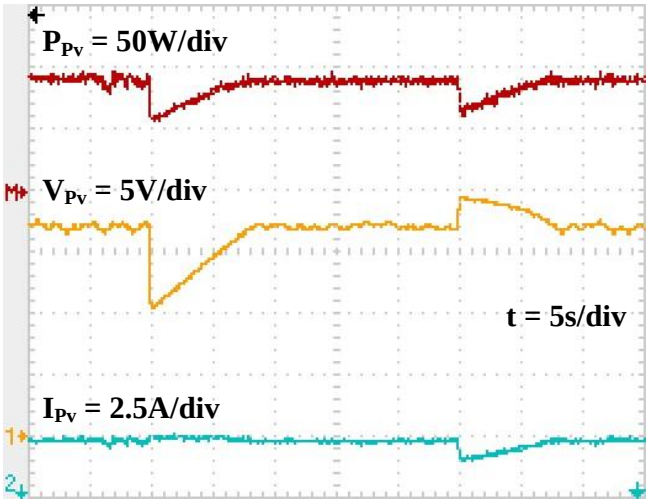

(c)

Fig. 3.23: Experimental results of the P&O method: (a) strong solar irradiance variation; (b) week solar irradiance variation; (a) load variation.

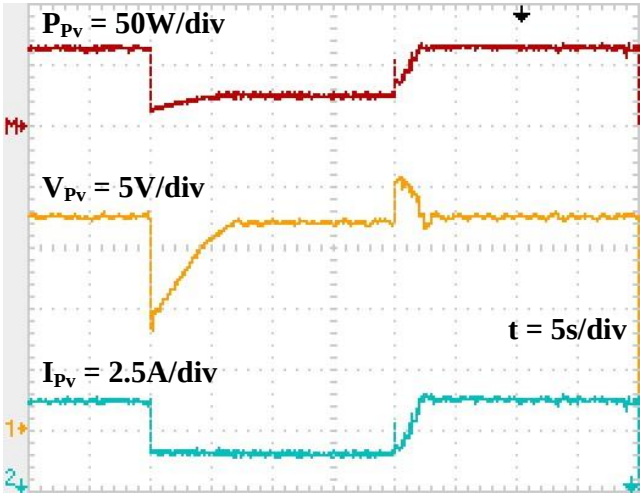

(a)

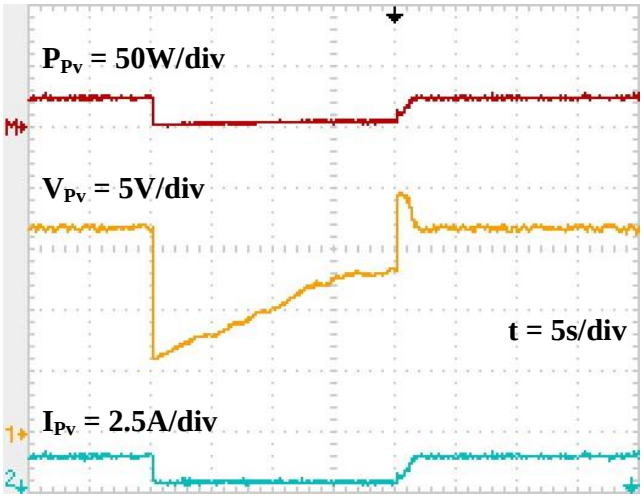

(b)

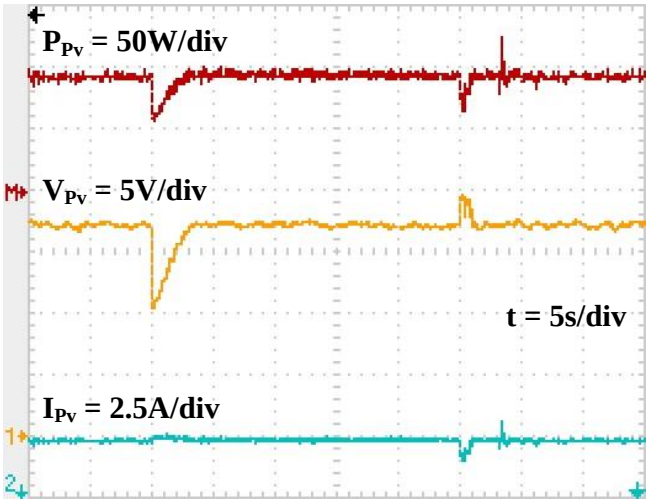

(c)

Fig. 3.24: Experimental results of the VSSINC method: (a) strong solar irradiance variation; (b) week solar irradiance variation; (a) load variation.

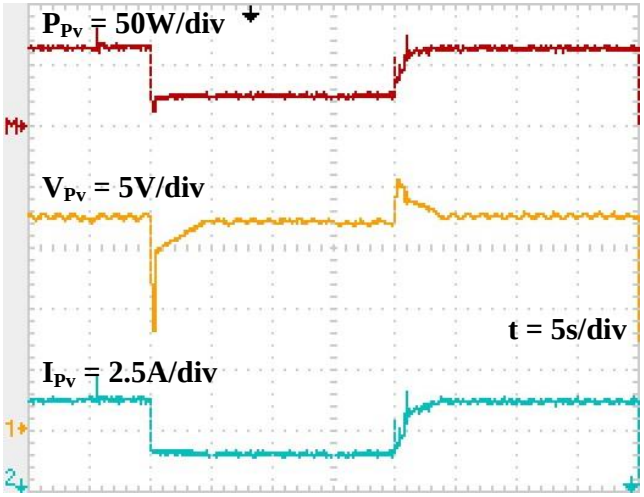

(a)

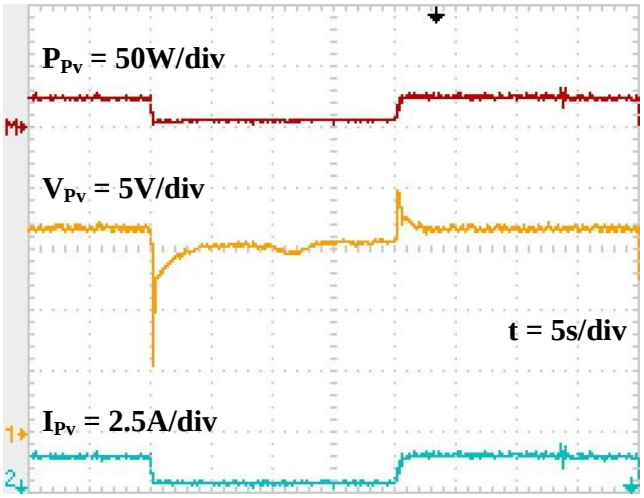

(b)

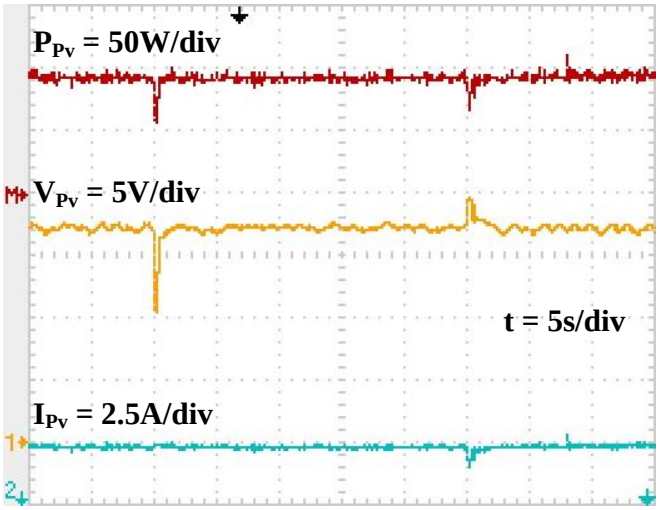

(c)

Fig. 3.25: Experimental results of the conventional Beta method: (a) strong solar irradiance variation; (b) week solar irradiance variation; (a) load variation.

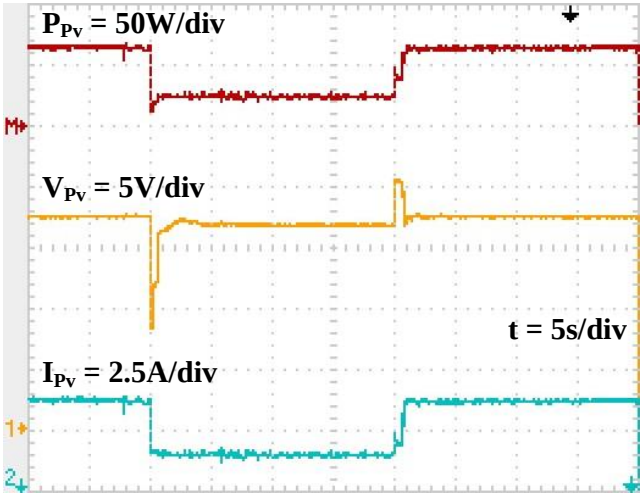

(a)

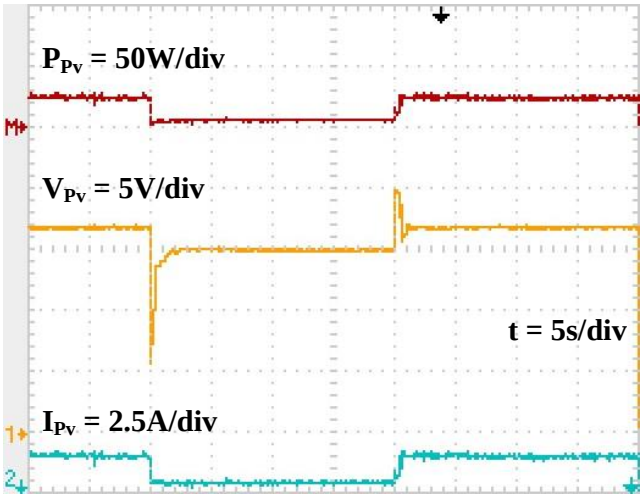

(b)

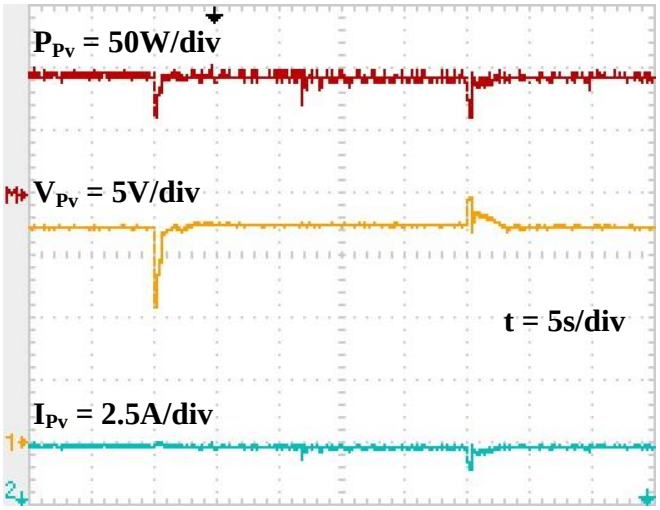

(c)

Fig. 3.26: Experimental results of the proposed method: (a) strong solar irradiance variation; (b) week solar irradiance variation; (a) load variation.

Chapter 4

Modified Beta Algorithm for Global Maximum Power Point Tracking (GMPPT)

In practice, the PV source generally consists of several PV modules, which are connected in series and formed into a PV string. As shown in Fig. 4.1, when the PV string is under the uniform insolation condition, the I-V curve and and P-V curve of the PV string (solid line) has one MPP. Therefore, the aforementioned MPPT methods in Chapter 2 and the proposed ASF-Beta & ZO-OP method can successfully track the MPP.

Typically, a bypass diode is added in parallel for each PV module for preventing hot spot effect when one or serval PV modules are shaded. However, adding the bypass diode will change the I-V characteristic curve. As shown in Fig. 4.1, there are multiple peaks on the I-V curve and P-V curve (dash line) when the PV string is under the partial shading condition (PSC). Generally, there are only one global MPP (GMPP) and several local MPPs (LMPP) among these peaks. Since the conventional MPPT methods are designed to track the single peak and they are not able to identify the GMPP, they may be trapped at the LMPP.

The content of this chapter has been published in the following paper:

1. **Li, X.**, Wen, H., Hu, Y., Jiang, L., Xiao, W., "Modified Beta Algorithm for GMPPT and Partial Shading Detection in Photovoltaic Systems", *IEEE Transactions on Power Electronics*, 33 (3), pp. 2172-2186, March 2018.

2. **Li, X.**, Wen, H., Chu, G., Hu, Y., Jiang, L., "A novel power-increment based GMPPT algorithm for PV arrays under partial shading conditions", *Solar Energy*, 169, pp. 353-361, 2018.

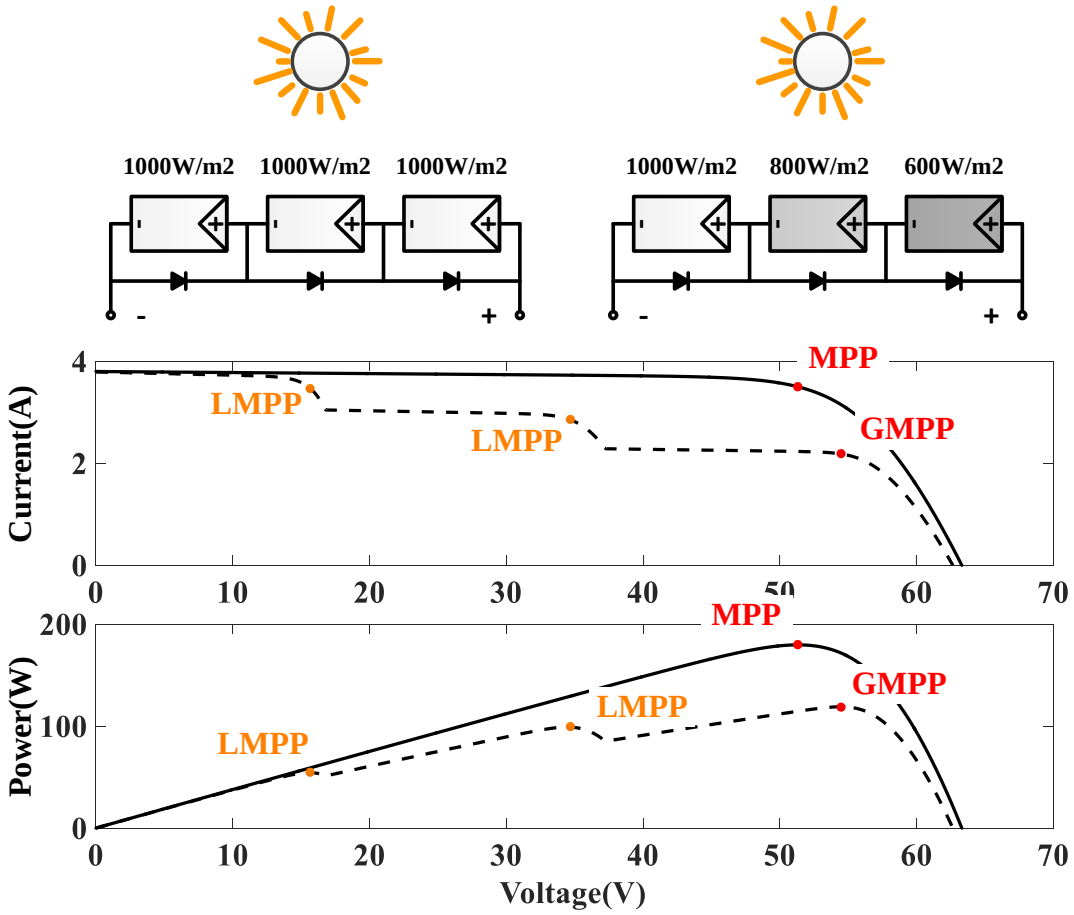

Fig. 4.1: I-V curve and and P-V curve of the PV string under uniform insolation condition and partial shading condition (PSC).

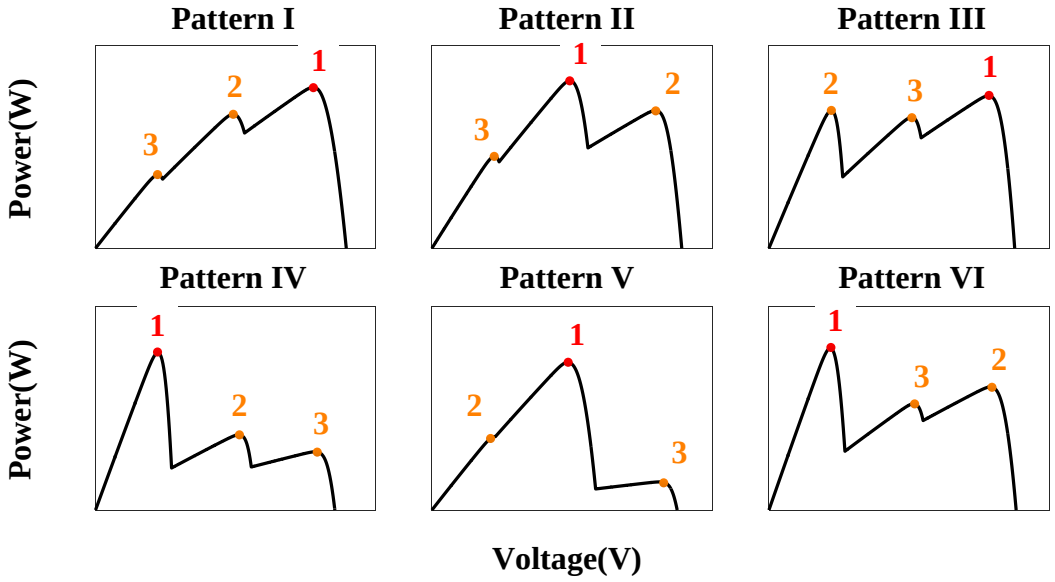

Fig. 4.2: Different PSC patterns for three PV modules connected in series in the PV string (3s1p).

4.1 Literature Review on the GMPPT Methods

In order to address the PSC issues, a great number of global maximum power point tracking (GMPPT) methods have been proposed and discussed [19, 76]. Based on the main features of the GMPPT methods, they can be categorized into several groups, namely segmental search methods [77–79], power increment methods [80, 81], soft computing (SC) methods [82–94], load line methods [95, 96] and $0.8V_{oc}$ model methods [97–100]. In the following section, these GMMPT methods will be compared and reviewed.

4.1.1 Various PSC Patterns

Due to the different shadow degrees of the PV string, many different PSC patterns can be formed. Taking three PV modules connected in series in the PV string (3s1p) as an example. As shown in Fig.4.2, there are six main PSC patterns for the 3s1p. The highest peak is denoted as 1, the middle peak is denoted as 2 and the lowest peak is denoted as 3. It should be noted that all of the PSC patterns in Fig. 4.2 can occur. Therefore, the GMPP method must be able to track all of the PSC patterns. In the following subsection, these PSC patterns will be used to demonstrate whether the reviewed GMPPT methods are able to track the GMPP.

4.1.2 Segmental Search Method

The basic idea of the segmental search method is to gradually reduce the searching range to find the GMPP. The segmental search methods are generally based on the mathematical theories, such as Lipschitz characteristics [77] and Fibonacci sequence [78, 79]. In this thesis, the dividing rectangles (DIRECT) method, which is based on the Lipschitz characteristics, is used to demonstrate the main features of the segmental search method.

According to [77], the Lipschitz condition can be written as:

$$|p(v) - p(v_1)| \leq M|v - v_1| \quad \forall v, v_1 \in [a, b] \tag{4.1}$$

where $p(v)$ refers to the power-voltage function; v_1 is a sampled point and v is a variable; M is Lipschitz constant, which is uniformly continuous and bounded on $[a, b]$. Then, the upper and lower bounds on the values of the function $p(v)$ refer to:

$$p(v_1) - M|v - v_1| \leq p(v) \leq \max_{v \in [a,b]} \{p(v)\} \leq p(v_1) + M|v - v_1| \tag{4.2}$$

If v_1 is at the center of $[a, b]$, it can be derived from (4.2) that

$$p(v) \leq \max_{v \in [a,b]} \{p(v)\} \leq p(v_1) + M\frac{b-a}{2} \tag{4.3}$$

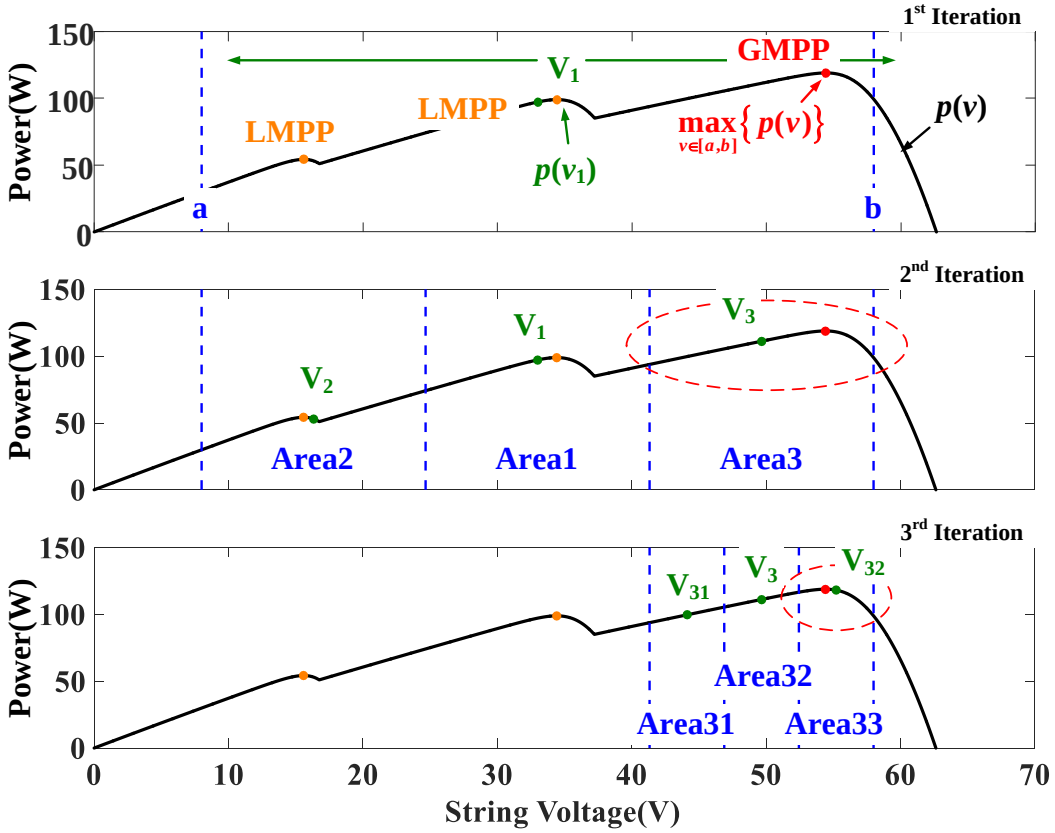

Fig. 4.3: Demonstration of the tracking process for the DIRECT method.

Fig. 4.3 demonstrates the tracking process for the DIRECT method, where $p(v)$ refers to the P-V curve; a and b refer to the lower and upper bounding, respectively; V_1 refers to the center point of $[a, b]$ and $p(v_1)$ refers to the value at the point V_1; $\max\limits_{v\in[a,b]}\{p(v)\}$ is equivalent to the value at the GMPP.

In the first iteration, the value at the point V_1 is sampled. Then, the interval of $[a, b]$ is divided into three subintervals, namely Area1, Area2 and Area3. The values at the center point in the sub-intervals, namely V_2 and V_3 in Area2 and Area3, respectively, are sampled too. The DIRECT method then evaluates three samples to decide the next sampling interval, which is defined as potentially optimal interval (POI). Assuming interval j is the POI and there exists a rate of change constant $\widetilde{K} > 0$ such that [101]:

$$p(v_j) + \widetilde{K}\frac{(a_j - b_j)}{2} \geq p(v_i) + \widetilde{K}\frac{(a_i - b_i)}{2} \quad \forall i \tag{4.4}$$

The inequality (4.4) implies that the interval with the highest function value at the center point is the POI. As a result, the Area3 is selected and a further triple division is made, namely Area31, Area32 and Area33. By continuously taking further divisions, the interval of $[a, b]$ can be effectively replaced by smaller subintervals successively. This process will be continuously repeated until the subinterval is close to the vicinity of the

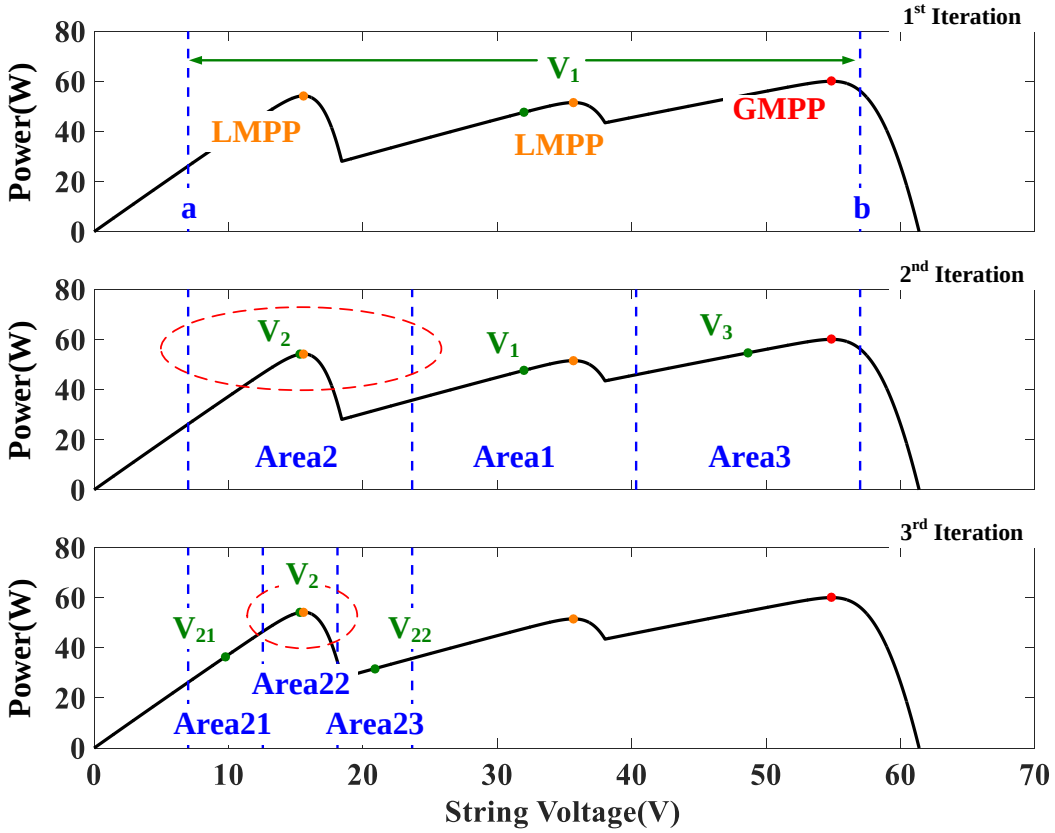

Fig. 4.4: Incorrect tracking of GMPP using the DIRECT method under a certain PSC pattern.

GMPP.

The advantages of the DIRECT method are its solid mathematical foundation and straight-forward algorithm implementation. However, the initial interval has to be selected properly since the DIRECT method may not track the GMPP under a certain PSC pattern. As shown in Fig. 4.4, the Area1 is selected as the POI since the value at V_2 is higher than that at V_3. As a consequence, a further triple division is made and the LMPP in the Area2 is misjudged as the GMPP.

4.1.3 Power Increment Method

The power increment method is firstly proposed in [80]. Fig. 4.5 demonstrates the tracking process of the power increment method [80]: Firstly, a fixed power interval is used to search the entire P-V curve. Then, the operating point progressively jumps upon higher power levels until no more power can be increased. Finally, the P&O method is employed to accurately locate the GMPP.

The advantage of the power increment method is its universality and effectiveness for various PSC patterns. However, the performance of the method in [80] is mainly

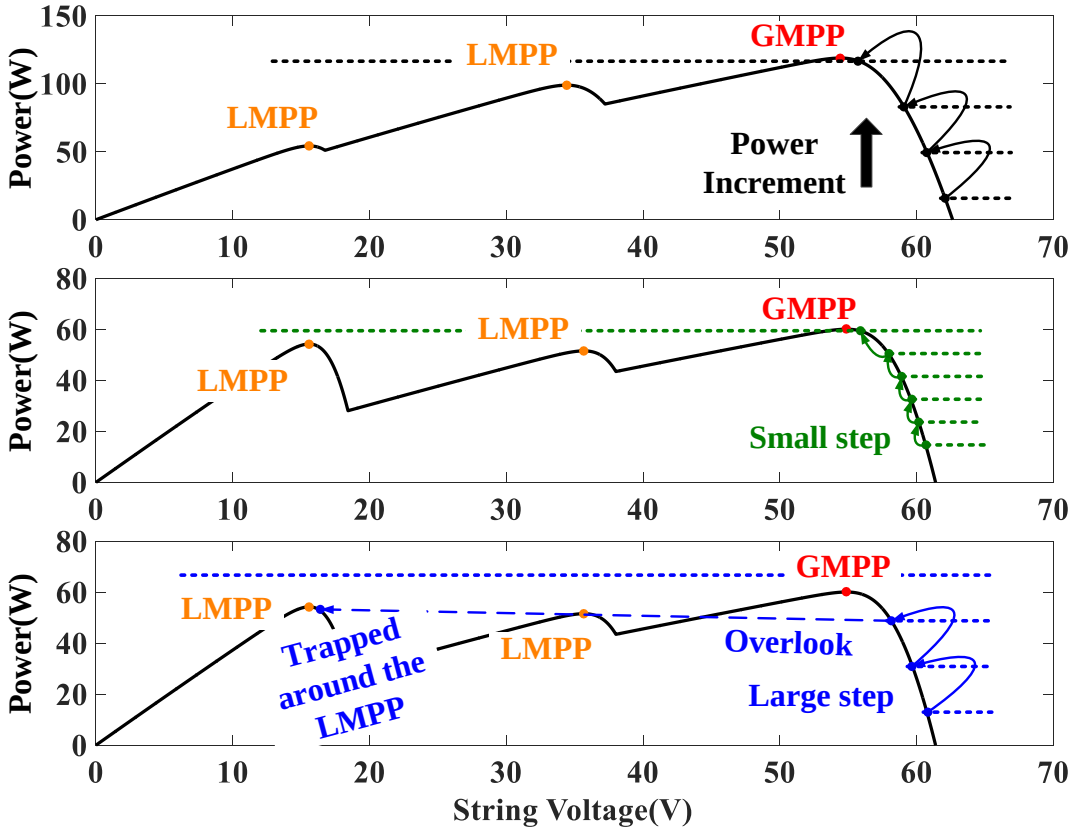

Fig. 4.5: Demonstration of the tracking process for the power increment method by E. Koutroulis.

determined by the value of the fixed power interval [76]. As shown in Fig. 4.5, a large power interval requires less tracking step to the GMPP while it may also result in the GMPP overlook. By contrast, a small power interval can avoid the overlook while it results in the GMPP overlook. Furthermore, a power command rather than duty cycle command or voltage command has to be directly used to control the DC-DC converter, which is also difficult to be implemented [76]. As a consequence, this method has to use a special control circuit.

In [81], a modified power increment method is proposed. Unlike the conventional power increment method, the modified method can use duty cycle command to control the DC-DC converter. The power, voltage and load lines rather than the fixed power interval are used and the next moving position can be determined. The results in [81] validates the modified power increment method has a higher accuracy than the conventional power incremental method. Its tracking process is demonstrated in Fig. 4.6.

Assuming that the PV system starts at the operating point P_1. The corresponding value of voltage $V(k)$, current $I(k)$ and power $P(k)$ can be measured. The reference power P_{ref}

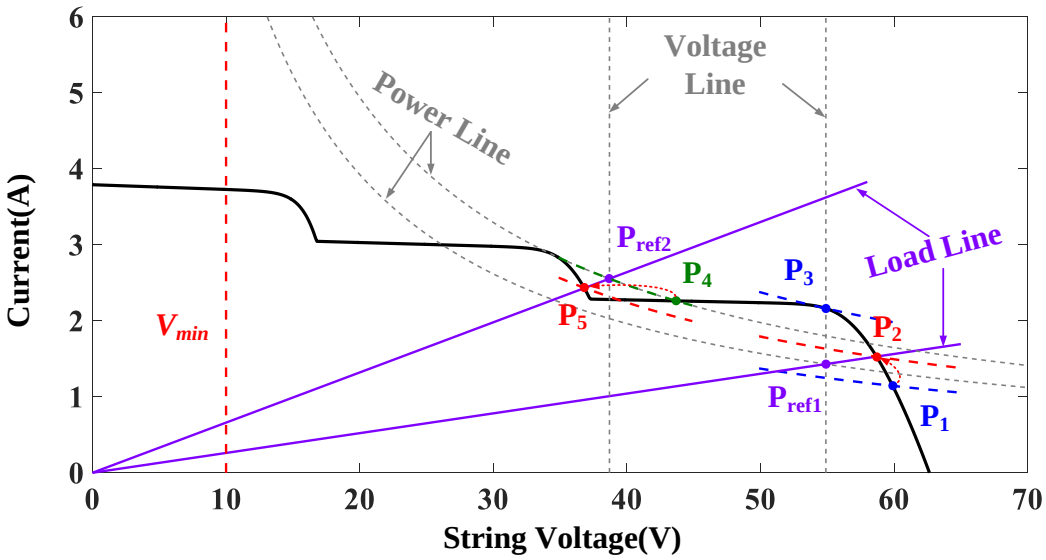

Fig. 4.6: Demonstration of the tracking process for the modified power increment method by X.Li.

and the reference voltage V_{ref} are then obtained by:

$$P_{ref} = P(k) + \Delta P \tag{4.5}$$

$$V_{ref} = V(k) - \Delta V \tag{4.6}$$

Then, the power and voltage lines (dash gray lines) are imposed on the I-V curve by P_{ref} and V_{ref}, respectively. The purple point, P_{ref1} (the intersection between these two lines), will become the next desired point. However, this intersection may be not always on the I-V curve. By assisting with the load line (purple line), $R_{pv,ref}$ is obtained by

$$R_{pv,ref} = P_{ref}/V_{ref} \tag{4.7}$$

Assuming a buck-boost converter is used, we have

$$M(d) = -\frac{d}{1-d} \tag{4.8}$$

Substitute (4.8) into (2.11), it can be derived as:

$$d = \frac{\sqrt{R_{load}}}{\sqrt{R_{load}} + \sqrt{R_{pv}}} \tag{4.9}$$

Substitute (4.7) into (4.9), the duty cycle in the next time $D(k+1)$ will be updated by

$$D(k+1) = \frac{\sqrt{R_{load}}}{\sqrt{R_{load}} + \sqrt{R_{pv,ref}}} \tag{4.10}$$

Then, the intersection between $R_{pv,ref}$ and the I-V curve will be the exactly desired point, P_2.

If $P(k)$ is larger than the previous one $P(k-1)$, the aforementioned processes will be repeated. When the operating point moves from the point P_3 to the point P_4, the value of power at the point P_4 is found smaller than that at the point P_3. It indicates that the point P_3 is one of the peaks and the point P_4 is located at the valley between the two peaks. Then, the calculation of P_{ref} will be changed as to avoid the GMPP overlook

$$P_{ref} = P(k) \tag{4.11}$$

Then, $D(k+1)$ will be updated by (4.10).

The aforementioned process will be repeated continuously until the operating point reaches V_{min}, which refers to the low voltage boundary (red dash line). If the measured voltage is lower than V_{min}, it indicates that the whole I-V curve is scanned. Then, the operating point will move to the point P_3, which is recorded as the maximum power. Finally, the P&O method will be activated to exactly locate the GMPP.

4.1.4 SC Methods

The SC methods include artificial bee colony (ABC) [91], particle swarm optimization (PSO) [82–88], FLC [89], simulated annealing (SA) [93], grey wolf optimization (GWO) [92], ant-colony optimization (ACO) [94], firefly algorithm (FA) [90], and so on. All of them show good performance under various PSC patterns. Among of the aforementioned methods, the PSO method is a powerful searching algorithm which was modeled from the pattern observed in bird flocking and fish schooling by Eberhart and Kennedy in 1995 [83]. Two of the most important characteristics of the PSO method are its ability to communicate information and learn from this information. Therefore, the PSO method is selected as an example to demonstrate the main features of SC Methods.

In order to adapt the PSO method in the PV system, a number of particles with different duty cycles d_i, or called particles positions, are used. Fig. 4.8 demonstrates the movement of particles during the GMPP tracking process.

$$d_i(k+1) = d_i(k) + v_i(k+1),\ i = 1, 2, ..., N \tag{4.12}$$

where v_i is the velocity of particle i, k is the number of perturbation iteration and N is the total number of particles.

$$v_i(k+1) = \omega v_i(k) + c_1 r_1 (P_{best,i} - d_i(k)) + c_2 r_2 (G_{best} - d_i(k)) \tag{4.13}$$

where ω is the inertia weight; $P_{best,i}$ is the personal best position of particles i and G_{best} is the global best position of the particles in the entire population; c_1 is the cognitive

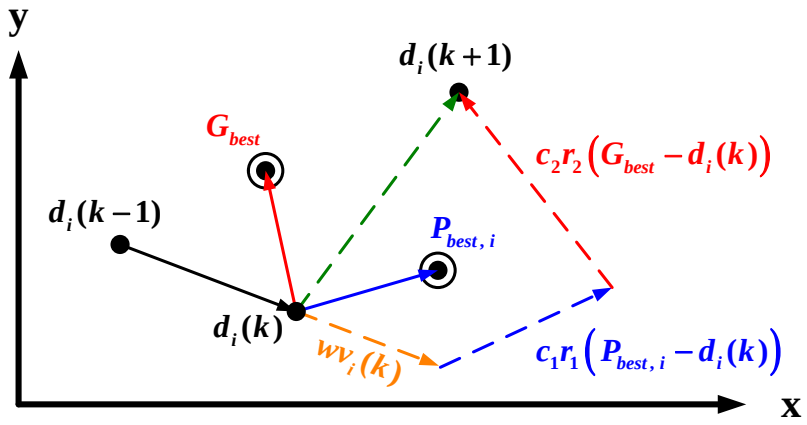

Fig. 4.7: Movement of particles during the GMPP tracking process.

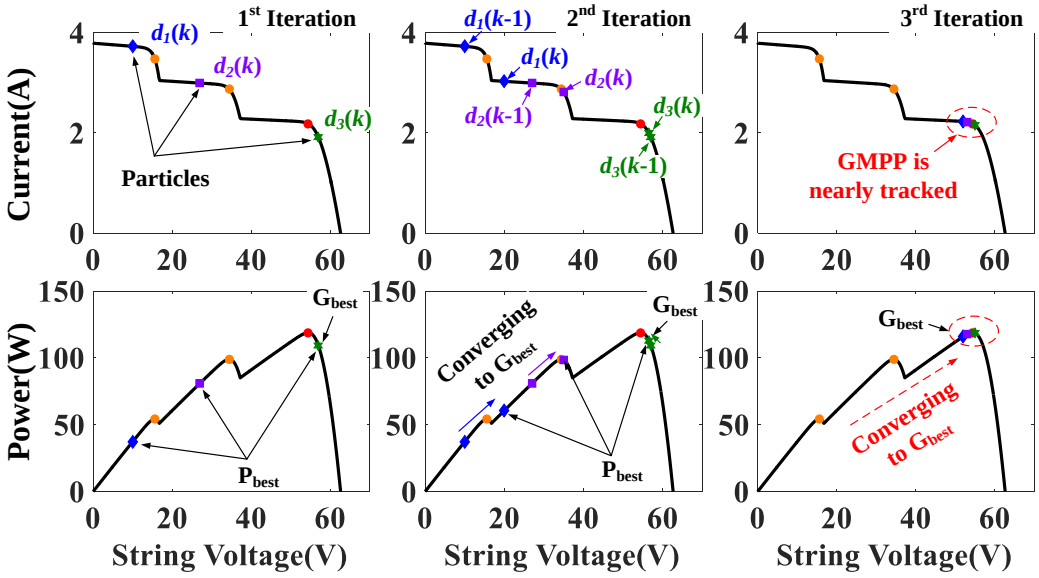

Fig. 4.8: Demonstration of the tracking process for the PSO method.

coefficient, c_2 is the social coefficient; and $r_1, r_2 \in U(0,1)$ which are random parameters. Furthermore, the corresponding power at the different positions of a particle, for every two consecutive iterations, is compared to obtain the best position with highest power. The function used to evaluate$P_{best,i}$ of each particle is described by

$$P(d_i(k+1)) > P(d_i(k)) \tag{4.14}$$

where $P(d_i(k))$ is the power at the duty cycle of the i^{th} particle in the k^{th} iteration.

Fig. 4.8 demonstrates the tracking process of the PSO method. Assuming that there are three particles used for the PSO method. In the first iteration, the three particles d_1, d_2 and d_3 are initialised which are marked with blue diamond, purple square and green hexagram, respectively. The term $P_{best,i} - d_i(k)$ in (4.13) is zero and the corresponding

velocity is only due to G_{best} term. Among these particles, d_3 is the G_{best} so d_1 and d_2 will converge towards G_{best} in the second iteration. Due to the fact that all of particles are better than their pervious iteration, the velocity direction of these particles remains unchanged and subsequently moves towards G_{best}. After several iterations, all of the particles will be converged to the vicinity of the GMPP.

According to the previous research [76], the PSO method has a relatively high accuracy to track the GMPP under different partial shadowing conditions. Furthermore, there is no oscillation once the GMPP is found, since the velocity of particles is zero. However, the main drawback of the standard PSO method is the long searching time for the re-initialization, which is caused by a large searching area and many tracking steps before convergence. When a large variation in the solar irradiance is happened, it is worthwhile to re-initialize the PSO method to track the new GMPP. On the other hand, when the solar irradiance experiences a small variation (which occur continuously in an actual PV system), the standard PSO method will have to be re-initialized multiple times to be able to track the MPP continuously. If the PSO algorithm is re-initialized for too small changes in the system, it will rarely be able to reach convergence. Consequently, this will result in a long tracking time and a high power losses [88]. Besides, many parameters related to the PSO method have to be properly tuned which is heavily relied on the designer's knowledge of the system.

4.1.5 Load Line Method

The load line method is proposed in [95, 96], and a linear function is preset as:

$$R_L = \frac{V_{string,oc}}{I_{string,sc}} \tag{4.15}$$

where $V_{string,oc}$ and $I_{string,sc}$ refer to the open-circuit voltage and the short-circuit current for the PV string, respectively.

Fig. 4.5 demonstrates the tracking process of the load line method. Assuming that the PV string is initially under the uniform insolation condition (black solid curve) and the operating point is at the point A (red dot). The tracking rules for the load line method are as follows:

When the PSC occurs, the operating point moves from the point A to the point B, which is marked as the sequence ①. At this time, the voltage reference V_{ref} is changed as:

$$V_{ref} = R_L \times I_{pv}(k) \tag{4.16}$$

As a consequence, the operating point will move to the point C, which is marked as the sequence ②. After that, the P&O method or the INC method will be used to track the exact MPP, which is marked as the sequence ③.

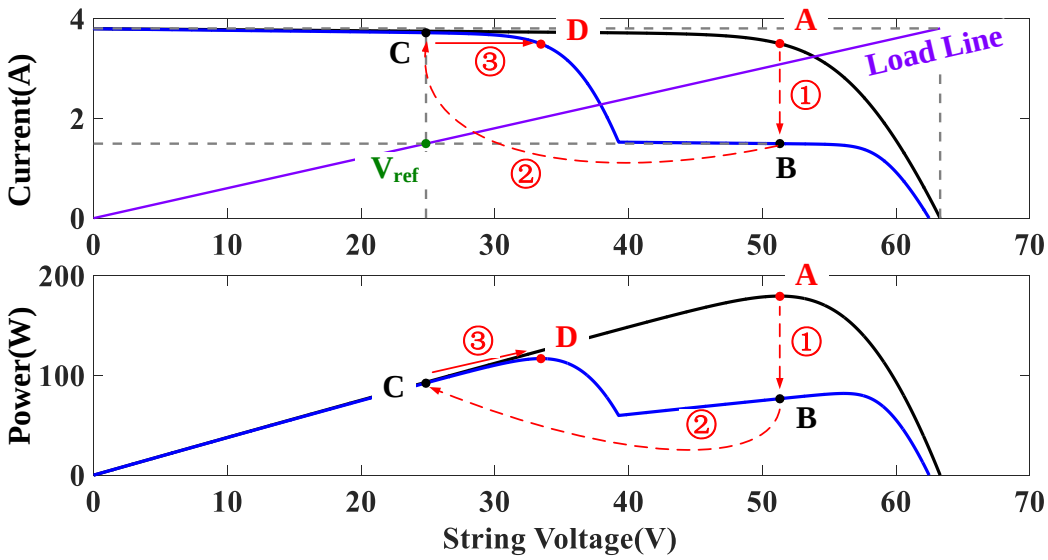

Fig. 4.9: Demonstration of the tracking process for the load line method.

The advantage of the load-line method is its fast tracking speed. Since only one step ② is need to move the operating point to the vicinity of GMPP, the tracking time is generally fast. However, the main drawback of this method cannot guarantee that the GMPPs can be always tracked.

Fig. 4.5 demonstrates the tracking process of the load line method under different PSC patterns. It is clearly seen that the load line method is able to find the right GMPP under the Pattern II. However, it is embarrassed that the point C is just trapped in the valley between the two peaks under the Pattern I and the Pattern III. As a consequence, the operating point may move towards either the left or the right. As shown in Fig. 4.5 , it is possible to find the right GMPP under the Pattern I, while it is impossible to find the right GMPP under the Pattern III.

4.1.6 0.8 Voc Model Method

$0.8V_{oc}$ model method is firstly proposed in [97] and modified in [98–100]. The $0.8V_{oc}$ model method assumes that the distance between any two successive peaks is around 80% of V_{oc}. Fig. 4.11 demonstrates the tracking process of the $0.8V_{oc}$ model method by H. Patel. Initially, the P&O method is used, which is marked as the sequence ①. When the first peak is tracked, a large voltage step, which is recommended around $0.7V_{oc}$, is applied to jump to the next peak, which is marked as the sequence ②. Then, the the P&O method is used again to track the next peak. This process is repeated until the current peak is lower than the previous one, which indicates that the previous one is the GMPP. Finally, the operating point comes back to the previous peak, which is marked as the sequence ③.

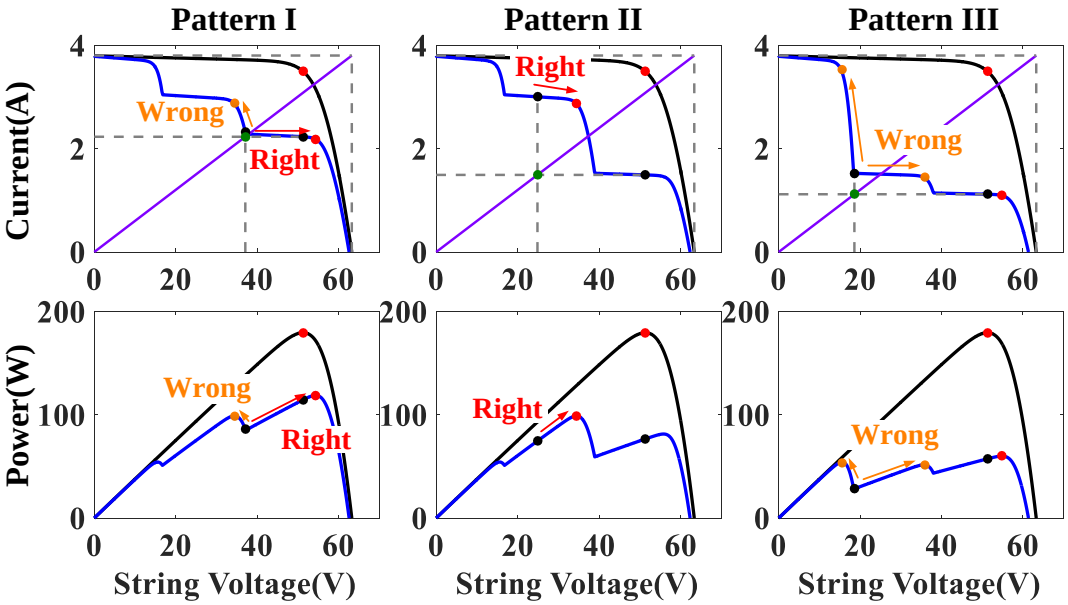

Fig. 4.10: Demonstration of the tracking process for the load line method under different PSC patterns.

The $0.8V_{oc}$ model method proposed by H. Patel is very straightforward and easy to be implemented. Furthermore, the global searching of this method is also very effective since only the vicinities of the $0.8V_{oc}$ areas rather than the whole P-V curve are searched. However, there are several drawbacks for this $0.8V_{oc}$ model method. Firstly, the overall tracking speed of this method is generally slow since each peak must be determined by the P&O method, marked as blue dots in Fig. 4.11.

Secondly, this method may overlook the GMPP due to the sequence ③. Fig. 4.12 demonstrates the failure tracking process of the $0.8V_{oc}$ model method by H. Patel. Assuming that the operating point starts from the left side. After one peak is tracked, the operating point will move to the next vicinity of $0.8V_{oc}$ area. If the next peak is lower than the previous one, it indicates that the previous one is the GMPP. Then, the algorithm will skip to search the next $0.8V_{oc}$ area and the operating point will move back the previous peak. However, if the real GMPP is just located at the skipped area, the algorithm will overlook this real GMPP, which is trapped at the LMPP.

Thirdly, even though the real GMPP is not always overlooked, the $0.8V_{oc}$ model is not always true as pointed out in [102]. Fig. 4.13 demonstrates that the voltage interval between the two successive peaks is generally larger than $0.8V_{oc}$. Therefore, an incorrect global peak will be detected by scanning the wrong region of the P-V curve.

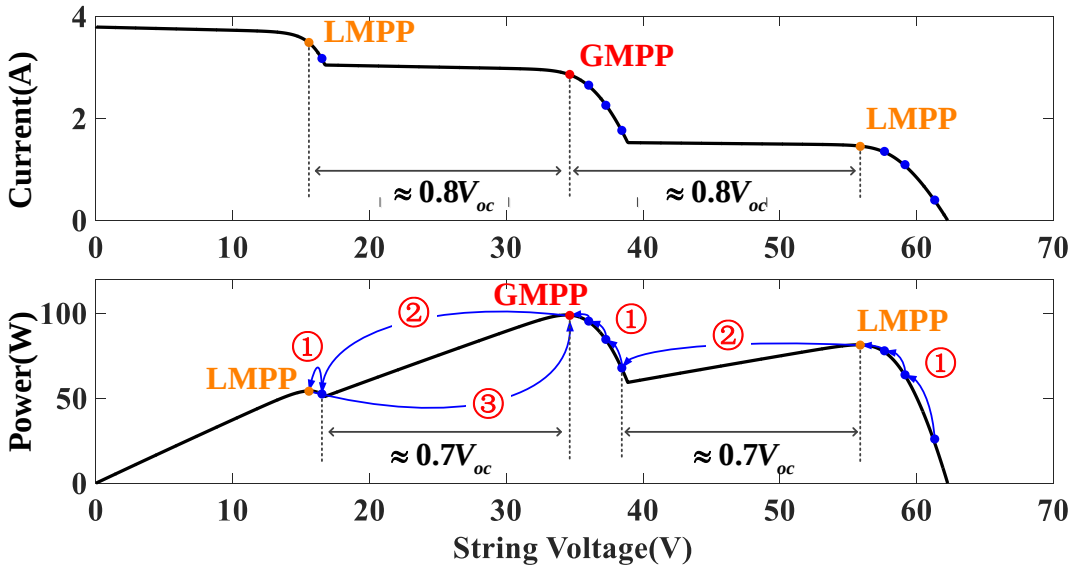

Fig. 4.11: Demonstration of the tracking process for the $0.8V_{oc}$ model method by H. Patel.

4.2 Proposed Beta Algorithm for GMPPT and Partial Shading Detection

4.2.1 PV String Equivalent Model

Fig. 4.14, Fig. 4.15 and Fig. 4.16 illustrate the operation stages of 3s1p PV string under the PSC. The I-V curve of the PV string is obtained by summing the voltage point-by-point for each value of the common current. The module A is fully illuminated with 1000W/m^2, while the module B and C are partially illuminated with 800W/m^2 and 600W/m^2, respectively. A bypass diode is connected in parallel with each PV module to avoid the occurrence of hot spot under the PSC [102]. Based on the number of conducted bypass diodes, three different operation stages are divided to analyze the operation of the PV string.

Fig. 4.14 demonstrates the stage I, where two bypass diodes are conducted. As shown in Fig. 4.14, the module B and C are bypassed and the PV string current flows through the module A. As a consequence, the string current I_{string} is determined by the characteristic of module A. At the meanwhile, the module B and C show the identical characteristics of independent voltage sources V_d, which refers to the forward voltage drop of the bypass diodes [103]. Here, the string voltage V_{String} can be demonstrated as:

$$V_{String} = V_{pv} + (-V_d) + (-V_d) \tag{4.17}$$

In the stage II, only the module C is bypassed, which can be simply represented as V_d. As shown in Fig. 4.15, I_{string} is mainly determined by the module B. At this time, the part of the I-V curve for module A is approximated as a straight line and the module A

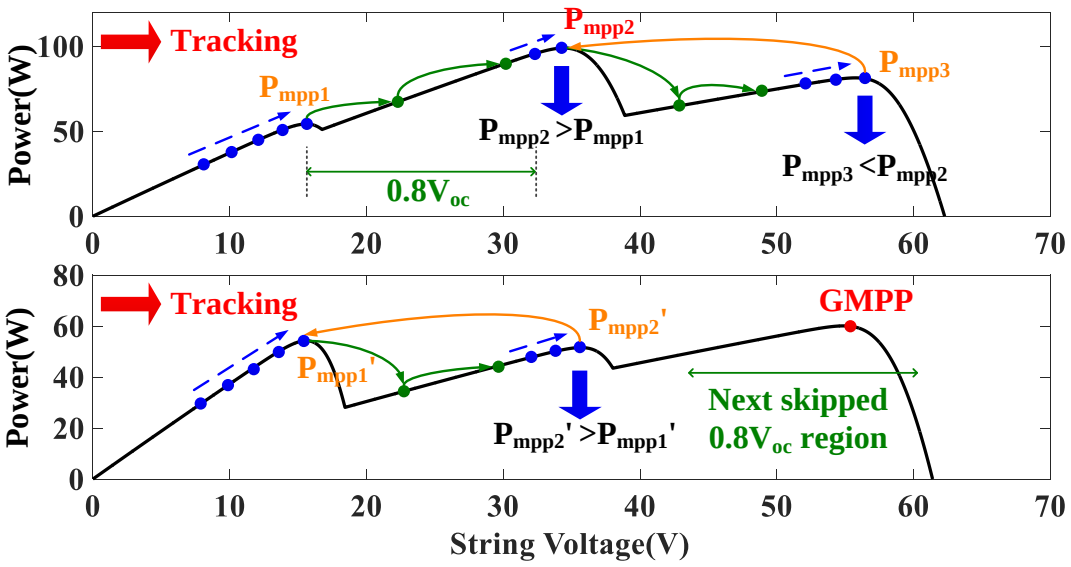

Fig. 4.12: Demonstration of the failure tracking for the $0.8V_{oc}$ model method by H. Patel.

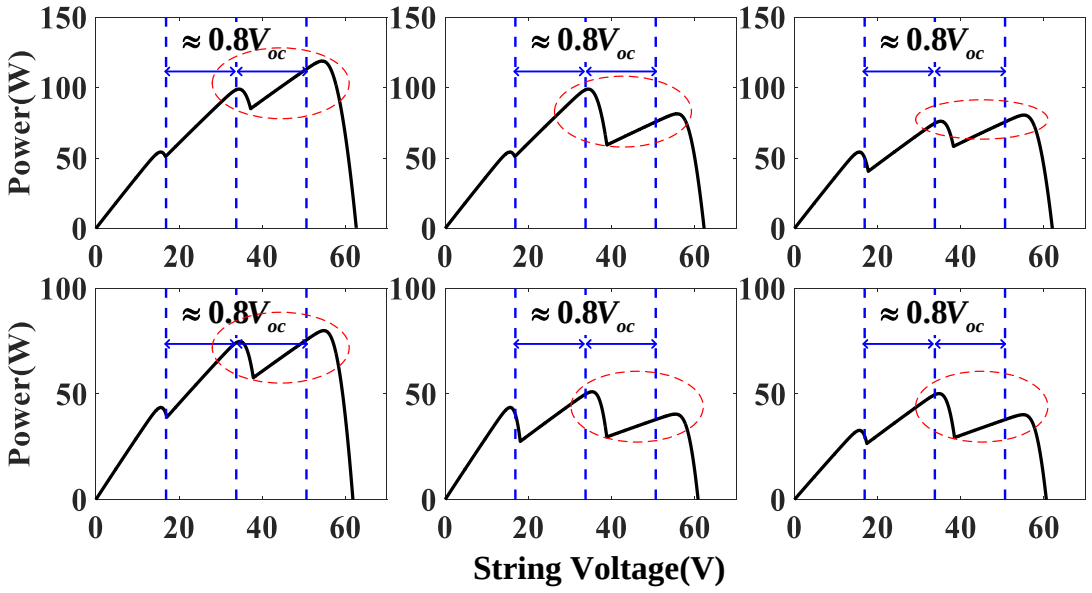

Fig. 4.13: Demonstration of the voltage interval between the two successive peaks.

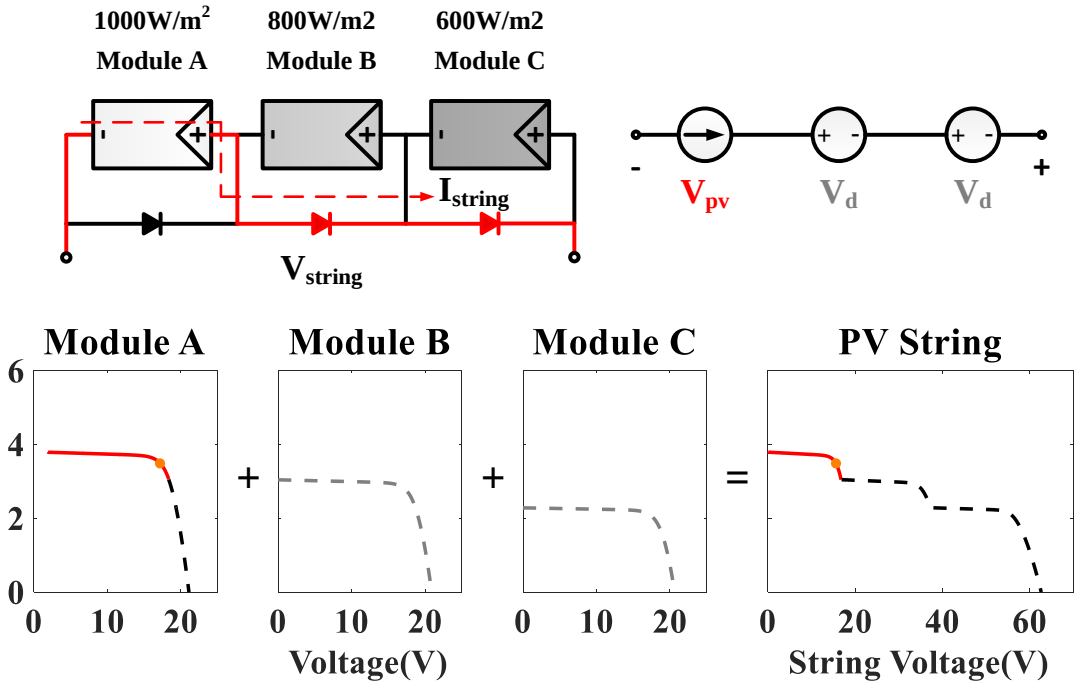

Fig. 4.14: Stage I of 3s1p PV string under the PSC.

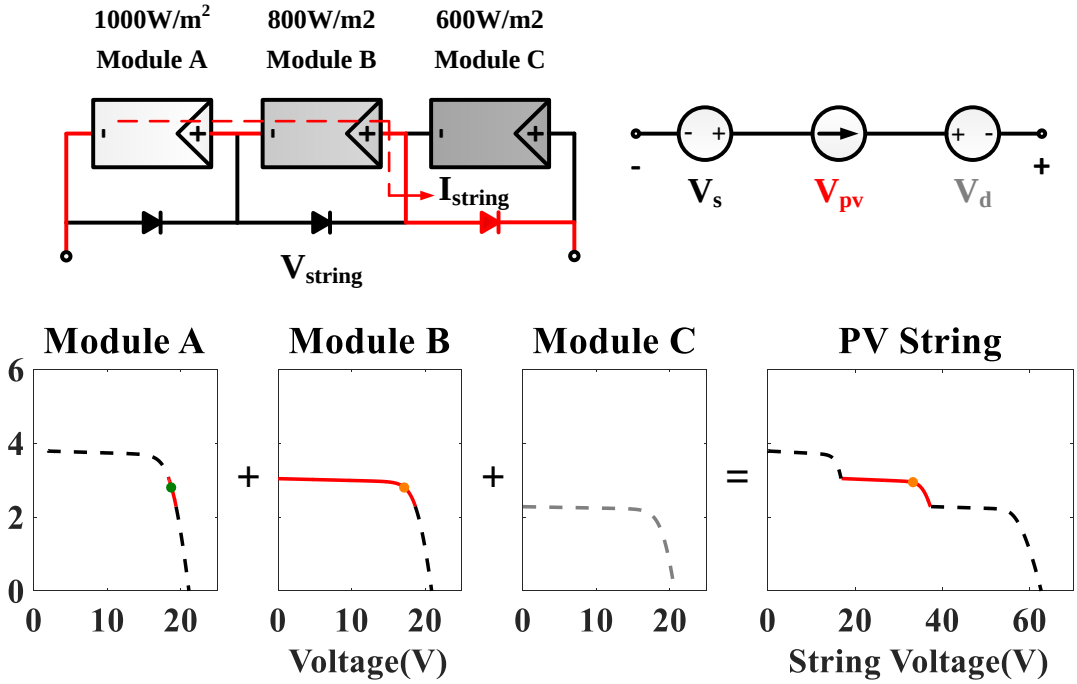

Fig. 4.15: Stage II of 3s1p PV string under the PSC.

can be regarded as a linear voltage source V_s [103]. Here, the string voltage V_{String} can be updated as:

$$V_{String} = V_s + V_{pv} + (-V_d) \tag{4.18}$$

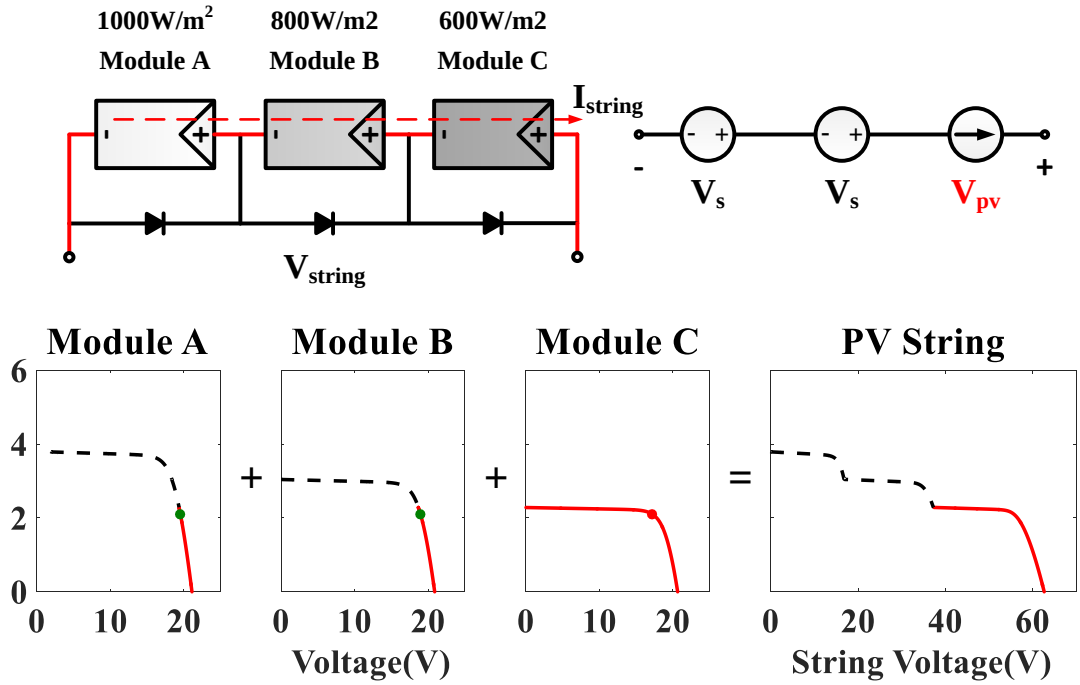

Fig. 4.16: Stage III of 3s1p PV string under the PSC.

In the stage III, no module is bypassed. As shown in Fig. 4.16, the module C takes the majority of the I-V characteristic of the PV string. Both of the module A and B represent as V_s and the string voltage V_{String} is updated as:

$$V_{String} = V_s + V_s + V_{pv} \tag{4.19}$$

From the aforementioned analysis, it can be seen that the I-V curve of the PV string is always determined by a key module [103]. Based on this phenomenon, tracking the whole PV string is equivalent to tracking each key modules of the PV string at the different voltage intervals. Therefore, the equivalent voltage of the key module V_{eq} can be written by

$$V_{eq} = V_{String} - (n-1) \times V_s + (m-n) \times V_d \tag{4.20}$$

where m indicates the total number of PV modules in one PV string, and n is obtained by

$$n = \begin{cases} 1, & 0 < V_{String} <= \alpha \cdot V_{oc} \\ 2, & \alpha \cdot V_{oc} < V_{String} <= 2 \cdot \alpha \cdot V_{oc} \\ ..., & \\ m, & (m-1) \cdot \alpha \cdot V_{oc} < V_{String} <= m \cdot \alpha \cdot V_{oc} \end{cases} \tag{4.21}$$

where V_{oc} refers to the open-circuit voltage of PV modules, α refers to a variable which is varying within 0.8 and 0.97 [102]. In order to make sure that every peak is in their own divided segment, α is set as 0.95 in this thesis.

In (4.20), V_d is set as $0.8V$ and V_s which is approximately expressed as [103, 104]

$$V_s \approx \frac{V_{MPP,stc} - V_{oc,stc}}{I_{MPP,stc}} \times I_{String} + V_{oc,stc} \tag{4.22}$$

where $V_{MPP,stc}$ and $I_{MPP,stc}$ refer to voltage and current at the MPP under the STC.

4.2.2 Modified Beta Method

With the aforementioned equivalent PV string model, the Beta method in [71, 72] can be modified to track the GMPP under the PSC. Substitute (4.20), (4.21) and (4.22) into (2.39), it can be derived as:

$$\beta_{eq} = ln\Big(\frac{I_{String}}{V_{eq}}\Big) - c \times V_{eq} \tag{4.23}$$

where β_{eq} refers to the equivalent value of β.

Fig. 4.17 shows the PV string$I$-V curve. By using (4.23), the equivalent V_{eq} and β_{eq} curves can be also plotted in Fig. 4.17. As shown in the top of Fig. 4.17, the PV string I-V curve is divided into four segments by using (4.21). The rightmost segment is not considered since the the power peaks unlikely occurs in there. Therefore, the left three segments of the equivalent I-V curves and β-V curves for the key modules are shown in the bottom of Fig. 4.17. It is clearly seen that all the peaks are located in the defined range of β.

4.2.3 Algorithm Flowchart and Tracking Process

Fig. 4.18 and Fig. 4.19 illustrate the main loop and the search mode, respectively. As illustrated in Fig. 4.18, the proposed method initially measures I_{String} and V_{String}, and V_{eq}, n, V_s and β_{eq}, which are determined by (4.20)-(4.23). Then, the proposed method is divided into three processes, namely the ASF-Beta, the ZO-PO and the search mode.

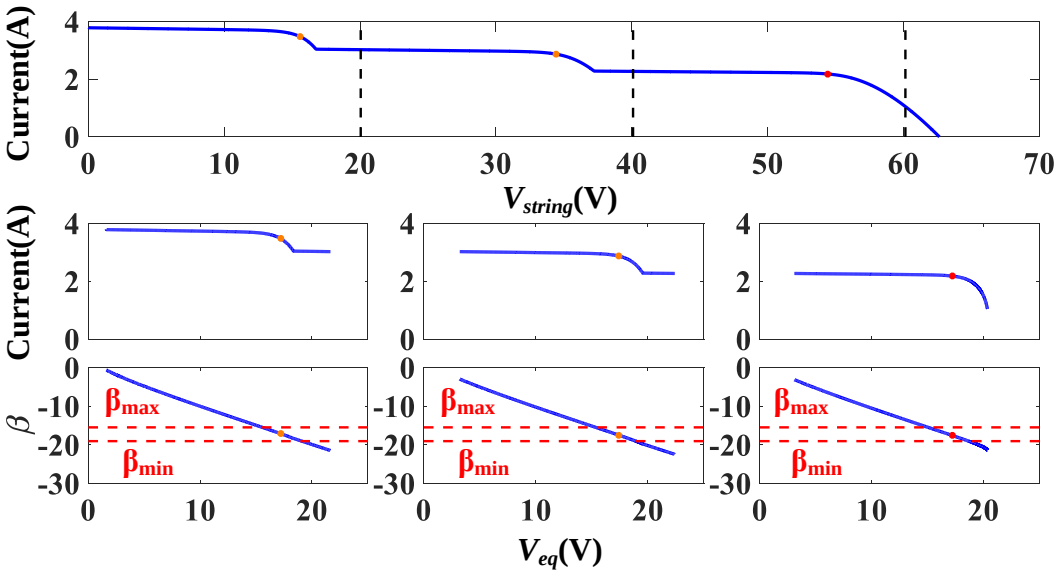

Fig. 4.17: PV string I-V curve and the equivalent V_{eq} and β_{eq} curves.

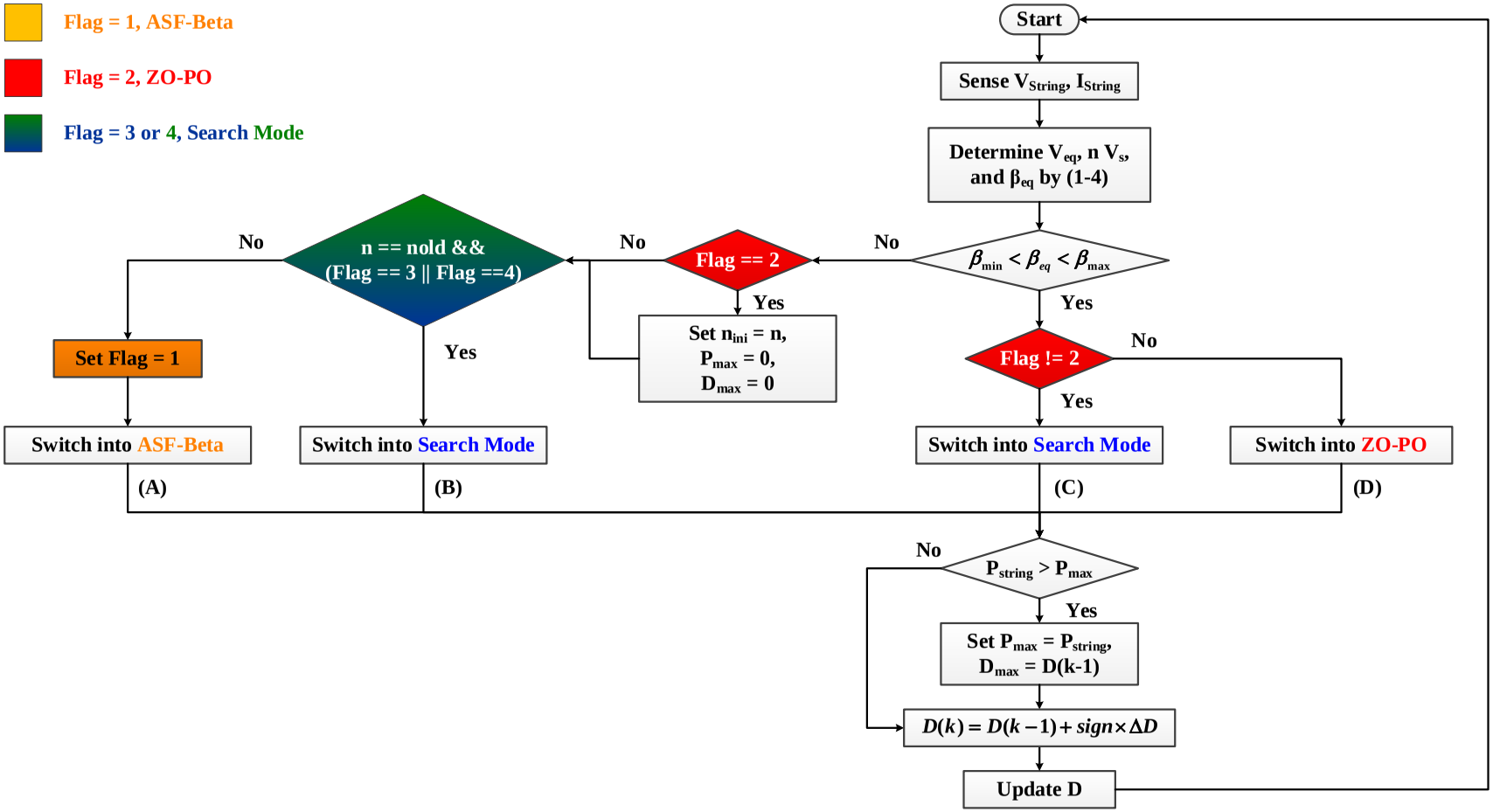

Fig. 4.18: Main loop for the flowchart of the proposed method.

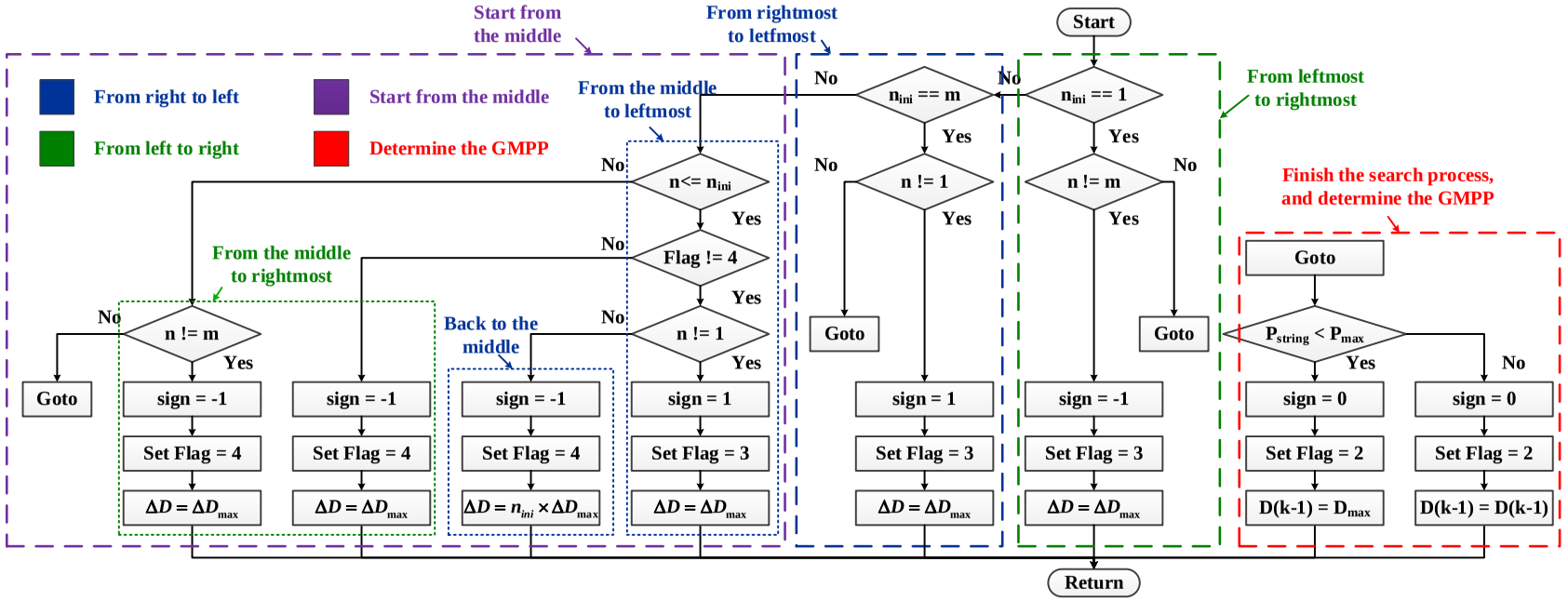

Fig. 4.19: Search mode for the flowchart of the proposed method.

In order to distinguish the tracking processes, the legends with various colors are marked in Fig. 4.18. The ASF-Beta is firstly used to locate the β range [71, 72]. Once the β range is reached, the search mode is activated and the operating point will move towards the next neighborhood of peaks, as shown in Fig. 4.19. Then, the next β range is reached by the ASF-Beta and the Search Mode is activated again. This process will be repeated until all of the β range are tracked. Finally, the area of the GMPP can be detected and the ZO-PO method is used to find the exact GMPP.

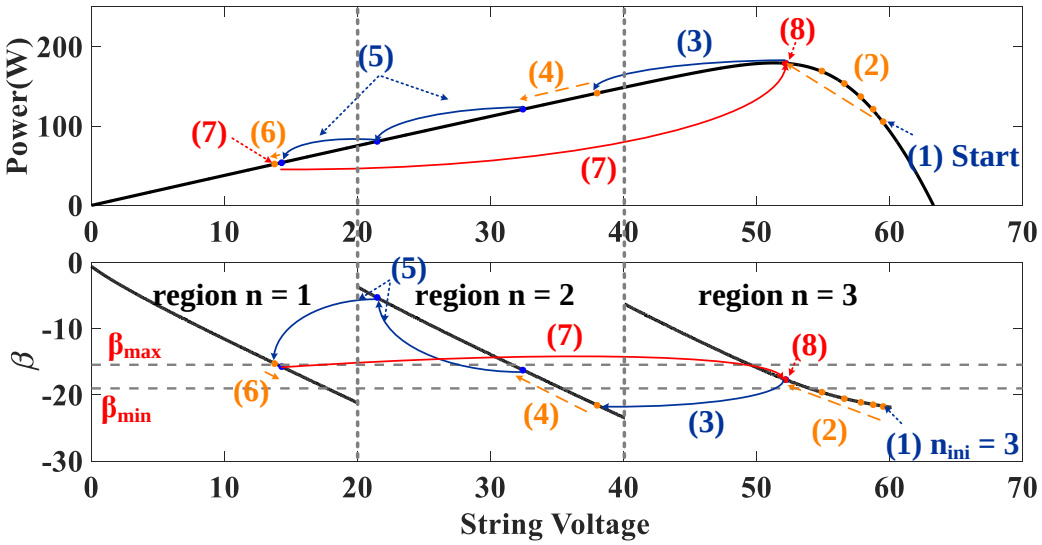

(a)

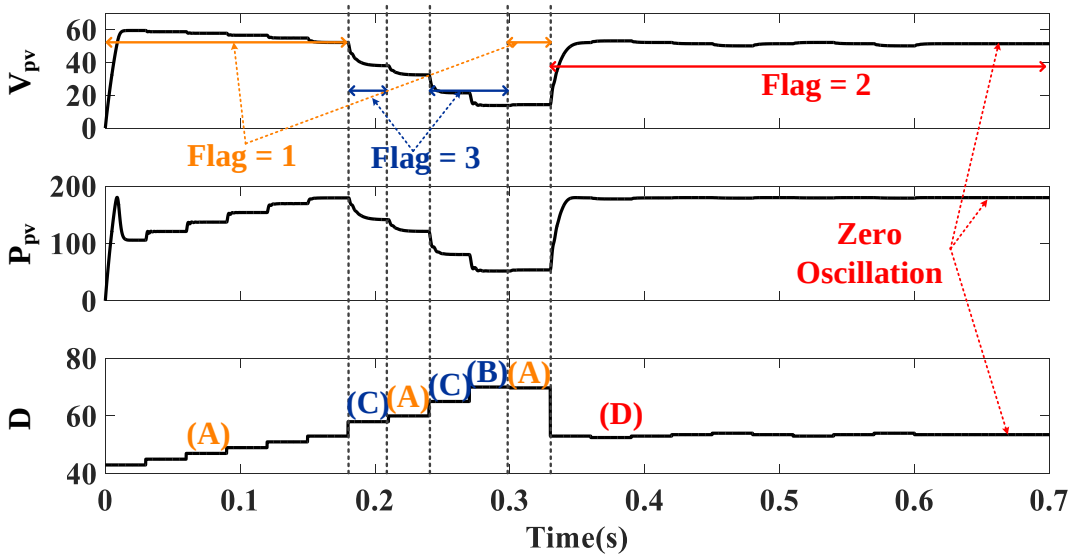

(b)

Fig. 4.20: Demonstration of the tracking process for the proposed method under the uniform condition. (a) Movements of the operating points. (b) Corresponding simulation results.

In order to help understand the proposed method, two examples of the tracking process is given in Fig. 4.20 and Fig. 4.21. Fig. 4.20 shows the PV system starts up under the uniform solar irradiance, where all of the PV modules are at 1000W/m^2. There are 8 processes as shown below:

(1) Initially, assuming the PV system starts up from the rightmost. The initial value of n, namely n_{ini}, is set as 3 and "Flag" is set as 1.

(2) Firstly, the branch (A) is went through, as illustrated in Fig. 4.20 (b). By using the ASF-Beta method, the operating point is gradually moving the β range in the third segment and reach it at time 0.18s.

(3) Then, the branch (C) is went through to activate the search mode. At this time, "$n_{ini} == m$" is satisfied so "sign" is set as 1 and "Flag" is set as 3. It indicates the operating point will move towards the left, marked as blue block in Fig. 4.19. At time 0.21s, the second β range in the second segment is reached.

(4) At time 0.24s, the ASF-Beta method is activated again to reach the next β range.

(5) Then, the branch (C) is went through to activate the search mode again. However, at the time 0.27s, the operating point is still in the second segment. Therefore, "$n = n_{old}\&\&(Flag == 3||Flag == 4)$" is satisfied, and the branch (B) is went through. As a consequence, the operating point is forced to move the next segment at time 0.3s.

(6) The ASF-Beta method is activated again and the β range in the first segment is reached at time 0.33s.

(7) After all of the β range has been searched, the algorithm goes to the determination process. It is found that the GMPP is located in the third segment.

(8) Finally, After several steps, the GMPP is located.

At time 1s, two of the modules are then shaded to 800W/m^2 and 600W/m^2 Thus, the tracking process of the PSC is demonstrated in Fig. 4.21 (a).

(1) At time 1.02s, it detects that the value of β_{eq} is out of the β range, which indicates the PSC is happened. At this time, the operating point is located in the second segment. Thus, n_{ini} is set as 2 and "Flag" is set as 1. P_{max} and D_{max} are cleared.

(2) Then, the branch (A) is went through and the the first β range is located at time 1.05s.

(3) Since both "$n_{ini} == m$" and "$n_{ini} == 1$" are not satisfied, the purple block of the search mode is went through, as shown in Fig. 4.19. Then, two steps are used to reach the first segment at time 1.11s.

(4) Since the operating point has been already in β range so the ASF-Beta method is skipped.

(5) Then, "Flag" is set as 4, which indicates that the leftmost has been already reached. Therefore, the operating point moves back to the second segment at time 1.14s and starts to move the third segment.

(6) Then, the operating point moves to the third segment at time 1.17s.

(7) The β range is located by ASF-Beta method again at time 1.23s.

(8) Finally, all of the β range have been searched, and the GMPP is detected in the current segment. Therefore, the branch (D) is went through and the ZO-PO method is activated.

Finally, Fig. 4.22 summarises the whole tracking process for the proposed method.

4.3 Simulation Results

Fig. 4.23 shows the system block diagram of the proposed PV system based on Buck-Boost converter. It consists of a PV string, resistive load, buck-boost converter and GMPPT controller. The input capacitor C_{in}, output capacitor C_{out}, inductor L and switching frequency for the boost converter are 470uF, 47uF, 1mH and 10kHz, respectively.

Fig. 4.24 shows the tested PSC patterns for the simulations. Three PV modules, Solarex MSX-60W, are connected in series. The electrical parameters of the Solarex MSX-60W is shown in 2.1.

In order to highlight the advantages of the proposed GMPPT method, the comparisons of the proposed GMPPT method with the power incremental method by [80] and the $0.8V_{oc}$ model method by [98] are simulated. Since the performance of the power incremental method relies upon the selected power search step, $\Delta P_{interval}$, different values of $\Delta P_{interval}$ are chosen as $20W$ and $10W$. Furthermore, since the power incremental method and the $0.8V_{oc}$ model methods utilize the P&O and INC method when the global search is done, the step size for them is chosen as 0.5%.

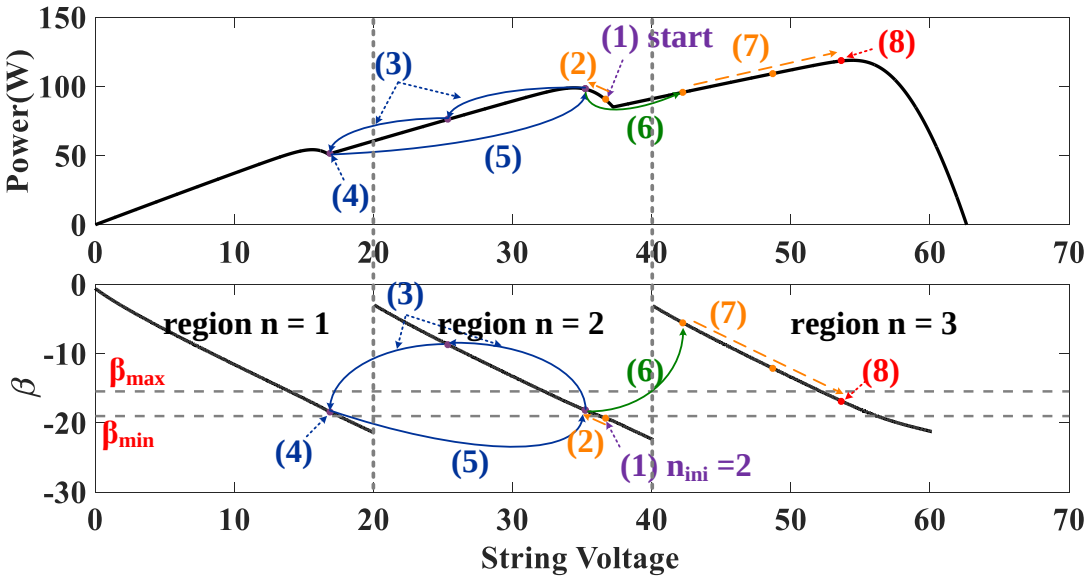

(a)

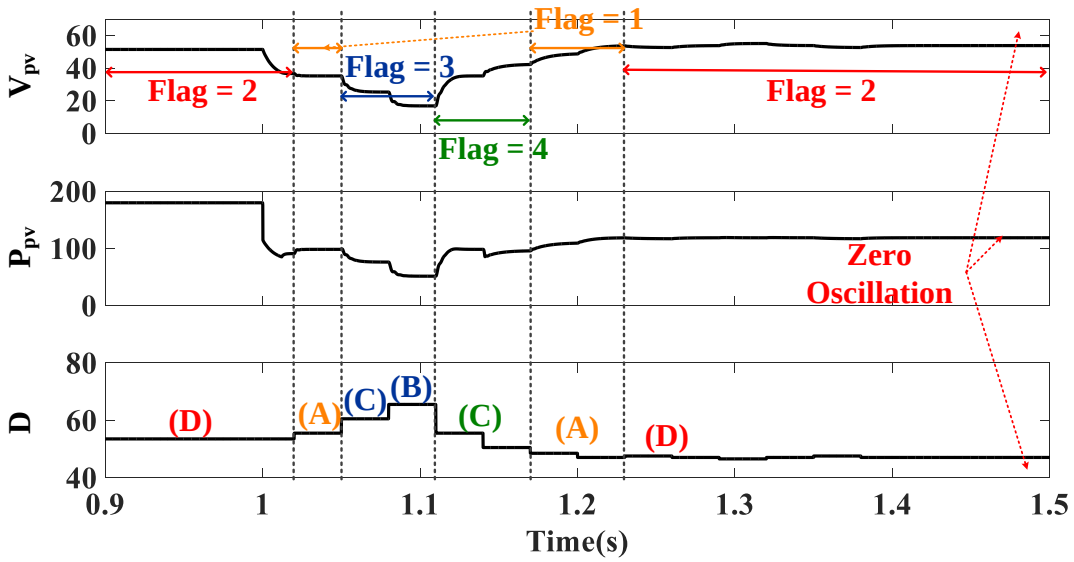

(b)

Fig. 4.21: Demonstration of the tracking process for the proposed method under the PSC. (a) Movements of the operating points. (b) Corresponding simulation results.

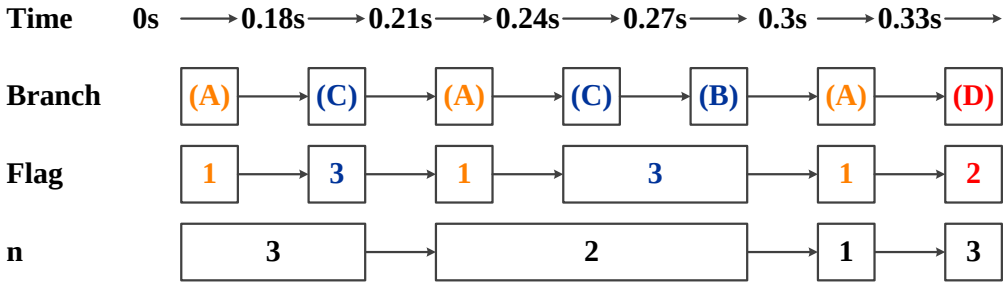

(a)

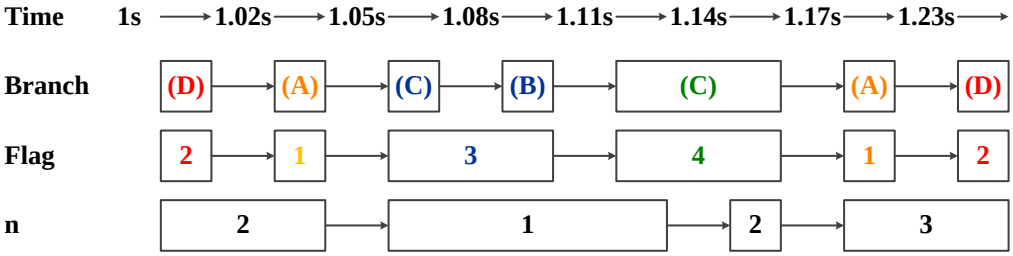

(b)

Fig. 4.22: Summarisation of the tracking process for the proposed method. (a) PV system under the uniform condition. (b) PV system under the PSC.

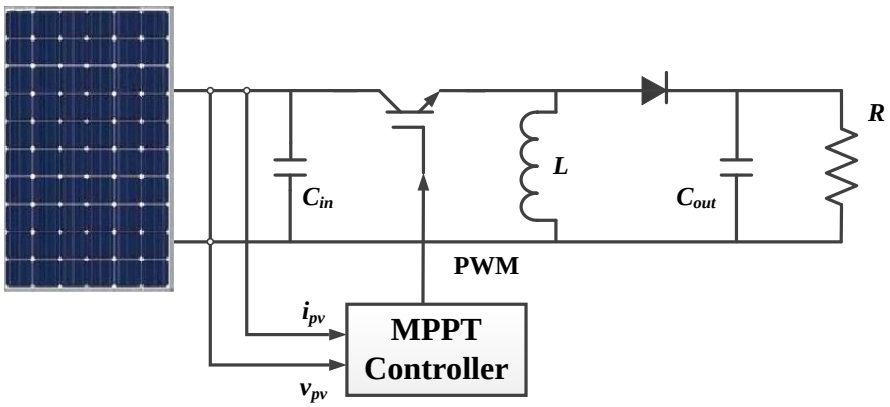

Fig. 4.23: System block diagram of the proposed PV system based on Buck-Boost converter.

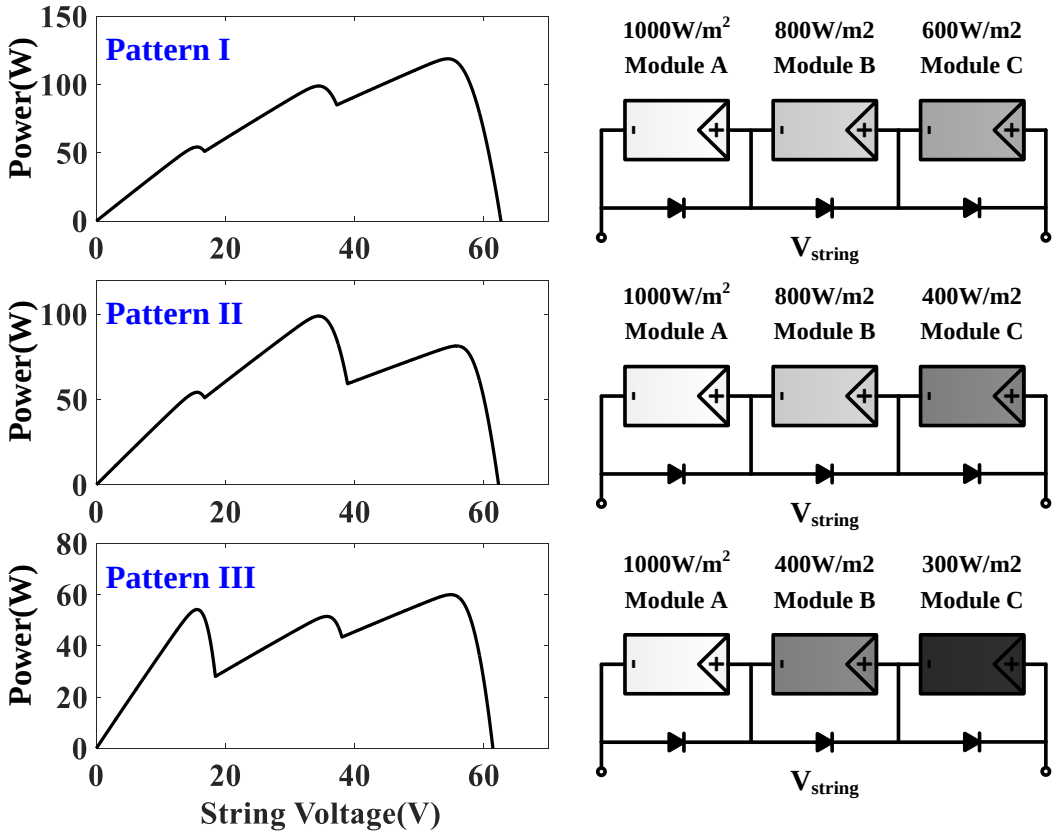

Fig. 4.24: Tested PSC patterns for the simulations.

4.3.1 Simulation Results for the Pattern I

The simulation results for pattern I is illustrated in Fig.4.25 to Fig.4.28. Fig.4.25 (a) shows the simulation results of pattern I for the power incremental method with $\Delta P_{interval} = 10W$. It can be seen that the power incremental method with a small $\Delta P_{interval}$ requires 0.45s to complete the global searching. Fig.4.25 (b) demonstrates the movements of the operating points. Initially, the operating point starts from the vicinity of V_{oc}, which is marked as P_1. Then, the operating point is followed as the trajectory movement as $P_1 \rightarrow \cdots \rightarrow P_7$ (in blue texts). At point P_7, it is found that the power at P_7 is lower than that at P_6, which indicates that point P_6 is one of the peak. Then, the operating point moves to point P_8, and the operating point is followed as the trajectory movement as $P_8 \rightarrow \cdots \rightarrow P_{14}$ (in green texts). At point P_{14} , the entire P-V curve has been searched and the power at P_6 is still the highest one. Therefore, the operating point comes back to point P_6, and the P&O method is activated to find the GMPP at point P_{15}.

Fig.4.26 (a) shows the simulation results of pattern I for the power incremental method with $\Delta P_{interval} = 20W$. It can be seen that the power incremental method with a large $\Delta P_{interval}$ just needs 8 steps to scan the whole P-V curve. However, it has to use extra

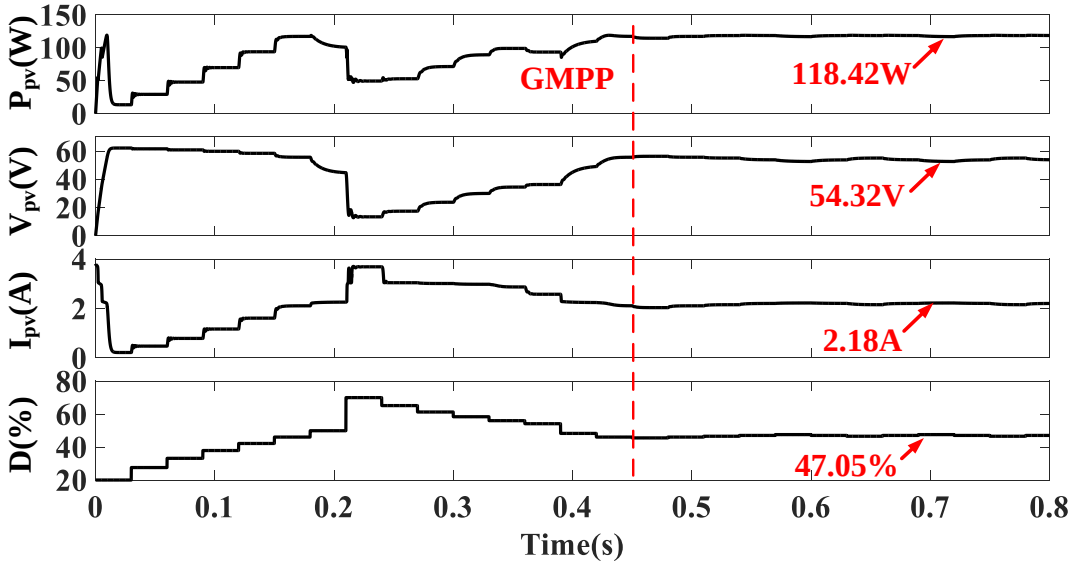

(a)

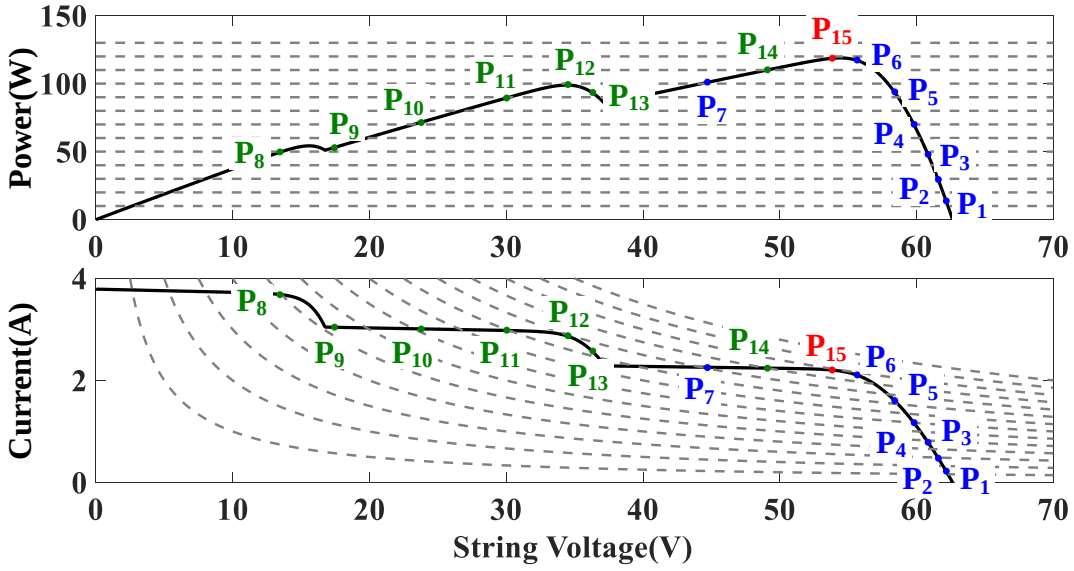

(b)

Fig. 4.25: Simulation results of pattern I for the power incremental method with $\Delta P_{interval} = 10W$: (a) simulation waveforms; (b) movements of the operating points.

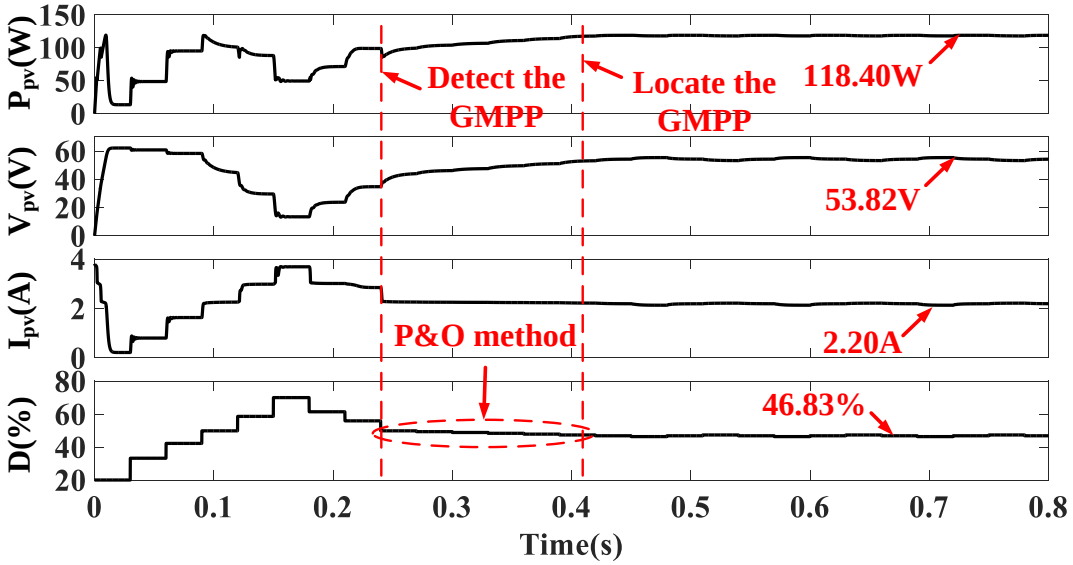

(a)

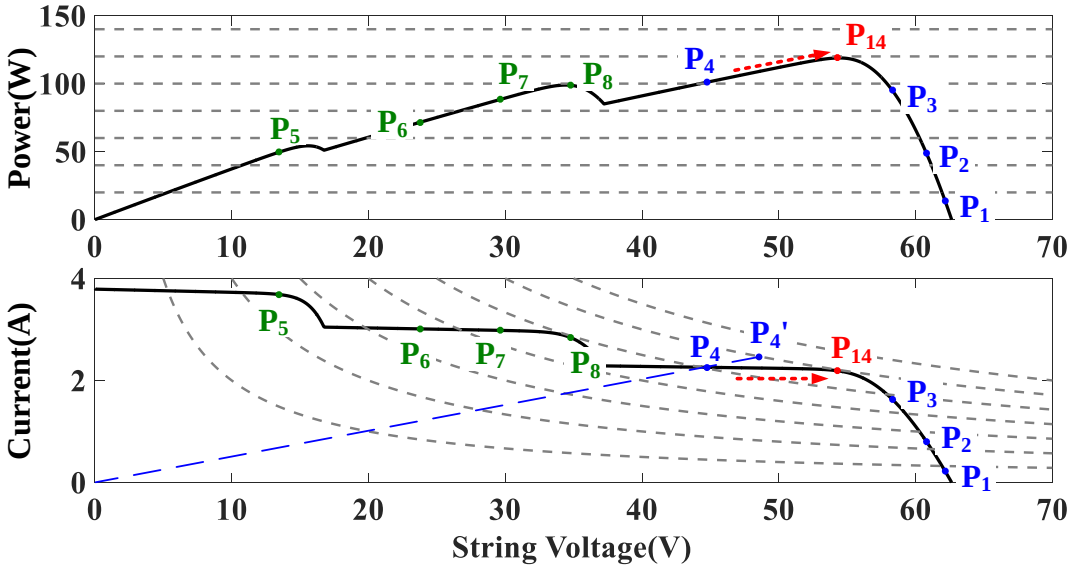

(b)

Fig. 4.26: Simulation results of pattern I for the power incremental method with $\Delta P_{interval} = 20W$: (a) simulation waveforms; (b) movements of the operating points.

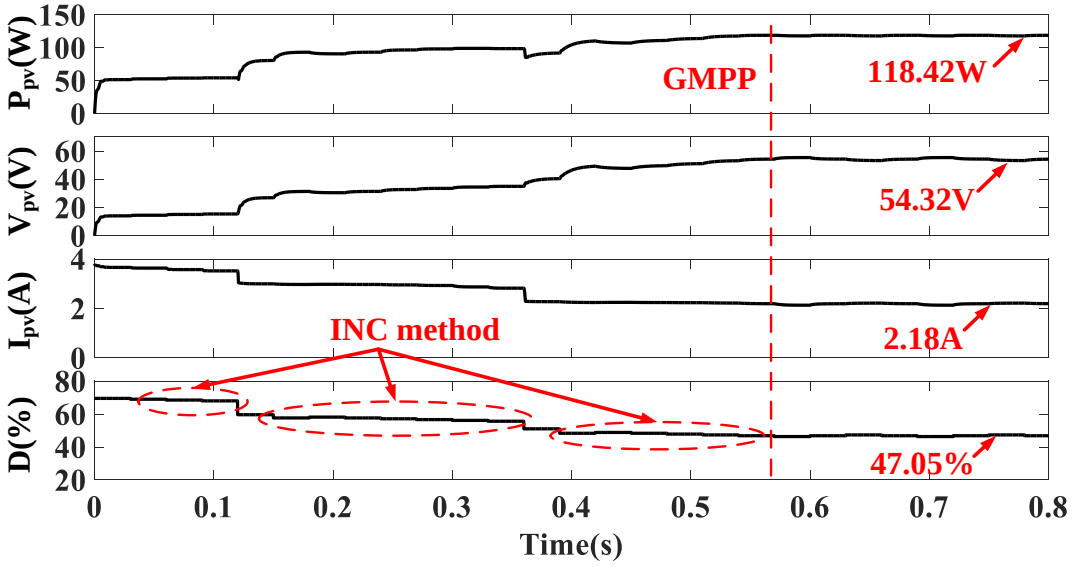

(a)

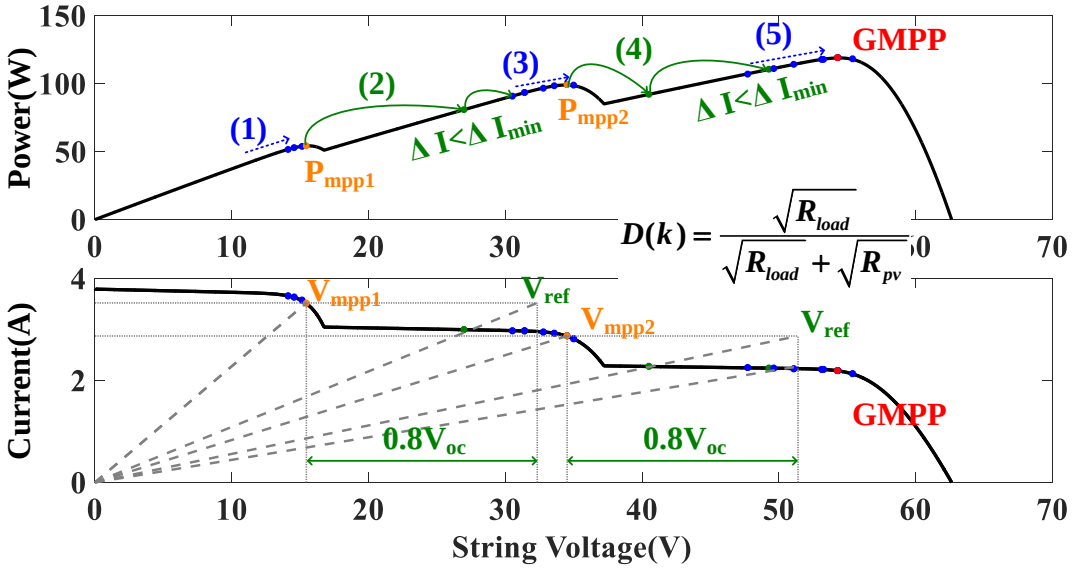

(b)

Fig. 4.27: Simulation results of pattern I for the $0.8V_{oc}$ model method: (a) simulation waveforms; (b) movements of the operating points.

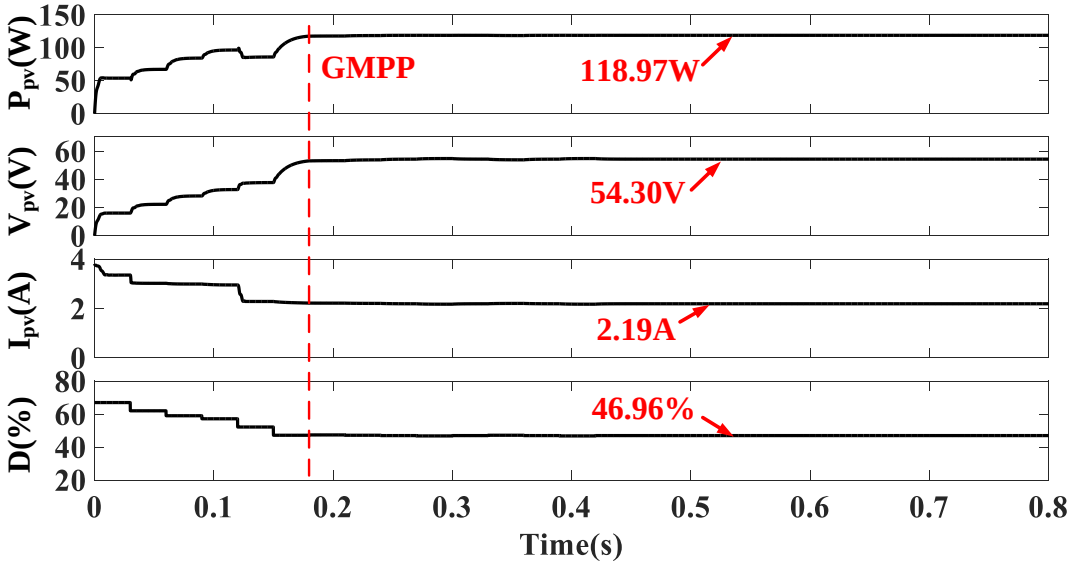

(a)

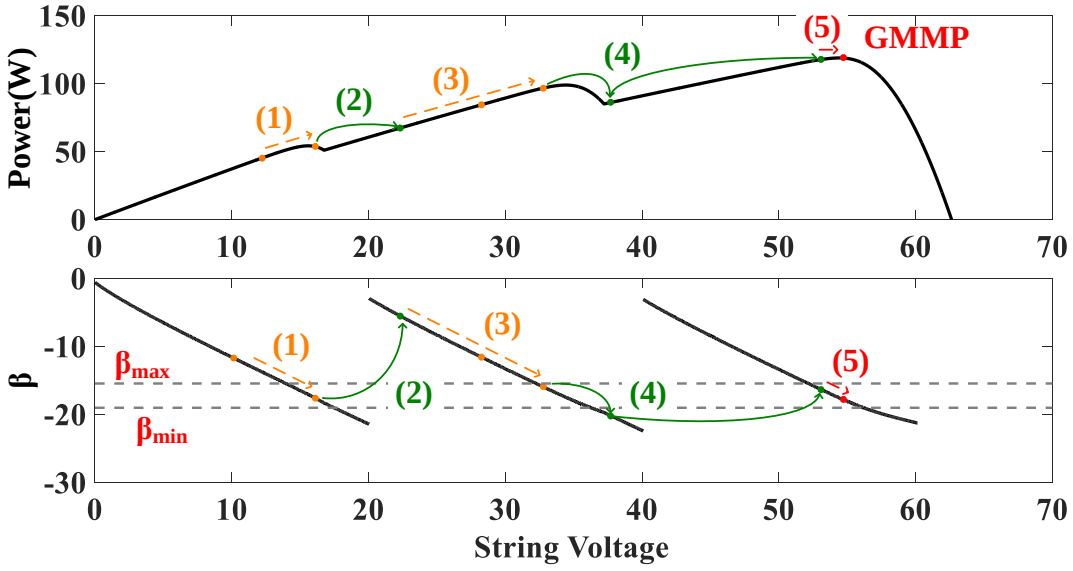

(b)

Fig. 4.28: Simulation results of pattern I for the proposed method: (a) simulation waveforms; (b) movements of the operating points.

0.18s to find the exact GMPP by P&O method. Fig.4.26 (b) demonstrates the movements of the operating point. The operating point starts from P_1 and gradually moves towards the higher power level. At the point P_3, the next operating point should be point P'_4. Unfortunately, the point P'_4 is not located on the P-V curve due to large $\Delta P_{interval}$. Therefore, the operating point moves to point P_4 and overlooks the first peak. Then, the operating point moves to point P_5 and follows the trajectory as $P_5 \rightarrow \cdots \rightarrow P_8$. Although the first peak is overlooked, P_4 is still higher than P_8 after the entire P-V curve has been searched. Therefore, the operating point comes back to point P_4, and more steps have to be used to move the GMPP at the point P_9

Fig.4.27 (a) shows the simulation results of pattern I for the $0.8V_{oc}$ model method. Since the INC method has to use to determine the exact locations of every peak, this method requires 0.57s to find the GMPP, which is the longest. Fig.4.27 (b) demonstrates the movements of the operating point. Initially, INC method is used and the blue dash arrow with (1) is marked. When the first peak is found, its subroutine is executed to skip towards the next $0.8V_{oc}$ area as marked green curve arrows with (2). In this subroutine, the reference voltage V_{ref} is determined by

$$V_{ref} = V_{mpp1} + 0.8 \times V_{oc} \tag{4.24}$$

where V_{mpp1} is the voltage at the first peak. Then, $D(k)$ is determined by

$$D(k) = \frac{\sqrt{R_{load}}}{\sqrt{R_{load}} + \sqrt{R_{pv}}} \tag{4.25}$$

where R_{pv} is determined by

$$R_{pv} = \frac{V_{ref}}{I_{string}(k-1)} \tag{4.26}$$

This subroutine is continuously repeated until the different in two successive current values ΔI is smaller than a threshold ΔI_{min}. Then, the INC method is used again and the second peak is found, which is marked as blue dash arrow with (3). As step (4), the subroutine is repeated again to move the next $0.8V_{oc}$ area. Finally, the third peak is found by the INC method and it is identified as the GMPP.

Fig.4.28 (a) shows the simulation results of pattern I for the proposed method. It can be seen that the proposed method only needs 6 steps to identify as the GMPP, which is much faster than the power incremental method and the $0.8V_{oc}$ model method. Furthermore, it should be noted that the proposed method does not have any oscillation at the steady-state stage while the other methods do. Fig.4.28 (b) demonstrates the movements of the operating point. Compared to the $0.8V_{oc}$ model method, the proposed method just reaches the vicinities of the each peak rather. Furthermore, compared to the power incremental method, the proposed method is more targeted. Thus, the proposed method is more effective to find the GMPP.

4.3.2 Simulation Results for Pattern II

Fig.4.29 shows the simulation results of pattern II for the power incremental method with $\Delta P_{interval} = 10W$. It can be seen that the power incremental method with a small $\Delta P_{interval}$ requires 14 steps to finish the global searching at time 0.42s. By contrast, as shown in Fig.4.29, the power incremental method with a large $\Delta P_{interval}$ only requires 9 steps to find the vicinity of GMPP.

The $0.8V_{oc}$ model method requires 23 steps to locate the GMPP. As shown in Fig.4.31, the INC method is used to track the exact peak in the the trajectory (1), (3) and (5). Therefore, the tracking time for the $0.8V_{oc}$ model method is the longest, which is 0.69s. By contrast, the proposed method requires less time to find the GMPP, which is 0.27s.

4.3.3 Simulation Results for Pattern III

Fig.4.33, Fig.4.34, Fig.4.35 and Fig.4.36 show the simulation results of pattern III. From the simulation results, only the proposed method and the power incremental method with $\Delta P_{interval} = 10W$ can correctly locate the GMPP, which requires $0.3s$ and $0.48s$ respectively. The the power incremental method with $\Delta P_{interval} = 20W$ and the $0.8V_{oc}$ model method can only track the leftmost peak.

From Fig.4.33 (b), it can be seen that the power incremental method with a small $\Delta P_{interval}$ is able to identify the GMPP. However, it has to use more than 15 steps to scan the whole P-V curve. By contrast, the power incremental method with a large $\Delta P_{interval}$ requires only steps to finish the scan, which is shown in Fig.4.34 (b). However, the real GMPP is overlooked and the leftmost LMPP is identified as the GMPP.

Fig.4.35 (b) demonstrates the movements of the $0.8V_{oc}$ model method under pattern III. When the second peak, P_{mpp2}, is found and compared with the first peak, P_{mpp1}, the $0.8V_{oc}$ model method returns the first peak. By contrast, the proposed method only needs 9 steps to finish the scan and correctly identify the GMPP. As shown in Fig.4.36 (b), the ASF-Beta method and the search mode are alternatively changed as following trajectory (1) $\rightarrow \cdots \rightarrow$ (5). At the trajectory (6), the GMPP is identified and the ZO-PO method is used to find the real GMPP.

4.4 Experimental Results

In order to verify the effectiveness of the proposed algorithm, the proposed method is compared with the power incremental method by [80] and the $0.8V_{oc}$ model method by [98] via the experiment. The experimental prototype is shown in Fig.4.37. A buck-boost converter is used as the power interface where the specification of the main components

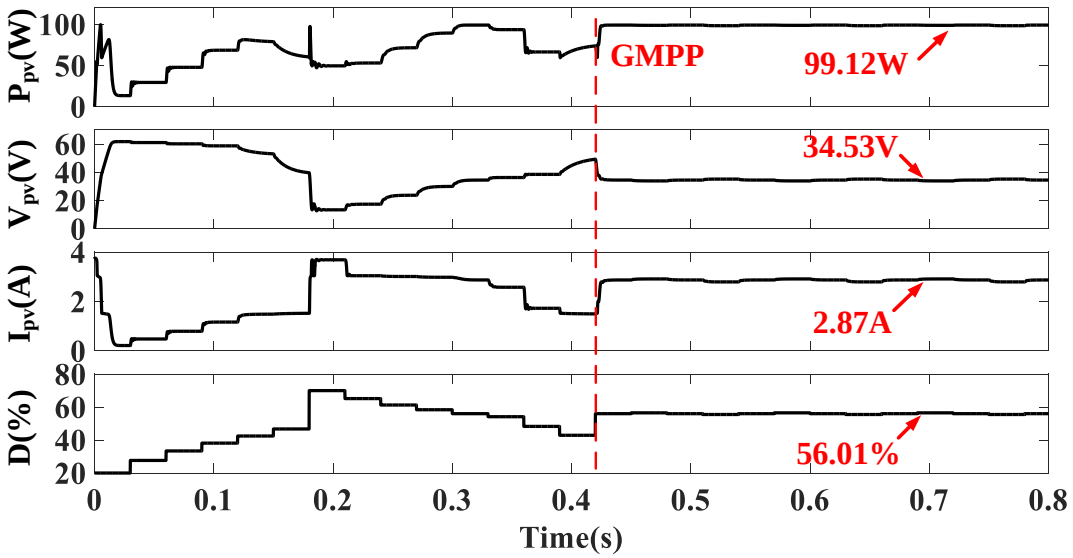

(a)

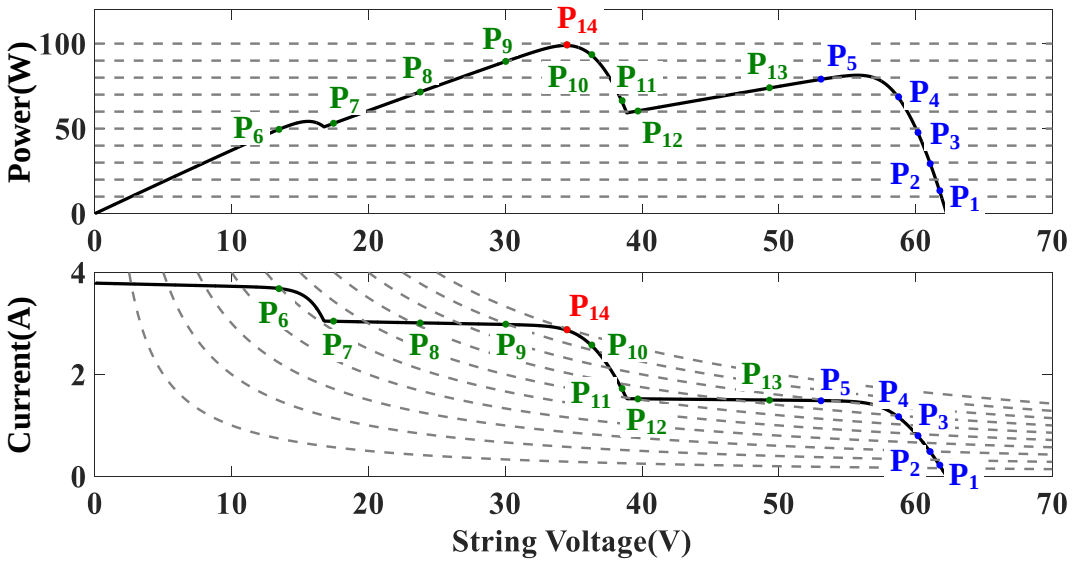

(b)

Fig. 4.29: Simulation results of pattern II for the power incremental method with $\Delta P_{interval} = 10W$: (a) simulation waveforms; (b) movements of the operating points.

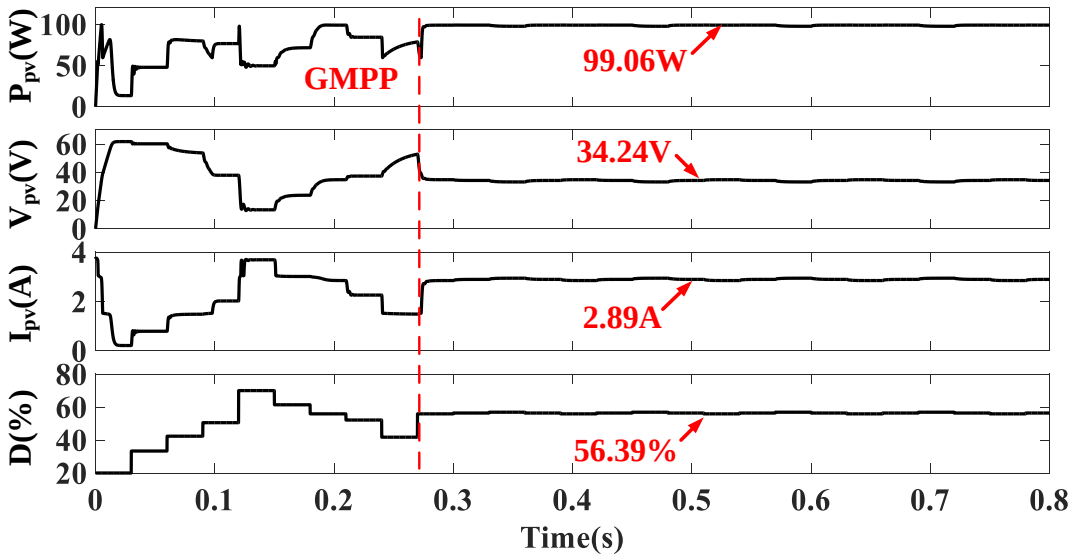

(a)

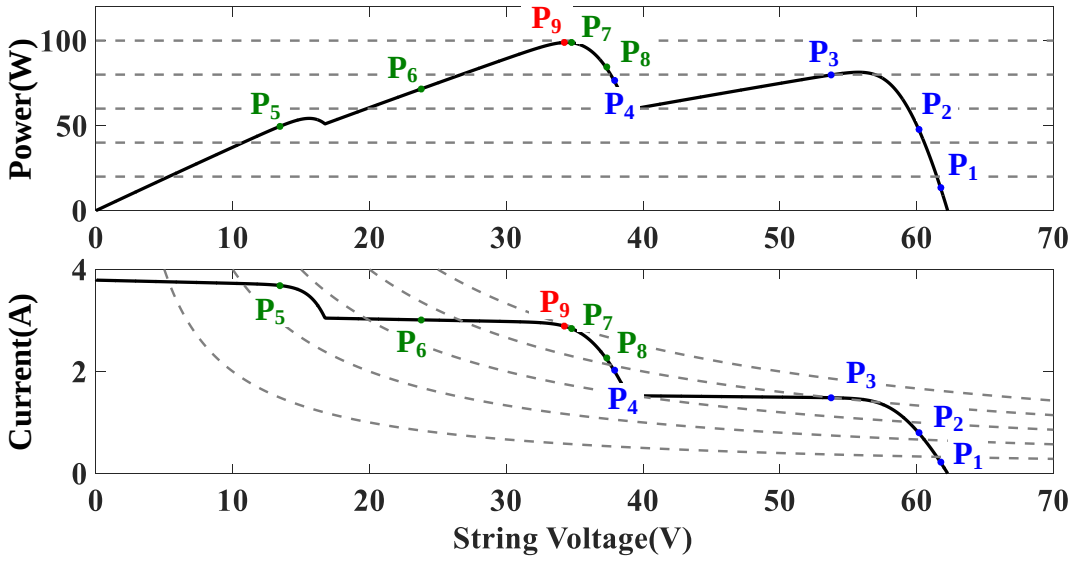

(b)

Fig. 4.30: Simulation results of pattern II for the power incremental method with $\Delta P_{interval} = 20W$: (a) simulation waveforms; (b) movements of the operating points.

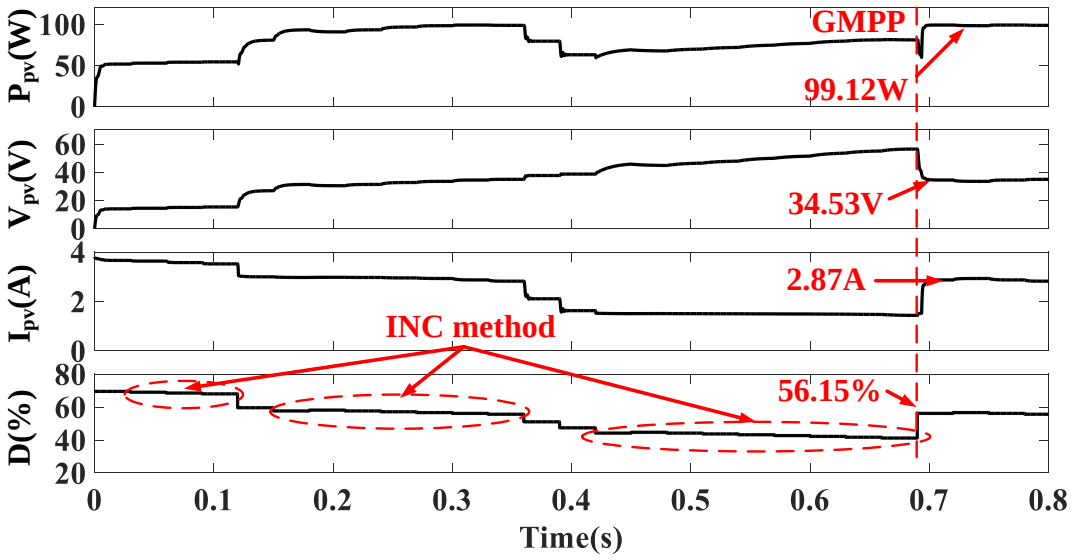

(a)

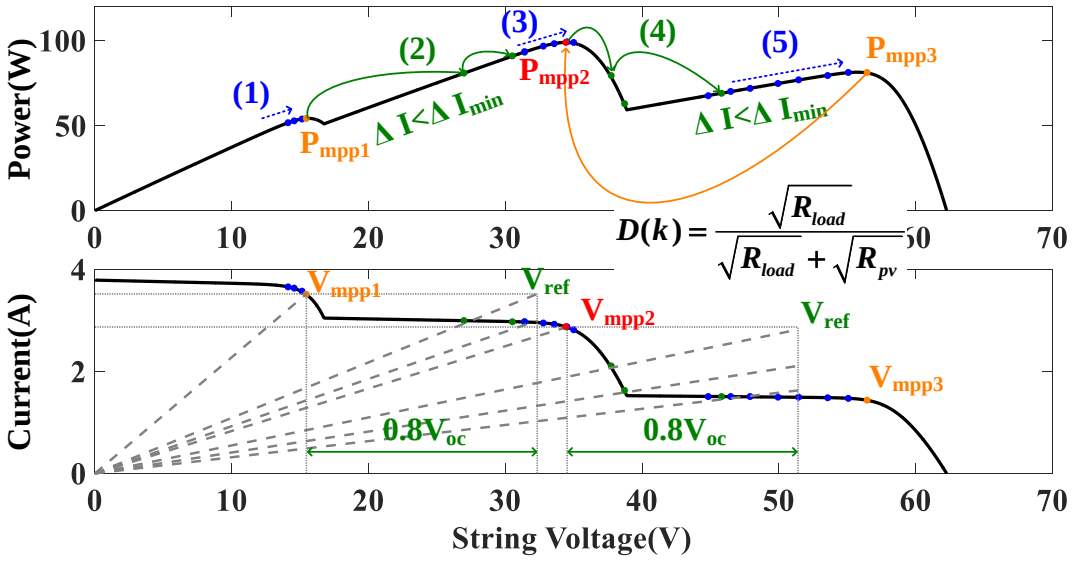

(b)

Fig. 4.31: Simulation results of pattern II for the $0.8V_{oc}$ model method: (a) simulation waveforms; (b) movements of the operating points.

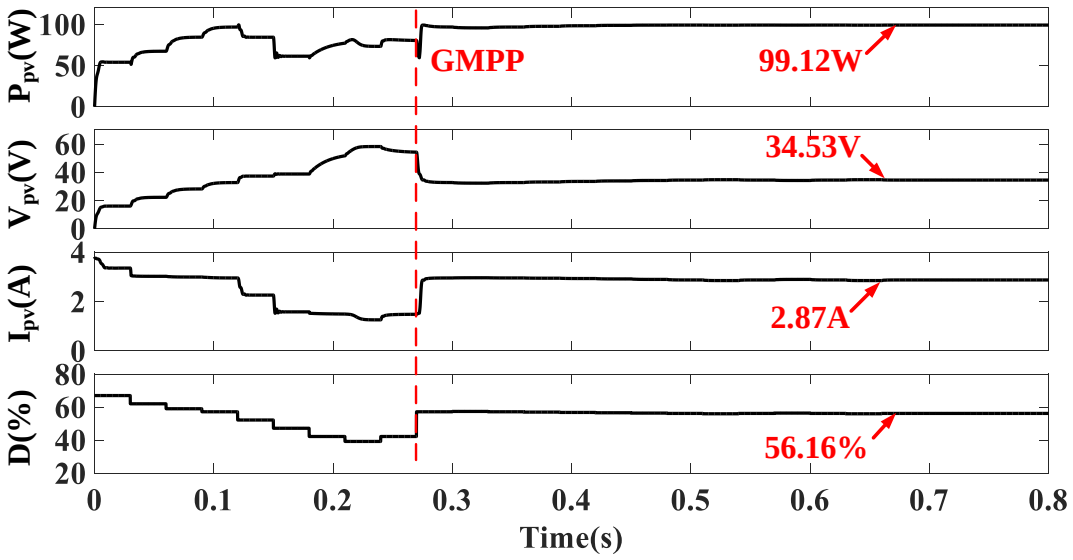

(a)

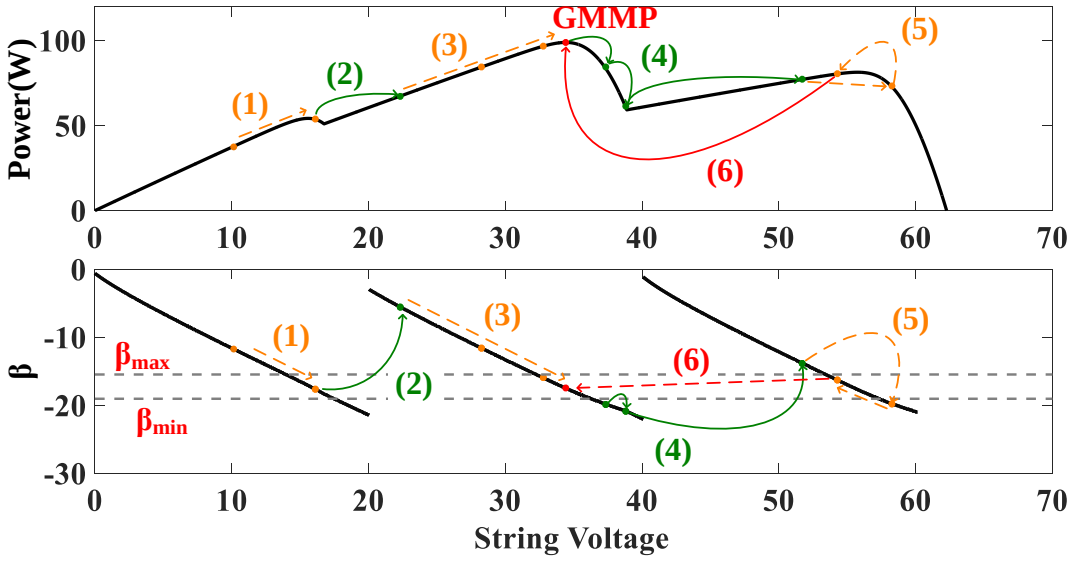

(b)

Fig. 4.32: Simulation results of pattern II for the proposed method: (a) simulation waveforms; (b) movements of the operating points.

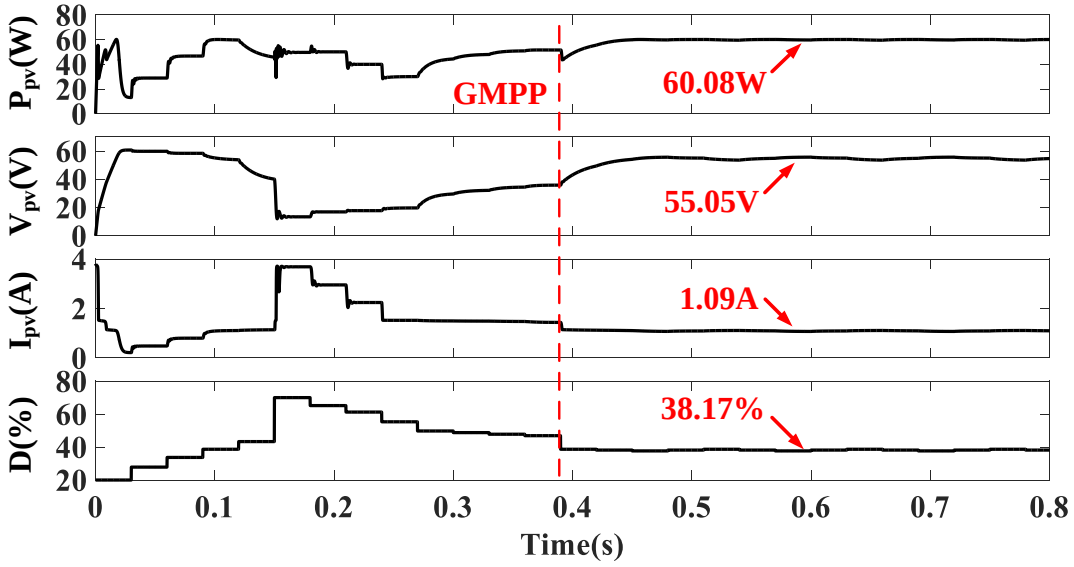

(a)

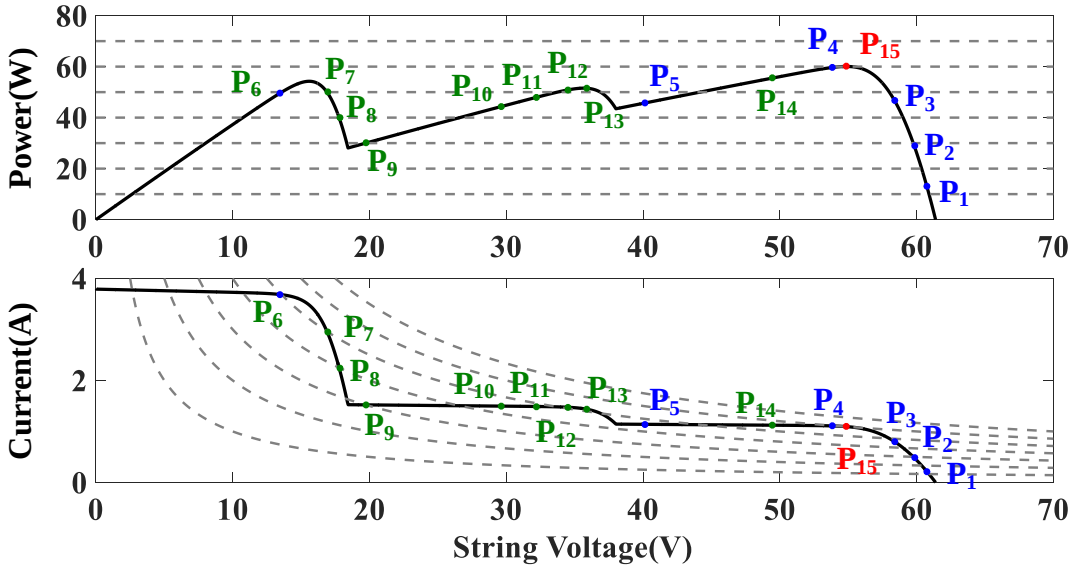

(b)

Fig. 4.33: Simulation results of pattern II for the power incremental method with $\Delta P_{interval} = 10W$: (a) simulation waveforms; (b) movements of the operating points.

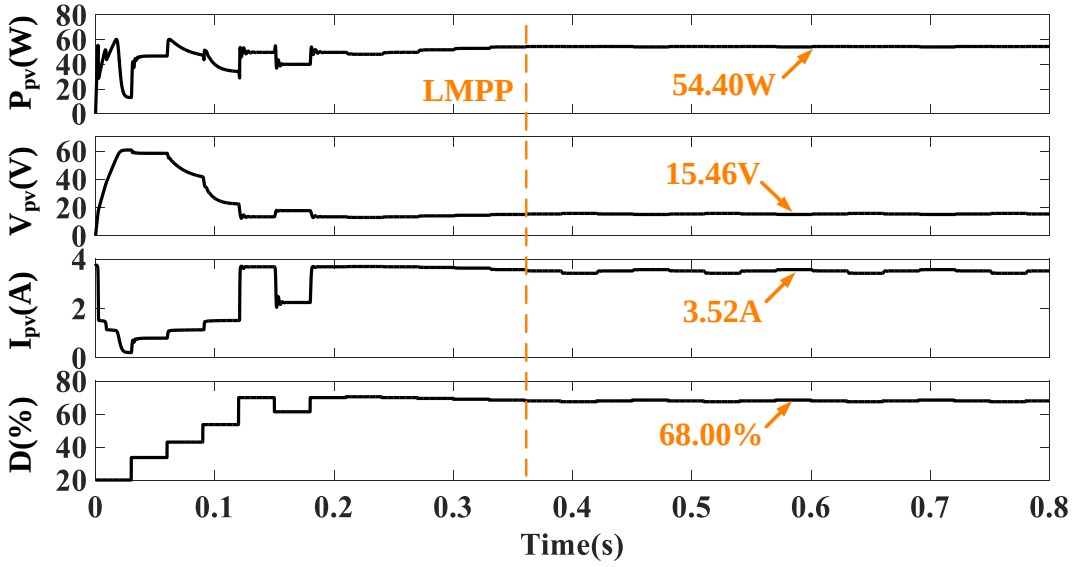

(a)

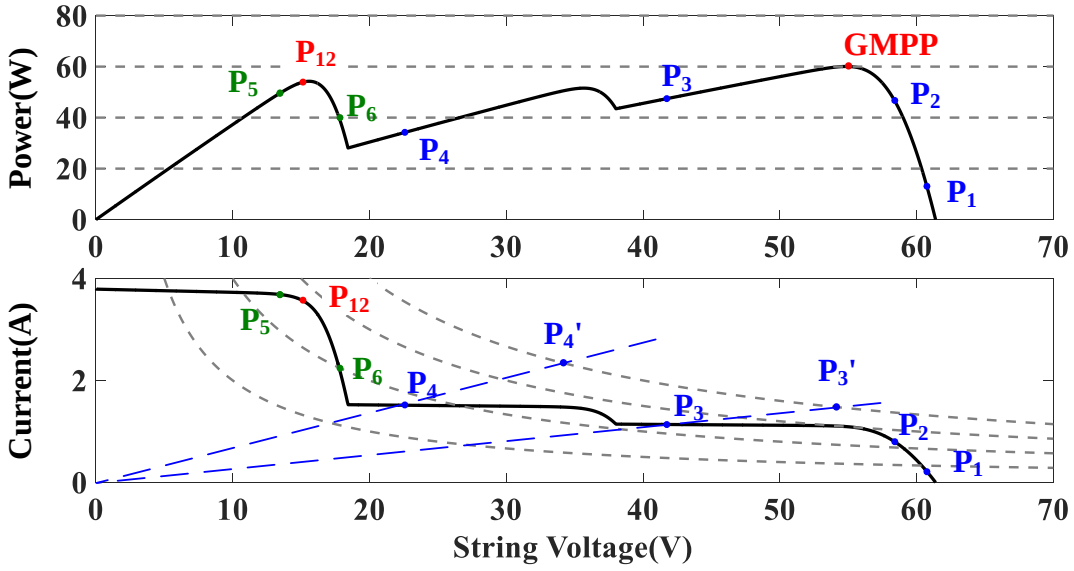

(b)

Fig. 4.34: Simulation results of pattern II for the power incremental method with $\Delta P_{interval} = 20W$: (a) simulation waveforms; (b) movements of the operating points.

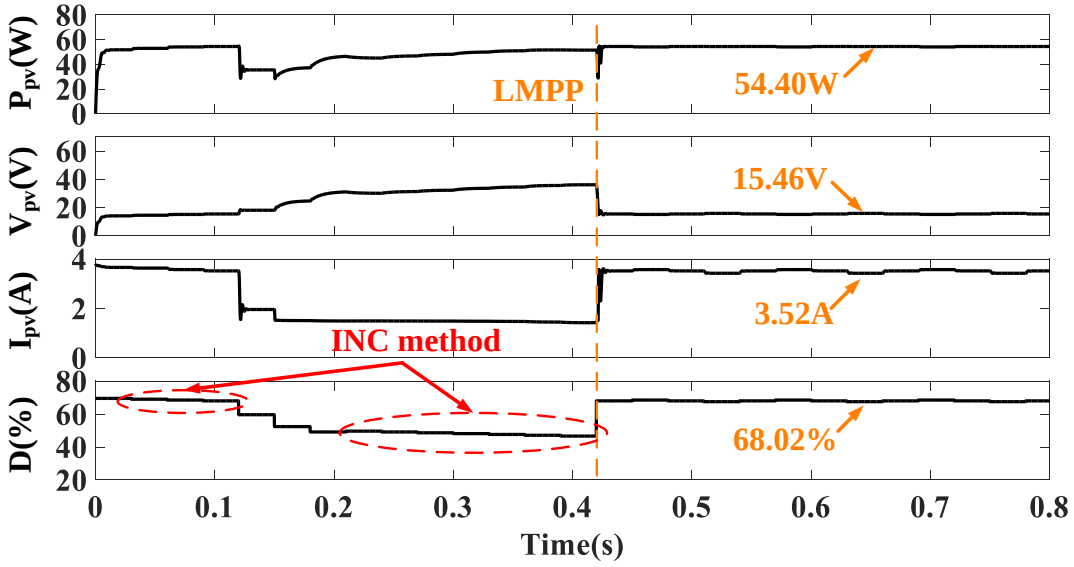

(a)

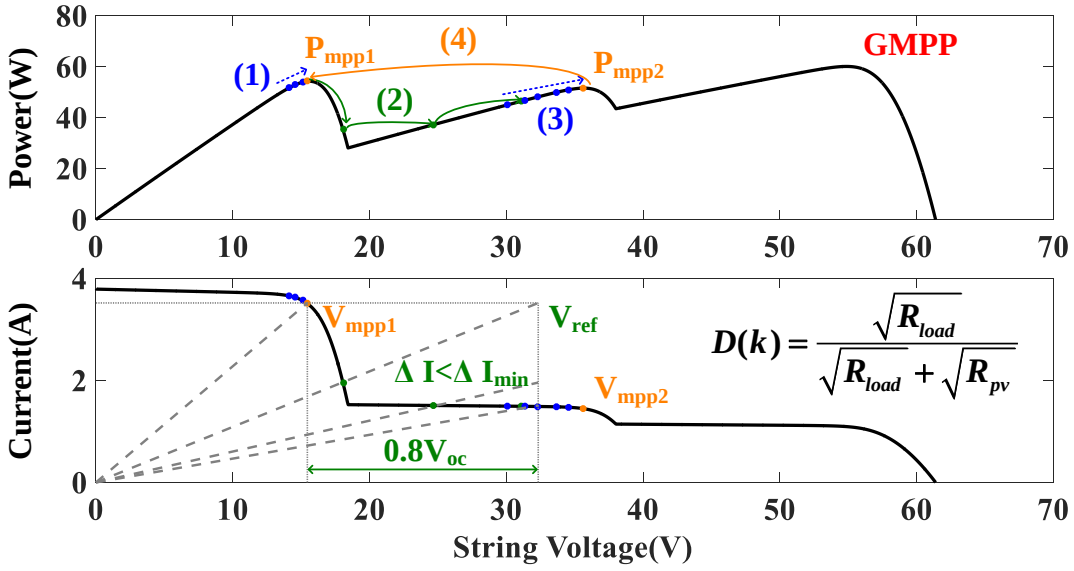

(b)

Fig. 4.35: Simulation results of pattern II for the $0.8V_{oc}$ model method: (a) simulation waveforms; (b) movements of the operating points.

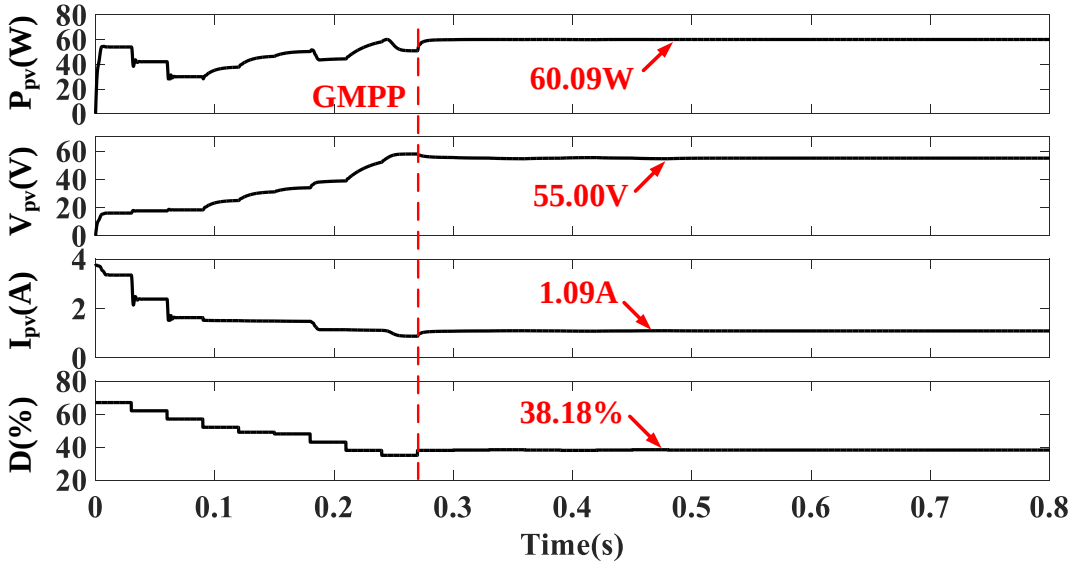

(a)

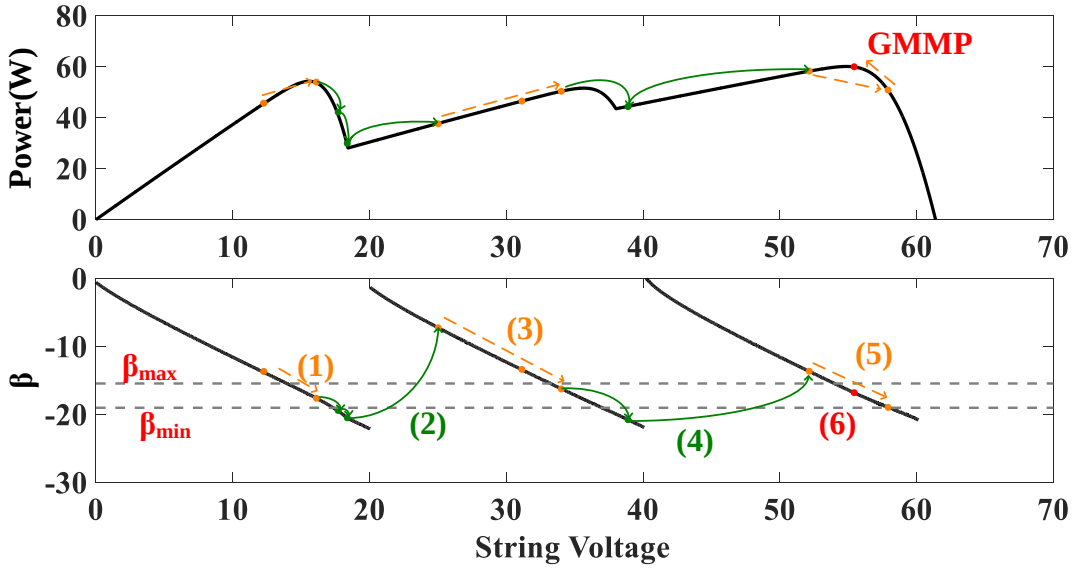

(b)

Fig. 4.36: Simulation results of pattern II for the proposed method: (a) simulation waveforms; (b) movements of the operating points.

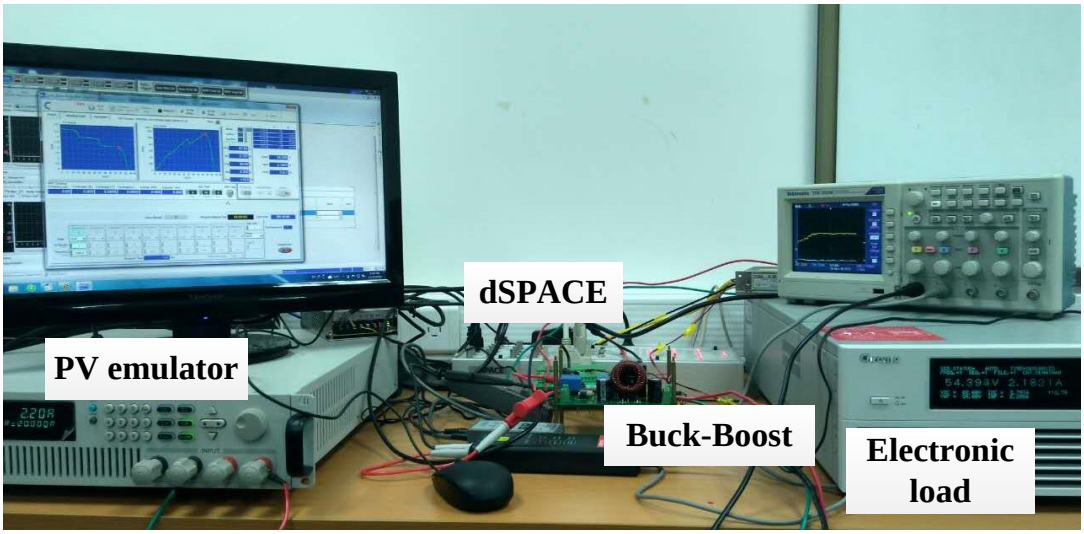

Fig. 4.37: Experimental test bench for the GMPPT.

Table 4.1: Main components specification for the prototype

Parameter	Value
Electrolytic capacitor C_{in}	$470uF$
Electrolytic capacitor C_{out}	$100uF$
Inductor L	$1mH$
IGBT	IRG4PH50U
Diode	RHRG30120
Current transducer	LA25-NP
Voltage transducer	LV25-P
Switching frequency	$20kHz$

is shown in Table 4.1. The PV emulator and control platform are same as the Chapter 3.

The three PSC patterns are used in the experiment, which are same as the simulation. In order to make a fair comparison, all of the methods have 2 seconds for the initial time, which is marked as the red dash lines.

Fig.4.38 and Fig.4.39 show the experimental results for pattern I. The power incremental method is also started from the vicinity of V_{oc}, whose duty cycle is set at 20%. At time t=2s, the power incremental method starts to search the P-V curve by using $\Delta P_{interval}$. For $\Delta P_{interval} = 10W$, 7.5s (15 steps) is needed to reach the vicinity of the GMPP. Unlike the simulation, the real GMPP is occasionally found by the power incremental method when $\Delta P_{interval} = 20W$ is used. Thus, the overall tracking time for the the power incremental method with $\Delta P_{interval} = 20W$ is only $4.5s$ (9 steps).

The $0.8V_{oc}$ model method uses the INC method to find the first peak, as shown in Fig.4.39 (a). When the first peak is found, a large voltage increment by $0.8V_{oc}$ is used to

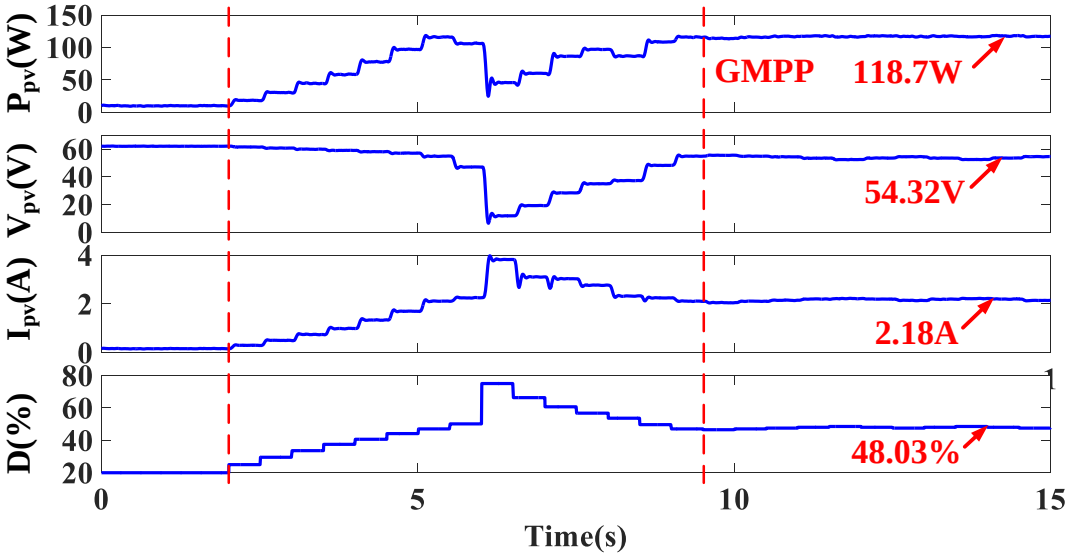

(a)

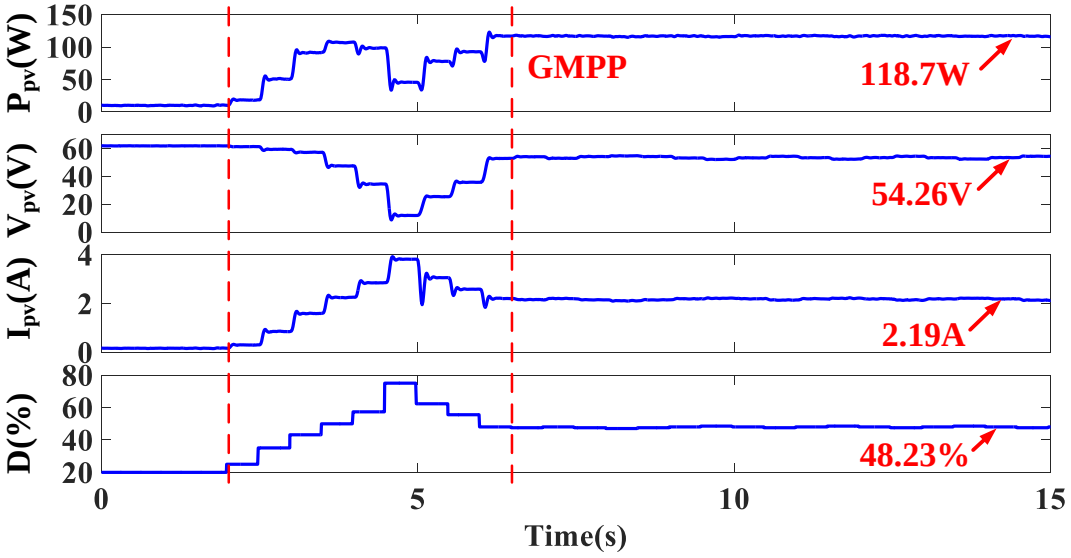

(b)

Fig. 4.38: Experimental results for pattern I: (a) the power incremental method with $\Delta P_{interval} = 10W$; (b) the power incremental method with $\Delta P_{interval} = 20W$.

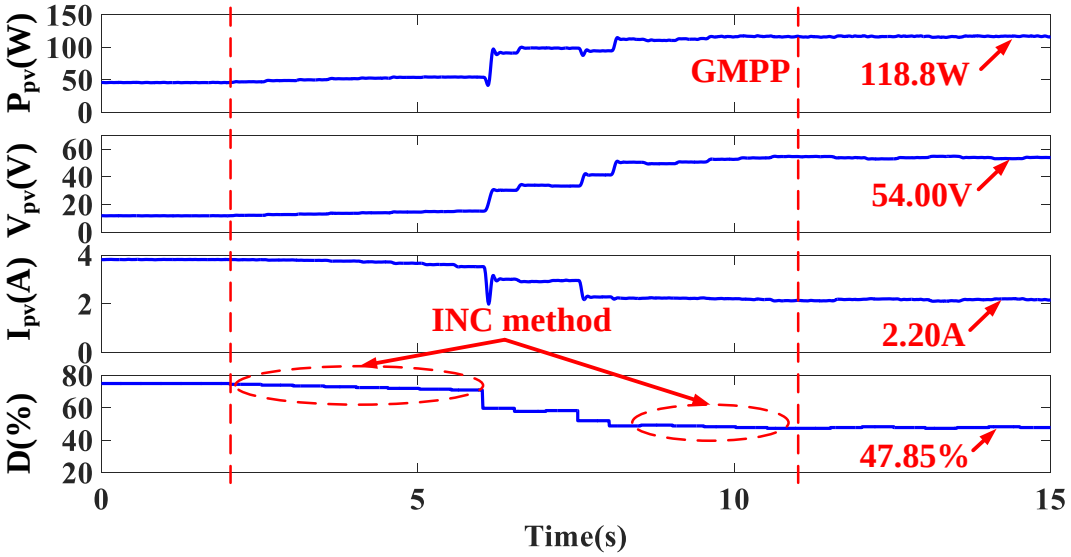

(a)

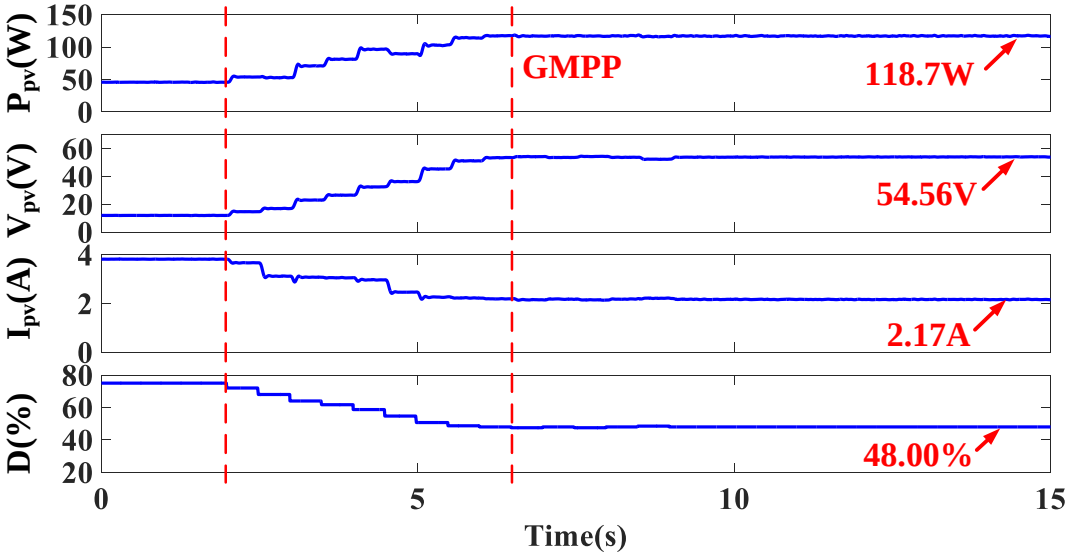

(b)

Fig. 4.39: Experimental results for pattern I: (a) the $0.8V_{oc}$ model method; (b) the proposed method.

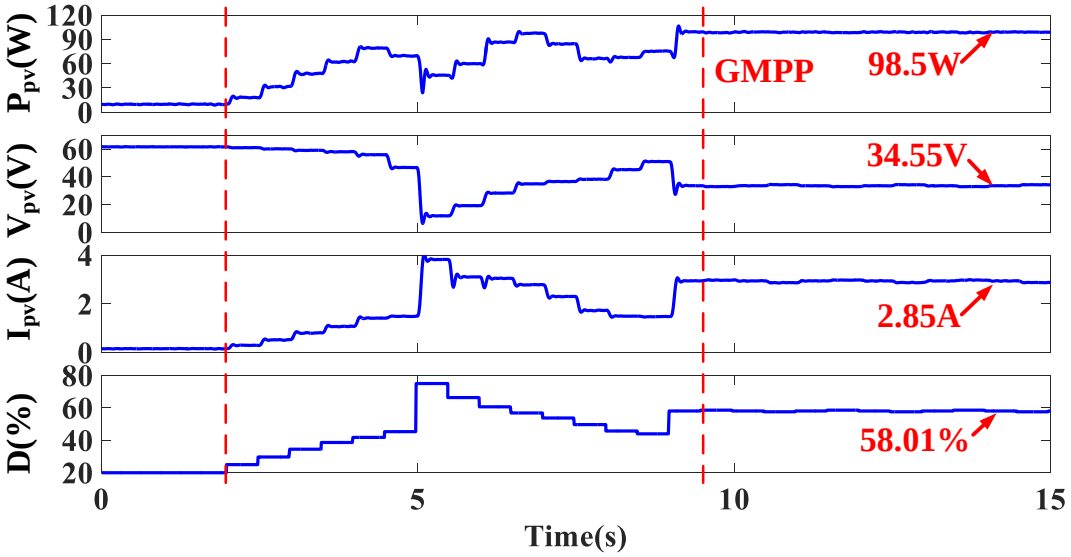

(a)

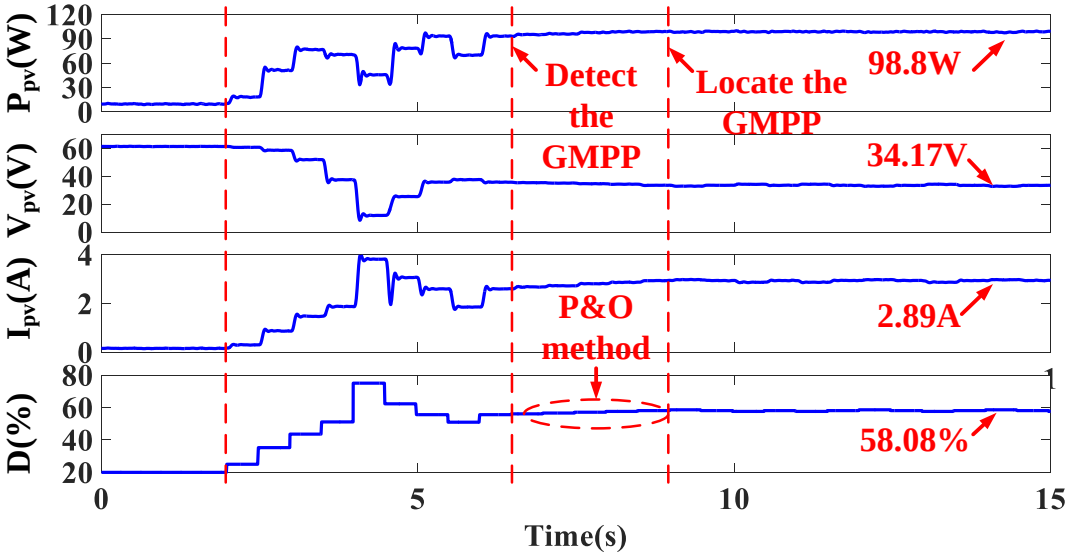

(b)

Fig. 4.40: Experimental results for pattern II: (a) the power incremental method with $\Delta P_{interval} = 10W$; (b) the power incremental method with $\Delta P_{interval} = 20W$.

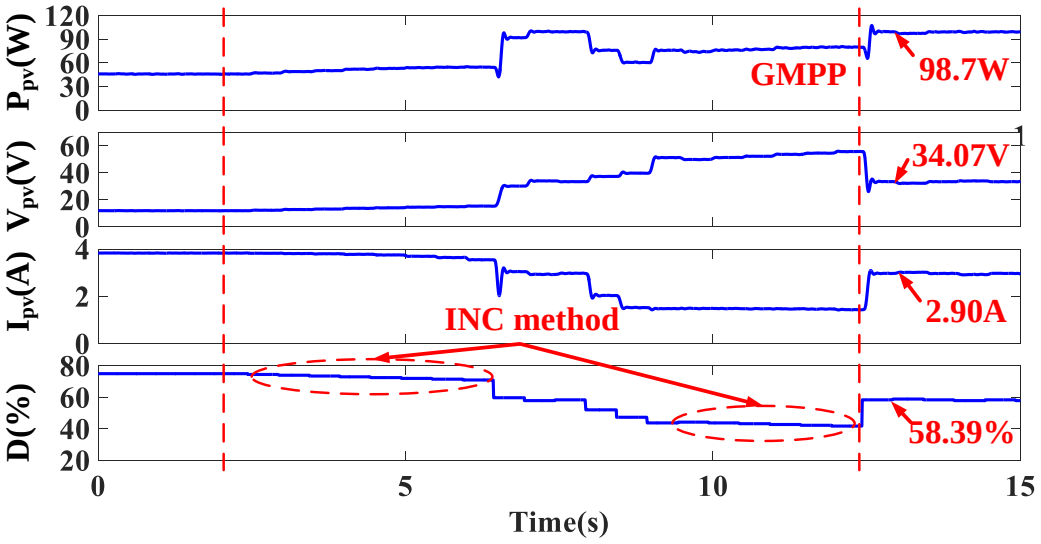

(a)

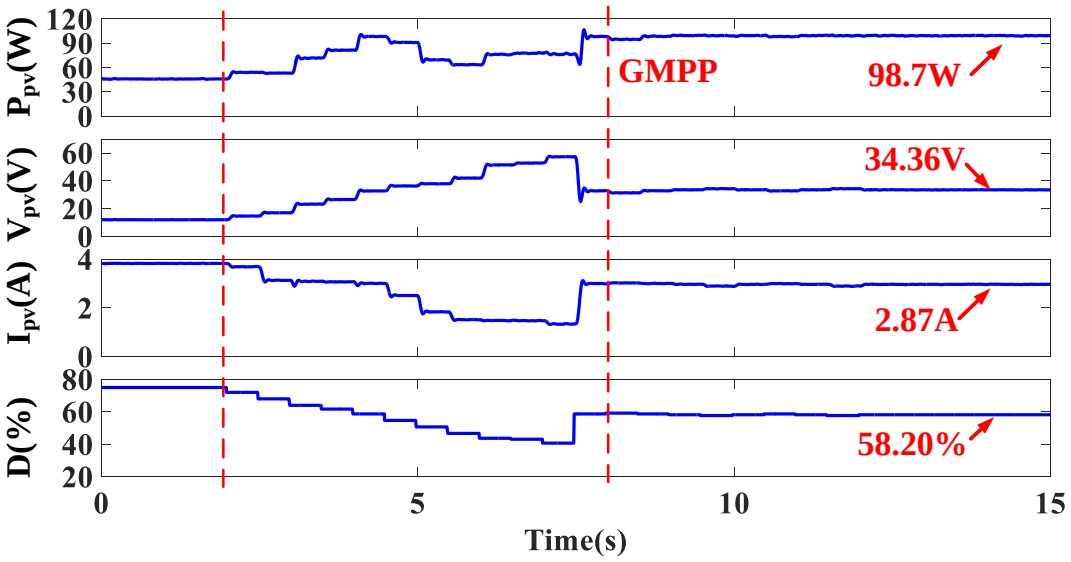

(b)

Fig. 4.41: Experimental results for pattern II: (a) the $0.8V_{oc}$ model method; (b) the proposed method.

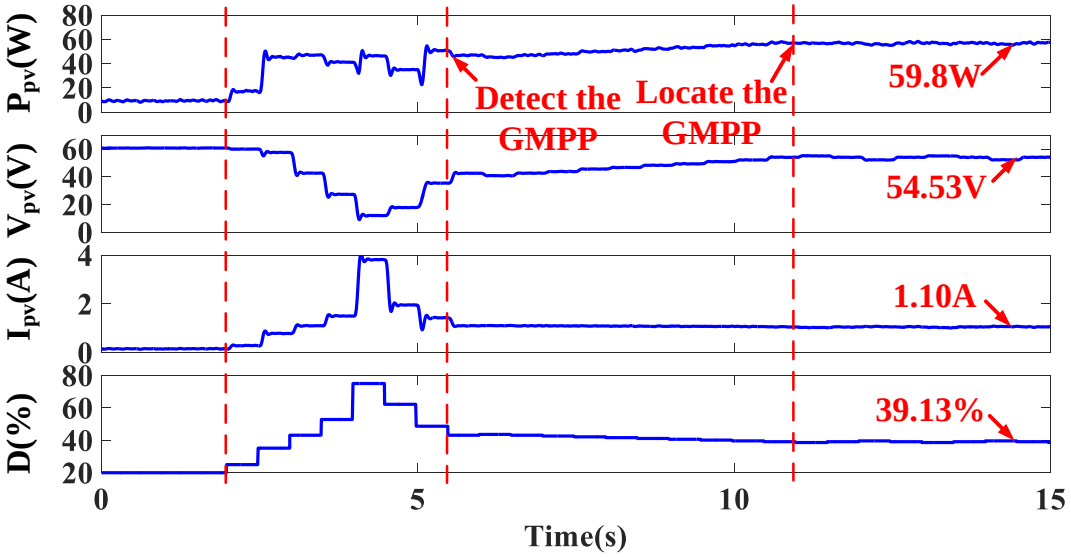

(a)

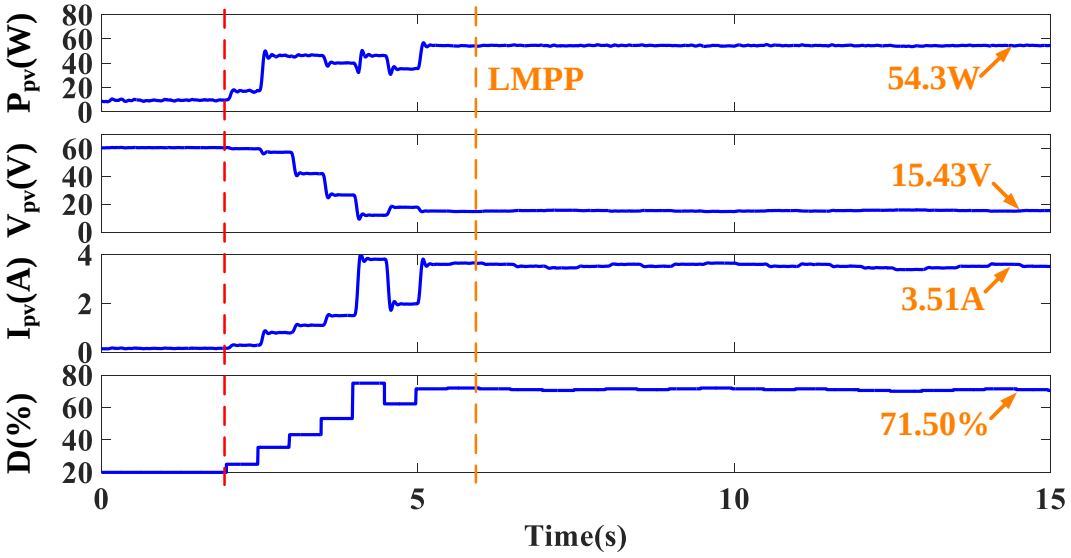

(b)

Fig. 4.42: Experimental results for pattern III: (a) the power incremental method with $\Delta P_{interval} = 10W$; (b) the power incremental method with $\Delta P_{interval} = 20W$.

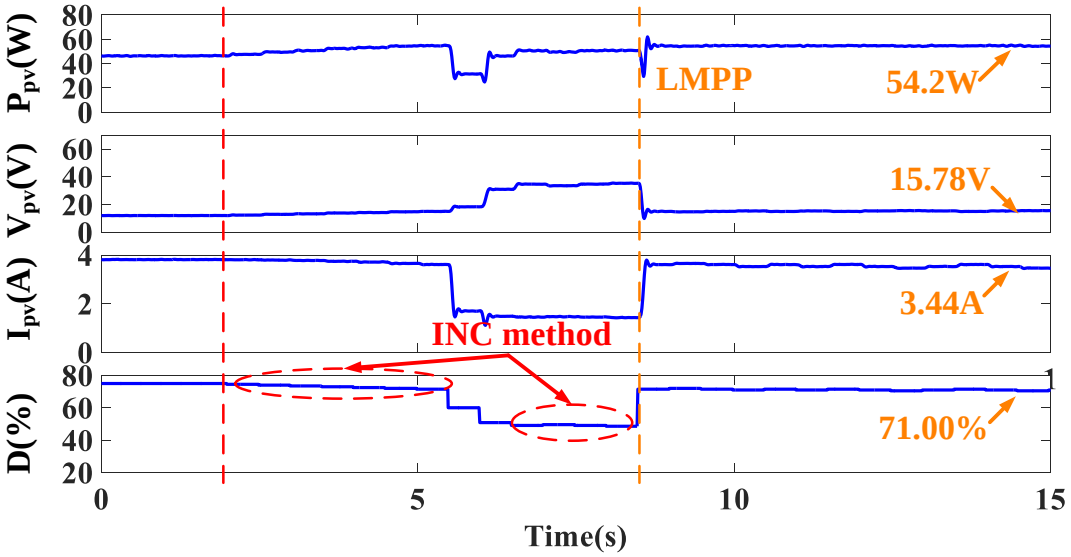

(a)

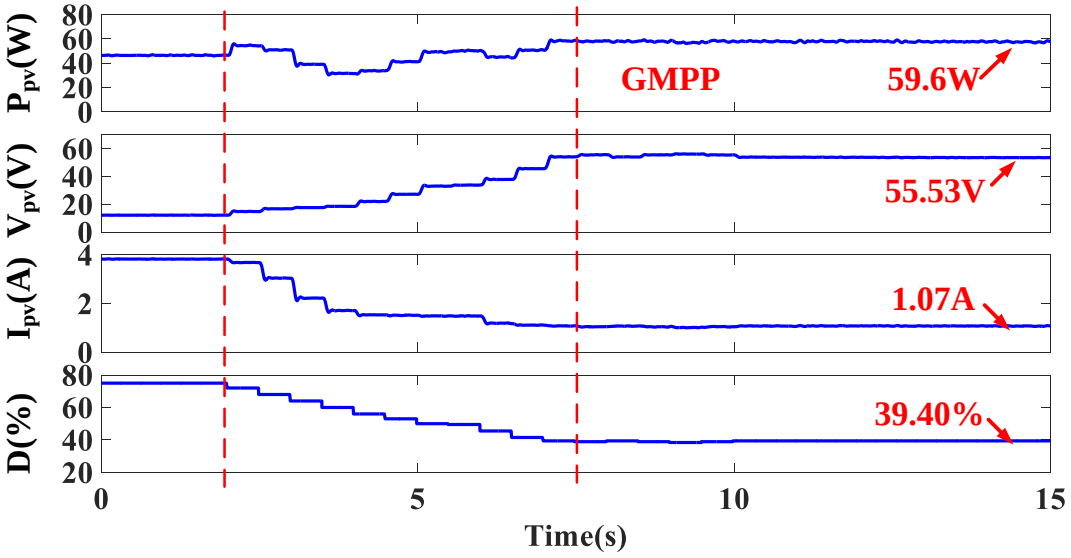

(b)

Fig. 4.43: Experimental results for pattern III: (a) the $0.8V_{oc}$ model method; (b) the proposed method.

reach the second peak. This $0.8V_{oc}$ model method requires 18 steps to locate the GMPP, which is also the longest as same as the simulation results. Compared to the $0.8V_{oc}$ model method, the proposed method only requires 9 steps to reach the GMPP. Furthermore, there is no oscillation for the proposed method at the steady-state while the other methods do.

For pattern II, the experimental results are illustrated in Fig.4.40 and Fig.4.41. The power incremental method with $\Delta P_{interval} = 20W$ requires 4.5s to detect the GMPP vicinity and extra 2.5s to find the real GMPP. Therefore, its overall tracking time is 7s, which is slightly longer than the proposed method (6s). Following the proposed method, the power incremental method with $\Delta P_{interval} = 10W$ requires 7.5s. The $0.8V_{oc}$ model method also requires the longest time (11s).

For pattern III, the experimental results are illustrated in Fig.4.42 and Fig.4.43. The power incremental method with $\Delta P_{interval} = 20W$ and the $0.8V_{oc}$ model method cannot correctly find the GMPP, which is similar to the simulation results. As shown in Fig.4.42 (b) and Fig.4.43 (a), the LMPP is located. The power incremental method with $\Delta P_{interval} = 10W$ requires the shortest time (3.5s) to detect the GMPP vicinity and extra 5.5s to find the real GMPP. Therefore, the proposed method is still the shortest (5.5s).

4.4.1 Evaluation of the Experimental Results

The summarization of these GMPPT method for the three PSC patterns is illustrated in Table 4.2. In Table 4.2, the term "Time" indicates the required tracking time for GMPP. Since both of the power incremental method with $\Delta P_{interval} = 20W$ and the $0.8V_{oc}$ model method can only track the LMPPs for pattern III, "Time" for these two method refer to the required tracking time for LMPP.

The terms "Tracking" refers to the dynamic tracking efficiency, which can be expressed as

$$\eta_{dyn} = \frac{\sum_0^{T_M} P_{pv}}{P_{max} \cdot T_M} \tag{4.27}$$

where P_{pv} and P_{max} refers to measured values of the power and the theoretical maximum value of the power, respectively; T_M refers to the total measurement time. T_M should be set as the required longest tracking time for all of the tested GMPPT method [74]. Therefore, in this thesis, T_M is set as 9s, 11s and 9s for Pattern I, Pattern II and Pattern III, respectively.

The term "Steady-state" refers to the steady-state efficiency. After the GMPP is found, the P&O method or INC method is used. Then, a three-level oscillation with a period of $4T_p$ is commonly happened [35, 75]. Therefore, the steady-state efficiency is expressed as

$$\eta_{stat} = \frac{\sum_{T_M}^{T_M+4\cdot T_p} P_{pv}}{P_{max} \cdot 4 \cdot T_p} \tag{4.28}$$

From Table 4.2, it is clearly seen that the proposed method has the highest dynamic and steady-state efficiency. Furthermore, it should be noted that the steady-state efficiency for the power incremental method with $\Delta P_{interval} = 20W$ and the $0.8V_{oc}$ model method are the lowest for Pattern III. The reason for that is that they are trapped at the LMPP.

Table 4.2: Comparison of the experimental results for different PSC patterns

Technique		Pattern I		Pattern II		Pattern III		
		Time	Tracking	Time	Tracking	Time	Tracking	Steady-state
Power incremental method	10W	7.5s	72.70%	7.0s	76.30%	9.0s	83.83%	98.05%
	20W	4.5s	82.04%	7.5s	85.23%	6.0s	86.84%	90.14%
$0.8V_{oc}$ model method		9.0s	69.37%	11.0s	69.54%	7.0s	89.19%	90.18%
Proposed method		4.5s	86.47%	6.0s	86.60%	5.5s	90.13%	99.12%

Chapter 5

Power Reserve Control With Simple Real-Time MPP Estimation

In recent years, PV systems have been increasingly integrated into the power grid [20]. As the penetration level of PV systems increases, a large number of conventional power plants will be replaced by the PV power plants [105]. As a consequence, the overall system inertia and the reserved power provided for the primary and secondary control will be reduced [106–108]. Therefore, the Rate of Change of Frequency (RoCoF) and the frequency deviation of the power system will be affected and consequently lead to critical frequency stability problems [109].

In order to overcome the frequency stability problems, grid regulations and network codes are continuously revised to deal with the intermittent nature of PV power and grid security [110]. Therefore, power reserve control (PRC) in PV systems is required to take part in the system frequency regulation. Usually, this PRC can be realized by two methods: providing energy storage devices or power curtailment [111]. The former normally uses batteries to realize the power reserve [112–114]. However, the drawbacks of this method is high initial investment and limited lifetime. Besides, integrating batteries into PV systems also increase the overall system cost and complexity, which is not so cost effective [115].

Alternatively, the power curtailment method is much simpler, lower implementation cost and easier to be adopted in the current power system [116–120]. The basic idea of this method is the PV systems working at a suboptimal power level rather the maximum power of PV panels by modifying the maximum power point tracking (MPPT) techniques, and then the active power can be reserved in order to realize potential grid support. Furthermore, the concept of the power curtailment method is also used for other utility scale technology [121], such as constant power generation control (CPGC) [122–124] and power ramp-rate control (PRRC) [125–129]. Although the main concern of this method is associated with energy loss caused by the curtailed PV power [130], the reduction of

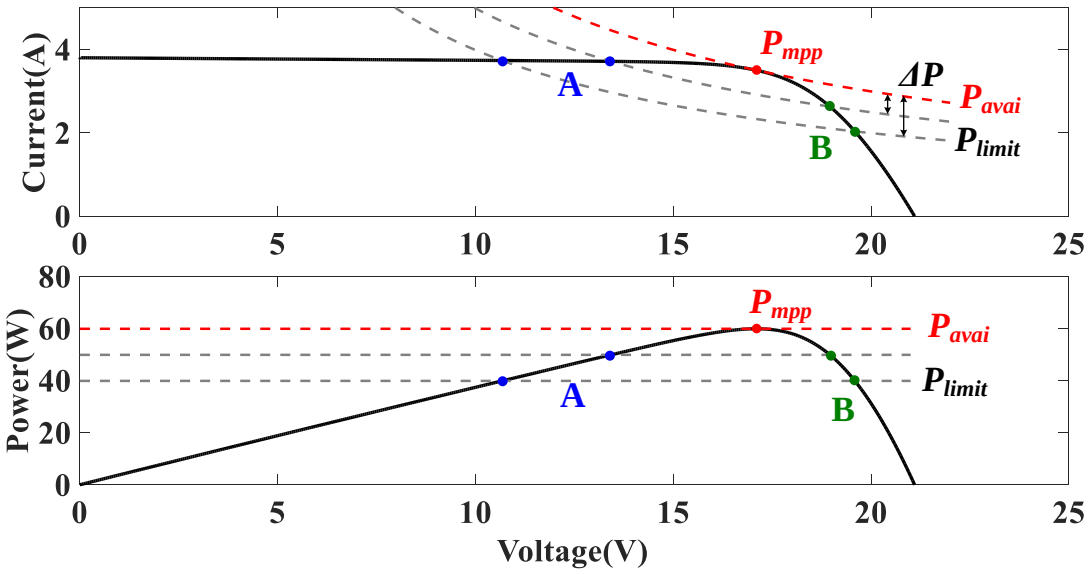

Fig. 5.1: I-V and P-V characteristic curves with the operating point at the curtailed level P_{limit}.

the energy can also reduce the thermal loading of switching devices. Consequently, the inverter lifetime can be increased as a compensation [131].

Fig. 5.1 shows the basic concept and typical curves of PV panels with the PRC. As shown in Fig. 5.1, the PV power P_{pv} is regulated at the curtailed level P_{limit}, which can be calculated as:

$$P_{pv} = P_{limit} = P_{avai} - \Delta P \tag{5.1}$$

where P_{avai} refers to the maximum available power and ΔP refers to the required amount of reserved power. Generally, ΔP is determined by the system operator. P_{avai} is affected by the weather conditions such as solar irradiance and temperature, thus, fast and effectively estimating P_{avai}, tracking P_{limit} and maintaining ΔP at a certain level under dynamic conditions is the key issue [132].

The content of this chapter has been published in the following paper:

1. **Li, X.**, Wen, H., Hu, Y., Jiang, L., Xiao, W., "A Novel Sensorless Photovoltaic Power Reserve Control With Simple Real-Time MPP Estimation", *IEEE Transactions on Power Electronics*, Accepted

5.1 Literature Review on PRC Methods

So far, many methods for the determination of the available power, P_{avai}, have been proposed and can be categorized into two categories: measurement based methods and curve-fitting based methods.

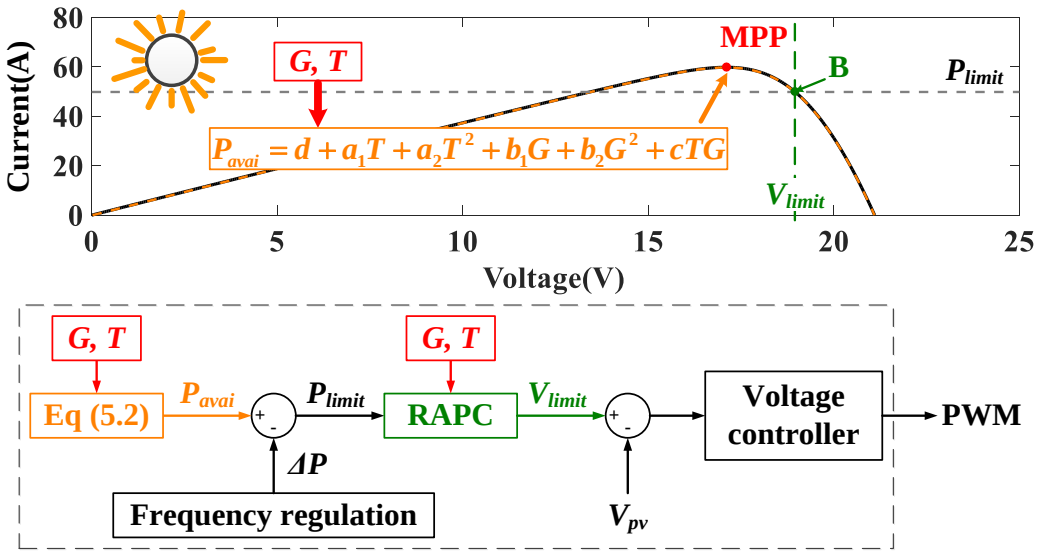

Fig. 5.2: Principle diagram of the P_{avai} measurement method for the PRC method by using solar irradiance and temperature sensors.

5.1.1 Measurement Based PRC Methods

In the first category, P_{avai} is measured rather than estimated. Besides, most of them have additional hardware requirements.

PRC Method by Using Solar Irradiance and Temperature Sensors

In [133, 134], combined with the PV array characteristic model, an accurate measurement of the solar irradiance and temperature is required to calculate P_{avai}. As shown in Fig. 5.2, a linear regression is used to calculate P_{avai}, as shown below:

$$P_{avai} = d + a_1 T + a_2 T^2 + b_1 G + b_2 G^2 + cTG \tag{5.2}$$

where G and T refer to the measured value of solar irradiance and temperature, respectively; d, a_1, a_2, b_1, b_2 and c are regression coefficients which are derived and stored in the PV controller's on-board memory. ΔP is changed by the frequency regulation block in order to response a grid frequency event. After P_{avai} and ΔP are obtained, P_{limit} can be calculated via (5.1). Then, the block, rapid active power control (RAPC), is used to convert P_{limit} into voltage command V_{limit}. Finally, the control signal PWM is obtained by comparing V_{limit} and the PV voltage V_{pv} via the voltage controller.

This method is straight-forward and very effective in obtaining P_{avai} in the real time. However, the additional sensors required for the solar irradiance and temperature measurement will increase the cost and complexity of the whole system. Besides, this method is difficult to be implemented in the existing system.

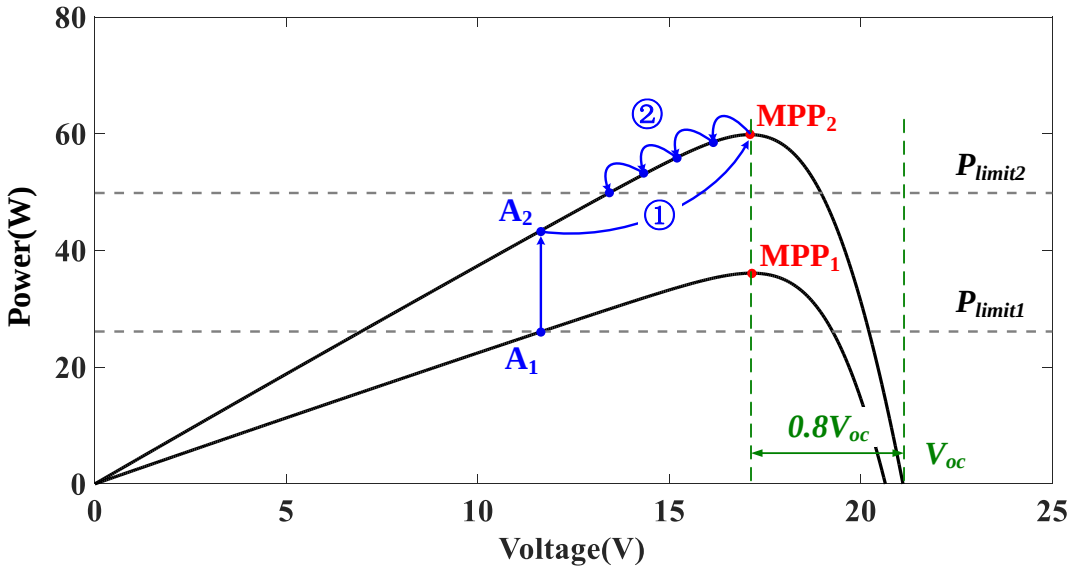

Fig. 5.3: Principle diagram of the P_{avai} measurement method for the PRC method by periodically entering MPPT mode.

PRC Method by Periodically Entering MPPT Mode

In [135], the system periodically enters the fractional open-circuit voltage MPPT mode to estimate P_{avai}. As shown in Fig. 5.3, the power at $80\%V_{oc}$ can be approximately regarded as P_{avai}. Assuming that the operating point is initially located at point A_1. When the solar irradiance is increased, the operating point will move to point A_2. Then, the operating point moves to the point at $0.8V_{oc}$ to measure the P_{avai}, which is marked as ①. Once P_{avai} is measured, this method perturbs the operating point until reaches the curtailed power P_{limit}, which is marked as ②.

This method is also very straightforward to understand and easy to be implemented in the existing system. However, this method is not able to obtain P_{avai} in the real time. Besides, since the dc-link capacitor will buffer the PV power increase during the operating point jumping to the point at $0.8V_{oc}$, the dc-link voltage is increased, which may raise over-voltage concern without proper control.

PRC Method by Using A Coordinate Control Strategy

In [136], a coordinated control strategy is proposed for PV strings in a master-slave mode. It assumes that two PV strings have similar solar irradiance and temperature profiles since they are located close to each other. As shown in Fig. 5.4, the master PV string uses the MPPT algorithm to track its MPP while the slave PV string directly utilizes the tracked MPP result as its P_{avai}. Even if the solar irradiance is changed, P_{avai} can be still obtained in the real time.

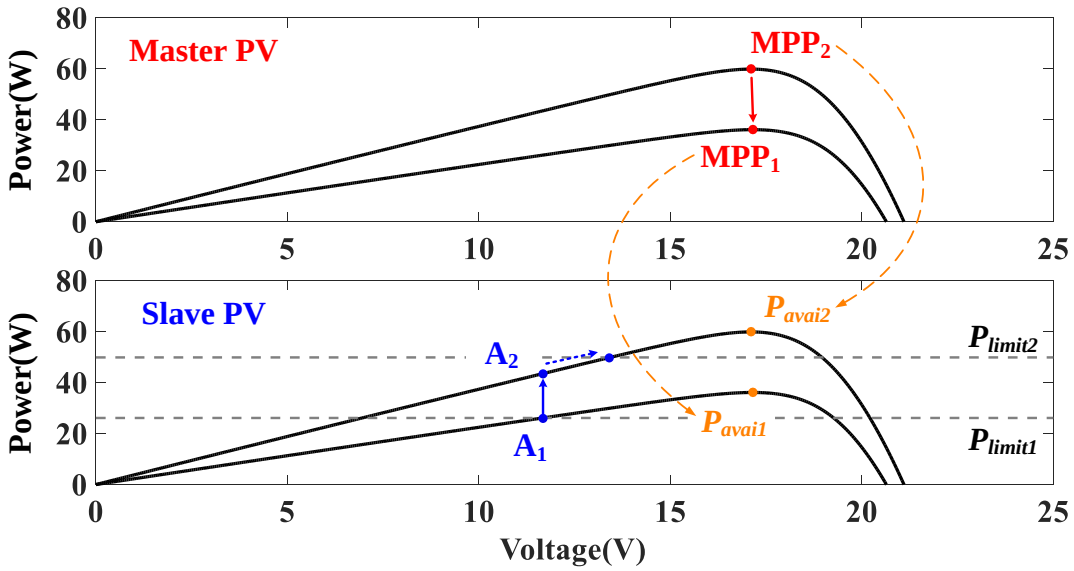

Fig. 5.4: Principle diagram of the P_{avai} measurement method for the PRC method by using a coordinate control strategy.

The advantage of this method is the accurate regulation of the reserved power and the stable operation. However, the two PV systems have to be identical rated power and geographically located close to each other with communication systems. It is also difficult to be implemented in the existing system.

5.1.2 Curve Fitting PRC Method

In the second category, the PRC methods generally use curve fitting to estimate P_{avai}. With serval sampled operating voltage and current points, the whole P-V curve can be fitted and P_{avai} can be estimated.

PRC Method by Using Newton Quadratic Interpolation (NQI) Method

In [137], the P-V curve is approximately fitted to a parabolic curve with three sampled points by the Newton quadratic interpolation (NQI) method, which is also called parabolic method [52, 54, 138]. Accordingly, the peak of this fitted parabolic curve is considered as P_{avai}.

Although the effectiveness of the NQI method has been validated in [137], the accuracy of estimated P_{avai} may be affected by the selection of the three sampled points [52]. As shown in Fig. 5.5, the different sampled points could result in different parabolic curves. As a consequence, the estimated P_{avai} is also varying and the accuracy of P_{avai} will be suffered. Besides, this method is not able to obtain P_{avai} in the real time.

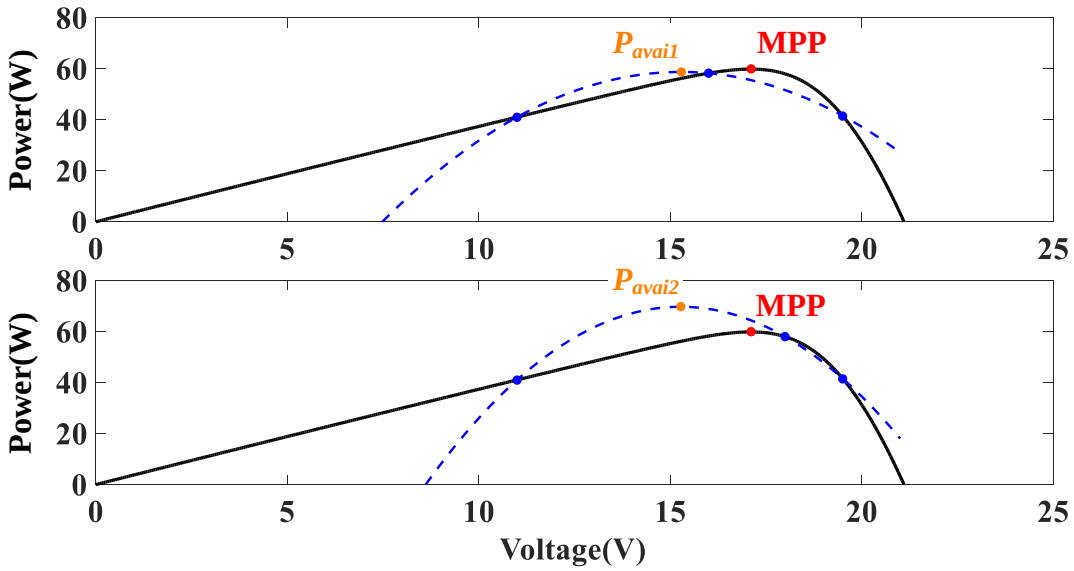

Fig. 5.5: Principle diagram of the P_{avai} estimation method for the PRC method by using a coordinate control strategy.

PRC Method by Using Least Squares (LSQ) Method

In [139], the least squares (LSQ) method is used for the P_{avai} estimation in real time. As shown in Fig. 5.6, this method samples a large set of current and voltage values at the right side of the MPP. With these sampled points, not only P_{avai} can be estimated, but the whole P-V curve can be obtained.

More important thing is that this method can estimate P_{avai} while the operating point is working at a reduced power level. However, the control implementation seems cumbersome since five parameters are required for the single-diode PV model in the real time MPP estimation. Furthermore, the operating point with a curtailed power level for this method is allocated at the right-hand side of the MPP, which may result in the instability issue during the fast decreasing irradiance condition [135].

5.1.3 Selection of the Suboptimal Point

As shown in Fig. 5.1, there are two possible suboptimal points to regulate the power working at P_{limit}, namely point A and B. Some of the relevant papers prefer the system working at point B due to higher converter efficiency and faster dynamic response [133, 134, 137, 139], while some of them prefer point A due to the concern about unstable operation at point B [135, 136]. Therefore, it is very essential to select the suboptimal point.

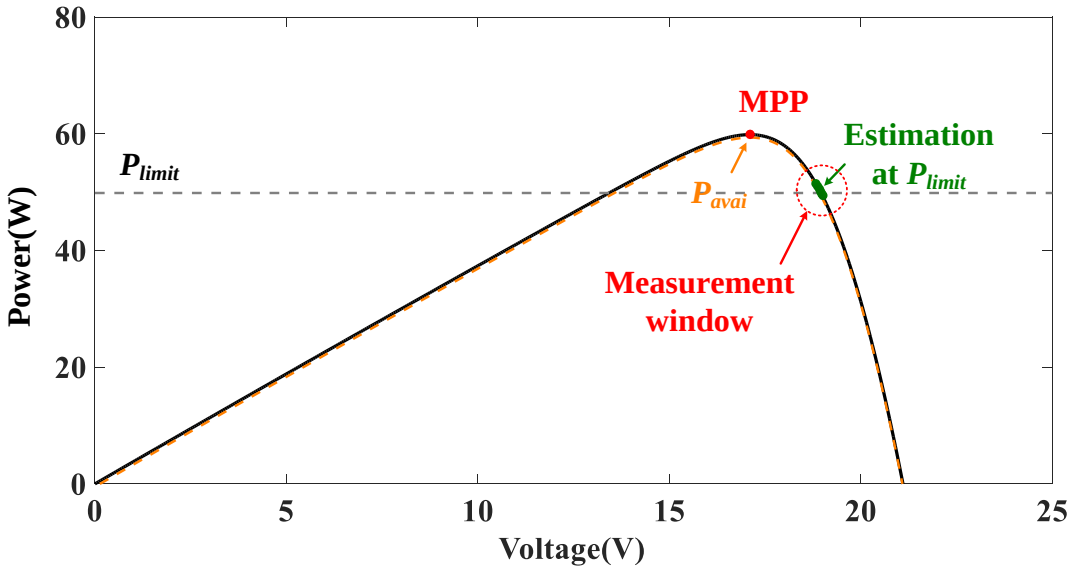

Fig. 5.6: Principle diagram of the P_{avai} estimation method for the PRC method by using least squares (LSQ).

Stability Issue

Fig. 5.7 demonstrates the stability issue when the solar irradiance is suddenly decreased. Assuming that the initial solar irradiance is 1000W/m^2 and $0.2P_{avai}$ is reserved for ΔP. When the solar irradiance is suddenly decreased to 600W/m^2 or 200W/m^2, the operating point at A and B will straightly go down along the dot lines.

As shown in Fig. 5.7, both A and B points will stay at the lower solar irradiance level. However, if higher percentage of P_{avai} (e.g., 50%) is reserved for ΔP, point B may fall into the area beyond the V_{oc} when the solar irradiance is decreased to 200W/m^2. It should be pointed out that PV systems are not allowed to immediately disconnect from the grid [136]. Under this condition, the PV system is not able to produce any power to the grid, so the PRC operation becomes unstable. However, compared to point B, whatever the solar irradiance is changed or percentage of P_{avai} is reserved, the PRC at point A is always stable.

Perturbation Interval

Apart from the stability issue, it is also important to choose the parameter of the perturbation interval T_p. T_p is used to ensure that the period between two successive perturbations is longer than the setting time of PV power transient [140]. Generally, T_p should be properly selected at the MPP region (or referred as the constant power region, CPR) [23]. However, when the PV system is regulated at either point A or point B, the system is actually working at the linear region of the I-V curve. As shown in Fig. 5.8, the linear

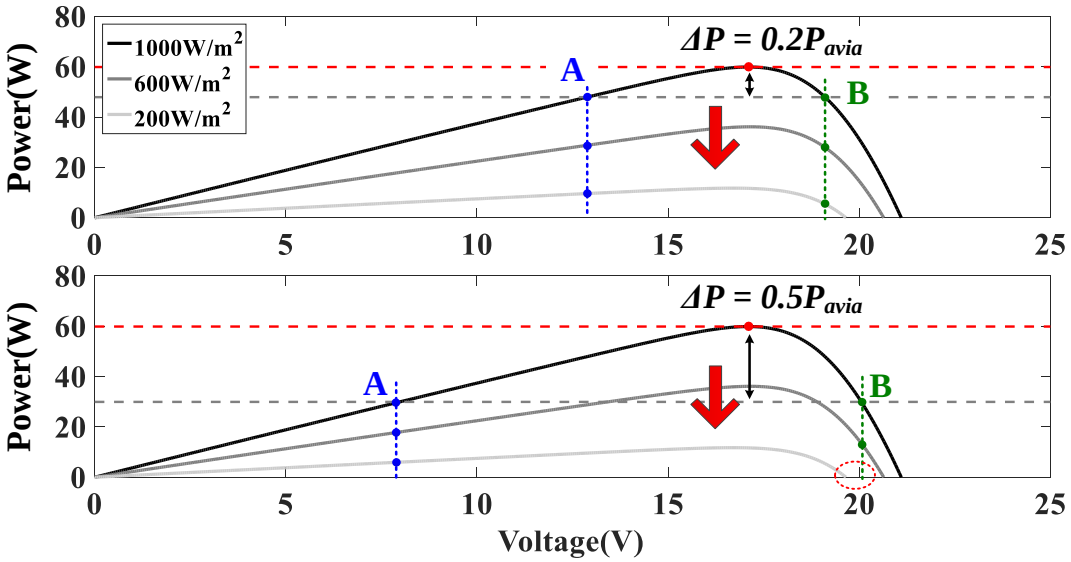

Fig. 5.7: Stability issue for the two suboptimal points when the solar irradiance suddenly is decreased.

regions at point A and point B are called as the constant current region (CCR) and the constant voltage region (CVR), respectively [141]. Therefore, the selection of T_p should be carried out considering the features of CCR or CVR if point A or point B is selected. According to [140], T_p in the CCR and the CVR can be derived by:

$$T_p \geq T_\varepsilon \cong -\frac{1}{\zeta \cdot \omega_n} \cdot \ln\left(\varepsilon\sqrt{1-\zeta^2}\right) \tag{5.3}$$

where $\omega_n = 1/\sqrt{L \cdot C_{in}}$, $\zeta = 1/(2 \cdot R_{pv}) \cdot \sqrt{L/C_{in}}$, and $\varepsilon = 0.1$.

Fig. 5.9 shows that PV power transients under different regions and different solar irradiance. A step change in duty cycle is used to sweep the I-V curve of the PV module. Since R_{pv} in the CCR is much smaller than that in CVR, the required setting time in the CCR is much longer than that in the CVR, as demonstrated in Fig. 5.9. In other words, a smaller T_p could be used in the CVR rather than the CCR. Therefore, the PRC at point B could have a faster tracking speed than that at point A.

5.1.4 Comparison and Discussion

The main features of the previous PRC methods are summarized in Table 5.1. As previously discussed, the aforementioned methods shows some limitations in terms of additional hardware requirements, implementation difficulty, and estimation speed.

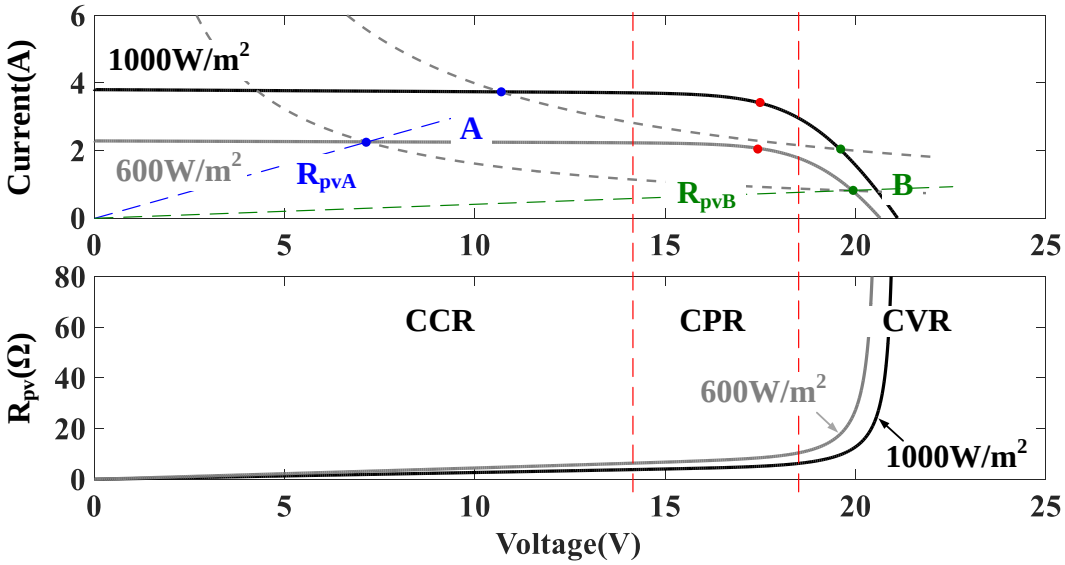

Fig. 5.8: Linear region of the I-V curve.

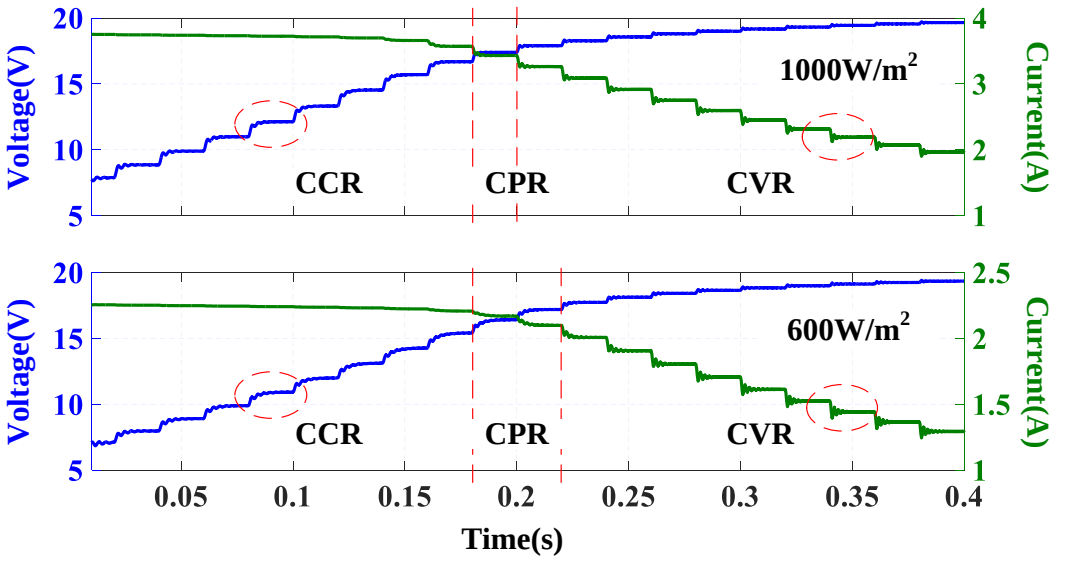

Fig. 5.9: PV power transient under different regions and different solar irradiance.

Table 5.1: Comparison among the previous P_{avai} estimation methods for the PRC method

Ref.	How to obtain P_{avai}	Additional hardware requirement	Real-Time	P_{limit} location	Implantation	Estimation speed
[133, 134]	Measurement	Solar irradiance and temperature sensors	Yes	Right	Complex	Fast
[135]	Measurement	No	No	Left	Simple	Medium
[136]	Measurement	Identical PV systems	Yes	Left	Simple	Medium
[137]	Estimation	No	No	Right	Complex	Slow
[139]	Estimation	No	Yes	Right	Complex	Fast

5.2 Proposed Power Reserve Control Method

In order to overcome the drawbacks of the previous PRC methods, a novel PRC strategy with simple real-time MPP estimation is proposed in this thesis. With the proposed control, two operating points at the left side of the true MPP are sampled to obtain the short-circuit current through estimation rather than the measurement by using additional hardware circuits. Then, the Lambert-W function is used to derive the MPP voltage and further the total available power P_{avai}. The proposed strategy requires no additional hardware such as the irradiance and temperature sensors, and it can be easily implemented in existing PV systems. With this strategy, cumbersome procedures of curve fitting with sophisticated operating points sampling and key parameters determination in the real-time MPP estimation by using the conventional PRC methods can be eliminated. This strategy is effective to provide the grid frequency support under various weather conditions even under fast solar irradiance changing condition. The proposed control can provide the grid frequency support through the direct converter duty cycle control.

5.2.1 Maximum Available Power Estimation

Due to the concern about the stability, point A is selected as the suboptimal point for the PRC. As aforementioned discussion, a higher T_p has to be used to ensure the setting time is long enough to reach the steady state. A pair of voltage and current in the CCR are sampled in this algorithm to estimate P_{avai}. It is undoubted that three or more sampled points can improve the algorithm robustness against noise caused by measurement bias. However, if three or more T_p time periods are required to estimate P_{avai}, the estimation speed will be affected. As a matter of fact, the noise can be effectively reduced by setting the higher T_p [142, 143], so it is not really necessary to sample more points. Therefore, the proposed method only requires two sampled points to estimate P_{avai}. The whole process of P_{avai} estimation is demonstrated in Fig. 5.10.

From Fig. 5.10, the CCR can be expressed in a linear formula. Assuming two any points in the current-source region is known, the slope of the linear formula can be expressed as

$$m = \frac{I(k) - I(k-1)}{V(k) - V(k-1)} \tag{5.4}$$

where m refers to the slope of the current-source region; $I(k)$ and $V(k)$ refer to the present value of sampled current and voltage, respectively; and $I(k-1)$ and $V(k-1)$ refer to the previous value of sampled current and voltage, respectively. Then, the intercept of this linear formula, namely short-circuit current (I_{sc}) can be also obtained:

$$I_{sc} = I(k) - mV(k) \tag{5.5}$$

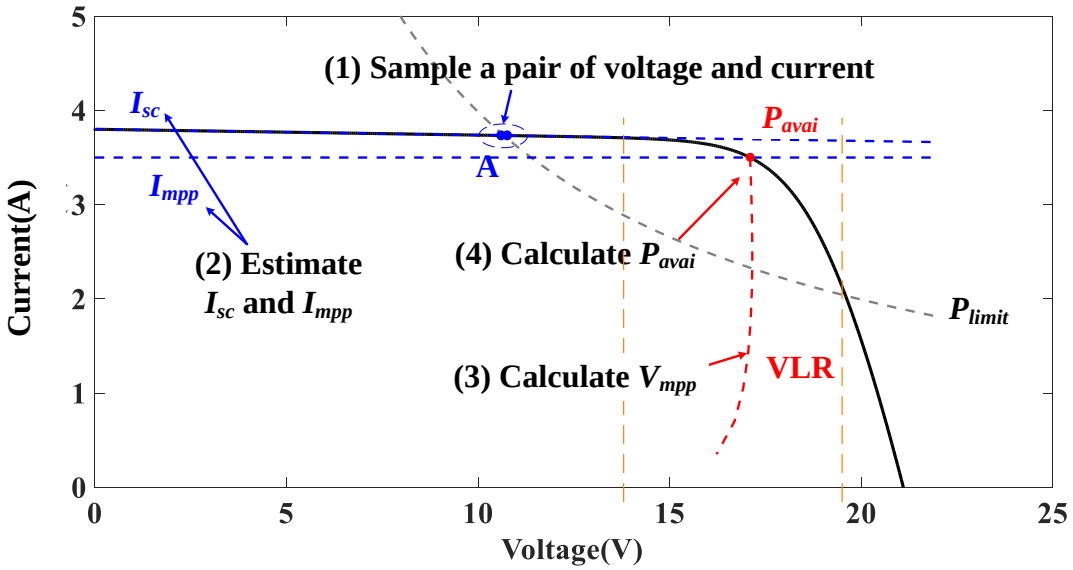

Fig. 5.10: Process of P_{avai} estimation.

Since current at the MPP (I_{mpp}) has a near linear relationship with I_{sc}, I_{mpp} can be expressed as:

$$I_{mpp} = K_{I_{sc}} I_{sc}, 0.78 < K_{I_{sc}} < 0.92 \tag{5.6}$$

where $K_{I_{sc}}$ is constant [15].

Furthermore, it can be also seen that the MPP locations for different solar irradiance levels approximately lie on a straight line called as voltage linear reference (VLR) [144], marked as a red dash line in Fig.5.10. Therefore, V_{mpp} can be approximately expressed as a linear relationship function [144] or a nonlinear relationship function by using Lambert-W function [145]. In this paper, Lambert-W function is used to obtain V_{mpp}, namely:

$$V_{mpp} \cong \eta W \left\{ \frac{I_{mpp}\left(1 + \frac{R_s + \sqrt{R_p R_s + R_s^2}}{R_p}\right)}{I_s} \right\} - R_s I_{mpp} \tag{5.7}$$

After I_{mpp} and V_{mpp} are obtained, P_{avai} can be estimated as

$$P_{avai} = P_{mpp} = V_{mpp} I_{mpp} \tag{5.8}$$

In order to accurately estimate P_{avai}, $K_{I_{sc}}$ is a critical parameter. The MSX-60W PV module is used as the PV source, which is shown in Table 2.1. The values of $K_{I_{sc}}$ under different solar irradiance and temperature are given in Fig. 5.11. If $K_{I_{sc}}$ is set as 0.92, P_{avai} can be calculated by the equations (5.4)-(5.8). Then, the difference between calculated P_{avai} and the real maximum power P_{real} is defined as P_{error}. From Fig. 5.11, the absolute value of P_{error} is only around 0.2W, which can be negligible.

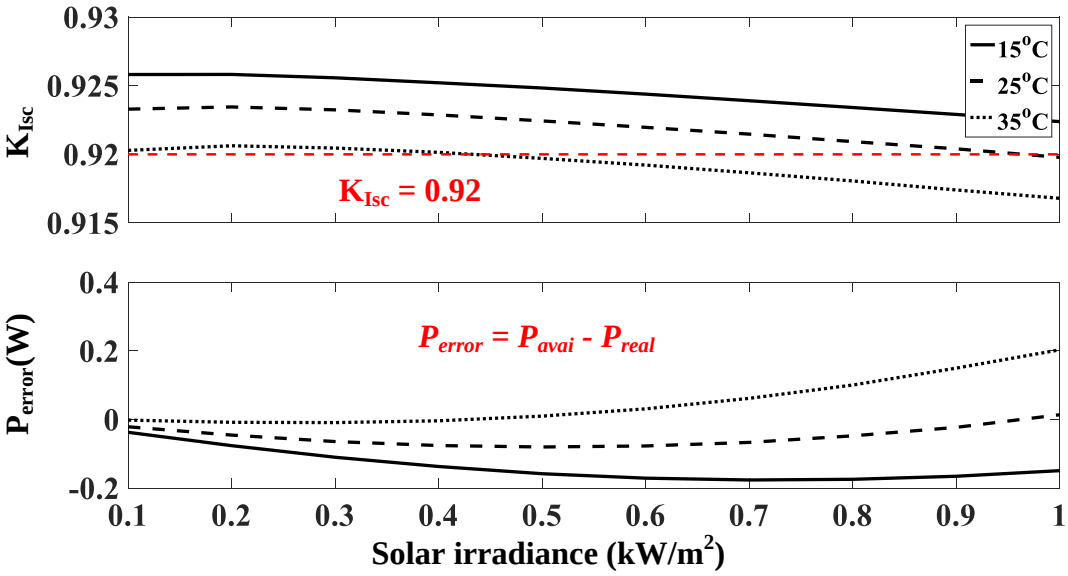

Fig. 5.11: $K_{I_{sc}}$ and P_{error} under different solar irradiance and temperature.

5.2.2 Proposed control scheme

In [135, 136], a two-stage grid-connected PV inverter is used to validate the PRC method that they proposed. It consists of two power converters, namely a PV-side DC-DC converter and a grid-side DC-AC inverter. Generally, the PV-side DC-DC converter is responsible to regulate the PV power working at P_{mpp} or P_{limit} and the grid-side DC-AC inverter is used to deliver the extracted PV power to the AC grid. Since the DC and AC power are decoupled in the two-stage configuration, the PV-side control and the grid-side control are also decoupled. Thus, a simplified PV system with a boost converter and a resistive load is used to validate the PRC method proposed in [139]. In this paper, the boost converter with a DC load is used for simplicity, as shown in Fig. 5.12.

As shown in Fig. 5.12, the proposed control scheme consists of two working modes, namely the MPPT and the PRC. The proposed control scheme samples V_{pv} and I_{pv} from the PV side and produces PWM to realize the MPPT or the PRC. $Flag$ and ΔP are two external signals provided by the system operator, which are feeded to the proposed control scheme. $Flag$ is used to switch the working modes between the MPPT and the PRC, and ΔP is set as the required amount of reserved power. Whichever the working mode is the MPPT or the PRC, P_{avai} will be sent to the system operator and the system operator can decide to choose $Flag$ or ΔP.

Fig. 5.13 shows the flowchart of the proposed control scheme. Initially, V_{pv} and I_{pv} are continually sampled, and then, $Flag$ and ΔP are provided by the system operator. If $Flag$ is equal to zero, the working mode will switch to the MPPT mode, marked as block 1 in Fig. 5.13. Then, a MPPT method, such as perturb and observe (P&O) method, is

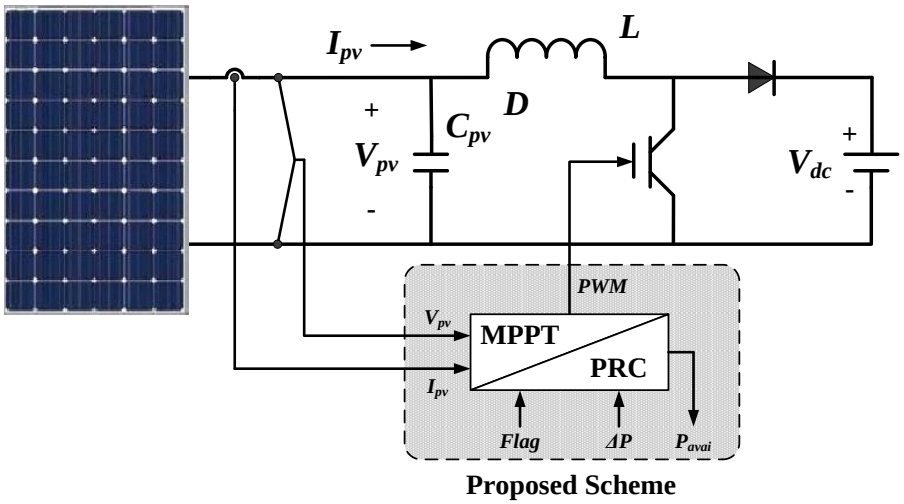

Fig. 5.12: Simplified PV system with a boost converter with the proposed control scheme.

used to track the MPP, and the present value of sampled power, $P(k)$, is set as P_{avai} in the steady-state stage. If $Flag$ is not equal to zero, the working mode will switch to the PRC mode, as marked a block 3 in Fig. 5.13. Then, I_{sc}, I_{mpp}, V_{mpp}, P_{avai} and P_{limit} can be determined in turn.

If the operating point is too far away from P_{limit}, a large step size should be used:

$$\Delta D = \begin{cases} \Delta D_{max},\ P(k) - P_{limit} > P_{th} & \text{(5.9a)} \\ -\Delta D_{max},\ P(k) - P_{limit} < -P_{th} & \text{(5.9b)} \end{cases}$$

ΔD refers to step size, ΔD_{max} refers to the maximum step size and P_{th} is defined as a threshold. Otherwise, the proposed algorithm will perturb around P_{limit} with a small step size.

$$\Delta D = \begin{cases} \Delta D_{min},\ P(k) > P_{limit} & \text{(5.10a)} \\ -\Delta D_{min},\ P(k) < P_{limit} & \text{(5.10b)} \end{cases}$$

where ΔD_{min} refers to the minimal step size.

As aforementioned discussion, P_{avai} can be estimated as long as the operating point at the CCR. Fig. 5.14 shows that the values of $\Delta I/\Delta V$ around P_{limit} are approximately equal to zero even though the solar irradiance is different. Therefore, $\Delta I/\Delta V$ can be used as an index, which determine whether the operating point is at the CCR Then, it can be expressed as:

$$m_{th} < m(k) = \frac{\Delta I}{\Delta V} = \frac{I(k) - I(k-1)}{V(k) - V(k-1)} < 0 \tag{5.11}$$

where $m(k)$ refers to the present value of $\Delta I/\Delta V$. Since the value of $\Delta I/\Delta V$ around P_{limit} is not exactly equal to zero at the CCR, a threshold, m_{th}, and a boundary are defined

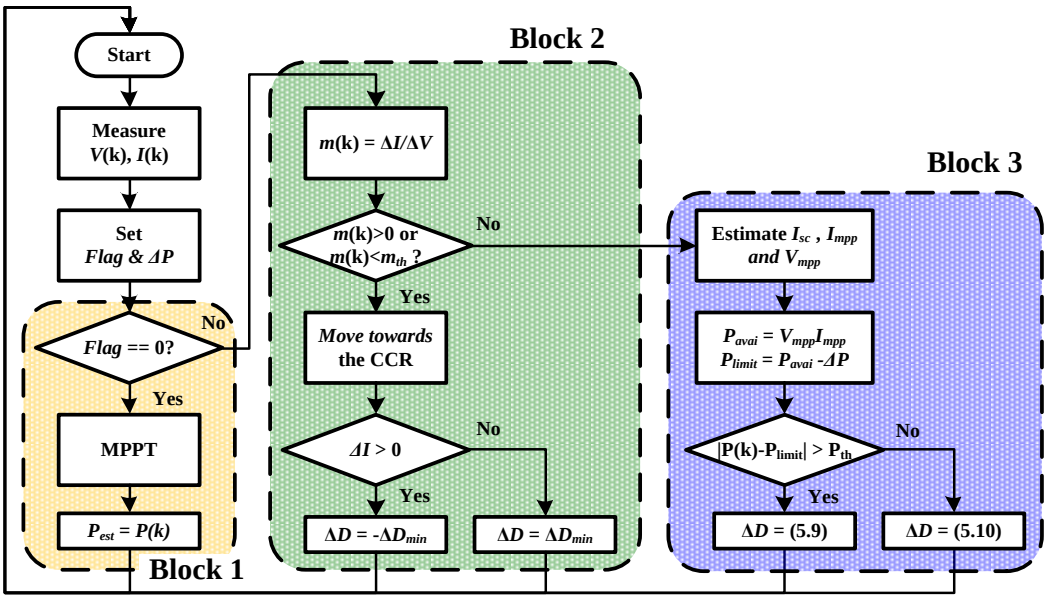

Fig. 5.13: Flowchart of the proposed control scheme.

in (5.11). As marked in a block 2 in Fig. 5.13, if the value of $m(k)$ is within this boundary, the algorithm will go through the block 3. Otherwise, the algorithm will go through the block 2 and move towards the CCR.

5.2.3 Grid Frequency Support Scheme

From Fig. 5.12, three signal ports, $Flag$, ΔP and P_{avai}, are encapsulated. The three encapsulated signal ports can be directly controlled by system operator. Therefore, how to use these signals to support the grid frequency responses will be demonstrated in this subsection.

Fig. 5.15 demonstrates how the proposed method supports the grid frequency response. Based on the changes of ΔP and ΔG, there are three possibilities:

Only ΔP changes

Assume that the solar irradiance is maintained unchanged. When a major contingency happens, such as a sudden reduction of the generator output power, the reserved power should be provided to response the grid frequency. Then, ΔP will be decreased by the system operator, as shown in Fig. 5.15 (a). If all of the reserved power have to immediately feed to the grid, $Flag$ in the flowchart Fig. 9 will be set as "0" and the operation mode will be changed to the MPPT mode by the system operator. Then, some fast MPPT methods, such as Beta method [71], can make the operating point immediately move the MPP within several seconds. After the grid frequency is restored back, $Flag$ is set as "1"

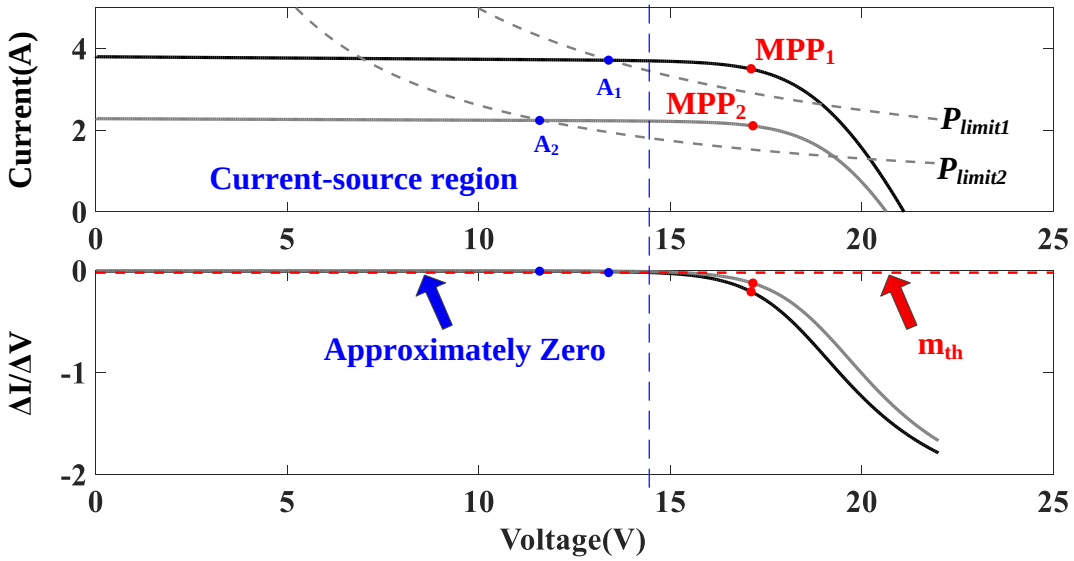

Fig. 5.14: I-V and ΔI-ΔV curve.

according to the flowchart shown in Fig. 9 and the operation mode is changed to the PRC mode in order to restore ΔP again, as shown in Fig. 5.15 (b).

It should be noted that the operating point is actually working at the PRC under this situation. The measured $m(k)$ is always satisfied with the equation (5.11), and the proposed method only goes through the block 3 in Fig. 5.13.

Only ΔG changes

Assume that ΔP is maintained unchanged. When the solar irradiance is changed, it is essential to maintain the reserved power ΔP always at a certain value during this period. Fig. 5.15 (c) and (d) demonstrates the changes of solar irradiance ΔG. Assuming that point A is the initial point before the change of ΔG happened and point C is the optimal point after the change of ΔG happened. Whatever ΔG decreases or increases, the operating point will directly go down or go up from A to B. At this time, since point B is already in the CCR, the proposed method just slightly perturbs the operating point as shown in the block 2 in Fig. 5.13. The perturbation in the converter duty cycle is expressed as:

$$\Delta D = \begin{cases} \Delta D_{min}, \ \Delta I < 0 & \text{(5.12a)} \\ -\Delta D_{min}, \ \Delta I > 0 & \text{(5.12b)} \end{cases}$$

Both of ΔP and ΔG will change

Fig. 5.15 (e)-(h) demonstrates the case with both the changes in ΔP and ΔG. Point A and C refer to the initial point and the optimal point, respectively. Whatever ΔP and ΔG decrease or increase, the operating point will directly go down or go up from A to B. From

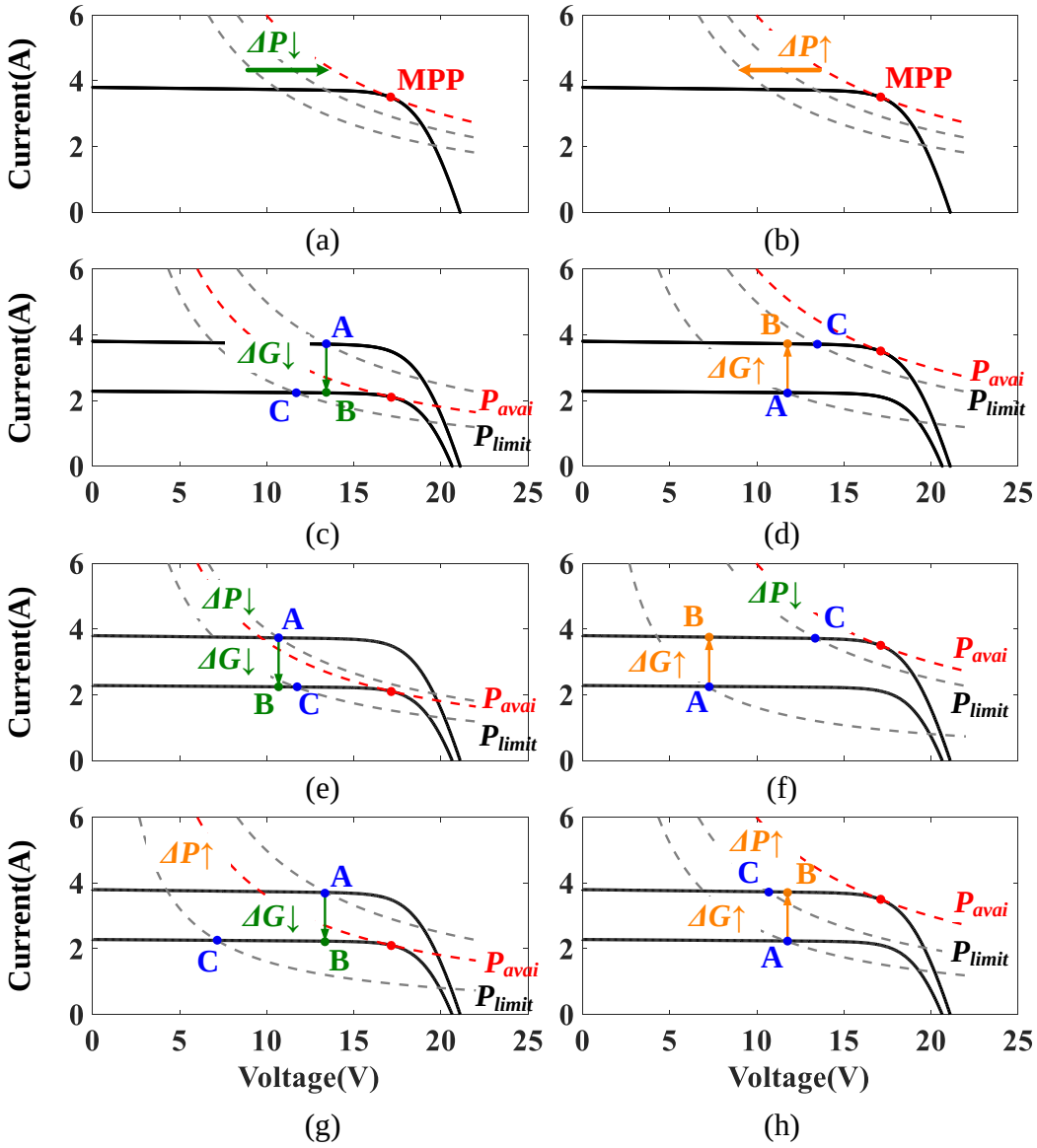

Fig. 5.15: Demonstration of grid frequency support scheme by the proposed method. (a) ΔP decreases; (b) ΔP increases; (c) ΔG decreases; (d) ΔG increases; (e) ΔP and ΔG decrease; (f) ΔP decreases and ΔG increases; (g) ΔP increases and ΔG decreases; (h) ΔP and ΔG increase.

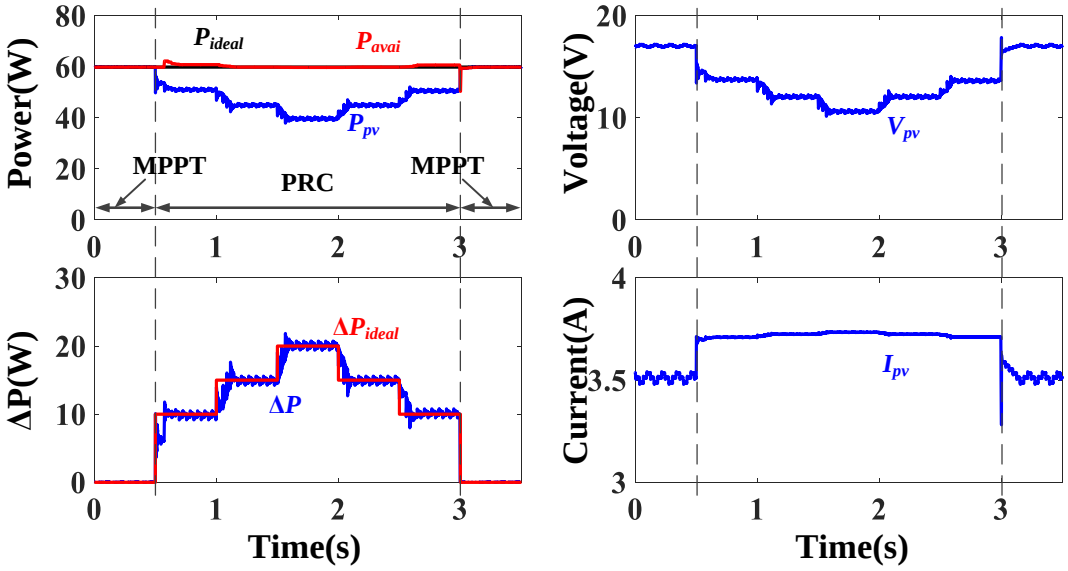

Fig. 5.16: Simulation results for the proposed control scheme when ΔP is changed.

Fig. 5.15 (e)-(h), whatever the changes in ΔP and ΔG are positive or negative, B is very close to C. Therefore, the proposed method just slightly perturbs the operating point with a small step size change obtained with the equation (5.10). Otherwise, considering that B is far away from C, a large step size change obtained from the equation (5.9) is used.

5.3 Simulation

In order to prove the effectiveness of the proposed control scheme, a boost converter is used, as shown in Fig. 5.12. The input capacitor, output capacitor, inductor and switching frequency for the boost converter are $470uF$, $47uF$, $1mH$ and $20kHz$, respectively. The output DC voltage is 24V. D_{min} and D_{max} are set as 0.5 and 2, respectively. $K_{I_{sc}}$ is set as 0.92 and m_{th} is set as -0.02. The perturbation time for the proposed method, T_p, is $0.03s$.

5.3.1 Reserved Power Command Change

Fig. 5.16 shows that simulation results for the proposed control scheme when ΔP is changed. P_{pv}, V_{pv} and I_{pv} refer to the PV output power, voltage and current, respectively. P_{avai} refers to the maximum available power estimated by the proposed control scheme and P_{ideal} refers to the ideal maximum power. ΔP refers to the power reserved by the proposed control scheme and ΔP_{ideal} refers to the power which should be reserved by the system.

Initially, the PV system works at the MPPT mode. At time 0.5s, the PRC is activated

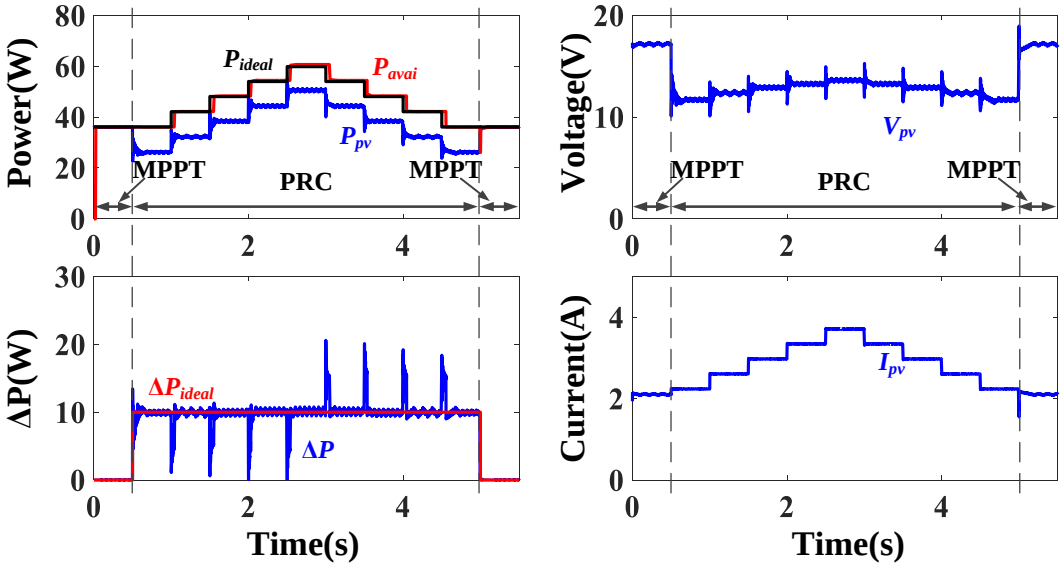

Fig. 5.17: Simulation results for the proposed control scheme when ΔG is changed.

and ΔP is set as 10W. After that, ΔP is changed in every 0.5s varying among 10W, 15W and 20W. Finally, the MPPT mode is activated at time 3s. During the whole simulation time, the solar irradiance maintains at 1000W/m^2.

As shown in Fig. 5.16, the proposed control scheme successfully tracks with the step changes of ΔP. The actual reserved power ΔP is just fitted to the profile of ΔP_{ideal}. Since the operating point is already in the CCR, P_{avai} can be directly obtained. To be more specific, it requires averagely 2 to 3 steps to response the step changes of ΔP. Therefore, the tracking speed is also very fast.

5.3.2 Solar Irradiance Change

Fig. 5.17 shows that simulation results for the proposed control scheme when ΔG is changed. ΔP is fixed at 10W during the whole simulation time, while the PRC mode is activated during the time 0.5s to 5s. The solar irradiance maintains at 600W/m^2 from 0s to 1s, and increases by 100W/m^2 in every 0.5s until it reaches 1000W/m^2. Then, the solar irradiance decreases by 100W/m^2 in every 0.5s until 600W/m^2. Finally, the solar irradiance maintains at 600W/m^2 again, from 4.5s to 5.5s.

As shown in Fig. 5.17, the proposed control scheme also successfully tracks when ΔG is changed. The proposed control scheme only needs 2 or 3 steps to reach the new P_{limit} when the solar irradiance changes. ΔP is just fitted to the profile of ΔP_{ideal} and ΔP almost maintains at 10W during the PRC mode.

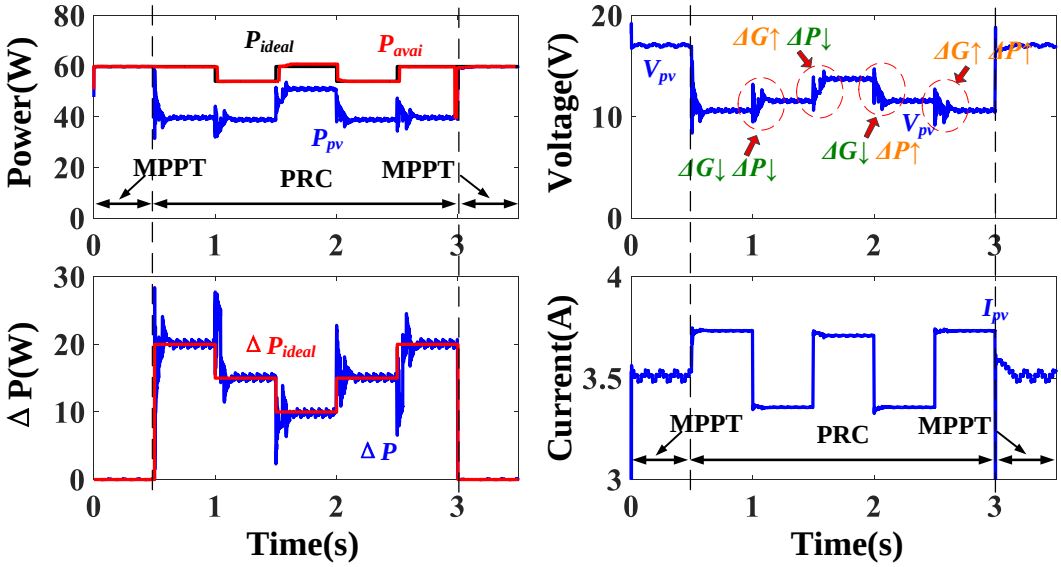

Fig. 5.18: Simulation results for the proposed control scheme when ΔP and ΔG are changed.

5.3.3 Both of Reserved Power Command and Solar Irradiance Change

Fig.5.17 shows that simulation results for the proposed control scheme when ΔP and ΔG are changed. The PRC mode is activated during the time 0.5s to 3s. The initial solar irradiance and ΔP are 1000W/m^2 and 20W, respectively. At time 1s, 1.5s, 2s and 2.5s, both of the solar irradiance and ΔP are changed as following trajectory:

- 1000W/m^2 $\rightarrow$ 900W/m^2 $\rightarrow$ 1000W/m^2 $\rightarrow$ 900W/m^2 $\rightarrow$ 1000W/m^2
- 20W $\rightarrow$ 15W $\rightarrow$ 10W $\rightarrow$ 15W $\rightarrow$ 20W

As shown in Fig. 5.17, the proposed control scheme also successfully tracks when ΔP and ΔG are changed. The proposed control scheme also needs 2 or 3 steps to reach the new P_{limit} and ΔP is just fitted to the profile of ΔP_{ideal}.

5.3.4 Comparison with the Other PRC Method

In order to highlight the advantages of the proposed method, the control scheme by A. Sangwongwanich [135] is used to make a comparison. Based on the operational principle in [135], the control scheme in [135] is well optimized. Same simulation setup as the proposed is used, the simulation results for the control scheme in [135] are shown in Fig. 5.19.

As description in [135], the fractional open-circuit voltage MPPT method is periodically used to measure P_{avai} rather to estimate it. As shown in Fig. 5.19, the operating

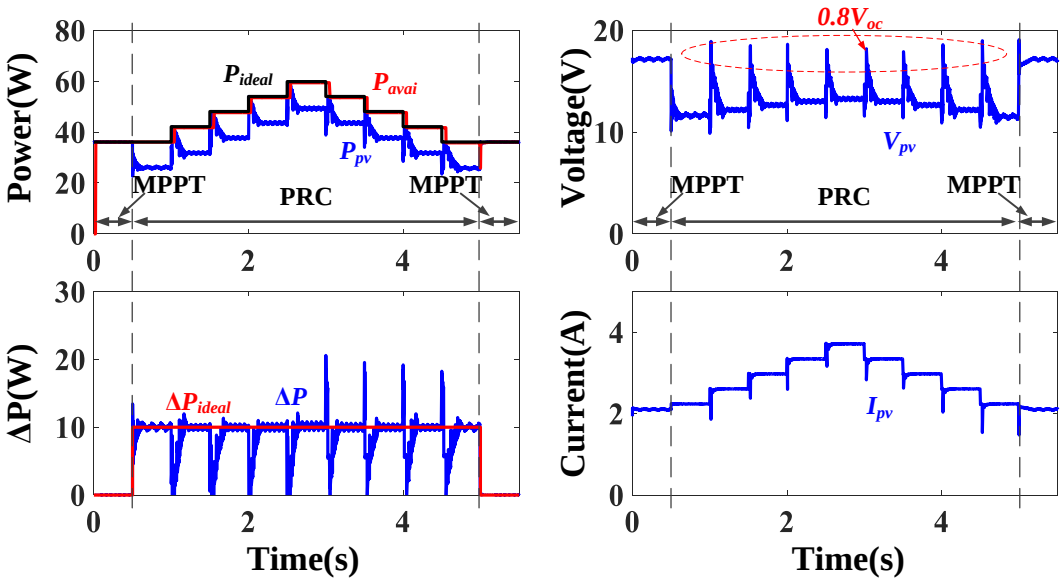

Fig. 5.19: Simulation results for the control scheme by A. Sangwongwanich when the solar irradiance is changed.

point directly moves to the position of $0.8V_{oc}$ when the solar irradiance changes. Once P_{avai} is measured, the operating point is gradually perturbed to P_{limit}. Power and voltage ripples during the changes of the solar irradiance can be clearly seen from Fig. 5.19.

In order to compare the performance of the proposed method and the control scheme in [135], the movements of the operating points and the corresponding operating trajectories by using these two methods are demonstrated in Fig. 5.20. Fig. 5.20 (a) illustrates the movements of the operating points by using the proposed method when the solar irradiance is increased. It can be seen that the operating point straightly goes up, marked as (1) in Fig. 5.20 (a). Since the operating point is already in the CCR, P_{avai} can be estimated at the optimal P_{limit}, marked as (2) in Fig. 5.20 (a). Compared to the proposed method, the control scheme in [135] has to move the position of $0.8V_{oc}$ to measure P_{avai} rather to estimate it. As a consequence, one more step as marked red text (2) in Fig. 5.20 (b) is needed. Furthermore, the movement to $0.8V_{oc}$ also causes several extra steps back to P_{limit}.

The operating trajectories by using the proposed method and the control scheme in [135] are also demonstrated in Fig. 5.20, where the red dots refer to the operating trajectory for the MPPT mode while the blue dots refer to that for the PRC mode. Unlike the control scheme in [135], the proposed control scheme only needs to work around the CCR to estimate P_{avai}. It is not necessary to sample the points around the MPP region. That is the reason why the proposed control will be regulated always operating at P_{limit}.

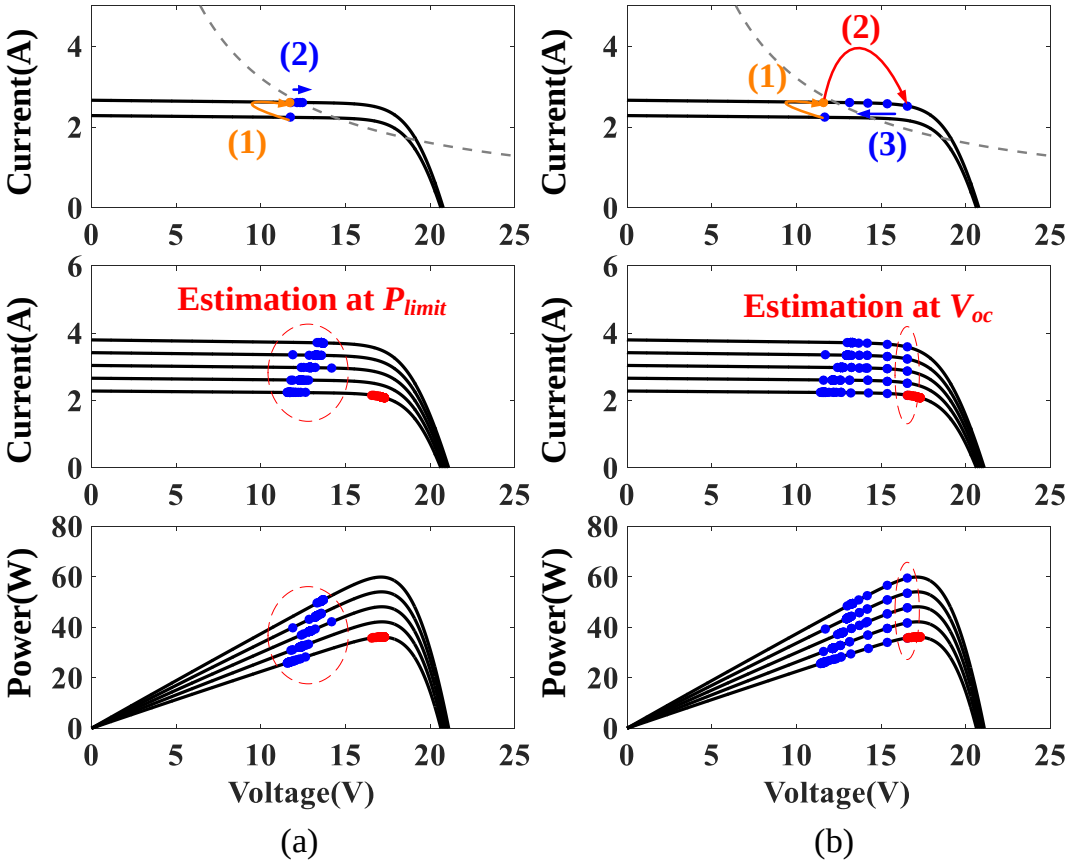

Fig. 5.20: Movements of the operating points and operating trajectory when the solar irradiance is increased. (a) Proposed method; (b) Method by A. Sangwongwanich [135].

5.4 Experimental results

In order to verify the effectiveness of the proposed PRC method, the experimental tests are carried out with the experimental prototypes shown in Fig. 5.21. Main specification of the main components are identical to the simulation. The PV emulator Chroma ATE-62050H-600S, which is a programmable DC supply, is used to emulate solar module characteristics. The dSPACE DS1104 is adopted as a control platform where the proposed PRC method is implemented in it. The electronic load, IT8514C+, is used and it works at the constant voltage (CV) mode The sampling time T_p for the proposed method in the experiments was set as $0.1s$.

Fig. 5.22 shows that experimental results for the proposed control scheme. A constant solar irradiance profile of $1000W/m^2$ is used to be evaluated. Three values of ΔP, namely 10W, 15W and 20W, are used to verify the effectiveness of the proposed method when ΔP changes. As shown in Fig. 5.22 (a), the proposed control scheme successfully tracks with the step changes of ΔP. The actual reserved power ΔP is just fitted to the profile of

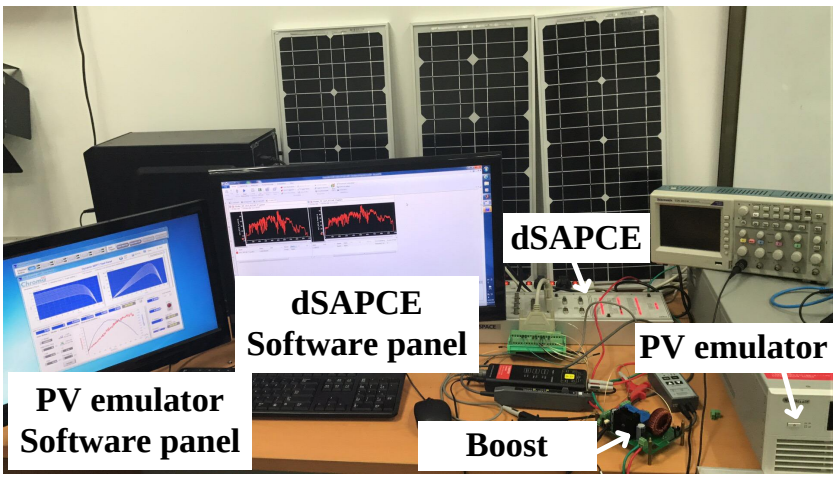

Fig. 5.21: Experimental setup of the simplified PV system with a boost converter.

ΔP_{ideal}.

Furthermore, the proposed method is also verified when the solar irradiance changes. Similar to the simulation, ΔP is fixed at 10W during the whole experiment time and the solar irradiance varies from $600W/m^2$ to $1000W/m^2$. As shown in Fig. 5.22 (b), the proposed control scheme also successfully tracks with the solar irradiance changes. The proposed control scheme only needs several steps to reach the new P_{limit} when the solar irradiance changes. ΔP is just fitted to the profile of ΔP_{ideal} and ΔP almost maintains at 10W during the PRC mode.

In order to further verify the effectiveness of the proposed method in real life, the real-field meteorological data are programmed in the PV emulator. The meteorological data of two distinct locations, namely University of Nevada, Las Vegas (UNLV) and Humboldt State University (HSU), California, are selected as shown in Fig. 5.23 (a) and Fig. 5.24 (a), respectively. It is noticeable that meteorological profiles in UNLV and HSU refer to a non-cloudy day and a cloudy day, respectively. Besides, the solar irradiation could vary dramatically in a daily day, however, the temperature just changes slightly.

It should be also noted that the original irradiance data is at 1 min resolution, which takes 7 to 8 hours to carry out the one experiment for one days data. In order to save the experimental time, the resolution of irradiance data has been updated as 2 seconds. Furthermore, a period of time (i.e, from 7:49:00 to 15:43:00 in UNLV and from 8:13:00 to 16:03:00 in HSU) is adopted to accelerate the experiment.

Fig. 5.23 (b) shows that the PRC mode with 10W reserved power is used in a clear day. It can be seen clearly that ΔP is just fitted to the profile of ΔP_{ideal} and the power reserve can be accurately controlled at 10W during the whole process. Besides, another test with the operational mode transition (i.e., MPPT→PRC→MPPT) is also verified in this clear day. As shown in Fig. 5.23 (c), it should be noted that the response time between the

MPPT mode and the PRC mode is also very quick and the power reserve can be accurately controlled at 10W during the PRC mode.

Fig.5.24 (b) and (c) show that the PRC mode with 10W and 20W reserved power and the operational mode transition is used in a cloudy day, respectively. It can be seen that the proposed method is also very effective under fast solar irradiance changing as well as operational mode changes. As a conclusion, these experimental results verify effectiveness of the proposed method under various weather conditions.

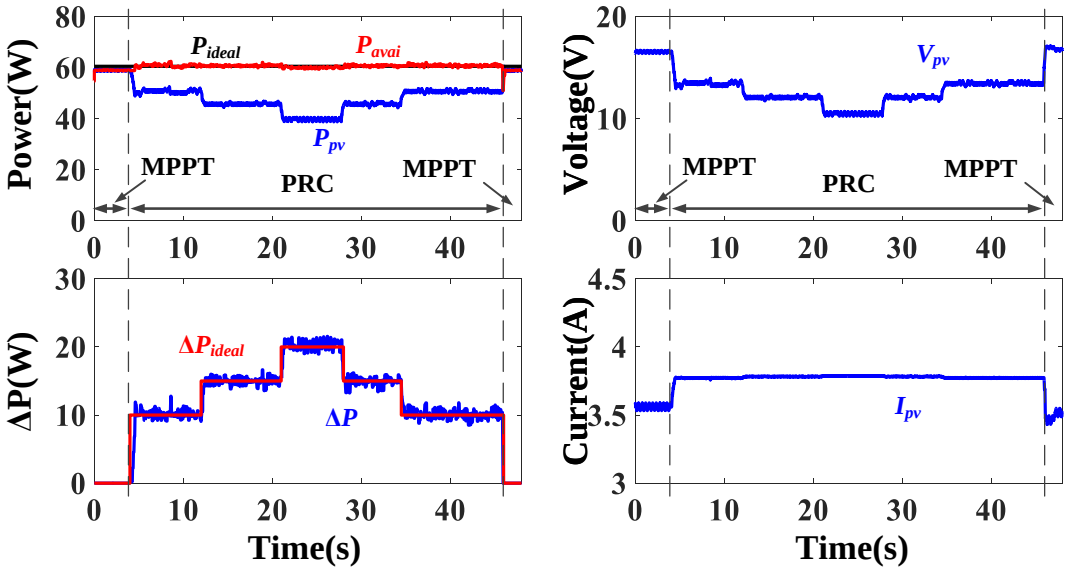

(a)

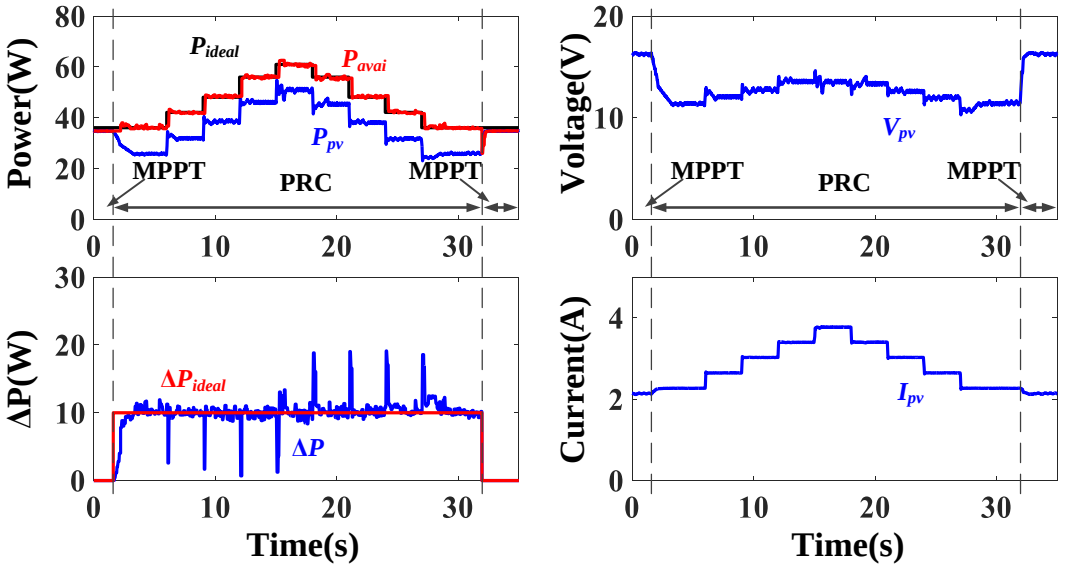

(b)

Fig. 5.22: Experimental results for the proposed control scheme. (a) ΔP is changed; (b) Solar irradiance is changed.

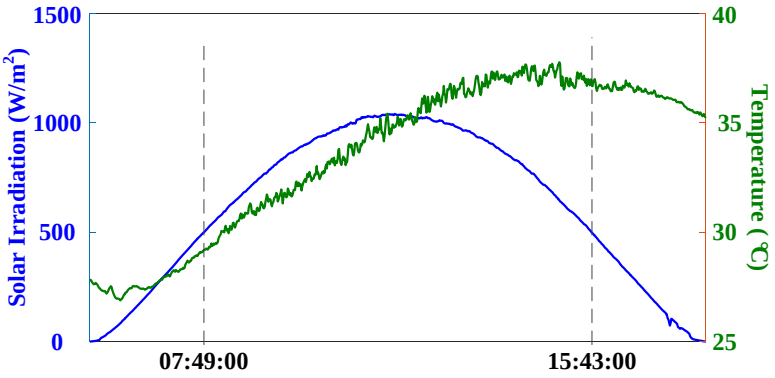

(a)

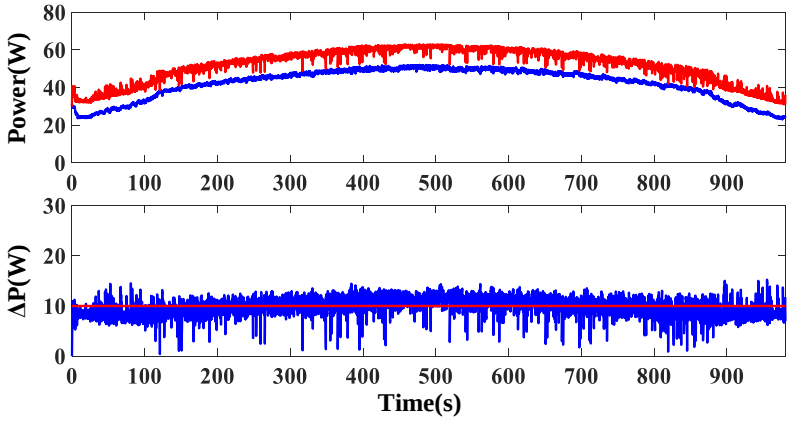

(b)

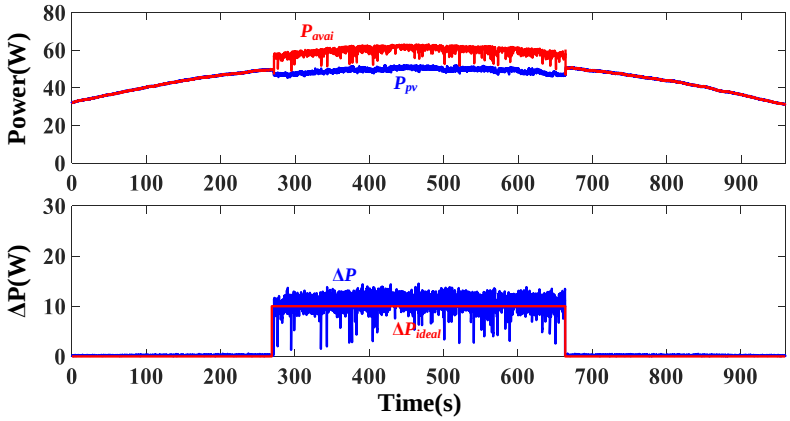

(c)

Fig. 5.23: Experimental results for the proposed control scheme under a clear day. (a) Solar irradiance and ambient temperature profiles in UNLV, Nevada, 24th Jul. 2015; (b) PRC mode with 10W reserved power is used in the whole process; (c) Both MPPT mode and RC mode with 10W reserved power are used.

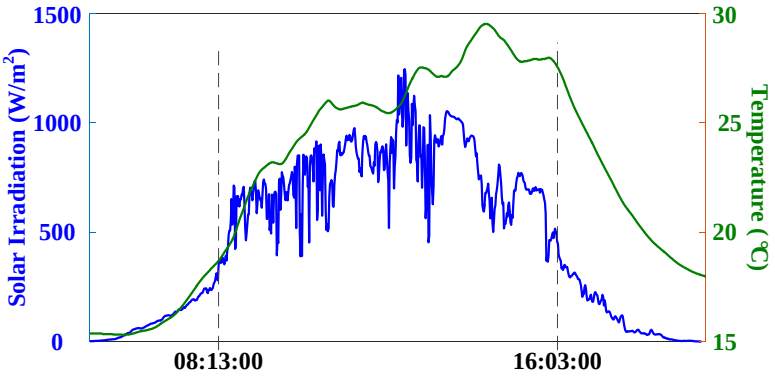

(a)

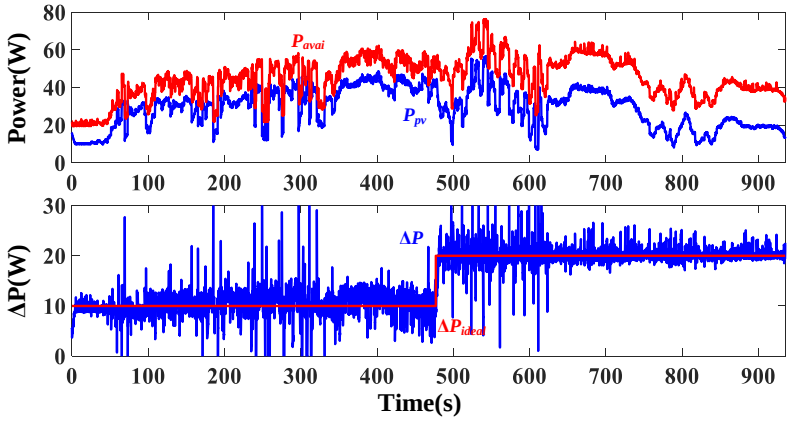

(b)

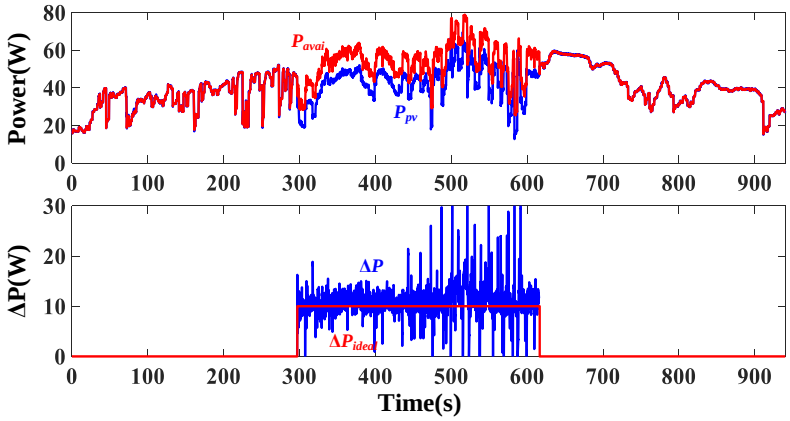

(c)

Fig. 5.24: Experimental results for the proposed control scheme under a cloudy day. (a) Solar irradiance and ambient temperature profiles in HSU, California, 31th Jul. 2015; (b) PRC mode with 10W and 20W reserved power are used; (c) Both MPPT mode and RC mode with 10W reserved power are used.

Chapter 6

Conclusions and Future Work

6.1 Conclusions

This thesis has investigated PV-side control for the PV system. The fast-converging speed MPPT method under the fast-changing weather conditions, the more accurate GMPPT method without failures and the more effective PRC method to estimate the MPP in the real time have been proposed. The improved performance by these proposed method has been validate by simulation and experiment. The applied algorithms are summarized as follows:

- The ASF-Beta method and the ZO-PO method are proposed to improve the MPPT dynamic and steady-state efficiency, respectively. The adaptive scaling factor is used by the proposed ASF-Beta method, which reduces the system dependency on the tuned parameters. Furthermore, the steady-state oscillations can be totally eliminated by the ZO-PO method. According to the simulation and experimental results, the dynamic and steady-state efficiency of the proposed method are approximately 95% and 99.8%, respectively, which are much higher than those of the conventional MPPT methods.

- The PV string equivalent model has been built up, thus, the I-V curve with multiple peaks can be equivalent represented as several I-V curves with single peak. Therefore, the GMPPT tracking for PV strings under various partial shading conditions is significantly simplified. Following this mathematical model, the conventional Beta method is modified to proposed a novel GMPPT method. Both simulation and experimental comparison of the proposed GMPPT method with other widely discussed algorithms are conducted for different PSC patterns. The overall dynamic tracking efficiency can reach average of 87% under different PSC patterns.

- The novel PRC method with simple real-time MPP estimation is proposed to overcome the drawbacks of the conventional PRC methods. Originated from the linear

characteristic of PV curves in the CCR and the Lambert-W function for voltage linear reference, P_{avai} is estimated separately in separate steps rather directly measured or estimated. The proposed PRC method does not require any additional hardware and cumbersome procedures of curve fitting with sophisticated operating points sampling by using the conventional PRC methods are also eliminated. The developed strategy exhibits fast speed and high robustness to estimate the MPP, and good compatibility with existing PV systems. Simulation and experimental results under various scenarios are provided to validate the effectiveness of the proposed strategy.

6.2 Future Work

6.2.1 GMPPT Method Based on Modified Voltage Lines

As pointed in Chapter 4, the 0.8Voc model is not always true, especially for long PV strings [102]. As shown in Fig. 6.1, some of the peaks are not really at the multiple of $0.8V_{oc}$. It may scan the wrong region of the P-V curve and lead to incorrect global peak detection [102]. As a consequence, the effectiveness of these methods may be affected.

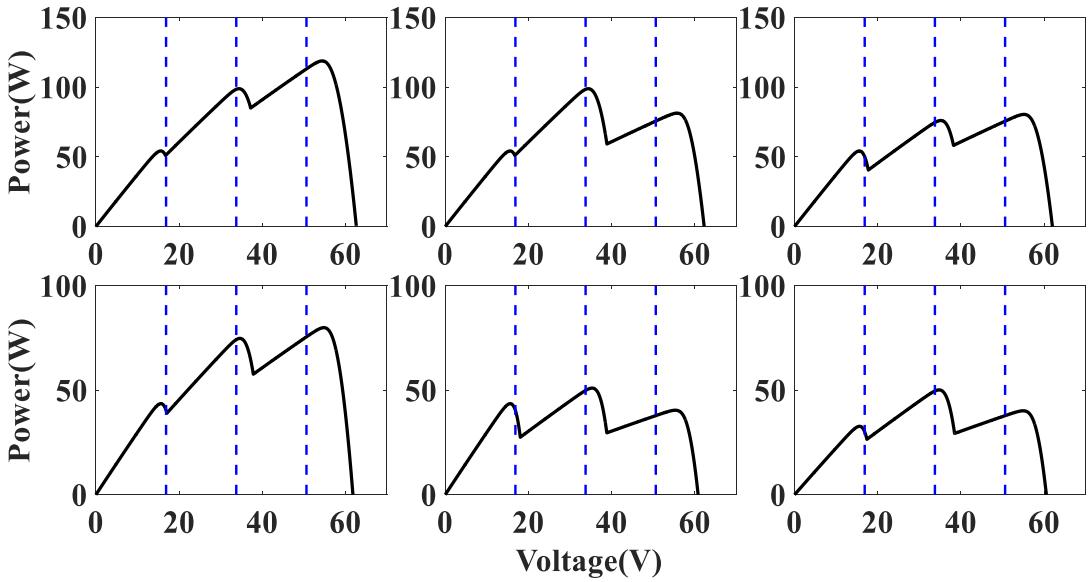

Fig. 6.1: Conventional voltage lines based on $0.8V_{oc}$ under the different PSC.

An explicit expression in (4.20), (4.21) and (4.22) can be used to obtain modified voltage lines, as demonstrated in Fig. 6.2. With the modified voltage lines, the locations of the multiple MPPs can be easily derived. Therefore, the adoption of this idea in proposing a new GMPPT method could be a promising work for the future

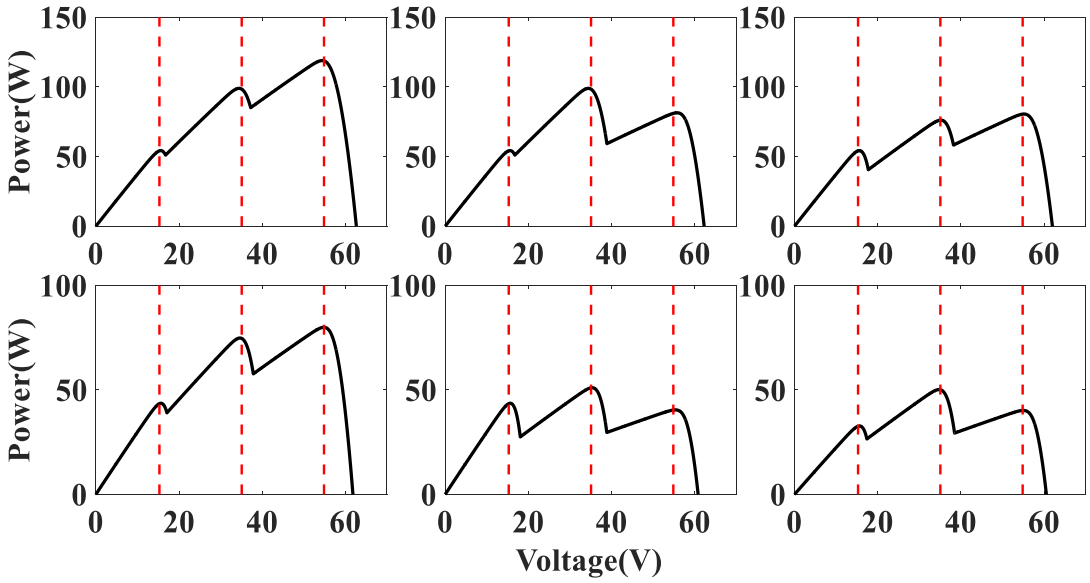

Fig. 6.2: Modified voltage lines based under the different PSC.

6.2.2 Distributed Maximum Power Point Tracking (DMPPT)

When the PV mismatch condition occur, power is partial lost, such as A2 area in Fig. 6.3; or some PV modules have to not work at their own MPP and the power in the area A1 has to be lost. Since the GMPPT techniques cannot efficiently solve this problem, distributed maximum power point tracking (DMPPT) architecture has been proposed.

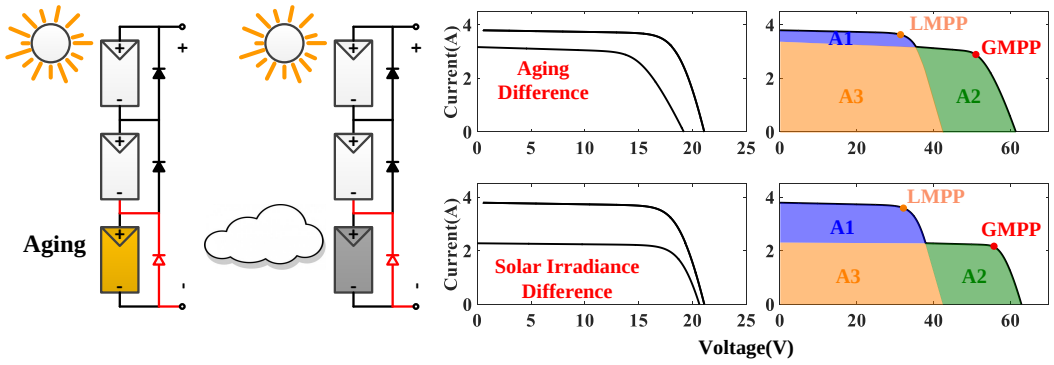

Fig. 6.3: Power loss caused by the PSC.

The DMPPT architectures can maintain high MPPT efficiency even under PV mismatching conditions because each PV module is individually controlled by an MPPT controller [146, 147]. Therefore, the PV mismatching problem caused by partial shadowing or PV aging can be radically solved. Generally, the DMPPT methods can be classified into two types as shown in Fig. 6.4 [146, 147]. As shown in Fig. 6.4(a), since the full power from PV modules has to be processed into DC-DC converters, it is called the full power processing (FPP). By contrast, only a fragment of power from PV modules need

to be processed through DC-DC converters, so it is called differential power processing (DPP).

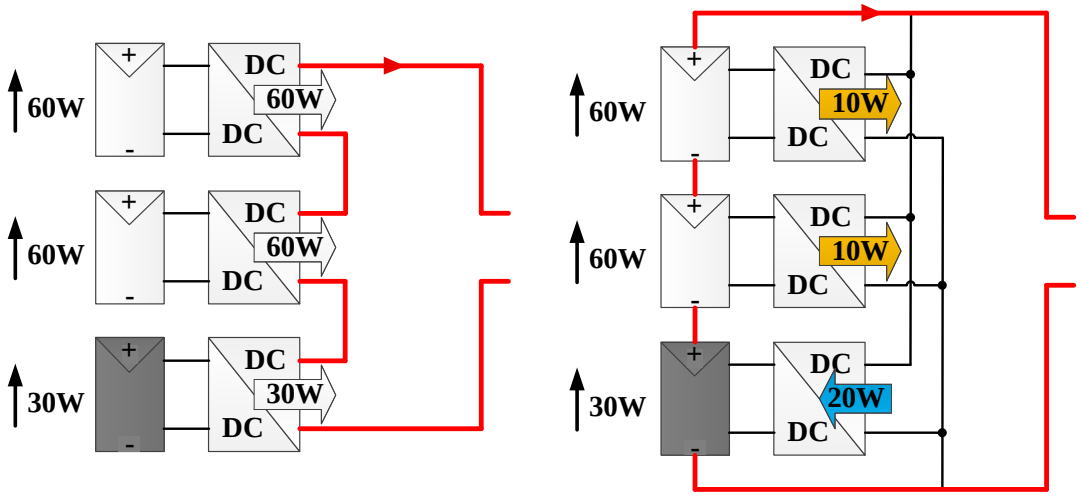

Fig. 6.4: Two architectures of the DMPPT: full power processing (FPP); differential power processing (DPP).

So far, both of the architectures have been proven as an effective way to solve PV modules mismatching, and both of them require to use MPPT controller for each DC-DC converters. Since conventional MPPT methods generally require both of current sensor and voltage sensor, the hardware implementation for both of the architectures is really high. Therefore, it is very necessary to proposed sensorless MPPT techniques to reduce the number of the required sensors.

Reference

[1] H. Ritchie and M. Roser, "Energy production & changing energy sources," https://ourworldindata.org/energy-production-and-changing-energy-sources, accessed Jul. 3, 2018.

[2] BP, "Bp energy outlook 2040 summary tables consumption," https://www.bp.com/en/global/corporate/energy-economics/energy-outlook/energy-outlook-downloads.html, released Feb. 2018.

[3] A. Shahsavari and M. Akbari, "Potential of solar energy in developing countries for reducing energy-related emissions," *Renew. Sust. Energy Rev.*, vol. 90, pp. 275–291, 2018.

[4] B. Wang, Q. Wang, Y. Wei, and Z. Li, "Role of renewable energy in chinas energy security and climate change mitigation: An index decomposition analysis," *Renew. Sust. Energy Rev.*, vol. 90, pp. 187–194, 2018.

[5] E. Lantz, R. Wiser, and M. Hand, "The past and future cost of wind energy," *National Renewable Energy Laboratory, Golden, CO, Report No. NREL/TP-6A20-53510*, 2012.

[6] F. Gotzens, H. Heinrichs, J.-F. Hake, and H.-J. Allelein, "The influence of continued reductions in renewable energy cost on the european electricity system," *Energy Strategy Rev.*, vol. 21, pp. 71 – 81, 2018.

[7] U. EIA, "Levelized cost and levelized avoided cost of new generation resources in the annual energy outlook 2018," https://www.eia.gov/outlooks/aeo/pdf/electricity_generation.pdf, released Mar. 2018.

[8] EPIA, "Global market outlook 2018-2022," http://solarpowereurope.org/reports/global-market-outlook-2018/?L=994, released Jul. 2018.

[9] F. fei Yang and X. gang Zhao, "Policies and economic efficiency of china's distributed photovoltaic and energy storage industry," *Energy*, vol. 154, pp. 221 – 230, 2018.

[10] X. Li, H. Wen, L. Jiang, W. Xiao, Y. Du, and C. Zhao, "An improved mppt method for pv system with fast-converging speed and zero oscillation," *IEEE Trans. Ind. Appl.*, vol. 52, no. 6, pp. 5051–5064, Nov. 2016.

[11] M. Dreidy, H. Mokhlis, and S. Mekhilef, "Inertia response and frequency control techniques for renewable energy sources: A review," *Renew. Sust. Energy Rev.*, vol. 69, pp. 144–155, 2017.

[12] Y. Yang and F. Blaabjerg, "Overview of single-phase grid-connected photovoltaic systems," *Electr. Pow. Compo. Sys.*, vol. 43, no. 12, pp. 1352–1363, 2015.

[13] F. Blaabjerg, R. Teodorescu, M. Liserre, and A. V. Timbus, "Overview of control and grid synchronization for distributed power generation systems," *IEEE Trans. Ind. Electron.*, vol. 53, no. 5, pp. 1398–1409, Oct. 2006.

[14] R. A. Mastromauro, M. Liserre, and A. Dell'Aquila, "Control issues in single-stage photovoltaic systems: Mppt, current and voltage control," *IEEE Trans. Ind. Inform.*, vol. 8, no. 2, pp. 241–254, May 2012.

[15] T. Esram and P. Chapman, "Comparison of photovoltaic array maximum power point tracking techniques," *IEEE Trans. Energy Convers.*, vol. 22, no. 2, pp. 439–449, Jun. 2007.

[16] B. Subudhi and R. Pradhan, "A comparative study on maximum power point tracking techniques for photovoltaic power systems," *IEEE Trans. Sustain. Energy*, vol. 4, no. 1, pp. 89–98, Jan. 2013.

[17] NREL, "Irradiance and meteorological data [online]," http://www.nrel.gov/midc/.

[18] J. Bai, Y. Cao, Y. Hao, Z. Zhang, S. Liu, and F. Cao, "Characteristic output of pv systems under partial shading or mismatch conditions," *Sol. Energy*, vol. 112, pp. 41–54, 2015.

[19] A. Bidram, A. Davoudi, and R. S. Balog, "Control and circuit techniques to mitigate partial shading effects in photovoltaic arrays," *IEEE J. Photovoltaics*, vol. 2, no. 4, pp. 532–546, Oct. 2012.

[20] S. Kouro, J. I. Leon, D. Vinnikov, and L. G. Franquelo, "Grid-connected photovoltaic systems: An overview of recent research and emerging pv converter technology," *IEEE Ind. Electron. Mag.*, vol. 9, no. 1, pp. 47–61, Mar. 2015.

[21] S. I. Nanou, A. G. Papakonstantinou, and S. A. Papathanassiou, "A generic model of two-stage grid-connected pv systems with primary frequency response and inertia emulation," *Electr. Pow. Syst. Res.*, vol. 127, pp. 186–196, 2015.

[22] Y. Yang, E. Koutroulis, A. Sangwongwanich, and F. Blaabjerg, "Pursuing photovoltaic cost-effectiveness: Absolute active power control offers hope in single-phase pv systems," *IEEE Ind. Appl. Mag.*, vol. 23, no. 5, pp. 40–49, Sep. 2017.

[23] N. Femia, G. Petrone, G. Spagnuolo, and M. Vitelli, *Power electronics and control techniques for maximum energy harvesting in photovoltaic systems*. CRC press, 2012.

[24] W. Xiao, *Photovoltaic Power System: Modeling, Design, and Control*. John Wiley & Sons, 2017.

[25] M. Villalva, J. Gazoli, and E. Filho, "Comprehensive approach to modeling and simulation of photovoltaic arrays," *IEEE Trans. Power Electron.*, vol. 24, no. 5, pp. 1198–1208, May 2009.

[26] S. Shongwe and M. Hanif, "Comparative analysis of different single-diode pv modeling methods," *IEEE J. Photovoltaics*, vol. 5, no. 3, pp. 938–946, May 2015.

[27] M. C. D. Piazza, M. Luna, G. Petrone, and G. Spagnuolo, "Translation of the single-diode pv model parameters identified by using explicit formulas," *IEEE J. Photovoltaics*, vol. 7, no. 4, pp. 1009–1016, Jul. 2017.

[28] R. Teodorescu, M. Liserre, and P. Rodriguez, *Grid converters for photovoltaic and wind power systems*. John Wiley & Sons, 2011, vol. 29.

[29] N. Karami, N. Moubayed, and R. Outbib, "General review and classification of different mppt techniques," *Renew. Sust. Energy Rev.*, vol. 68, pp. 1–18, 2017.

[30] L. V. Hartmann, M. A. Vitorino, M. B. d. R. Correa, and A. M. N. Lima, "Combining model-based and heuristic techniques for fast tracking the maximum-power point of photovoltaic systems," *IEEE Trans. Power Electron.*, vol. 28, no. 6, pp. 2875–2885, Jun. 2013.

[31] Y. Mahmoud, M. Abdelwahed, and E. F. El-Saadany, "An enhanced mppt method combining model-based and heuristic techniques," *IEEE Trans. Sustain. Energy*, vol. 7, no. 2, pp. 576–585, Apr. 2016.

[32] L. Cristaldi, M. Faifer, M. Rossi, and S. Toscani, "An improved model-based maximum power point tracker for photovoltaic panels," *IEEE Trans. Instrum. Meas.*, vol. 63, no. 1, pp. 63–71, Jan. 2014.

[33] E. Bianconi, J. Calvente, R. Giral, E. Mamarelis, G. Petrone, C. A. Ramos-Paja, G. Spagnuolo, and M. Vitelli, "A fast current-based mppt technique employing sliding mode control," *IEEE Trans. Ind. Electron.*, vol. 60, no. 3, pp. 1168–1178, Mar. 2013.

[34] Y. Hu, W. Cao, J. Wu, B. Ji, and D. Holliday, "Thermography-based virtual mppt scheme for improving pv energy efficiency under partial shading conditions," *IEEE Trans. Power Electron.*, vol. 29, no. 11, pp. 5667–5672, Nov. 2014.

[35] N. Femia, G. Petrone, G. Spagnuolo, and M. Vitelli, "Optimization of perturb and observe maximum power point tracking method," *IEEE Trans. Power Electron.*, vol. 20, no. 4, pp. 963–973, Jul. 2005.

[36] M. A. Elgendy, B. Zahawi, and D. J. Atkinson, "Assessment of perturb and observe mppt algorithm implementation techniques for pv pumping applications," *IEEE Trans. Sustain. Energy*, vol. 3, no. 1, pp. 21–33, Jan. 2012.

[37] M. Elgendy, B. Zahawi, and D. Atkinson, "Operating characteristics of the p&o algorithm at high perturbation frequencies for standalone pv systems," *IEEE Trans. Energy Convers.*, vol. 30, no. 1, pp. 189–198, Mar. 2015.

[38] A. Safari and S. Mekhilef, "Simulation and hardware implementation of incremental conductance mppt with direct control method using cuk converter," *IEEE Trans. Ind. Electron*, vol. 58, no. 4, pp. 1154–1161, Apr. 2011.

[39] M. A. Elgendy, B. Zahawi, and D. J. Atkinson, "Assessment of the incremental conductance maximum power point tracking algorithm," *IEEE Trans. Sustain. Energy*, vol. 4, no. 1, pp. 108–117, Jan. 2013.

[40] X. Li and H. Wen, "Evaluation of different maximum power point tracking techniques by using en 50530 dynamic test standard," in *2016 IEEE International Conference on Power Electronics, Drives and Energy Systems (PEDES)*, Dec. 2016, pp. 1–6.

[41] X. Li, H. Wen, and Y. Hu, "Evaluation of different maximum power point tracking (mppt) techniques based on practical meteorological data," in *2016 IEEE International Conference on Renewable Energy Research and Applications (ICRERA)*, Nov. 2016, pp. 696–701.

[42] D. Sera, R. Teodorescu, J. Hantschel, and M. Knoll, "Optimized maximum power point tracker for fast-changing environmental conditions," *IEEE Trans. Ind. Electron*, vol. 55, no. 7, pp. 2629–2637, Jul. 2008.

[43] T. K. Soon and S. Mekhilef, "Modified incremental conductance mppt algorithm to mitigate inaccurate responses under fast-changing solar irradiation level," *Sol. Energy*, vol. 101, no. 0, pp. 333–342, 2014.

[44] M. Killi and S. Samanta, "Modified perturb and observe mppt algorithm for drift avoidance in photovoltaic systems," *IEEE Trans. Ind. Electron*, vol. 62, no. 9, pp. 5549–5559, Sep. 2015.

[45] F. Liu, S. Duan, F. Liu, B. Liu, and Y. Kang, "A variable step size inc mppt method for pv systems," *IEEE Trans. Ind. Electron*, vol. 55, no. 7, pp. 2622–2628, Jul. 2008.

[46] A. Pandey, N. Dasgupta, and A. Mukerjee, "High-performance algorithms for drift avoidance and fast tracking in solar mppt system," *IEEE Trans. Energy Convers.*, vol. 23, no. 2, pp. 681–689, Jun. 2008.

[47] F. Zhang, K. Thanapalan, A. Procter, S. Carr, and J. Maddy, "Adaptive hybrid maximum power point tracking method for a photovoltaic system," *IEEE Trans. Energy Convers.*, vol. 28, no. 2, pp. 353–360, Jun. 2013.

[48] A. Ahmed, R. Li, M. Sol, and P. Joung-hu, "A fast pv power tracking control algorithm with reduced power mode," *IEEE Trans. Energy Convers.*, vol. 28, no. 3, pp. 565–575, Sep. 2013.

[49] Q. Mei, M. Shan, L. Liu, and J. Guerrero, "A novel improved variable step-size incremental-resistance mppt method for pv systems," *IEEE Trans. Ind. Electron*, vol. 58, no. 6, pp. 2427–2434, Jun. 2011.

[50] W. Xiao and W. Dunford, "A modified adaptive hill climbing mppt method for photovoltaic power systems," in *Proc. 2004 IEEE 35th Annu. Power Electron. Spec. Conf.*, vol. 3, Jun. 2004, pp. 1957–1963 Vol.3.

[51] Y.-T. Chen, Z.-H. Lai, and R.-H. Liang, "A novel auto-scaling variable step-size mppt method for a pv system," *Sol. Energy*, vol. 102, pp. 247–256, 2014.

[52] N. Femia, D. Granozio, G. Petrone, G. Spagnuolo, and M. Vitelli, "Predictive & adaptive mppt perturb and observe method," *IEEE Trans. Aero. Elec. Sys.*, vol. 43, no. 3, pp. 934–950, Jul. 2007.

[53] P. Fu-Sheng and C. Ru-Min, "A new algorithm to photovoltaic power point tracking problems with quadratic maximization," *IEEE Trans. Energy Convers.*, vol. 25, no. 1, pp. 262–264, Mar. 2010.

[54] P. Fu-Sheng, C. Ru-Min, K. Shin Hong, and L. Tai-Sheng, "Performance evaluation of parabolic prediction to maximum power point tracking for pv array," *IEEE Trans. Sustain. Energy*, vol. 2, no. 1, pp. 60–68, Jan. 2011.

[55] A. Messai, A. Mellit, A. Massi Pavan, A. Guessoum, and H. Mekki, "Fpga-based implementation of a fuzzy controller (mppt) for photovoltaic module," *Energy Convers. Manage.*, vol. 52, no. 7, pp. 2695–2704, 2011.

[56] A. El Khateb, N. Abd Rahim, J. Selvaraj, and M. Uddin, "Fuzzy-logic-controller-based sepic converter for maximum power point tracking," *IEEE Trans. Ind. Appl.*, vol. 50, no. 4, pp. 2349–2358, Jul. 2014.

[57] B. Alajmi, K. H. Ahmed, S. J. Finney, and B. W. Williams, "Fuzzy-logic-control approach of a modified hill-climbing method for maximum power point in microgrid standalone photovoltaic system," *IEEE Trans. Power Electron.*, vol. 26, no. 4, pp. 1022–1030, Apr. 2011.

[58] A. Al Nabulsi and R. Dhaouadi, "Efficiency optimization of a dsp-based standalone pv system using fuzzy logic and dual-mppt control," *IEEE Trans. Ind. Informat.*, vol. 8, no. 3, pp. 573–584, Aug. 2012.

[59] M. A. Masoum, H. Dehbonei, and E. F. Fuchs, "Theoretical and experimental analyses of photovoltaic systems with voltage and current-based maximum power-point tracking," *IEEE Trans. Energy Convers.*, vol. 17, no. 4, pp. 514–522, Dec. 2002.

[60] T. Noguchi, S. Togashi, and R. Nakamoto, "Short current pulse based maximum power point tracking method for multiple photovoltaic-and-converter module system," *IEEE Trans. Ind. Electron.*, vol. 49, no. 1, pp. 217–223, Feb. 2002.

[61] J. H. Teng, W. H. Huang, T. A. Hsu, and C. Y. Wang, "Novel and fast maximum power point tracking for photovoltaic generation," *IEEE Trans. Ind. Electron.*, vol. 63, no. 8, pp. 4955–4966, Aug. 2016.

[62] J. M. Blanes, F. J. Toledo, S. Montero, and A. Garrigs, "In-site real-time photovoltaic i-v curves and maximum power point estimator," *IEEE Trans. Power Electron.*, vol. 28, no. 3, pp. 1234–1240, Mar. 2013.

[63] M. J. Z. Zadeh and S. H. Fathi, "A new approach for photovoltaic arrays modeling and maximum power point estimation in real operating conditions," *IEEE Trans. Ind. Electron.*, vol. 64, no. 12, pp. 9334–9343, Dec. 2017.

[64] M. Sokolov and D. Shmilovitz, "A modified mppt scheme for accelerated convergence," *IEEE Trans. Energy Convers.*, vol. 23, no. 4, pp. 1105–1107, Dec. 2008.

[65] V. V. R. Scarpa, S. Buso, and G. Spiazzi, "Low-complexity mppt technique exploiting the pv module mpp locus characterization," *IEEE Trans. Ind. Electron*, vol. 56, no. 5, pp. 1531–1538, May. 2009.

[66] T. K. Soon and S. Mekhilef, "A fast-converging mppt technique for photovoltaic system under fast-varying solar irradiation and load resistance," *IEEE Trans. Ind. Informat.*, vol. 11, no. 1, pp. 176–186, Feb. 2015.

[67] Y.-H. Liu and J.-W. Huang, "A fast and low cost analog maximum power point tracking method for low power photovoltaic systems," *Sol. Energy*, vol. 85, no. 11, pp. 2771–2780, 2011.

[68] S. Jain and V. Agarwal, "A new algorithm for rapid tracking of approximate maximum power point in photovoltaic systems," *IEEE Power Electron. Lett.*, vol. 2, no. 1, pp. 16–19, Mar. 2004.

[69] M. de Brito, L. Galotto, L. Sampaio, G. de Azevedo e Melo, and C. Canesin, "Evaluation of the main mppt techniques for photovoltaic applications," *IEEE Trans. Ind. Electron*, vol. 60, no. 3, pp. 1156–1167, Mar. 2013.

[70] S. Jain and V. Agarwal, "Comparison of the performance of maximum power point tracking schemes applied to single-stage grid-connected photovoltaic systems," *IET Electr. Power Appl.*, vol. 1, no. 5, pp. 753–762, Sep. 2007.

[71] X. Li, H. Wen, L. Jiang, Y. Hu, and C. Zhao, "An improved beta method with autoscaling factor for photovoltaic system," *IEEE Trans. Ind. Appl.*, vol. 52, no. 5, pp. 4281–4291, Sep. 2016.

[72] X. Li, H. Wen, L. Jiang, W. Xiao, Y. Du, and C. Zhao, "An improved mppt method for pv system with fast-converging speed and zero oscillation," *IEEE Trans. Ind. Appl.*, vol. 52, no. 6, pp. 5051–5064, Nov. 2016.

[73] W. Xiao, H. H. Zeineldin, and Z. Peng, "Statistic and parallel testing procedure for evaluating maximum power point tracking algorithms of photovoltaic power systems," *IEEE J. Photovoltaics*, vol. 3, no. 3, pp. 1062–1069, Jul. 2013.

[74] H. Yohan, S. N. Pham, Y. Taegeun, C. Kookbyung, B. Kwang-Hyun, and K. Yong Sin, "Efficient maximum power point tracking for a distributed pv system under rapidly changing environmental conditions," *IEEE Trans. Power Electron.*, vol. 30, no. 8, pp. 4209–4218, Aug. 2015.

[75] F. Paz and M. Ordonez, "Zero oscillation and irradiance slope tracking for photovoltaic mppt," *IEEE Trans. Ind. Electron*, vol. 61, no. 11, pp. 6138–6147, Nov. 2014.

[76] Y.-H. Liu, J.-H. Chen, and J.-W. Huang, "A review of maximum power point tracking techniques for use in partially shaded conditions," *Renew. Sust. Energ. Rev.*, vol. 41, pp. 436–453, 2015.

[77] T. L. Nguyen and K. S. Low, "A global maximum power point tracking scheme employing direct search algorithm for photovoltaic systems," *IEEE Trans. Ind. Electron*, vol. 57, no. 10, pp. 3456–3467, Oct. 2010.

[78] N. A. Ahmed and M. Miyatake, "A novel maximum power point tracking for photovoltaic applications under partially shaded insolation conditions," *Electr. Pow. Syst. Res.*, vol. 78, no. 5, pp. 777–784, 2008.

[79] R. Ramaprabha, M. Balaji, and B. Mathur, "Maximum power point tracking of partially shaded solar pv system using modified fibonacci search method with fuzzy controller," *Int. J. Elec. Power Energ. Sys.*, vol. 43, no. 1, pp. 754 – 765, 2012.

[80] E. Koutroulis and F. Blaabjerg, "A new technique for tracking the global maximum power point of pv arrays operating under partial-shading conditions," *IEEE J. Photovoltaics*, vol. 2, no. 2, pp. 184–190, Apr. 2012.

[81] X. Li, H. Wen, G. Chu, Y. Hu, and L. Jiang, "A novel power-increment based gmppt algorithm for pv arrays under partial shading conditions," *Sol. Energy*, vol. 169, pp. 353 – 361, 2018.

[82] M. Miyatake, M. Veerachary, F. Toriumi, N. Fujii, and H. Ko, "Maximum power point tracking of multiple photovoltaic arrays: A pso approach," *IEEE Trans. Aero. Elec. Sys.*, vol. 47, no. 1, pp. 367–380, Jan. 2011.

[83] Y. H. Liu, S. C. Huang, J. W. Huang, and W. C. Liang, "A particle swarm optimization-based maximum power point tracking algorithm for pv systems operating under partially shaded conditions," *IEEE Trans. Energy Convers.*, vol. 27, no. 4, pp. 1027–1035, Dec. 2012.

[84] K. Ishaque, Z. Salam, M. Amjad, and S. Mekhilef, "An improved particle swarm optimization (pso) based mppt for pv with reduced steady-state oscillation," *IEEE Trans. Power Electron.*, vol. 27, no. 8, pp. 3627–3638, Aug. 2012.

[85] K. Ishaque and Z. Salam, "A deterministic particle swarm optimization maximum power point tracker for photovoltaic system under partial shading condition," *IEEE Trans. Ind. Electron*, vol. 60, no. 8, pp. 3195–3206, Aug. 2013.

[86] K. L. Lian, J. H. Jhang, and I. S. Tian, "A maximum power point tracking method based on perturb-and-observe combined with particle swarm optimization," *IEEE Trans. Ind. Electron*, vol. 4, no. 2, pp. 626–633, Mar. 2014.

[87] M. Seyedmahmoudian, R. Rahmani, S. Mekhilef, A. M. T. Oo, A. Stojcevski, T. K. Soon, and A. S. Ghandhari, "Simulation and hardware implementation of new maximum power point tracking technique for partially shaded pv system using hybrid depso method," *IEEE Trans. Sustain. Energy*, vol. 6, no. 3, pp. 850–862, Jul. 2015.

[88] C. Manickam, G. R. Raman, G. P. Raman, S. I. Ganesan, and C. Nagamani, "A hybrid algorithm for tracking of gmpp based on p o and pso with reduced power oscillation in string inverters," *IEEE Trans. Ind. Electron*, vol. 63, no. 10, pp. 6097–6106, Oct. 2016.

[89] B. N. Alajmi, K. H. Ahmed, S. J. Finney, and B. W. Williams, "A maximum power point tracking technique for partially shaded photovoltaic systems in microgrids," *IEEE Trans. Ind. Electron*, vol. 60, no. 4, pp. 1596–1606, Apr. 2013.

[90] K. Sundareswaran, S. Peddapati, and S. Palani, "Mppt of pv systems under partial shaded conditions through a colony of flashing fireflies," *IEEE Trans. Energy Convers.*, vol. 29, no. 2, pp. 463–472, Jun. 2014.

[91] K. Sundareswaran, P. Sankar, P. S. R. Nayak, S. P. Simon, and S. Palani, "Enhanced energy output from a pv system under partial shaded conditions through artificial bee colony," *IEEE Trans. Sustain. Energy*, vol. 6, no. 1, pp. 198–209, Jan. 2015.

[92] S. Mohanty, B. Subudhi, and P. K. Ray, "A new mppt design using grey wolf optimization technique for photovoltaic system under partial shading conditions," *IEEE Trans. Sustain. Energy*, vol. 7, no. 1, pp. 181–188, Jan. 2016.

[93] S. Lyden and M. E. Haque, "A simulated annealing global maximum power point tracking approach for pv modules under partial shading conditions," *IEEE Trans. Power Electron.*, vol. 31, no. 6, pp. 4171–4181, Jun. 2016.

[94] K. Sundareswaran, V. Vigneshkumar, P. Sankar, S. P. Simon, P. S. R. Nayak, and S. Palani, "Development of an improved p&o algorithm assisted through a colony of foraging ants for mppt in pv system," *IEEE Trans. Ind. Informat.*, vol. 12, no. 1, pp. 187–200, Feb. 2016.

[95] G. Carannante, C. Fraddanno, M. Pagano, and L. Piegari, "Experimental performance of mppt algorithm for photovoltaic sources subject to inhomogeneous insolation," *IEEE Trans. Ind. Electron*, vol. 56, no. 11, pp. 4374–4380, Nov. 2009.

[96] Y. H. Ji, D. Y. Jung, J. G. Kim, J. H. Kim, T. W. Lee, and C. Y. Won, "A real maximum power point tracking method for mismatching compensation in pv array under partially shaded conditions," *IEEE Trans. Power Electron.*, vol. 26, no. 4, pp. 1001–1009, Apr. 2011.

[97] H. Patel and V. Agarwal, "Maximum power point tracking scheme for pv systems operating under partially shaded conditions," *IEEE Trans. Ind. Electron*, vol. 55, no. 4, pp. 1689–1698, Apr. 2008.

[98] K. S. Tey and S. Mekhilef, "Modified incremental conductance algorithm for photovoltaic system under partial shading conditions and load variation," *IEEE Trans. Ind. Electron*, vol. 61, no. 10, pp. 5384–5392, Oct. 2014.

[99] K. Chen, S. Tian, Y. Cheng, and L. Bai, "An improved mppt controller for photovoltaic system under partial shading condition," *IEEE Trans. Sustain. Energy*, vol. 5, no. 3, pp. 978–985, Jul. 2014.

[100] Y. Wang, Y. Li, and X. Ruan, "High-accuracy and fast-speed mppt methods for pv string under partially shaded conditions," *IEEE Trans. Ind. Electron*, vol. 63, no. 1, pp. 235–245, Jan. 2016.

[101] D. R. Jones, C. D. Perttunen, and B. E. Stuckman, "Lipschitzian optimization without the lipschitz constant," *J. Optim. Theory Appl.*, vol. 79, no. 1, pp. 157–181, 1993.

[102] J. Ahmed and Z. Salam, "An improved method to predict the position of maximum power point during partial shading for pv arrays," *IEEE Trans. Ind. Informat.*, vol. 11, no. 6, pp. 1378–1387, Dec. 2015.

[103] E. I. Batzelis, G. E. Kampitsis, S. A. Papathanassiou, and S. N. Manias, "Direct mpp calculation in terms of the single-diode pv model parameters," *IEEE Trans. Energy Convers.*, vol. 30, no. 1, pp. 226–236, Mar. 2015.

[104] E. I. Batzelis, I. A. Routsolias, and S. A. Papathanassiou, "An explicit pv string model based on the lambert w function and simplified mpp expressions for operation under partial shading," *IEEE Trans. Sustain. Energy*, vol. 5, no. 1, pp. 301–312, Jan. 2014.

[105] Y. Liu, S. You, J. Tan, Y. Zhang, and Y. Liu, "Frequency response assessment and enhancement of the u.s. power grids toward extra-high photovoltaic generation penetrations-an industry perspective," *IEEE Trans. Power Syst.*, vol. 33, no. 3, pp. 3438–3449, May 2018.

[106] S. Eftekharnejad, V. Vittal, G. T. Heydt, B. Keel, and J. Loehr, "Impact of increased penetration of photovoltaic generation on power systems," *IEEE Trans. Power Syst.*, vol. 28, no. 2, pp. 893–901, May 2013.

[107] ——, "Small signal stability assessment of power systems with increased penetration of photovoltaic generation: A case study," *IEEE Trans. Sustain. Energy*, vol. 4, no. 4, pp. 960–967, Oct. 2013.

[108] B. Tamimi, C. Caizares, and K. Bhattacharya, "System stability impact of large-scale and distributed solar photovoltaic generation: The case of ontario, canada," *IEEE Trans. Sustain. Energy*, vol. 4, no. 3, pp. 680–688, Jul. 2013.

[109] M. Dreidy, H. Mokhlis, and S. Mekhilef, "Inertia response and frequency control techniques for renewable energy sources: A review," *Renew. Sust. Energ. Rev.*, vol. 69, pp. 144–155, 2017.

[110] Y. Bae, T.-K. Vu, and R.-Y. Kim, "Implemental control strategy for grid stabilization of grid-connected pv system based on german grid code in symmetrical low-to-medium voltage network," *IEEE Trans. Energy Convers.*, vol. 28, no. 3, pp. 619–631, Sep. 2013.

[111] W. A. Omran, M. Kazerani, and M. M. A. Salama, "Investigation of methods for reduction of power fluctuations generated from large grid-connected photovoltaic systems," *IEEE Trans. Energy Conver.*, vol. 26, no. 1, pp. 318–327, Mar. 2011.

[112] G. Delille, B. Francois, and G. Malarange, "Dynamic frequency control support by energy storage to reduce the impact of wind and solar generation on isolated power system's inertia," *IEEE Trans. Sustain. Energy*, vol. 3, no. 4, pp. 931–939, Oct. 2012.

[113] S. Chen, T. Zhang, H. B. Gooi, R. D. Masiello, and W. Katzenstein, "Penetration rate and effectiveness studies of aggregated bess for frequency regulation," *IEEE Trans. Smart Grid*, vol. 7, no. 1, pp. 167–177, Jan. 2016.

[114] J. C. Hernndez, P. G. Bueno, and F. Sanchez-Sutil, "Enhanced utility-scale photovoltaic units with frequency support functions and dynamic grid support for transmission systems," *IET Renew. Power Gen.*, vol. 11, no. 3, pp. 361–372, 2017.

[115] P. C. Sekhar and S. Mishra, "Storage free smart energy management for frequency control in a diesel-pv-fuel cell-based hybrid ac microgrid," *IEEE Trans. Neur. Net. Lear. Syst.*, vol. 27, no. 8, pp. 1657–1671, Aug. 2016.

[116] B. I. Craciun, T. Kerekes, D. Sera, and R. Teodorescu, "Frequency support functions in large pv power plants with active power reserves," *IEEE J. Em. Sel. Top. P.*, vol. 2, no. 4, pp. 849–858, Dec. 2014.

[117] C. Rahmann and A. Castillo, "Fast frequency response capability of photovoltaic power plants: The necessity of new grid requirements and definitions," *Energies*, vol. 7, no. 10, pp. 6306–6322, 2014.

[118] C. Rahmann, V. Vittal, J. Ascui, and J. Haas, "Mitigation control against partial shading effects in large-scale pv power plants," *IEEE Trans. Sustain. Energy*, vol. 7, no. 1, pp. 173–180, Jan. 2016.

[119] P. Zarina, S. Mishra, and P. Sekhar, "Exploring frequency control capability of a pv system in a hybrid pv-rotating machine-without storage system," *Int. J. Elec. Power Energy Syst.*, vol. 60, pp. 258 – 267, 2014.

[120] R. Luthander, D. Lingfors, and J. Widn, "Large-scale integration of photovoltaic power in a distribution grid using power curtailment and energy storage," *Sol. Energy*, vol. 155, pp. 1319 – 1325, 2017.

[121] A. Sangwongwanich, Y. Yang, and F. Blaabjerg, "Development of flexible active power control strategies for grid-connected photovoltaic inverters by modifying mppt algorithms," in *2017 IEEE 3rd International Future Energy Electronics Conference and ECCE Asia (IFEEC 2017 - ECCE Asia)*, Jun. 2017, pp. 87–92.

[122] ——, "High-performance constant power generation in grid-connected pv systems," *IEEE Trans. Power Electron.*, vol. 31, no. 3, pp. 1822–1825, Mar. 2016.

[123] A. Sangwongwanich, Y. Yang, F. Blaabjerg, and H. Wang, "Benchmarking of constant power generation strategies for single-phase grid-connected photovoltaic systems," *IEEE Trans. Ind. Appl.*, vol. 54, no. 1, pp. 447–457, Jan. 2018.

[124] H. D. Tafti, A. I. Maswood, G. Konstantinou, J. Pou, and F. Blaabjerg, "A general constant power generation algorithm for photovoltaic systems," *IEEE Trans. Power Electron.*, vol. 33, no. 5, pp. 4088–4101, May 2018.

[125] B. Crciun, T. Kerekes, D. Sra, R. Teodorescu, and U. D. Annakkage, "Power ramp limitation capabilities of large pv power plants with active power reserves," *IEEE Trans. Sustain. Energy*, vol. 8, no. 2, pp. 573–581, Apr. 2017.

[126] Y. Karimi, H. Oraee, M. S. Golsorkhi, and J. M. Guerrero, "Decentralized method for load sharing and power management in a pv/battery hybrid source islanded microgrid," *IEEE Trans. Power Electron.*, vol. 32, no. 5, pp. 3525–3535, May 2017.

[127] Y. Karimi, H. Oraee, and J. M. Guerrero, "Decentralized method for load sharing and power management in a hybrid single/three-phase-islanded microgrid consisting of hybrid source pv/battery units," *IEEE Trans. Power Electron.*, vol. 32, no. 8, pp. 6135–6144, Aug. 2017.

[128] M. Saleh, L. Meek, M. A. S. Masoum, and M. Abshar, "Battery-less short-term smoothing of photovoltaic generation using sky camera," *IEEE Trans. Ind. Inform.*, vol. 14, no. 2, pp. 403–414, Feb. 2018.

[129] X. Chen, Y. Du, H. Wen, L. Jiang, and W. Xiao, "Forecasting based power ramp-rate control strategies for utility-scale pv systems," *IEEE Trans. Ind. Electron.*, pp. 1–1, 2018.

[130] Y. Yang, E. Koutroulis, A. Sangwongwanich, and F. Blaabjerg, "Pursuing photovoltaic cost-effectiveness: Absolute active power control offers hope in single-phase pv systems," *IEEE Ind. Appl. Mag.*, vol. 23, no. 5, pp. 40–49, Sep. 2017.

[131] Y. Yang, H. Wang, F. Blaabjerg, and T. Kerekes, "A hybrid power control concept for pv inverters with reduced thermal loading," *IEEE Trans. Power Electron.*, vol. 29, no. 12, pp. 6271–6275, Dec. 2014.

[132] E. I. Batzelis, S. Papathanassiou, and B. C. Pal, "Pv system control to provide active power reserves under partial shading conditions," *IEEE Trans. Power Electron.*, pp. 1–1, 2018.

[133] A. Hoke, E. Muljadi, and D. Maksimovic, "Real-time photovoltaic plant maximum power point estimation for use in grid frequency stabilization," in *Proc. IEEE 16th Control Model. Power Electron. (COMPEL)*, July 2015, pp. 1–7.

[134] A. F. Hoke, M. Shirazi, S. Chakraborty, E. Muljadi, and D. Maksimovic, "Rapid active power control of photovoltaic systems for grid frequency support," *IEEE J. Em. Sel. Top. P.*, vol. 5, no. 3, pp. 1154–1163, Sep. 2017.

[135] A. Sangwongwanich, Y. Yang, and F. Blaabjerg, "A sensorless power reserve control strategy for two-stage grid-connected pv systems," *IEEE Trans. Power Electron.*, vol. 32, no. 11, pp. 8559–8569, Nov. 2017.

[136] A. Sangwongwanich, Y. Yang, F. Blaabjerg, and D. Sera, "Delta power control strategy for multistring grid-connected pv inverters," *IEEE Trans. Ind. Appl.*, vol. 53, no. 4, pp. 3862–3870, Jul. 2017.

[137] H. Xin, Y. Liu, Z. Wang, D. Gan, and T. Yang, "A new frequency regulation strategy for photovoltaic systems without energy storage," *IEEE Trans. Sustain. Energy*, vol. 4, no. 4, pp. 985–993, Oct. 2013.

[138] Y. Liu, H. Xin, Z. Wang, and T. Yang, "Power control strategy for photovoltaic system based on the newton quadratic interpolation," *IET Renew. Power Gen.*, vol. 8, no. 6, pp. 611–620, Aug. 2014.

[139] E. I. Batzelis, G. E. Kampitsis, and S. A. Papathanassiou, "Power reserves control for pv systems with real-time mpp estimation via curve fitting," *IEEE Trans. Sustain. Energy*, vol. 8, no. 3, pp. 1269–1280, Jul. 2017.

[140] J. Kivimki, S. Kolesnik, M. Sitbon, T. Suntio, and A. Kuperman, "Revisited perturbation frequency design guideline for direct fixed-step maximum power point tracking algorithms," *IEEE Trans. Ind. Electron*, vol. 64, no. 6, pp. 4601–4609, Jun. 2017.

[141] W. Xiao, W. G. Dunford, P. R. Palmer, and A. Capel, "Regulation of photovoltaic voltage," *IEEE Trans. Ind. Electron.*, vol. 54, no. 3, pp. 1365–1374, Jun. 2007.

[142] H. Al-Atrash, I. Batarseh, and K. Rustom, "Effect of measurement noise and bias on hill-climbing mppt algorithms," *IEEE Trans. Aero. Electron. Sys.*, vol. 46, no. 2, pp. 745–760, Apr. 2010.

[143] A. M. Latham, R. Pilawa-Podgurski, K. M. Odame, and C. R. Sullivan, "Analysis and optimization of maximum power point tracking algorithms in the presence of noise," *IEEE Trans. Power Electron.*, vol. 28, no. 7, pp. 3479–3494, Jul. 2013.

[144] V. V. R. Scarpa, S. Buso, and G. Spiazzi, "Low-complexity mppt technique exploiting the pv module mpp locus characterization," *IEEE Trans. Ind. Electron*, vol. 56, no. 5, pp. 1531–1538, May. 2009.

[145] S. Kolesnik, M. Sitbon, S. Lineykin, E. Batzelis, S. Papathanassiou, T. Suntio, and A. Kuperman, "Solar irradiation independent expression for photovoltaic generator maximum power line," *IEEE J. Photovoltaics*, vol. 7, no. 5, pp. 1416–1420, Sep. 2017.

[146] M. Kasper, D. Bortis, and J. W. Kolar, "Classification and comparative evaluation of pv panel-integrated dcdc converter concepts," *IEEE Trans. Power Electron.*, vol. 29, no. 5, pp. 2511–2526, 2014.

[147] W. Xiao, M. S. E. Moursi, O. Khan, and D. Infield, "A review of grid-tied converter topologies used in photovoltaic systems," *IET Renew. Power Gen.*, vol. 10, no. 10, pp. 1543–1551, 2016.